

# **Development of Optical Microchip Sensor for Biomolecule Detection**

A thesis submitted in fulfilment of the requirement for the degree of

## **Doctor of Philosophy**

**Engineering (Nanotechnology)**

By **Mahdieh Nemati**



**THE UNIVERSITY**  
*of* **ADELAIDE**

**School of Chemical Engineering**

**Faculty of Engineering, Computer, and Mathematical Sciences**

**The University of Adelaide**

**April 2018**



# DEDICATION

To My Parent

*with strong and gentle souls who taught me to believe in hard work  
and enriched me with their endless love*

&

My husband

*For his love, sacrifices and my shining armour*

**BLANK PAGE**

# TABLE of CONTENTS

Development of Optical Microchip Sensor for Biomolecule Detection	
Table of contents.....	i
Declaration.....	iii
Acknowledgments.....	v
Abstract.....	vii
List of publications.....	x
<b>Chapter 1.</b>	
Introduction and literature review.....	1
1.1. Biosensors background.....	2
1.2. Nanoporous Anodic Alumina (NAA).....	6
1.2.1. History of NAA.....	6
1.2.2. Nanofabrication of NAA.....	6
1.2.3. Structural engineering of NAA.....	11
1.3. Surface modification of NAA.....	15
1.3.1. Chemical vapour deposition (CVD).....	18
1.3.2. Metal sputtering deposition.....	20
1.4. NAA platform for optical biosensing.....	21
1.4.1. NAA based optical sensors.....	22
1.5. Reflectometric interference spectroscopy (RiFS).....	25
1.5.1. Principle.....	25
1.5.2. RiFS for sensing and biosensing.....	27
1.5.3. Nanoporous based RiFS sensors.....	29
1.5.4. NAA integrated with RiFS sensors.....	33
1.6. From sensing to applications: integration of molecular biology with biosensor devices.....	36
1.7. Research gaps for NAA based optical interferometry biosensing.....	37
1.8. Objectives.....	38
1.9. Thesis structure.....	39
1.10. References.....	41
<b>Chapter 2.</b>	
Method and Materials.....	65
2.1. Materials and chemicals.....	67
2.2. Electrochemical anodization for fabrication of nanoporous anodic alumina.....	67
2.2.1. The anodization system.....	67
2.2.2. Fabrication of nanoporous anodic alumina photonic films (NAA-PF).....	69
2.2.3. Fabrication of nanoporous anodic alumina rugate filter (NAA-RF).....	70
2.2.4. Fabrication of bilayered nanoporous anodic alumina (BL-NAA).....	70
2.3. Surface chemistry functionalization using CVD.....	71
2.4. Real-time monitoring of target analyte using reflectometric interference Spectroscopy (RiFS).....	72
2.5. Molecular genetic analysis.....	73
2.5.1. Genomic DNA preparation.....	73
2.5.2. Bioinformatics analysis.....	74
2.5.3. PCR amplification and sequencing.....	76
2.5.4. Padlock probe ligation and rolling circle amplification (RCA).....	76
2.6. References.....	78

<b>Chapter 3.</b>	
Enzymatic sensor combining NAA and RIfS.....	81
Label-free real-time quantification of enzyme levels by interferometric spectroscopy combined with gelatin-modified nanoporous anodic alumina photonic films.....	83
<b>Chapter 4.</b>	
NAA rugate filters combined with RIfS for pharmaceutical detection.....	100
Assessment of binding affinity between drugs and human serum albumin using nanoporous anodic alumina photonic crystals.....	102
<b>Chapter 5.</b>	
Bilayered NAA combined with RIfS for multi-point sensing purposes.....	118
Fabrication and optimization of bilayered nanoporous anodic alumina structures as multi-point sensing platform.....	120
<b>Chapter 6.</b>	
Integration of molecular biology with biosensor devices.....	145
Towards detection of single nucleotide polymorphism associated with phosphine resistance in <i>Tribolium Castaneum</i> using ligation-rolling circle amplification.....	147
<b>Chapter 7.</b>	
Conclusion and recommendations for future works.....	169
7.1. Conclusion.....	171
7.1.1. Summary.....	171
7.1.2. Label-free real-time quantification of enzyme levels by interferometric spectroscopy combined with gelatin-modified nanoporous anodic alumina photonic films.....	172
7.1.3 Assessment of binding affinity between drugs and human serum albumin using nanoporous anodic alumina photonic crystals.....	173
7.1.4. Structural engineering and optimization of bilayered nanoporous anodic alumina structures as multi-point sensing platform.....	175
7.1.5 Towards detection of single nucleotide polymorphism associated with phosphine resistance in <i>Tribolium Castaneum</i> using ligation-rolling circle amplification....	176
7.2. Recommendations for future works.....	176

# DECLARATION

I certify that this work contains no material which has been accepted for the award of any other degree or diploma in any university or other tertiary institution and, to the best of my knowledge and belief, contains no material previously published or written by another person, except where due reference has been made in the text. In addition, I certify that no part of this work will, in the future, be used in a submission for any other degree or diploma in any university or other tertiary institution without the prior approval of the University of Adelaide and where applicable, any partner institution responsible for the joint-award of this degree.

I give consent to this copy of my thesis when deposited in the University Library, being made available for loan and photocopying, subject to the provisions of the Copyright Act 1968. The author acknowledges that copyright of published works contained within this thesis resides with the copyright holder(s) of those works. I also give permission for the digital version of my thesis to be made available on the web, via the University's digital research repository, the Library catalogue and also through web search engines, unless permission has been granted by the University to restrict access for a period of time.

Name: Mahdiah Nemati

Signed ..... Date .....

**BLANK PAGE**



## ACKNOWLEDEMENTS

Thanks to the almighty as I am standing on the verge of a great milestone in my life.

I wish to extend my gratitude to a number of people that have made this research a success.

I would like to thank my supervisor, Professor Dusan Losic, for believing in me and being a great mentor. He has taught me that the key to a successful career is passion and hard work and for that I am sincerely grateful. During the last few years, his wisdom, immense knowledge and optimism has been a great motivation to me. He has created the foundation on which I have been able to build my research career on. It was a real privilege and an honour for me to share of him exceptional scientific knowledge but also of him extraordinary human qualities.

I also would like to thank to my co-supervisor Doctor Kelly Hill for her constant support, availability and constructive suggestions, which were determinant for the accomplishment of the work presented in this thesis.

A special thanks to Doctor Abel Santos, for his sincere cooperation in the work described in chapter 3 and 4.

I am indebted and grateful to Mrs. Zohreh Sirous from SAAB Galley for the financial support of my PhD scholarship. Apart from her support, I highly appreciate the many kindnesses and amazing moral supports she has given to me.

To all the members of the Losic Research Group, not forgetting the ones who have embarked on a different path to pursue their respective careers, I would like to express my deepest appreciation. I believe that no research is a success without a great team. I would like to extend particular appreciation to Shervin Kabiri, Dr. Diana N.H. Tran, Dr. Tushar Kumeria, Dr. Shaheer Guirguis Maher Makar, Dr. Tran Thanh Tung, Dr. Md Julker Nine, Ramesh

Karunagaran, Faisal Alotaibi, who in many ways made my PhD program easier to overcome every obstacle.

I must write a few words for my great uncle “Mr. Abbas Nemati” who is a true welcoming and wonderful person. I would like to express my deepest appreciation for his generous and constant encouragement throughout my research period.

In my radiant sentiment to place on record my best regards, deepest sense of gratitude to my landlord “Mrs. Jacqueline Cookes” for her caring and precious guidance which were extremely valuable for my study and life.

Last but not least, I am truly grateful to my beloved family: my fantastic father and mother, my husband, my merciful brother and his wife and my lovely and gorgeous niece. The feeling I have for them cannot be expressed in words. Their love and care are the greatest energy that drives me to take my dreams come true. I am indeed blessed to be surrounded by so much love.

## ABSTRACT

Optical sensors play vital roles in many applications in today's world. Photonic technologies used to design and engineer optical sensing platforms can provide distinctive advantages over conventional detection techniques. For instance, when compared to electronic and magnetic sensing systems, optical sensors require physically smaller equipment and have the capability for delivering more analytical information (e.g. spectroscopic signatures). In addition, demand for low-cost and portable bio-analyte detections is a growing area for applications in healthcare and environmental fields. Among other factors to achieve reliable results in terms of selectivity and sensitivity is key for the detection of bio-analytes with analytical relevance. Commonly used bio-analytical techniques (e. g. high performance liquid chromatography) have been appropriately designed based on qualitative and quantitative analysis. However, the requirement of expensive equipment, and complexity of procedures (e.g. biomolecule labelling, calibrations, etc.) restrict the board applicability and growth of these techniques in the field of biosensing. Optical sensors tackle these problems because they enable selective and sensitive detection of analytes of interest with label-free, real-time, and cost-effective processes. Among them, optical interferometry is increasingly popular due label-free detection, simple optical platforms and low-cost design. An ideal substrate with high surface area as well as biological/chemical stability against degradation can enable the development of advanced analytical tools with broad applicability. Nanoporous anodic alumina has been recently envisaged as a powerful platform to develop label-free optical sensors in combination with different optical techniques.

This thesis presents a high sensitive label-free biosensor design combining nanoporous anodic alumina (NAA) photonic structures and reflectometric interference spectroscopy (RIFS) for biomedical, food and agricultural applications. NAA is a suitable optical sensing platform due to its optical properties; a high surface area; its straightforward, scalable, and cost-

competitive fabrication process, and its chemical and mechanical stability towards biological environments. Our biosensor enables real-time screening of any absorption and desorption event occurring inside the NAA pores. A proper selection of bio-analytes were able to be detected using this platform which offers unique feature in terms of simplicity and accuracy. The most relevant components of this thesis are categorised as below:

1. *Self-ordered NAA fabrication and detection of an enzymatic analyte as a biomarker for cancer diagnosis:* Fabrication of NAA photonic films using two step electrochemical anodization and chemical functionalisation. Detection of trace levels of analyte enzyme and its quantification by selective digestion. The NAA photonic film with the enzyme acts as a promising combination for a real-time point-of-care monitoring system for early stages of disease.
2. *NAA rugate filters used to establish the binding affinity between blood proteins and drugs:* Design, fabrication, and optimisation of NAA anodization parameters using sinusoidal pulse anodization approach (i.e. anodization offset and anodization period) to produce rugate filter photonic crystals that provide two comparative sensing parameters. Establishment of highly sensitive and selective device capable for drug binding assessments linked to treating a wide range of medical conditions.
3. *NAA bilayers and food bioactive compound detection:* Design, fabrication, and optimisation of NAA anodization parameters (i.e. anodization time and number of anodization steps) to obtain NAA bilayered photonic structures that display the effective response of NAA geometry with different types of nano-pore engineering. The photonic properties of the NAA bilayer were studied at each layer of nano-structure under specific binding of human serum albumin and quercetin as target agent.

4. *Single nucleotide polymorphism (SNP) detection*: The design and implementation of a Ligation-Rolling Circle Amplification assay to detect a single nucleotide polymorphism associated with insecticide resistance in a pest beetle species, *Tribolium castaneum*. This proof-of-concept SNP detection assay has the potential to provide a method compatible with a biosensor platform such as NAA. This demonstrates the first step towards the potential development of a genotyping biosensor, and a real-world application of insecticide resistance monitoring.

The results presented in this thesis are expected to enable innovative developments on NAA sensing technology that could result in highly sensitive and selective detection systems for a broad range of bio-analytes detections.

## LIST OF PUBLICATIONS

According to the “Specifications for Thesis (2017)” of The University of Adelaide, the thesis contains the following list of publications that have been published during the period of my Ph.D. candidature. The works done during my Ph.D. have produced 5 journal papers and 2 conference proceedings/poster presentations.

### Peer-reviewed journal publication:

- 1- **Mahdiah Nemati**, Abel Santos, Tushar Kumeria, Dusan Losic. Label-free real-time quantification of enzyme levels by interferometric spectroscopy combined with gelatin-modified nanoporous anodic alumina photonic films. *Analytical Chemistry* 87 (17) (2015) 9016-9024.

[Impact factor: 6.320]

- 2- **Mahdiah Nemati**, Abel Santos, Cheryl Suwen Law, Dusan Losic. Assessment of binding affinity between drugs and human serum albumin photonic crystals. *Analytical Chemistry* 88 (11) (2016) 5971-5980.

[Impact factor: 6.320]

- 3- Cheryl Suwen Law, Abel Santos, **Mahdiah Nemati**, Dusan Losic. Structural engineering of nanoporous anodic alumina photonic crystals by sawtooth-like pulse anodization. *ACS Applied Materials & interfaces* 8(21) (2016), 13542-13554.

[Impact factor: 7.504]

- 4- Cheryl Suwen Law, Georgina M. Sylvia, **Mahdiah Nemati**, Jingxian Yu, Dusan Losic, Andrew D. Abell, and Abel Santos. Engineering of surface chemistry for enhanced sensitivity in nanoporous interferometric sensing platforms *ACS Applied Materials & interfaces* 9 (10) (2017), 8929-8940.

[Impact factor: 7.504]

- 5- **Mahdieh Nemati**, Abel Santos, Dusan Losic. Fabrication and Optimization of Bilayered Nanoporous Anodic Alumina Structures as Multi-Point Sensing Platform, *Sensors*, 18(2), 470 (2018).

[Impact factor: 2.677]

### Conference proceedings:

- 1- **Mahdieh Nemati**, Abel Santos, Tushar Kumeria, Dusan Losic. Gelatine-Modified Nanoporous Anodic Alumina Photonic Films for Detection of Enzyme Biomarkers by Interference Spectroscopy. **ICONN 2016**, International Conference on Nanoscience and Nanotechnology, February 7-11.

[Poster Presentation]

- 2- **Mahdieh Nemati**, Abel Santos, Dusan Losic. Advanced Engineering Of Nanoporous Anodic Alumina Rugate Filters For Pharmaceutical Applications. **Chemeca Conference 2016**, Chemical Engineering- Regeneration, Recovery and Reinvention. September 25-28.

[Poster Presentation]

**BLANK PAGE**



# CHAPTER 1.

---

## Introduction and Literature Review

**Chapter-1** provides introductory components of the thesis showing significant of the general field of the study followed by a comprehensive literature review of the current knowledge and discussing different methodologies used in this field. Finally, the outline of thesis structure and brief contents aid aims and objectives of the individual chapter is summarized.

## 1.1. Biosensors Background

A biological sensor, more commonly known as a biosensor, can be defined as an analytical device that combines a biological element with a physiochemical detector which can be easily understood by an observer <sup>1</sup>. A typical biosensor basically consists of a) a sensing platform; which enables to the target bio-element to bind or be captured, and b) a bio-transducer; which measures that recognition event and c) produce a readable signal. The signal can be an electronic, optical signal or visual colorimetric detection. The signal is then interpreted by a monitoring system; which displays the binding event as final output <sup>1-3</sup> (**Figure 1.1**). In general, biological receptors are involved with sensing platform and transducer to generate the corresponding detection signals. Looking into the past, the concept of biosensors underwent a transformation about 50 years ago, when analytical devices combined with transducers were developed to detect a concentration of chemical species in biological sources<sup>4-8</sup>. The idea unveiled the broader view to developing more efficient pharmaceutical, healthcare, and environmental sensing tools. In order to design effective biosensors, specific features have been typically investigated. For example, transducer type, labelling strategy, and surface chemistry are critical factors to consider in the development of biosensors <sup>2,4</sup>.

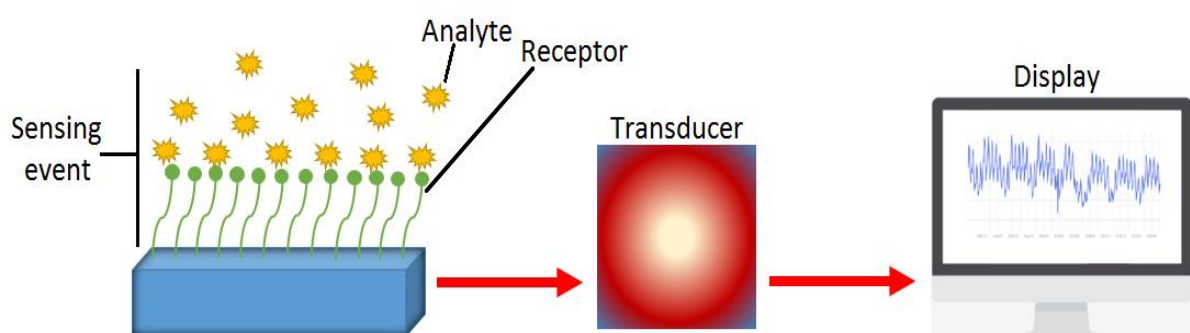


**Figure 1.1.** Schematic illustration of a typical label-free sensor and its main three components.

There are many types of biosensors based on detection principle or transducers but two most widespread types, are based on optical and electrochemical detection. Although electrochemical analytical sensing features greater sensitivity and precision for detection, these detection techniques require complicated and multi-faceted procedures. Optical sensing technology has been demonstrated to provide small footprint device, low power consumption, low cost, and easy preparation<sup>9</sup>. Due to those advantages, they are becoming more popular alternatives to electrochemical-based sensors in many biological applications<sup>10</sup>. In the past few decades, optical sensing has been adopted for use with a variety of bio-elements and using different types of spectroscopy for detection which are widely utilized in the field of biotechnology, biomedical applications and pharmaceuticals<sup>11-12</sup>. The other advantage of this method of optical transduction is eligibility to supply real-time monitoring, label-free, and parallel determination of sensing parameters<sup>13</sup>.

Most biosensors use a labelling strategy, which relies on radioactive or fluorescent tag molecules that are attached to the detection agent to screen the sensing reaction. However, although this label-based strategy can provide very sensitive detection limit (e.g. even up to single molecule), the labelling process has a high cost and is a labour intensive function<sup>14</sup>, which cause un-attractive feature of this method for specific biological applications. These limitations were addressed by label-free sensing devices, which do not require label molecules<sup>15</sup>. Label-free biosensing devices are usually based on changes in physical property such as density, refractive index and wavelength changes<sup>11, 16, 17</sup>. All these alterations act in response to binding of a receptor to the target molecule.

The optical biosensors have been demonstrated to be powerful analytical devices widely employed for the measurement of biomolecules, pharmaceutical agents, nucleic acid molecules for biomedical, pharmaceutical, environmental screening and toxic agent detection.<sup>18-22</sup>. In

addition to their analytical applications, optical biosensors become a key tool for characterization and quantifying biomolecular interactions and other fundamental phenomena<sup>22</sup>. Typically optical sensors can be classified based on detection principles including: UV-vis spectroscopy, optical waveguide spectroscopy, surface enhanced Raman spectroscopy, Refractometric, Surface Plasmon Resonance (SPR), reflectometric interference spectroscopy (RIfS), photoluminescence, and etc.<sup>23-27</sup>. Among all these techniques, SPR due to its high sensitivity has been most commonly utilised for a wide range of commercial applications specifically biological detection. However, SPR method suffers from some difficulties (e. g. failure to detect signals for fast reactions, the bulkiness of instrumentation and expensive, metal thickness accuracy for coatings, large sample volumes, and difficult to combine with other detection methods)<sup>28-30</sup>.

Recently, miniature and portable label-free biosensors are being developed to open the ability of on-site support for self-diagnosis applications. The need for fast diagnostics created an intensive research focus for point-of-care like devices. An active area of research with regards to these types of point-of-care devices is in the materials used to generate for optical signals and their association with highly selective and sensitive optical platforms. Nanostructural materials such as porous silicon, Si nanowires, gold nanoparticles, titania nanotubes, and nanoporous anodic alumina, graphene sheets, etc, are explored for this application<sup>31-35</sup>. Amongst this range of nano-optical materials, the combination of nanoporous substrates with optical sensing devices has been promising. For example, the integration of RIfS-based detection method with nanoporous materials depicted a clear functionality in biological trend<sup>26,27</sup>. In this regard, the nanoporous structure provides a high surface area to a volume ratio which increases the possibility for a higher number of receptors, and therefore an increased possibility of detecting a receptor-analyte interaction. Herein, RIfS has been proven as a sensitive and simple sensing method integrated nanoporous structure<sup>26</sup>. This optical

technique is based on white light interference directed vertically at a nanoporous thin film. This causes partial reflection of beams at certain wavelength which results in an interference spectrum which can be detected by single beam and microprocessor spectrometry. This resulting interference spectrum allows one to observe the binding behaviour of interacting molecules. Any association or dissociation of analyte molecules causes a change in physical thickness of a thin layer. The physical thickness monitoring fulfils a mathematical calculation which also depends on the effective refractive index of the thin film. This screening can provide real-time processing with exclusive dynamics about the binding reaction <sup>36</sup>.

This PhD thesis is mainly focused on exploring RIfS using electrochemically engineered nanoporous anodic alumina (NAA) for platform a low-cost, easy-to-use, simple, portable, and sensitive biosensing system for versatile biomedical and industrial applications. For this purpose, NAA platform is designed and engineered with optimised pore structures features such as pore size geometry to advance their performance for RIfS based biosensing. Major perspectives of this thesis are; a) fabrication and optimization of pore geometry for NAA structural engineering to enhance optical sensitivity, b) surface chemistry modification for high selectivity towards biomolecules, c) real-time screening of the binding event between receptor and biomolecule analytes using RIfS detection method. d) isolation and purification of target agents from living sources (i.e. genetic material from insect cells), The following literature review will provide a comprehensive collection on the efforts for developing NAA structural engineering and surface chemistry modification strategies for bio-analytes based on RIfS optical system.

## **1.2. Nanoporous Anodic Alumina (NAA)**

### **1.2.1. History of NAA**

NAA is a self-ordered material with honeycomb-like structure and high density arrays of uniform and parallel nanopores formed by electrochemical oxidation of aluminium in liquid electrolytes (anodization) in particular conditions (i.e. electric current, voltage, temperature, and etc.). Anodization of aluminium has been discovered since early last century in the 1930s and further elaborated in 1950s-1970s for corrosion protection and as decorative coatings<sup>37-39</sup>. Starting in the late 1980s, NAA began to attract interest in the field of nanotechnology due to its uniform nanostructure particularly for the deposition of the arrays of nanowires<sup>40-42</sup>. Later in the 1990s, nanofabrication of NAA template appeared<sup>43-47</sup>. Then, NAA becomes very popular for design and synthesis of different nanostructures (i.e. nanowires and nanotubes). NAA-based nanomaterials have a wide range of applications including nanoelectronics, photonics devices, energy conversion to nanoporous substrates, nanotags for bioanalysis, and so on<sup>48-52</sup>. Currently, the use of NAA in nanotechnology continues to grow rapidly. The significance of NAA in science and technology has been understood by the fact that its chemistry and structure could be precisely and accurately engineered at the nanoscale over very large areas and in practical formats, enabling development of new materials and products with desired properties and functionality<sup>53</sup>.

### **1.2.2. Nanofabrication of NAA**

The development of aluminium anodization created a huge interest to discover more about this material and as a result, more efforts were put in to research its chemical and physical properties<sup>39</sup>. Electrochemical anodization on aluminium have been studied in a wide array of acidic electrolyte including oxalic acid, phosphoric acid, citric acid and sulfuric acid using both

AC and DC power supply<sup>25,27,54</sup>. The effort placed to understand the mechanism of aluminium anodic oxide construction as well as the effect of fabrication parameters on porous morphology through current density and temperature. **Figure 1.2** illustrates the pore geometry features of aluminium oxide structure. Geometry criteria of NAA such as pore diameter  $d_p$ , interpore distance  $d_{int}$ , and pore length  $L_p$  have been considered as significant features affecting NAA sensing properties<sup>55-61</sup>.

Two-step fabrication process of nanoporous anodic alumina structure was discovered by Masuda and colleagues as the method to prepare highly ordered porous structure with a high level of reproducibility<sup>47,62</sup>. This approach elucidated that the surface of aluminium substrate forms like dimples and pits during the first step of anodization. Although, after the first step the nanoporous oxide layer is removed in a selective way, the created patterns act as nucleation and reproduction sites for self-ordering of cylindrical nanopores. The advantages of this two-step anodization approach are as a low-cost production, simple and easy process, and capability of large-scale fabrication for commercial purposes. This can compete to techniques like lithography which are expensive and complicated. A simple illustrative scheme of electrochemical setup (**Figure 1.2c**) is presented to produce NAA with cylindrical pore structure (**Figure 1.2b**). It is schematically shown that required size of Al foil is packed in a specific holder, so called anodization cell. Whilst, the anodization cell contains a certain aqueous acid electrolyte, is connected to a power supply as an anode electrode and platinum wire which is installed in anodization cell acts as a cathode electrode. This designed connection with the application of specific voltage causes electrochemical circuit. This reaction starts nucleation and grows perpendicular nanopores on Al surface material.

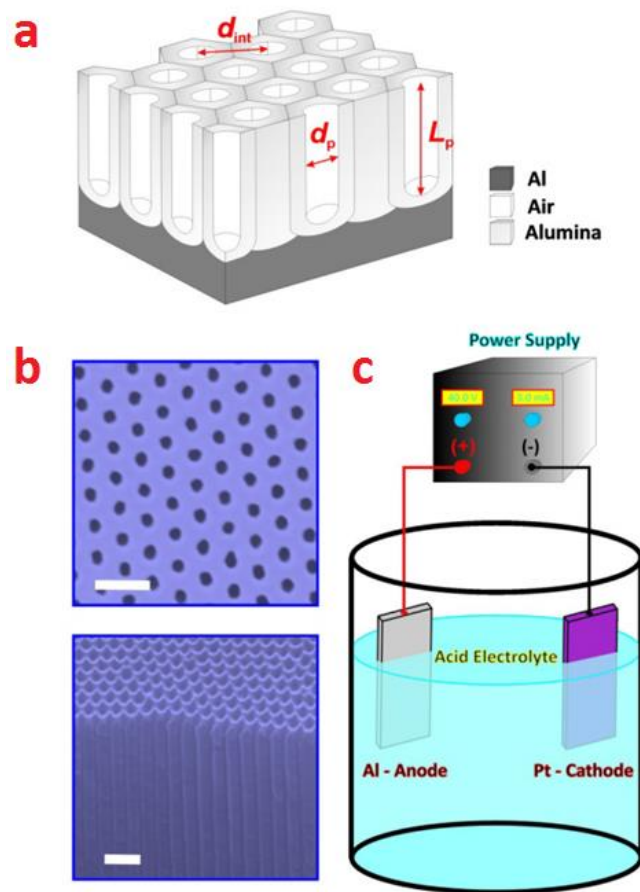


**Figure 1.2.** Schematic illustration of a basic electrochemical anodization cell for NAA fabrication (Source [27]). (a) Geometry criteria of NAA (e.g. pore diameter  $d_p$ , inter-pore distance  $d_{int}$  and pore length  $L_p$ ). (b) Top and cross-sectional view (scales bar 400 nm and 250 nm, respectively).

In terms of the nanostructure of anodised alumina, scanning electron microscopy (SEM) technology displayed hexagonal arranged shape cells with cylindrical nanopores perpendicularly to the aluminium substrate (**Figure 1.3**).



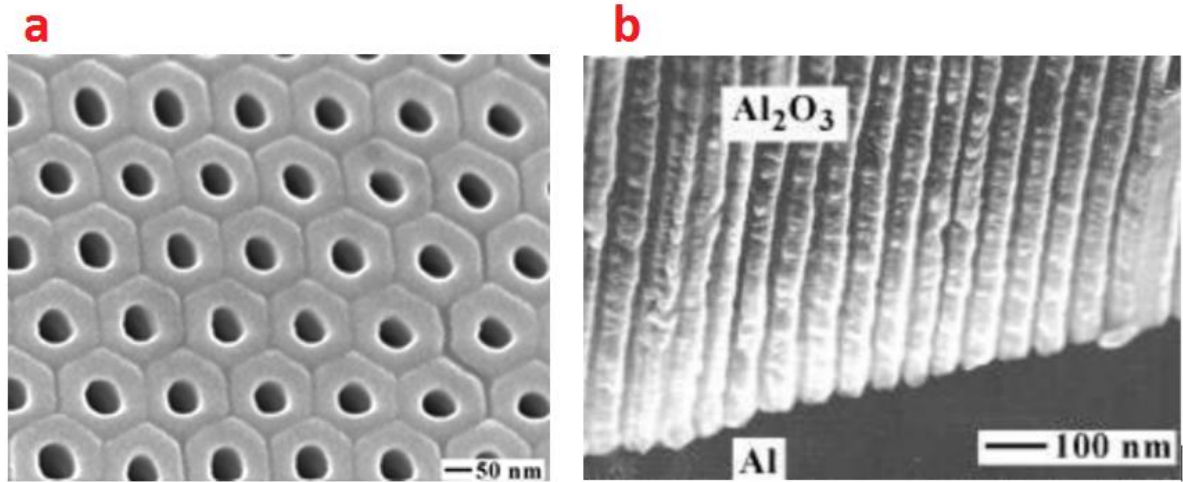


**Figure 1.3.** SEM images of typical cell configuration of perfectly ordered NAA fabricated using electrochemical anodization. a) Hexagonal arrangement of NAA. b) Cross sectional view of a typical NAA. Both images show the perfect organisation of nanopores with cylindrical structure (source [63]).

The electrochemical synthesis of the self-ordered and perpendicular nanopores is basically a steady state reaction of two main processes; the first one is the foundation of aluminium oxide ( $\text{Al}_2\text{O}_3$ ) and second step of oxide layer dissolution at the specific pore nucleation sites <sup>64</sup>. This mechanism creates a barrier layer of  $\text{Al}_2\text{O}_3$  which grows at the interface of Al through electrostatic attraction between charged ions (e. g.  $\text{Al}^{3+}$  and  $\text{O}^{2-}$ ). However, as the second process, the produced  $\text{Al}_2\text{O}_3$  dissolves at the interface of electrolyte. This results in a distribution of electric field leading to localized nanopore growth. On Second,  $\text{Al}_2\text{O}_3$  is dissolved at the alumina-electrolyte interface due to uneven distribution of electric field on the oxide layer resulting in localized heating and dissolution. Therefore, the formation of  $\text{Al}_2\text{O}_3$  is continuous reactions of dissolution of  $\text{Al}_2\text{O}_3$  and diffusion of Al cations whilst generating hydrogen ( $\text{H}_2$ ) and oxygen ( $\text{O}_2$ ) molecules. The following equations explain the electrochemical reactions during NAA production:

i) Formation of alumina (alumina- aluminium interface)



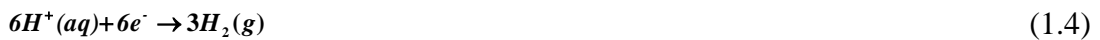
ii) Dissolution of alumina (alumina-electrolyte interface)



iii) Diffusion of aluminium cations (oxide barrier layer)



iv) Hydrogen production (electrolyte-platinum interface as cathode)



v) Oxygen production (electrolyte-alumina interface as anode)



The produced NAA pores are determined as certain structural parameters such as pore length;  $L_p$ , pore diameter;  $d_p$ , interpore distance;  $d_{int}$  and oxide barrier layer thickness;  $S_{obl}$ . These parameters are described in **Figure 1.3a**. It is well-proved that these nanopores structural parameters can be accurately tuned via anodization conditions. For example, it has been reported that pore diameter and pore length can be modified in the range of 10-400 nm and from nm to  $\mu m$ , respectively. Barrier layer thickness also ranges between 30-250, and interpore distance between 50-600 nm<sup>11-13, 25</sup>. As mentioned above, this ability to tune the pore structure of NAA is a result of anodization parameter modification<sup>64, 65</sup>.

In principal, the anodization parameters including applied current density, temperature, electrolyte type and concentration and have been known the most effective parameters in order to control the pore geometry of the NAA. Generally, an aqueous solution of oxalic acid ( $H_2C_2O_4$ ), phosphoric acid ( $H_3PO_4$ ), and sulphuric acid ( $H_2SO_4$ ) used to prepare NAA with specific geometry at 40, 195, and 25 voltage, respectively<sup>66-71</sup>. Besides all these acid electrolytes, other diverse acid electrolytes have been utilised for the process of NAA fabrication, including tartaric, malonic, citric, maleic and sulfamic acids<sup>72-77</sup>. However, it was

understood that the nanopores from the second group of electrolytes are not well-ordered. On the other hand, low or mild electric field condition, called mild anodization (MA) and high electric field condition, called hard anodization (HA) addressed slow and fast growth rate of nanopores, respectively. MA regime offers slow and rate-limited ionic transport reactions across Al-Al<sub>2</sub>O<sub>3</sub> interface whilst HA processed nanopore growth tens of time higher<sup>54, 56-59, 78</sup>. Note that, the pore geometry can be engineered by post processing steps like wet chemical etching which provides specific pore shape and dimensions. Therefore, a variety of nanopore geometries have been fabricated by modifying of anodization conditions including funnel tubes, multi-structured nanopores and periodically perforated pores<sup>79-85</sup>.

### **1.2.3. Structural Engineering of NAA**

It is explained in the previous part that by applying a different range of electrochemical anodization approaches, specific pore geometry (i.e., porosity, thickness, and multilayered structure) can be designed. The ability to engineer the geometry of NAA structure has encouraged researchers to exclusively produce nanostructures with specific optical properties such as distributed Bragg reflectors (DBRs), rugate filters, microcavities and waveguides, multilayered NAA and other photonic and optical structures<sup>27</sup>. To the purpose, the type and protocol of anodization (i. e., alternating current, voltage or duration of anodization process) and anodization profiles (i.e., sinusoidal, pseudo-sinusoidal, stepwise, saw-like and so on) are mainly considered<sup>27</sup>. The specifically design of morphology and geometry of NAA and consequent tune light interaction lead to optimise and develop optical properties of NAA (i.e., effective medium)<sup>86-89</sup>.

Cyclic anodization approach using periodic and slow changes of electrical signals opened up an innovative perspective offering controlled morphology of pore structure with periodic changes of shapes and diameters <sup>80</sup>. This periodic modulation could effectively modulate light reflection with periodic changes of shapes and diameters. Many exciting applications <sup>90</sup> based on these nanostructured periodic structures of NAA, the Distributed Bragg reflector NAA-DBR structure was demonstrated with periodically compositional of MA and HA regimes, studies showed that porosity of NAA can be tailored with modified light reflection and two different active ranges of wavelength. This matter depicted the important role of the nanostructure with optical characteristics. Through adjusting anodization temperature between 7 to 14°C during NAA-DBR fabrication was also possible to tune the transmission spectra in the specific desired wavelength range <sup>91</sup>. The stacked multiple layers of DBR could cover the transmission peak in the whole visible light range. Again, utilizing cyclic anodization approach, a simplified voltage cycle NAA-DBRs were fabricated in depth nanopore engineering, which resulted to modulate transmittance criteria in the range of visible to near infrared <sup>92</sup>. Ferré-Borrull and colleagues further investigated the transmittance modulation of NAA-DBRs considering anodization time, number of anodization cycles, and pore widening time <sup>93</sup>. By means of this investigation, it obtained the contribution of a higher number of cycles in order to enhance the range of wavelengths that can be reflected. Anodization temperature was also recognized as a crucial factor which linearly rates 42 nm wavelength redshift per 1°C. However, the anodization temperature change did not affect noticeably the obtained ranges of reflected wavelengths or subsequent pore widening.

NAA rugate filters (NAA-RFs) were fabricated by others and our group under galvanostatic anodization using sinusoidal current signal showing new possibility to engineer complex NAA structures and generate exciting optical and photonic properties unlike NAA-DBRs, the photonic structure of NAA-RFs, displayed single section reflectivity that is highly

dependent on the period of a sinusoidal current profile as well as pore opening time <sup>94</sup>. The sinusoidal anodization profile was used for fabrication of NAA-RFs controlling different anodization parameters such as anodization period, anodization offset, and anodization current density that showed reflection response across UV-visible-infrared spectrum <sup>95</sup>.

The other efforts focused on controlling pore diameter modulation of NAA structure utilising discontinuous anodization approach <sup>96</sup>. In that study, the generation of pore modulation was performed by voltage pulses under MA and thermal-acidic conditions. The pore modulation morphology could be controlled by tuning the relax time between consecutive voltage pulses. Thus, the origin of the resulting NAA structure was attributed to the formation of a gel-like layer under particular thermal-acidic conditions. Another innovative geometry control approach for NAA structure is reported multistep mild anodization <sup>97</sup>. Using this approach, anodization profile could be precisely tailored by interactive control of anodising time, etching time, and cyclic times obtain funnel, pencil, parabola, cone, and trumpet pore shapes. Funnel-like pore geometry of NAA is reported in several studies <sup>81, 82, 98</sup>. This multilayered NAA structure has larger pore diameter on the top layer and smaller pore diameter at the bottom layer which is generally produced by following sequentially anodising and pore widening steps. Using the modulation approach a precisely controlled of pore length was also carried out <sup>81</sup>.

Inverted type of funnel-like NAA structures were fabricated with increasing pore diameter from top to bottom <sup>98</sup>. This fabrication approach utilised by the combination of annealing temperature, anodization steps and chemical etching. The fabrication method was performed by taking advantage of varied chemical dissolution rates of NAA with annealing temperature leading in-depth engineering of nanopores. Similar to the typical funnel-like NAA, the resulting inverted funnel-like NAA featured a multilayered structure with photonic properties. The other represented multilayered of NAA are stratified, hierarchical, and three-dimensional

which have been fabricated using innovative anodization techniques <sup>79-85, 97-99</sup>. Hierarchical pore geometry of NAA depicted hexagonal concavities of interior nanopores which generated by changing anodization parameters (e. g. anodization voltage, type and concentration of acid electrolyte) during the second step of anodization <sup>99</sup>.

**Figure 1.4** illustrates SEM images of some of the most representative NAA structures fabricated by different electrochemical anodization approaches. The figure obviously shows the effect of mild/hard anodization regimes and anodization parameters on pore length, pore diameter and constant interpore distance involved in engineered NAA structure.

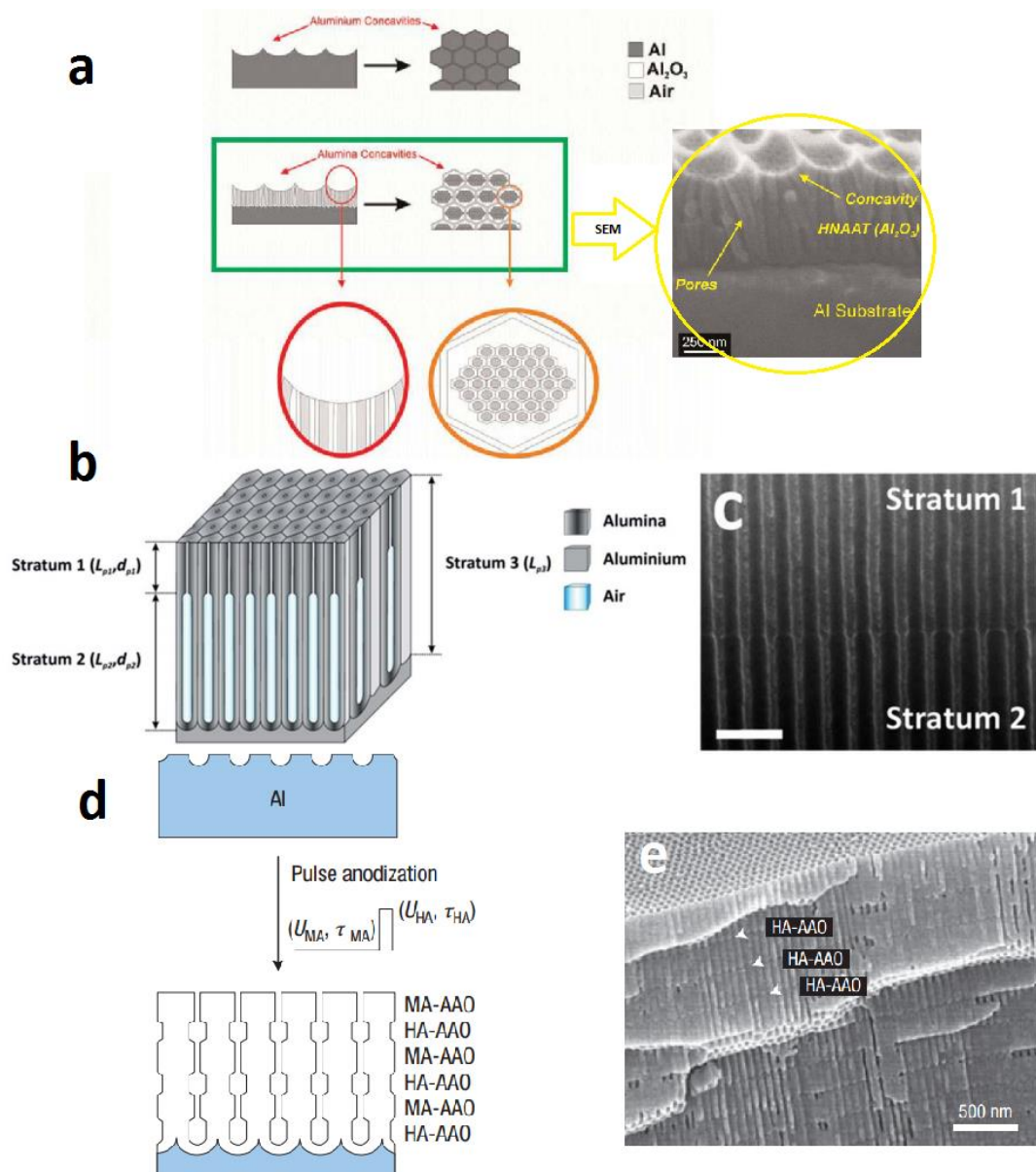


**Figure 1.4.** (a) Schematic illustration for cross-sectional and top view SEM images for hierarchical NAA structure (b) and (c) Schematic illustration for cross-sectional and top view SEM images for stratified inverted NAA structure (d) (e) cross-sectional and top view SEM images for 3D NAA structure by switching the anodization between MA and HA regimes (sources [99], [98], and [79]).

### 1.3. Surface Modification of NAA

During the chemical dissolution of NAA with electrolytes (e. g. oxalic acid, sulfuric acid and phosphoric acid), some electrolytic impurities (e. g. oxalate, sulfate, and phosphate) remain and distribute as stratified-structure of NAA. It is shown that the chemically stratified structure

of NAA exists as gradient layers where outer layer are predominantly accumulated by impurities than inner layers, which are mainly pure  $\text{Al}_2\text{O}_3$  (**Figure 1.5**). This onion-like configuration is introduced as a variety of layers<sup>98</sup>. A self-colouring strategy with the aid of photoluminescence characteristics measurement established the concept for presence incorporated chemical layers after specific chemical etching steps<sup>100</sup>.

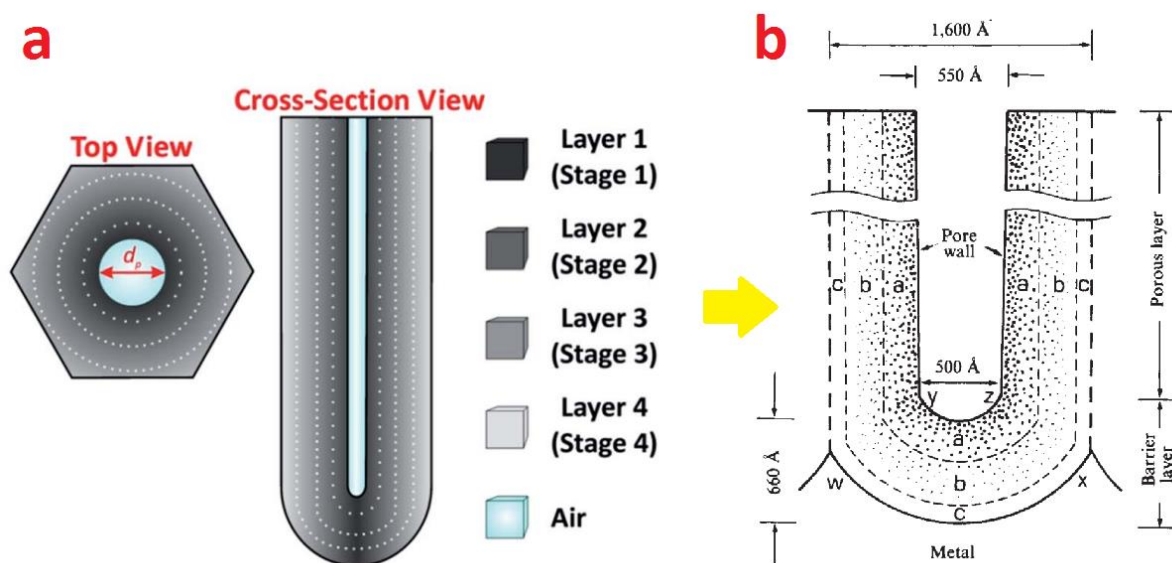


**Figure 1.5.** Schematic illustration of chemically stratified structure of NAA. (a) Top and cross-sectional view of NAA showing four different stage of NAA dissolution under acidic condition, which is configured onion-like structure (source [98]). (b) The distribution of color in a NAA pore based on gravity, indication coloured materials locate in outer region with decreasing steeply in the next regions (source [100]).

The presence of acidic impurities in the stratified-structure of NAA makes it possible to activate hydroxyl groups (-OH) on the outer layer. Hydroxyl groups can be easily modified with different chemical functionalisation protocols. Chemical functionalisation of NAA surface is required due to two main reasons including NAA structure protection against acidic analytes and creating selective surface chemistry for specific analytes. The surface chemistry modification techniques for NAA has been reviewed in two major division including wet-chemical and gas-phase techniques<sup>84</sup>. Jani *et al.* categorized typical chemical techniques as self-assembled monolayers, polymer modifications, electrochemical deposition of metals, sol-gel chemistry and electro-less metal deposition. Other techniques in gas-phase include



chemical vapour deposition, thermal vapour deposition, atomic layer deposition and plasma polymerization. These techniques can be combined for the specific application (e. g. molecular separation, biosensing and drug delivery and others) <sup>101, 102</sup>. Note that, the further surface functionalisation of NAA is required for immobilisation of specific target molecules (**Figure 1.6**).

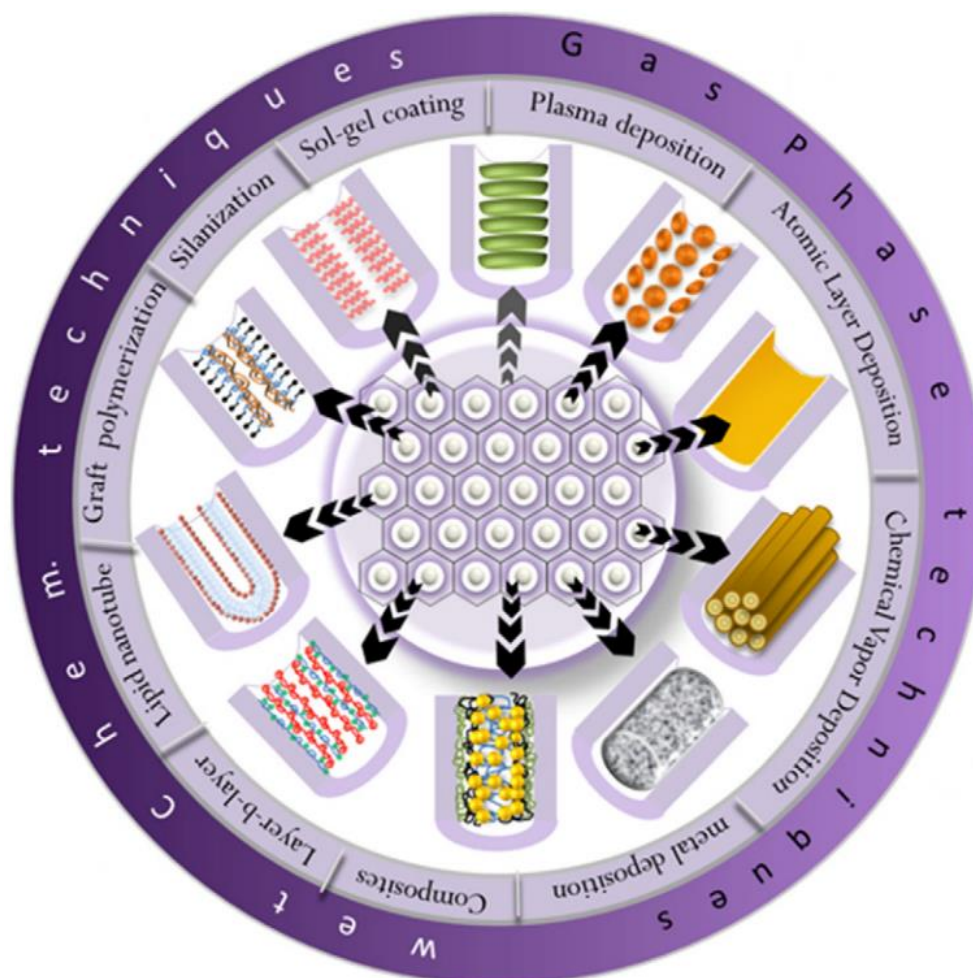


**Figure 1.6.** The range of approaches can be utilised for NAA surface modification via two main categories of gas phase and wet chemical technique (source [84]).

Herein, a brief review of the main approach used to modify NAA surface chemistry in this project namely gas phase technique is presented. Two methods of chemical vapour deposition and metal sputtering are mainly considered. Chemical vapour deposition (CVD) technique provides the chemically selective surface of NAA for binding to specific target analyte

molecules whereas sputter coating of metal is used for enhancing the reflection intensity of the NAA based biosensing platform.

### 1.3.1. Chemical Vapour Deposition (CVD)

Chemical vapour deposition involves the reaction of gaseous reagents which are activated by light, heat or plasma and in order to form a stable film on a substrate <sup>103</sup>. This technique offers fast growth rate of molecules deposition with excellent control of coating thickness and homogenous coverage. A number of applications including carbon layers growth on anodic aluminium oxide (AAO), aminosilanes, phenylphosphonic acid and others have been successfully prepared onto NAA surface for specific applications <sup>104-107</sup>. Amongst these surface activating agents, aminosilanes are identified as stable molecules due to activation of strong covalent bonds of Al-O-Si (**Figure 1.7**). The approach employs hydroxyl groups of inheriting NAA surface by reacting them with aminosilanes and then subsequent functionalisation can be easily possible using primary amine modification protocols. Furthermore, it is proven that silanisation of NAA for subsequent bio-molecule immobilisation is preserved route <sup>108-110</sup>. In this thesis, silanisation process is selected due to its stability and versatility towards biomolecules during sensing process.

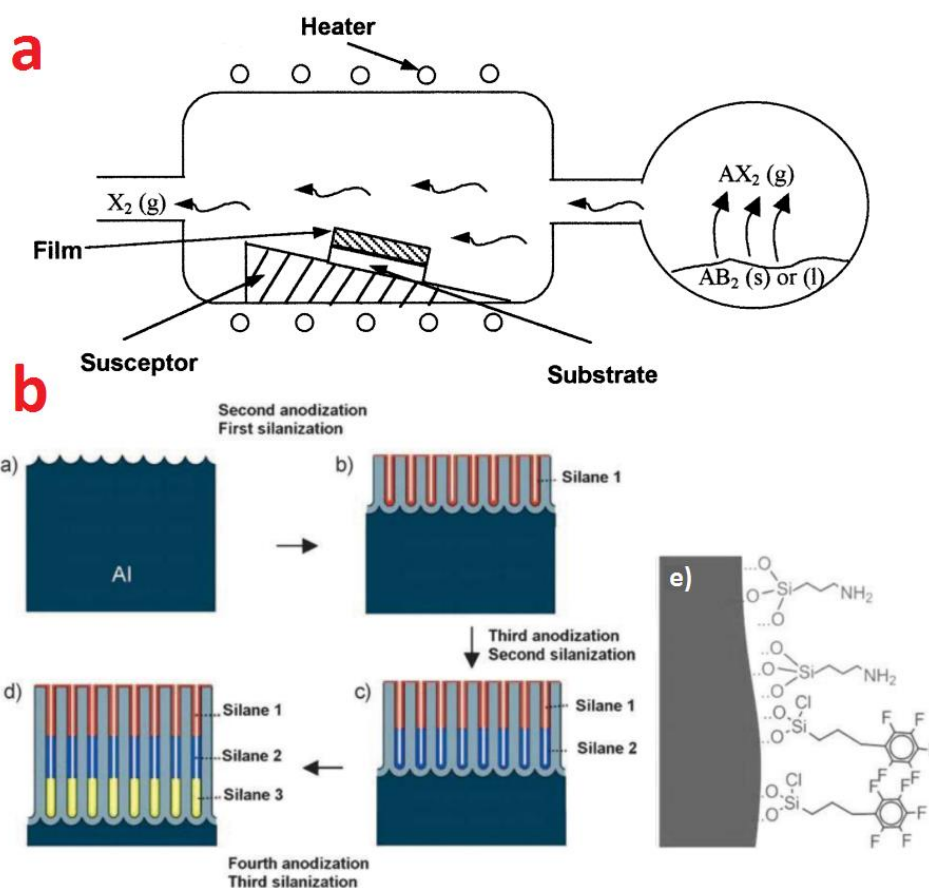


**Figure 1.7.** Chemical vapour deposition technique and its application for silanisation of NAA. A) Schematic diagram of CVD process illustrating formation of a stable solid coating from liquid/solid chemical by gas phase reaction which occurs near a heated surface (source [103]). B) Multi-layered surface functionalization of multi-layered NAA using three types of silane molecules (source [107]).

Several strategies to tailor surface wettability of NAA has been explored in order to tune its hydrophobicity characteristics. For example, octadecyltrimethoxysilane were utilized to enhance the hydrophobicity behaviour for membrane concepts <sup>111</sup>. In that way, the nanopore alumina membrane was so hydrophobic that they were not wetted by water. In the case of mineral oil separation, transport mechanism involved in the solvent extraction of oil-phase which are confined to the pores. Subsequently, the membrane showed better selective transport than the typical membrane. Other hydrophilic groups used with silane for functionalisation are reported as poly (ethylene-glycol)-silanes, ethoxy-silanes and others <sup>112, 113</sup>. Besides tuning the surface wettability of NAA membrane, biocompatibility control of silane functionalised of pore

structures is also investigated as a function of cellular immunoisolation <sup>114</sup>. The results depicted silane functionalisation is a safe method for biomolecules under vivo and vitro conditions. Therefore, they were vastly used for immobilisation biomolecules such as cells and biotin <sup>115</sup>, <sup>116</sup>.

Amino-propyltriethoxy silane (APTES) is the most popular used silane for the purpose of surface chemistry modification to attach biomolecules using amino groups. APTES-modified NAA templates have been used to immobilize nanoparticles (e. g. Au and Pd nanoparticles), or nanotubes inside nanopores in order to make a conductive structure <sup>117</sup>. Losic and co-workers demonstrated the surface modification of NAA with layers of silanization. Using different types of silanes (e. g. N-triethoxysilylpropyl-(O-polyethyleneoxide) urethane (PEG-silane), pentafluorophenyl-dimethylpropylchloro-silane (PFPTES), and APTES), a multi-functionalities surface was obtained <sup>107</sup>. These studies showed that NAA can be precisely modified with desired surface chemistry (silane molecules) and used for immobilization of biomolecules required for biosensing.

### **1.3.2. Metal Sputtering Deposition**

Sputtering deposition known as a physical vapour deposition has been explored using a variety of metals including silver, gold, platinum, nickel, titanium, etc. This solid modification approach is frequently used to improve the chemical stability of NAA material, conductivity, electrochemical, transport and more important making highly attractive surface for optical properties <sup>118</sup>. In this regards, it provides a convenient and powerful tool for fast and controlled deposition of metal thin-films. For example, pieces of research have been exploited hexagonal arrangement of NAA membranes with the silver coating to prepare SERS substrates <sup>119, 120</sup>. It is reported an Ag layer deposited film by using a direct-current magnetron sputtering system had high Raman signal due to abundance of hot spots from silver nanoparticles <sup>119</sup>, **Figure 1.8**,

Other studies have discussed sensor's sensitivity for preparing active sensing platforms for fibre Bragg grating (FBG) sensors where coated FBG showed significant optical response compared to standard FBG <sup>121-123</sup>. Furthermore, the sputtering deposition capability was enormous for using it as a fantastic model for enhancement of optical spectral of NAA coated with gold, especially gold offered a perfect surface chemistry for biomolecules <sup>124, 26</sup>.

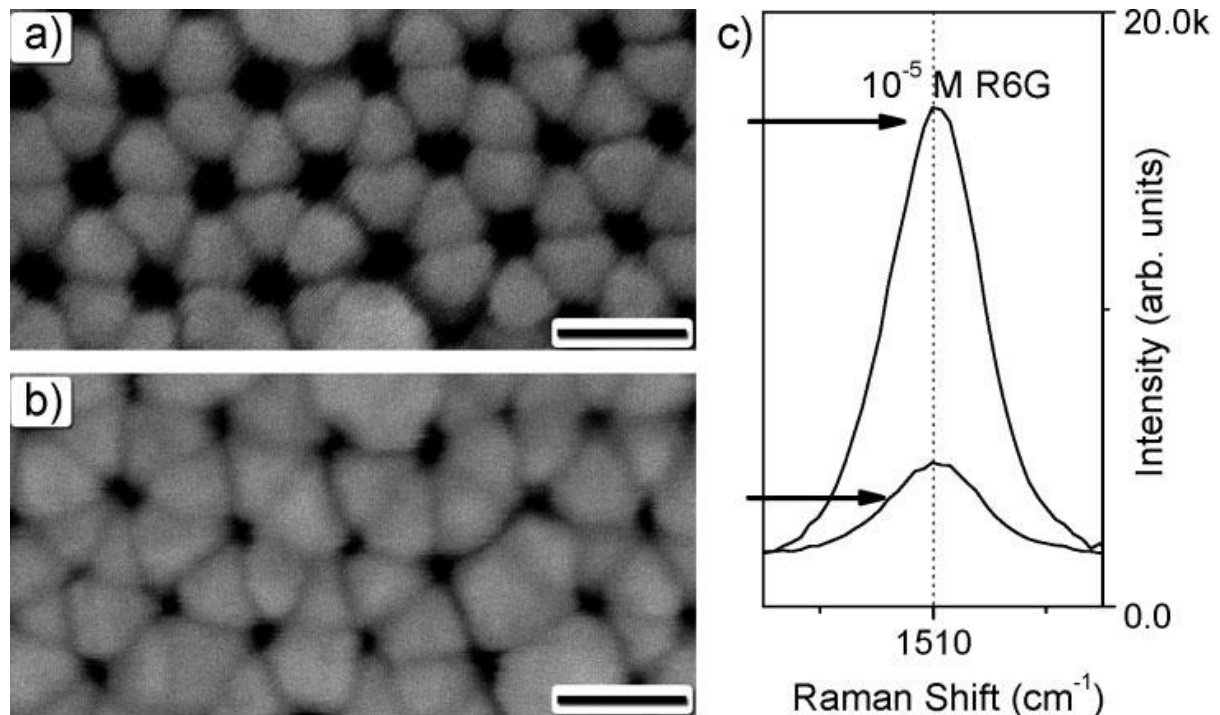


**Figure 1.8.** SEM images obtained from the Ag-coated AAO membranes formed using different Ag sputtering times of (a) 15 and (b) 20 min. The scale bar is 100 nm. (c) SERS spectra of Rhodamine 6G-adsorbed Ag-coated polyacrylic acid membranes corresponding to those in (a) and (b), demonstrating the intensity variation of the SERS signal at 1510  $\text{cm}^{-1}$ .

## 1.4. NAA Platform for Optical Biosensing

NAA provides many advantages due to their chemical stability for biosensing providing stable optical signals without further passivation with biomolecules conditions <sup>125</sup>. NAA can interact with light in a stable signal and generate extraordinary reflectance, transmittance, and absorbance. In particular, NAA with photoluminescence (PL) light emission display inimitable optical interactions. It is worth noticing that the light interaction of NAA is highly relevant to its chemical and structural features. NAA displays excellent transmission, reflection, wave-

guiding, and photoluminescence properties<sup>25, 27, 126</sup>. These optical responses met the requirements for designing highly selective and sensitive biosensors. In addition, the flexibility of NAA based on miniaturization and integration into microfluidic devices make another interesting feature for developing portable biosensing devices<sup>11-13, 67</sup>. Other optical advantages of NAA are that the nanoporous structure can be engineered using different electrochemical anodization approaches as exclusively mentioned in previous parts and enhance its inherent optical properties. This is the fundamental aspect to obtain higher sensitive biosensors. Additionally, the high surface area of NAA pores allows biomolecules to accommodate a large number. This requires the capability of chemical assembly to operate the analyte-receptor binding event.

#### **1.4.1. NAA Based Optical Sensors**

Regarding these excellent optical features of NAA mentioned in previous sections this section will review the new generation of optical biosensors based on NAA platform has been explored for the purpose of bio-analytes detection. In this context, NAA optical biosensors displayed significant sensitivity and selectivity detection in a range of applications such as environmental, clinical, food control and so on. They are mostly focused on integrating Localised Surface Plasmon Resonance (LSPR), photoluminescence (PL), Surface-enhanced Raman scattering (SERS) and RIfS techniques with NAA platform (**Figure 1.9**). Comprehensive review studies about optical sensing based on NAA is provided in reference<sup>25, 27</sup>. Furthermore, **Table 1**, summarized the most advances in the development of optical NAA sensors for the application of biomolecules.

In overall, NAA combined with RIfS generated well-resolved peaks capable of label-free and real-time in situ monitoring of binding events. This caused high interests to use NAA-RIfS sensing system in particular through miniaturisation for real-life applications.

**Table1.** Summary of optical sensing systems based on nanoporous anodic alumina, their detection technique, bio- applications, performance and references.

Optical Technique	Analyte	Detection Limit/Concentration	Ref.
PL	Trypsin	0.1 mg·mL <sup>-1</sup>	[127]
	Trypsin	40 µg·mL <sup>-1</sup>	[128]
	DNA	100 mM	[129]
LSPR	Avidin	10 µg·mL <sup>-1</sup>	[130]
	Anti-5-Fluorouracil	100 mg·mL <sup>-1</sup>	[130]
	DNA	10 pM	[131]
	BSA	60 nM	[132]
	Invertase	10 nM	[133]
	Melittin	100 ng·mL <sup>-1</sup>	[130]
	SERS	Para-Nitrophenol	10 <sup>-6</sup> M
	Cancer cell	Single cell	[135]
	Cytochrome <i>c</i>	1 mg·mL <sup>-1</sup>	[136]
RIS	DNA	2 nmol·cm <sup>-2</sup>	[137]
	Tumor Cells	1000 cells·mL <sup>-1</sup>	[36]
	Immunoglobulin	0.1 mg·mL <sup>-1</sup>	[138]

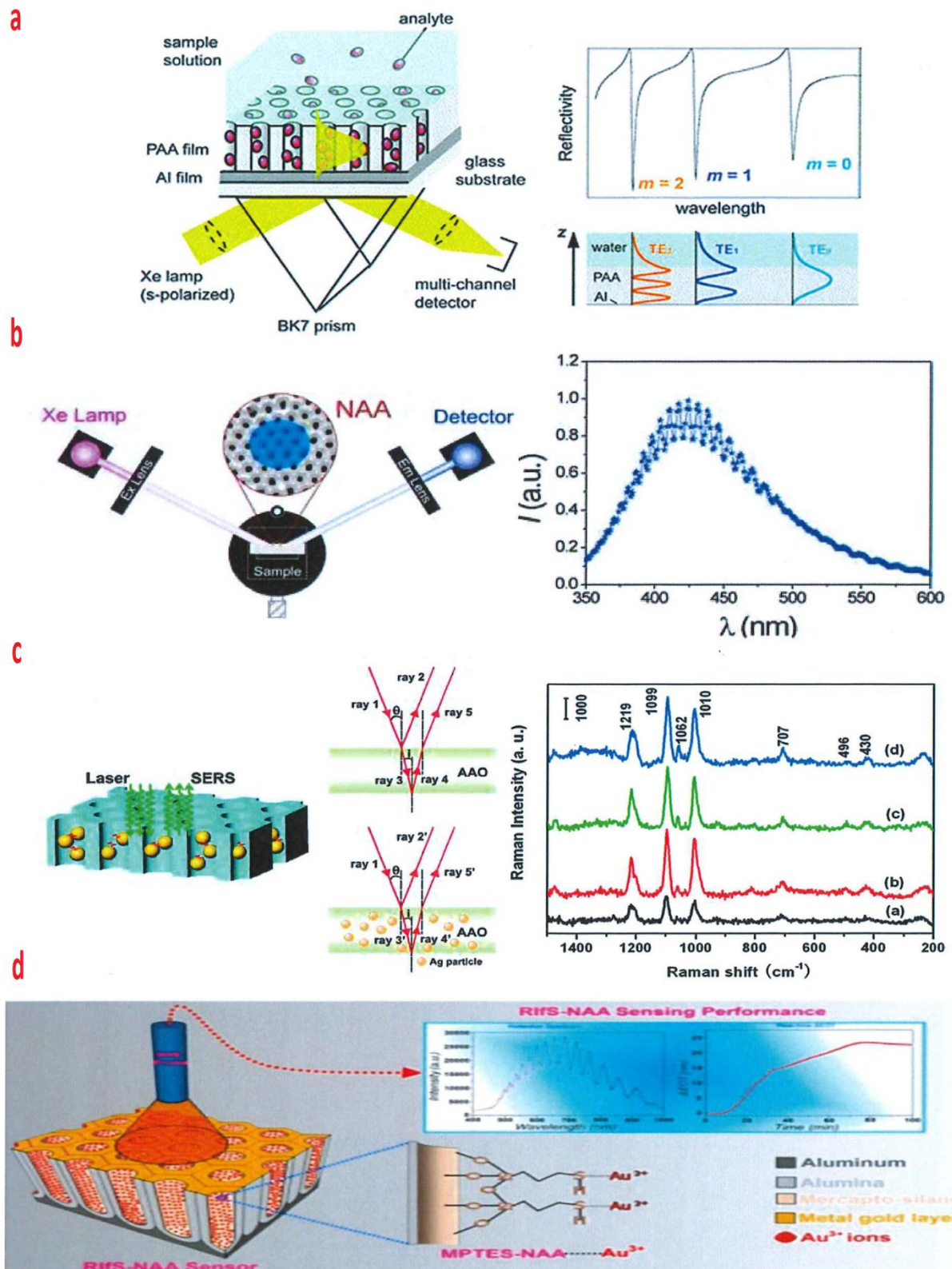


**Figure 1.9.** Four optical sensing techniques combined with NAA for developing highly sensitive optical sensors, a) SPR based on NAA (source [139]), b) PL based on NAA (source [140]), c) SERS based on NAA (source [141]), and d) RIFS based on NAA (source [142])<sup>26</sup>.



## 1.5. Reflectometric Interference Spectroscopy (RIfS)

### 1.5.1. Principle

Reflectometric Interference Spectroscopy (RIfS) is a simple and robust analytical method in terms of label-free and high sensitivity. This optical detection method is based on white light interference at transparent thin layers. The unique structure of thin films causes light reflection/transmittance, called interference phenomenon<sup>143, 144</sup>. This phenomenon is inspired by nature when the interference of reflected beams at translucent membrane cover results in colourful sight for butterflies, beetles, and natural pearls and causes its advantage to display vivid colours<sup>145, 146</sup>. For example, the wings of butterflies consist of a translucent and colourless membrane which is covered by thin layers of lamellae. Light reflects from lamellae layers which result in the interference of reflected beams and cause the beautiful colour of wings<sup>146</sup>. Similarly, this can be simulated using an artificial thin film and shining white light to get reflected from two interfaces layers including the thin film-artificial material interface (bottom of the thin film) and thin film-air interface (top of the thin film) (**Figure 1.10a**). The light reflects at two interfaces because of the difference in their optical length and results alternative of the maxima and minima in the reflection pattern. These light reflections create the reflection pattern which demonstrates the differential interferometry at specific wavelengths. The measurement of the optical pattern is calculated as Fabry-Pérot interference by the Fabry-Pérot interference equation, given below.

$$OT_{eff} = 2n_{eff}L\cos\theta = m\lambda \quad (1.6)$$

According to this equation,  $n_{eff}$  is the effective refractive index of NAA,  $L$  is the physical thickness of NAA as the thin film and  $m$  is the order of the fringe located at the representative wavelength  $\lambda$ <sup>147-149</sup>. According to **Eq. (1.6)**, any changes in the physical thickness and in the

effective refractive index of the thin film directly appear as a wavelength peak shift of the interference. This interference shift is known as the basis of label-free detection and real-time and in situ screening of analyte-receptor binding events of molecules using RIfS. A generic biosensor based RIfS comprises of a sensing platform functionalized and immobilized receptor for specific detection of biomolecule analytes such as proteins, antibodies, oligonucleotides, or pharmaceutical agents either through covalent binding or simple absorption as a result of changes in the effective refractive index of the thin film-sensing platform which is perceived in interference pattern shift <sup>147</sup>. These informative changes in RIfS not only depicts qualitative report about the interaction event of analyte-receptor but also provides quantitative analysis because the proportional shift in the reflection fringes directly depends to the amount of absorbed analyte on the thin film surface. The integration of sensing platform in a flow cell allows a real-time screening of any binding/unbinding event onto the surface.

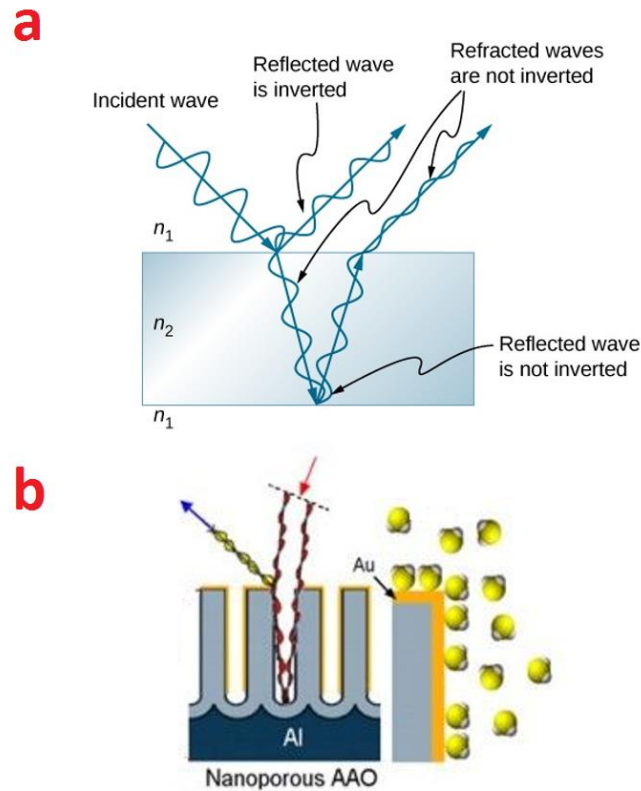


**Figure 1.10.** (a) A schematic showing Fabry-Perot interference of light rays reflected from top and bottom layer of a thin film. (b) Fabry-Perot interference from NAA (source [150]).

Nanoporous thin films such as nanoporous alumina, porous silicon, and titania nanotube arrays are able to generate Fabry-Perot interference fringes with interference spectra, which is also conducted by **Eq. (1.5)** (**Figure 1.10b**). Nanoporous films for specific capturing target analytes act in the same way as explained before for ordinary planar films. The local effective refractive index changes when binding receptor-analyte occur. This induces a red shift in interference spectra. Because, nanoporous films bear much higher surface area in order to capture more receptor molecules on the thin film surface than planar thin films, the refractive index changes are basically higher resulting in a larger red shift in the interference spectra. This matter showed nanoporous thin films based RIfS are much more sensitive compared to planar thin films. Real-time monitoring of nanoporous RIfS detection tool is also advantageous for understanding the entire mechanism of analyte-receptor binding reaction and can be continuously screened. This capability of real-time and in situ monitoring of RIfS sensing tool determine the understanding mechanism and kinetics of receptor-analyte binding event. For this reason, by applying Fast Fourier Transform (FFT) to the reflection interference spectrum, effective optical thickness ( $OT_{\text{eff}}$ ) can be obtained by calculation of “ $2n_{\text{eff}}L$ ” in **Eq. (1.6)**. Fourier spectrum converts interference spectrum to simpler peaks representing  $OT_{\text{eff}}$  changes in real-time, which is easy to follow surface changes especially in the case of bio-recognition tests <sup>151</sup>.

### **1.5.2. RIfS for Sensing and Biosensing**

Reflectometric Interference Spectroscopy (RIfS) as a label-free and highly sensitive tool was initially used for optical detection by G. Gauglitz *et al.* where a white light was guided onto the sensing film in perpendicular incidence generating interference fringe pattern <sup>152</sup>. Determinations of a large variety of biological and chemical molecules with RIfS have been reported by Gauglitz’s group. They utilized an array of different thin planar films including

metal oxides, metals, glass substrates coated with silicon oxide, and so on<sup>147-149, 153, 154</sup>. A series of receptors and capturing molecules including proteins, antibodies, oligonucleotides, aptamers, and nanoparticles were applied for studying biomolecular sensing using planar films. Those studies depicted that the recognition procedure (i.e. receptor-analyte binding) results in the increase in refractive index medium leading to shifts in the interference spectra and subsequent changes of effective optical thickness ( $OT_{\text{eff}}$ ) of the thin films. The  $OT_{\text{eff}}$  (as sensing parameter) can be calculated between a variation of wavelength inverse ( $1/\lambda$ ) and its fringe order ( $m$ )<sup>107, 108</sup>. Polymer planar thin films have been utilized for RIfS based sensing systems for label-free detection of various target molecules (**Figure 1.11**) including organic pollutants, DNA, glycopeptides, peptide nucleic acid and hydrochlorocarbons<sup>155-159</sup>.

The development of RIfS based sensing systems with planar thin films (e. g. glass substrates coated with polymer film) was conducted to diode-array spectrometer as the detector. This strategy introduced simplified and low cost RIfS optical sensor system because of lack requirement of fibre optic light guides. Light emitting diodes (LEDs) could produce interference pattern by only four wavelengths which led to a high light-emitting intensity. The LEDs were focused onto a planar sensing platform without using an optical fibre and then reflected light was collected by a photodiode (converts light to an electrical current), at the normal angle. This innovative fibre-free of RIfS sensor declined spectral information without loss of the RIfS performance.  $OT_{\text{eff}}$  changes were also monitored in the case of volatile organic compounds<sup>160</sup>. An advanced and complicated RIfS based sensor was developed for parallel screening of multiple biomolecules using microplate platform (i.e. with different surface chemistry) and multiplexer optical processor with multiple interference filters which resulted the reflection of light produced different wavelengths and subsequently different interference pattern. This light multiplexer complex made the possibility to monitor analyte interaction events on single sensing substrate via calculation of optical thicknesses<sup>161</sup>. Other RIfS systems

were also configured using polymer thin film coated glass substrate which was operating in total internal reflectance (TIR) mode used for detection of antibodies and proteins <sup>162, 159</sup>.

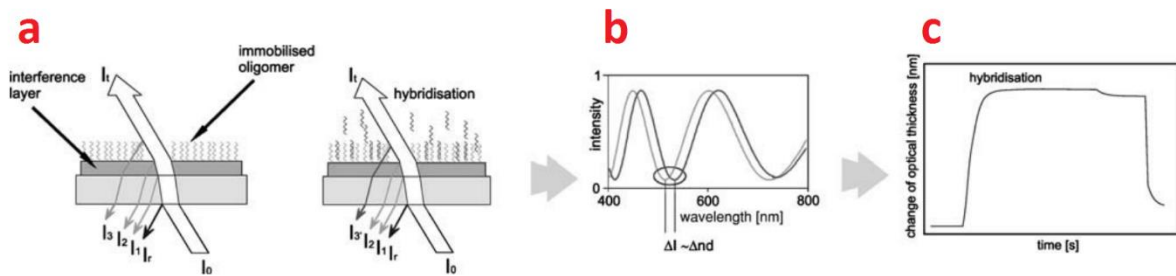


**Figure 1.11.** (a) Schematic illustration of RIfS detection using planar thin-film substrate (e. g. glass substrate with polymer coated), (b) interference pattern and reflected beams output, and (c) effective optical thickness (EOT) obtained from the interference spectrum by applying FFT. EOT changes during hybridization event onto surface (Source [163]).

### 1.5.3. Nanoporous Structural Based RIfS Sensors

Although, all these investigations revealed a high-throughput of sensing strategy, the low surface area of planar sensing substrates limited the practical performance of such systems. To tackle this matter, nanoporous thin films (e. g. nanoporous anodic alumina, porous silicon, nanoporous zinc oxide, cerium oxide and titania nanotubes) were introduced as potential alternatives <sup>70, 164-169</sup>. At the early stage of research on the combination of RIfS and porous material, organic solvents were detected inside pores of porous silicon (i.e. thin film) <sup>170</sup>. That report initially showed the importance of porous silicon to receive large changes in refractive index.

It is demonstrated anodic electrochemical etching of porous silicon creates changes in its porosity (e. g. refractive index) along the pores thickness. This ability allows fabricating a complex pore structure in porous silicon to generate photonic crystals such as multilayered pore structure, rugate filters, Bragg reflectors and microcavities <sup>171-174</sup>. It is discovered that photonic structures like microcavities display a uniform reflection peak along interference

fringes. However, interference fringes from rugate filters display a large stop-band in middle of the optical spectrum. These differences in the optical spectra of such structures made the advantage for the development of a variety of optical sensors for many applications as mentioned before. Porous silicon rugate filters demonstrated both the optical signatures (i.e. interference fringes and reflection peaks) have been used for sensing substrate, which presents high reflectivity spectrum with sinusoidal varying refractive index<sup>175</sup>. The other type of porous silicon structure for optical sensing purposes have been introducing as layered or stacked porous silicon which has been fabricated studied for multiple sensing applications. For instance, two-layered porous silicon structure with large pores on top layer and smaller pores at the bottom was prepared by sequentially reducing current density during electrochemical etching<sup>151, 176, 177</sup>. Due to the different porosity of each layer, a complex interference pattern was observed in the reflection spectrum. This showed that each layer could act as an interferometer individually (**Figure 1.12**). The complex reflection spectrum presented multiple signals corresponding to the effective optical thickness of each layer in the Fourier transform spectra. Such two layered structures could be beneficial for selective detection of a mixture of molecules (e.g. bovine serum albumin and sucrose). This happened because of size-exclusion feature that does allow small molecules easily fit both layers whereas large molecules can only place into large pores on the top layer, which is an appropriate strategy for selective detection of various large and small target molecules, simultaneously. Additionally, this structure was advantageous for the process of enzyme degradation monitoring when enzyme immobilization occurred in the top layer and collection of degraded molecules in the bottom layer<sup>178</sup>.

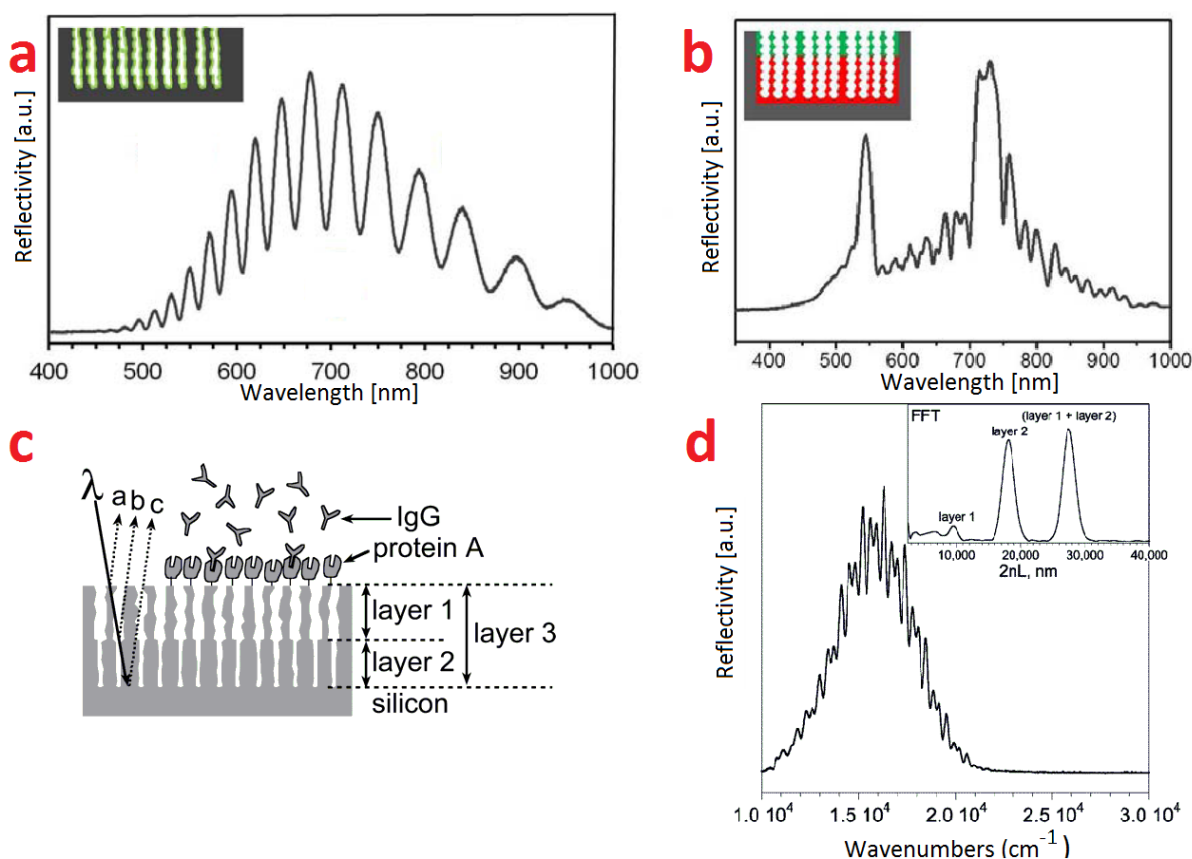


**Figure 1.12.** Optical sensors based on porous silicon with different porosity. a) Interference pattern generated from single-layered porous silicon. b) Interference pattern generated from a double-layer rugate structure porous silicon (source [179]). c) Double-layer biosensor based on porous silicon, and d) its corresponding interference pattern and fast Fourier transform spectrum in which layers are assigned as depicted (source [176]). Images are adapted with permission.

A few more studies investigated composites substances of porous silicon with titania or carbon in order to improve the stability of porous silicon against oxidation which results in surface degradation of porous silicon<sup>180, 181</sup>.

The use of porous silicon (PSi) have been mainly considered as a suitable candidate due to large surface area and high level of sensitivity to develop RIfS sensors for chemical and bio analytes detections including steroid (e. g. dexamethasone), antibodies, sugars (e. g. sucrose, glucose), proteins (e. g. streptavidin, bovine serum albumin), enzymes (e. g. protease, gelatinase), DNA and so on<sup>171, 172, 176, 182-189</sup>. The large surface of porous silicon substrate enabled a large amount of molecular interactions over a small surface area which caused a low

limit of detection of 9 fg/mL for DNA molecules during hybridisation test <sup>172</sup>. Besides quantitative and qualitative detection of these target molecules, it could also be possible to reduce detection time by integration of porous silicon chip into the direct flow cell (**Figure 1.13a**) <sup>190</sup>.

Although PSi combined the unique advantages of simplicity and extraordinary capabilities to be integrated into high-throughput for optical label-free biosensors, this nanoporous material is not particularly stable under biological environment because it is sensitive to nucleophilic attack which results formation of bonds between undesired molecules. The nucleophilic attack leads to a collapse of nanopore structure <sup>189</sup>. The other problem of using porous silicon structure towards biological area is the formation of covalent bonds between silicon and carbon from organic monolayer, which the structure demonstrated corrosion and dissolution at pH > 8<sup>190</sup>. The instability of pore structure causes in a decrease in the refractive index over time and instability in the interference signal. Therefore, other material (e. g. NAA) application opened up innovative ideas for effective fabrication of interferometric biosensors <sup>138</sup>.



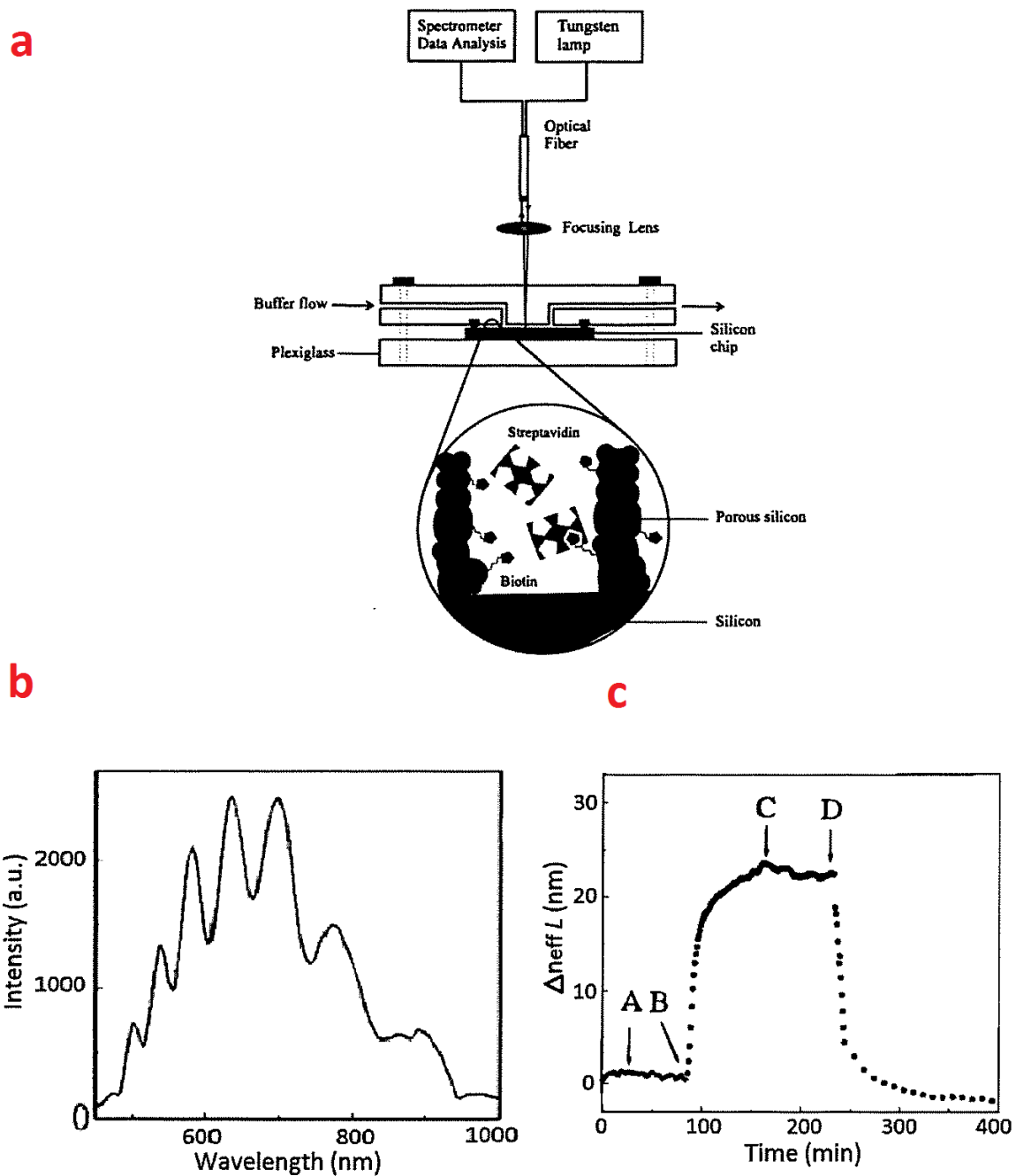


**Figure 13.** a) Schematic illustration of RIFS from nanoporous substrate, b) interference pattern generated, and c) effective optical thickness (EOT) obtained by FFT application on the interference pattern (source [169]).

#### 1.5.4. NAA Integrated with RIFS Sensors

In the case of NAA, several advantages rather than other nanoporous material such as porous silicon and titania nanotubes are discussed. NAA present excellent physical and chemical properties. For example, NAA has demonstrated the capability due to its controllable

nanoporous structure in comparison to porous silicon. NAA pore geometry can be structurally engineered using different anodization approaches. NAA surface chemistry can be varied using a variety of biomolecules without any loss in the nanopore structure. NAA is also more optically active compared with titania nanotubes<sup>11, 13, 28, 67, 107</sup>. NAA such as porous silicon create Fabry-Pérot modes in an interferometer generating interference fringe pattern in RIfS system<sup>138</sup>. Therefore, optical sensing of biomolecules target analytes can be obtained through real-time measurement of effective optical thickness (**Figure 1.14**). It is reported that combination of NAA with RIfS system offers a highly sensitive and selective detection system for a wide range of biomolecules (e. g. DNA and antibody-antigen), organic molecules and metal ions<sup>137, 138, 191-194</sup>.

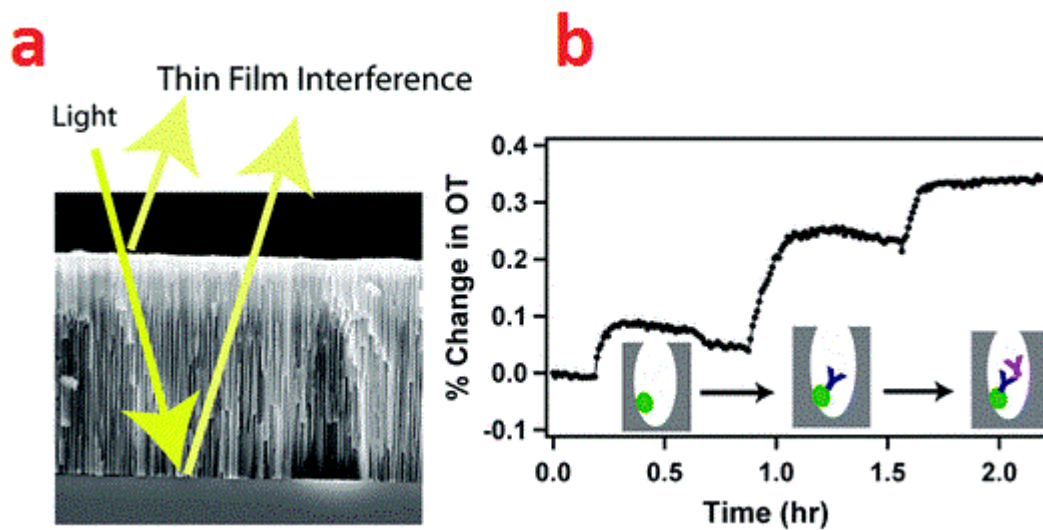


**Figure 1.14.** A label-free nanoporous anodic alumina biosensor. a) Nanoporous alumina structure used as thin film platform. b) Real-time biomolecular binding monitoring based on optical thickness changes (source [138]).

Many studies were performed to optimise the interference signal for enhancement of highly sensitive RIfS system. This optimisation of interference signal was carried out by controlling the shift in effective optical thickness signal where different pore geometry of NAA was applied. It was observed that application of different pore widening time revealed the shift

in effective optical thickness in the case of interferometric immunoassay system. It proved that NAA with larger pore diameter could present better sensing performance in RIfS <sup>193</sup>. The influence of pore diameter over the effective optical thickness was further analysed with three different pore diameter as a function of the interaction between human IgG and anti-human IgG. This study was also in good agreement with the expected higher sensitivity upon larger pore diameter in reflectance interference spectroscopy <sup>194</sup>. Another comprehensive study was about the effect of pore diameter, pore length and surface coatings (e. g. metal deposition) as suitable parameters to tune optical characteristics of NAA structure <sup>195</sup>. The authors demonstrated pore geometry parameters criteria such as pore diameter/pore length are more effective in their collective rather than their individual contribution. Metal coatings (e. g. gold and platinum) was used on top the surface of NAA for detection of gas sensing (e. g. hydrogen sulphide and hydrogen) <sup>196</sup>. The coatings were found as an excellent beneficial method for sensitivity and selectivity where gold layer was sensitive for hydrogen sulphide and platinum showed sensitivity for hydrogen. Additionally, platinum- coated NAA enabled significant sensitivity of interferometric fringe pattern with high signal-to-noise ratio, as a function of immunoglobulin antibodies detection <sup>197</sup>. This immune biosensor demonstrated more sensitivity of NAA than porous silicon. Furthermore, a bi-layered NAA structure was also employed for bovine serum albumin detection based on size-exclusion purposes <sup>198</sup>. This engineered NAA structure was gold-coated on the top surface in order to enhance RIfS signal. This structure generated a complex reflective spectrum presenting multiple reflection peaks corresponding to respective optical layers. Another study showed that NAA can act as biomedical implant compatible platform for drug release (e. g. indomethacin) in situ <sup>199</sup>. The drug release mechanism was controlled under dynamic flow condition by measuring the optical thickness changes in RIfS system. This ultrasensitive optical sensor also demonstrated the excellent capability of RIfS towards environmental target analytes. The performance of the

RIfS system enhanced because of structurally engineered of NAA rugate filter leading to improvement in the effective optical medium of nanopores <sup>200</sup>.

## **1.6. From Sensing to Applications: Integration of Molecular Biology with Biosensor Devices**

Typical molecular biology techniques (e. g. nucleic acid amplification assays for genotyping) require the samples to be sent to a laboratory for detection and analysis. These analytical methods allow for high accuracy and sensitivity and low detection limits. Despite these advantages, they are expensive, time consuming and require the use of highly trained personnel. These challenges are very important and need to be overcome for rapid requirement applications such as medical diagnosis <sup>201, 202</sup>. Emerging robust, low-cost, and easy-to-use sensing technologies lead to ability to perform analysis more efficiently. Moreover, enhanced sensors offer the potential integration of the molecular biology techniques within a specific transducing system capable of analysing samples on-site <sup>203</sup>. For this purpose, nucleic acid-based strategy is frequently reported technique integrated in a biosensor <sup>204</sup>. Particularly, isothermal nucleic acid amplification has been widely employed for variety of bio-analyte detection with bacterial and viral origins <sup>205-208</sup>. To detect these kind of bio-analytes, the applicability of different amplification approaches have been explored including reverse transcription polymerase chain reaction (RT-PCR), loop-mediated isothermal amplification (LAMP), helicase-dependant amplification (HAD), strand displacement amplification (SDA), and rolling circle amplification (RCA) <sup>209</sup>. Recently, RCA demonstrated practical advantages compared to other amplification methods where a foodborne pathogen (e.g. *Salmonella*) was rapidly detected during a single-step amplification at two different temperatures <sup>210</sup>. This robustness and high sensitivity of RCA strategy can be applied in widespread applications like,

proteomics, diagnostics, nanotechnology, drug discovery, and biosensing<sup>211</sup>. RCA integration with a biosensor device is highly considered as signal-amplification tool due to high speed synthesis long (more than 1000 bases), tandemly-repetitive, linear strand DNA chain by a short circular template (less than 100 bases). RCA reaction can provide amplification products up to 10<sup>4</sup>-fold copies of template<sup>212</sup>. Moreover, RCA-based biosensor is known as highly versatile detection tool because of its capability of label-free detection and real-time monitoring<sup>213</sup>. Specifically, a sensitive label-free pesticide detection is well-established using electrochemical sensor integrated with RCA<sup>214</sup>. The strategy depicted highly sensitivity with a detection limit as low as 2.1 µg/L. Finally, the outcomes of RCA-based biosensors proved that the technology is not only beneficial for high performance detection, but also it could overcome the labour-intensive and expensive features of similar devices (i.e. microarrays)<sup>215</sup>.

## **1.7. Research Gaps for NAA Based Optical Interferometry Biosensing**

Nanoporous anodic alumina, porous silicon, and titania nanotube arrays are an attractive platform for optical sensing purposes. Amid these nanoporous materials, NAA offers several advantages such as thermal stability, chemical resistance, large specific surface area, versatile nanostructure modification, and more importantly high level of biocompatibility. Additionally, the ability to tune its optical characteristics makes NAA an even more interesting substrate for optical biosensing. Previously, NAA based sensors have been reported using a variety of optical detection techniques such as SPR and SERS. However, the combination of NAA with those techniques is limited by the cost, bulkiness, inability to carry out real-time sensing, and the requirement for precise structural control and metal coatings. RIfS bridges these gap in combination with NAA and can be used to set up a highly selective and sensitive, label-free, portable and biocompatible sensing system. Therefore, developing NAA based biosensors

using RIFS is a promising concept. Previous studies that have shown NAA based interferometric biosensing have had limitations in regards to sensitivity, selectivity and multi analyte sensing. To address some of these limitations more work is required and several key parameters should be considered:

1. Structural geometry of NAA in order to provide more flexibility for sensing
2. Surface chemistry modification of NAA for selective detection of biomolecules
3. Integration of NAA with RIFS and improving its interferometric performances towards specific biomolecules and multi analyte detection
4. Specific applications such as nucleic acid amplification assay for single nucleotide polymorphism (SNP) detection.

## 1.8. Objectives

The purpose of this thesis is to develop highly sensitive biosensing platforms based on NAA-RIFS which is focused on following aims.

**Aim 1.** To explore NAA based interferometric biosensor for highly sensitive enzyme detection.

The specific objectives are:

- ✚ To develop reproducible fabrication protocols to fabricate NAA with the effective structural pore geometry to generate intensive interference signal from NAA.
- ✚ To characterize the sensing performance of prepared NAA by estimating the changes in effective optical thickness and their sensing performances.
- ✚ To investigate chemical selectivity of the biosensor towards model biomolecules.

**Aim 2.** To explore and optimise NAA based interferometric biosensor for binding affinity assessment between drug and human serum albumin. The specific objectives are:

- ✚ To fabricate NAA rugate filters for optimisation of interference signal from NAA.
- ✚ To characterize the sensing performance by estimating the changes in effective optical thickness and wavelength.
- ✚ To analyse fabrication parameters and their incorporation in sensitivity.

**Aim 3.** To explore and optimise NAA based interferometric biosensor for multi-point sensitivity assessment. The specific development areas are:

- ✚ To fabricate bilayered NAAs and explore their nano-structural features.
- ✚ To characterize the sensing performance by estimating the changes in effective optical thickness at each layer.
- ✚ To evaluate bilayered NAA structures for high performance multi-point sensing.

**Aim 4.** To explore solution-based ligation-Rolling circle amplification technique for detection of single nucleotide polymorphism site from a pesticide resistant gene. Specific objectives are:

- ✚ To confirm the genetic mutation associated with the resistant *Tribolium castaneum* strain by sequencing the relevant gene region.
- ✚ To design and test probe and primers for a Ligation-Rolling Circle Amplification assay capable of testing for the pesticide resistance-associated molecular marker in the stored grain pest *Tribolium castaneum*.

## 1.9. Thesis Structure

This thesis includes 7 chapters. This section summarises all the chapters in this thesis and explains how each chapter addresses the aforementioned objectives to develop a highly sensitive NAA based biosensing device.

**Chapter 1** intends to provide a brief overview of biosensors and their applications. The literature review is provided on optical biosensor concepts, nanoporous anodic alumina, its structural fabrication and engineering, and its surface chemistry modification. Details of reflectometric interference spectroscopy as the transduction system is provided. In the last section of this chapter, the idea based on molecular biotechnology integration into sensors is pinpointed.

**Chapter 2** gives out more details of materials and methods including the electrochemical anodization process for fabrication of NAA, its surface chemistry modification, and sensing process. This chapter also includes the molecular biology methods used in this project.

**Chapter 3** demonstrates the application of NAA platform for enzyme sensing in trace level detection using RIfS detection method. The study is published as Journal paper in Analytical Chemistry.

**Chapter 4** presents development of a method for improving the sensing performance of NAA using pulse anodization. This approach was demonstrated by preparing structures in NAA, known as NAA rugate filters (NAA-RFs) with higher sensitivity. Different types of NAA-RFs are prepared and optimized based on their sensing performance assessed by affinity binding assessment of a variety of biomolecules during this project. The study is published as Journal paper in Analytical Chemistry.

**Chapter 5** presents the performance of the engineered NAA platforms with double layer (funnel) geometry of NAA with different pore diameters to evaluate their applicability for multi analyte sensing. The Study is submitted as Journal paper in Sensors.



**Chapter 6** presents the preliminary development of a genotyping assay that would be potentially adaptable to a NAA-RIFs biosensing platform in the future. The development of an L-RCA assay (solution-based assay) for specific SNP detection is demonstrated.

**Chapter 7** summarizes the research results for this thesis and provides a perspective for future applications of NAA based optical biosensors with proposed future directions.

## 1.10. References

1. Vestergaard, M. D.; Kerman, K.; Tamiya, E., An overview of label-free electrochemical protein sensors. *Sensors* **2007**, *7(12)*, 3442-3458.
2. Scheller, F. W.; Wollenberger, U.; Warsinke, A.; Lisdat, F., Research and development in biosensors. *Current Opinion in Biotechnology* **2001**, *12*, 35-40.
3. Nakamura, H.; Karube, I., Current research activity in biosensors. *Analytical and bioanalytical chemistry* **2003**, *377*, 446-468.
4. Wong, S. S.; Joselevich, E.; Wooley, A. T.; Cheung, C. L.; Lieber, C. M., Covalently functionalized nanotubes as nanometer-sized probes in chemistry and biology. *Nature* **1998**, *394*, 52-55.
5. Clark, LC., Monitor and control of blood and tissue oxygenation. *Transactions – american society for artificial internal organs* **1956**, *2*, 41-48.
6. Clark, LC.; Lyons, C., Electrode systems for continuous monitoring cardiovascular surgery. *Annals of the New York academy of sciences* **1962**, *102*, 29-45.
7. Updike, SJ.; Hicks GP., The enzyme electrode. *Nature* **1967**, *214*, 986-988.
8. Guilbault, GG.; Montalvo, J., A urea specific enzyme electrode. *Journal of the american chemical society* **1969**, *91*, 2164-2169.
9. Bellan, L.M.; Wu, D.; Langer, R.S., Current trends in nanobiosensor technology. *WIREs nanomedicine and nanobiotechnology* **2011**, *3*, 229-246.

10. Guo, X., Surface plasmon resonance based biosensor technique: a review. *Journal of biophotonics* **2012**, *7*, 438-501.
11. Spichiger-Keller, U. E., Chemical sensors and biosensors for medical and biological applications. *John Wiley & Sons*: **2008**, DOI: 10.1002/9783527612284.
12. Lenarczauk, T.; Głąb, S.; Koncki, R., Application of prussian blue-based optical sensor in pharmaceutical analysis. *Journal of pharmaceutical and biomedical analysis* **2001**, *26*, 163-169.
13. Nirschl, M.; Reuter, F.; Vörös, J., Review of transducer principles for label-free biomolecular interaction analysis. *Biosensors* **2011**, *1*, 70-92.
14. Cooper, M. A., Label-free screening of bio-molecular interactions. *Analytical and bioanalytical chemistry* **2003**, *377*, 834-842.
15. Sadeghi, J.; Ghasemi, A.H.B.; Latifi, H., A label-free infrared opto-fluidic method for real-time determination of flow rate and concentration with temperature cross-sensitivity compensation. *Royal society of chemistry* **2016**, *16*, 3957-3968.
16. Taylor, R. F., Schultz J. S., Eds. Handbook of chemical and biological sensors. CRC Press, **1996**.
17. Soloman, S., Ed. *Sensors handbook*. McGraw-Hill Inc. **2009**.
18. Wolfbeis (Ed.) O.S., Fiber optic chemical sensors and biosensors. *Boca Raton, CRC Press*, **1991**.
19. Brecht, A.; Gauglitz G., Optical probes and transducers, *Biosensors Bioelectronics*, **1995**, *10*, 923–936.
20. Gauglitz, G., Opto-chemical and opto-immuno sensors. *Sensor, VCH Verlagsgesellschaft, Weinheim*, **1996**, *1*.
21. Boisdé G.; Harmer, A., chemical and biochemical sensing with optical fibers and waveguides, *London, Artech House, Boston* **1996**.

22. Homola, J.; Yee, S.S.; Gauglitz, G., Surface plasmon resonance sensors: review. *Sensors and actuators B* **1999**, *54*, 3-15.
23. Damborský, P.; Švitel, J.; Katrlík, J., Optical biosensors. *Essays in biochemistry* **2016**, *60*, 91-100.
24. Fan, X.; White, I. M.; Shopova, S. I.; Zhu, H.; Suter, J. D.; Sun, Y., Sensitive optical biosensors for unlabeled targets: A review. *analytica chimica acta* **2008**, *620*, 8-26.
25. Santos, A.; Kumeria, T.; Losic, D., Nanoporous anodic aluminum oxide for chemical sensing and biosensors. *TrAC Trends in Analytical Chemistry* **2013**, *44*, 25-38.
26. Kumeria, T.; Santos, A.; Losic, D., Nanoporous anodic alumina platforms: engineered surface chemistry and structure for optical sensing applications. *Sensors* **2014**, *14*, 11878-11918.
27. Santos, A.; Kumeria, T.; Losic, D., Nanoporous anodic alumina: a versatile platform for optical biosensors. *Materials* **2014**, *7*, 4297-4320.
28. Pattnaik, P., Surface plasmon resonance. *Applied biochemistry and biotechnology* **2005**, *126*, 79-92.
29. Homola, J., Ed. Surface plasmon resonance based sensors. Vol. 4. *Springer Science & Business Media*, **2006**.
30. Willets, K. A.; Van Duyne, R. P., Localized surface plasmon resonance spectroscopy and sensing. *Annu. Rev. Phys. Chem.* **2007**, *58*, 267-297.
31. Loh, K. P.; Bao, Q.; Eda, G.; Chhowalla, M., Graphene oxidized as a chemically tunable platform for optical applications. *Nature chemistry* **2010**, *2*, 1015-1024.
32. Qu, Y.; Liao, L.; Li, Y.; Zhang, H.; Huang, Y.; Duan, X., Electrically conductive and optically active porous silicon nanowires. *Nano letters* **2009**, *9(12)*, 4539-4543.
33. Mor, K. G.; Shankar, K.; Paulose, M.; Varghese, O. K.; Grimes, C. A., Enhanced photocleavage of water using titania nanotube arrays. *Nano letters* **2005**, *5(1)*, 191-195.

34. Ferfeh-Borrull, J.; Xifré- Pérez, E.; Pallaréz, J.; Marsal, L. F., Optical properties of nanoporous anodic alumina and derived applications. *Springer Series in Materials Science, Nanoporous Alumina* **2015**, 185-217.
35. Pumera, M., Graphene in biosensing. *Materials Today* **2011**, *14* (7-8), 308-315.
36. Kumeria, T.; Kurkuri, M. D.; Diener, K. R.; Parkinson, L.; Losic, D., Label-free reflectometric interference microchip biosensor based on nanoporous alumina for detection of circulating tumour cells. *Biosensors and Bioelectronics* **2012**, *35*, 167-173.
37. Setoh, S.; Miyata, A., Researches on anodic film of aluminium II, anodic behaviours of aluminium in aq. solutions of oxalic acid. *Scientific Papers of the institute of Physical and Chemical Research Tokyo* **1932**, *19*, 237.
38. Keller, F.; Hunter, M. S.; Robinson, D. L., Structural features of oxide coatings on aluminium. *Journal of the Electrochemical Society* **1953**, *100*(9), 411-419.
39. O'sullivan, J.; Wood, G., The morphology and mechanism of formation of porous anodic films on aluminium. *Proceedings of the Royal Society of London. A. Mathematical and Physical Sciences* **1970**, *317*, 511-543.
40. Preston, C. K.; Moskovits, M., New technique for the determination of metal particle size in supported metal catalysts. *The Journal of Physical Chemistry* **1988**, *92*, 2957-2960.
41. Saito, M.; Kirihara, M.; Taniguchi, T.; Miyagi, M., Micropolarizer made of the anodized alumina film. *Applied Physics Letters* **1989**, *55*, 607.
42. AlMawlawi, D.; Coombs, N.; Moskovits, M., Magnetic properties of Fe deposited into anodic aluminium oxide pores as a function of particle size. *Journal of Applied Physics* **1991**, *70*, 4421.
43. Preston, C. K.; Moskovits, M., Optical characterization of anodic aluminium oxide films containing electrochemically deposited metal particles. 1. Gold in phosphoric acid anodic aluminium oxide films. *The Journal of Physical Chemistry* **1993**, *97*, 8495-8503.

44. Routkevitch, D.; Bigioni, T.; Moskovits, M.; Xu, J. M. Electrochemical fabrication of CdS nanowire arrays in porous anodic aluminum oxide templates. *The Journal of Physical Chemistry* **1996**, *100*(33), 14037-14047.
45. Routkevitch, D.; Tager, A. A.; Haruyama, J.; Almawlawi, D.; Moskovits, M.; Xu, J. M., Nonlithographic nano-wire arrays: fabrication, physics, and device applications. *IEEE Transactions on Electron Devices* **1996**, *43*(10), 1646-1658.
46. Hulteen, J. C.; Martin, C. R., A general template-based method for the preparation of nanomaterials. *Journal of Materials Chemistry* **1997**, *7*, 1075-1087.
47. Masuda, H.; Fukuda, K., Ordered metal nanohole arrays made by a two-step replication of honeycomb structures of anodic alumina. *Science* **1995**, *268*, 1466-1468.
48. Ribes, À.; Xifré -Pérez, E.; Aznar, E.; Sancenón, F.; Pardo, T.; Marsal, L. F.; Martínez-Mañez, R., Molecular gated nanoporous anodic alumina for the detection of cocaine. *Scientific Reports* **2016**, *6*, 38649.
49. Byun, J.; Lee, J. I.; Kwon, S.; Jeon, G.; Kim, J. K., Highly ordered nanoporous alumina on conducting substrates with adhesion enhanced by surface modification: universal templates for ultrahigh-density arrays of nanorods. *Advanced Materials* **2010**, *22*, 2028-2032.
50. Parviz, B. A.; Ryan, D.; Whitesides, G. M. Using self-assembly for the fabrication of nano-scale electronic and photonic devices, *IEEE Transactions on Advanced Packaging* **2003**, *26* (3), 233-241.
51. Rattier M. *et al.*, Toward ultrahigh-efficiency aluminum oxide microcavity light-emitting diodes: guided mode extraction by photonic crystals, *IEEE Journal of Selected Topics in Quantum Electronics* **2002**, *8* (2), 238-247.
52. Oelhafen, P.; Schüler, A., Nanostructured materials for solar energy conversion. *Solar Energy* **2005**, *79*(2), 110-121.

53. Shingubara, S., Fabrication of nanomaterials using porous alumina templates. *Journal of Nanoparticle Research* **2003**, *5*, 17-30.
54. Li, A.; Müller, F.; Birner, A.; Nielsch, K.; Gösele, U., Hexagonal pore arrays with a 50–420 nm interpore distance formed by self-organization in anodic alumina. *Journal of applied physics* **1998**, *84*, 6023-6026.
55. Akahori, H.; Fukushima, T., Study on the hydration of alumite by electron microscopy and electron micro diffraction. *Journal of Electron Microscopy* **1964**, *13*, 162-171.
56. Thompson, G.; Furneaux, R.; Wood, G.; Richardson, J.; Goode, J., Nucleation and growth of porous anodic films on aluminium. *Nature* **1978**, *272*, 433-435.
57. Akahori, H., Electron microscopic study of growing mechanism of aluminium anodic oxide film. *Journal of Electron Microscopy* **1961**, *10*, 175-185.
58. Keller, F.; Hunter, M.; Robinson, D., Structural features of oxide coatings on aluminum. *Journal of the Electrochemical Society* **1953**, *100*, 411-419.
59. Lee, W.; Ji, R.; Gösele, U.; Nielsch, K., Fast fabrication of long-range ordered porous alumina membranes by hard anodization. *Nature materials* **2006**, *5*, 741-747.
60. Masuda, H.; Satoh, M., Fabrication of gold nanodot array using anodic porous alumina as an evaporation mask. *Japanese Journal of Applied Physics* **1996**, *35*, 126- 129.
61. Thompson, G.; Xu, Y.; Skeldon, P.; Shimizu, K.; Han, S.; Wood, G., Anodic oxidation of aluminium. *Philosophical Magazine B* **1987**, *55*, 651-667.
62. Masuda, H.; Yamada, H.; Satoh, M.; Asoh, H.; Nakao, M.; Tamamura, T., Highly ordered nanochannel-array architecture in anodic alumina. *Applied Physics Letters* **1997**, *71*, 2770-2772.
63. Chu, S-Z.; Wada, K.; Inoue, S.; Isogai, M.; Yasumori, A., Fabrication of ideally ordered nanoporous alumina films and integrated alumina nanotubule arrays by high-field anodization. *Adevanced Materials* **2005**, *17*, 2115-2119.

64. Lee, W.; Park, S.-J., Porous anodic aluminum oxide: anodization and templated synthesis of functional nanostructures. *Chemical reviews* **2014**, *114*, 7487-7556.
65. Lee, W.; Kim, J.-C.; Gösele, U., Spontaneous current oscillations during hard anodization of aluminum under potentiostatic conditions. *Advanced Functional Materials* **2009**, *20*, 21-27.
66. Nielsch, K.; Choi, J.; Schwirn, K.; Wehrspohn, R. B.; Gösele, U., Self-ordering regimes of porous alumina: the 10 porosity rule. *Nano letters* **2002**, *2*, 677-680.
67. Sulka, G. D., Highly ordered anodic porous alumina formation by self-organized anodizing in Nanostructured materials in electrochemistry. *Wiley VCH Verlag GmbH & Co.* **2008**, 1-116.
68. Jessensky, O.; Müller, F.; Gösele, U., Self-organized formation of hexagonal pore arrays in anodic alumina. *Applied Physics Letters* **1998**, *72*, 1173-1175.
69. Schwirn, K.; Lee, W.; Hillebrand, R.; Steinhart, M.; Nielsch, K.; Gösele, U., Self-ordered anodic aluminum oxide formed by H<sub>2</sub>SO<sub>4</sub> hard anodization. *ACS nano* **2008**, *2*, 302-310.
70. Masuda, H.; Yada, K.; Osaka, A., Self-ordering of cell configuration of anodic porous alumina with large-size pores in phosphoric acid solution. *Japanese Journal of Applied Physics* **1998**, *37*, L1340.
71. Masuda, H.; Hasegawa, F.; Ono, S., Self-ordering of cell arrangement of anodic porous alumina formed in sulfuric acid solution. *Journal of the electrochemical society* **1997**, *144*, L127-L130.
72. Ono, S.; Saito, M.; Asoh, H., Self-ordering of anodic porous alumina formed in organic acid electrolytes. *Electrochimica Acta* **2005**, *51*, 827-833.

73. Surganov, V.; Morgen, P.; Nielsen, J.; Gorokh, G.; Mozalev, A., Study of the initial stage of aluminium anodization in malonic acid solution. *Electrochimica Acta* **1987**, *32*, 1125-1127.
74. Surganov, V.; Gorokh, G., Anodic oxide cellular structure formation on aluminum films in tartaric acid electrolyte. *Materials Letters* **1993**, *17*, 121-124.
75. Chu, S.; Wada, K.; Inoue, S.; Isogai, M.; Katsuta, Y.; Yasumori, A., Large-scale fabrication of ordered nanoporous alumina films with arbitrary pore intervals by critical-potential anodization. *Journal of The Electrochemical Society* **2006**, *153*, B384-B391.
76. Ono, S.; Saito, M.; Ishiguro, M.; Asoh, H., Controlling factor of self-ordering of anodic porous alumina. *Journal of The Electrochemical Society* **2004**, *151*, B473-B478.
77. Mozalev, A.; Mozaleva, I.; Sakairi, M.; Takahashi, H., Anodic film growth on Al layers and Ta–Al metal bilayers in citric acid electrolytes. *Electrochimica acta* **2005**, *50*, 5065-5075.
78. Vasudevan, A. K.; Doherty, R. D., Eds. Aluminum alloys-contemporary research and applications. Vol. 31, *Elsevier* **2012**.
79. Lee, W.; Schwirn, K.; Steinhart, M.; Pippel, E.; Scholz, R.; Gösele, U., Structural engineering of nanoporous anodic aluminium oxide by pulse anodization of aluminium. *Nature nanotechnology* **2008**, *3*, 234-239.
80. Losic, D.; Lillo, M., Porous alumina with shaped pore geometries and complex pore architectures fabricated by cyclic anodization. *Small* **2009**, *5*, 1392-1397.
81. Santos, A.; Formentín, P.; Pallarès, J.; Ferré-Borrull, J.; Marsal, L. F., Structural engineering of nanoporous anodic alumina funnels with high aspect ratio. *Journal of Electroanalytical Chemistry* **2011**, *655*, 73-78.
82. Nagaura, T.; Takeuchi, F.; Inoue, S., Fabrication and structural control of anodic alumina films with inverted cone porous structure using multi-step anodizing. *Electrochimica Acta* **2008**, *53*, 2109-2114.



83. Nagaura, T.; Takeuchi, F.; Yamauchi, Y.; Wada, K.; Inoue, S., Fabrication of ordered Ni nanocones using a porous anodic alumina template. *Electrochemistry Communications* **2008**, *10*, 681-685.
84. Jani, A. M. M.; Losic, D.; Voelcker, N. H., Nanoporous anodic aluminium oxide: Advances in surface engineering and emerging applications. *Progress in Materials Science* **2013**, *58*, 636-704.
85. Losic, D.; Losic Jr, D., Preparation of porous anodic alumina with periodically perforated pores. *Langmuir* **2009**, *25*, 5426-5431.
86. Santos, A., Nanoporous anodic alumina photonic crystals: fundamentals, developments and perspectives. *Journal of Materials Chemistry C* **2017**. (5), 5581-5599.
87. Santos, A.; Pereira, T.; Law, C. S.; Losic, D., Rational engineering of nanoporous anodic alumina optical bandpass filters. *Nanoscale* **2016**. (8), 14846-14857.
88. Santos, A.; Law, C. S.; Lei, D. W. C.; Pereira, T.; Losic, D., Fine tuning of optical signals in nanoporous anodic alumina photonic crystals by apodized sinusoidal pulse anodization. *Nanoscale* **2016**. (8), 18360-18375.
89. Martín, J.; Martín-González, M.; Fernández, J. F.; Caballero-Calero, O., Ordered three-dimensional interconnected nanoarchitectures in anodic porous alumina. *Nature communications* **2014**, *5*, DOI:10.1038/ncomms6130.
90. Sulka, G. D.; Hnida, K., Distributed Bragg reflector based on porous anodic alumina fabricated by pulse anodization. *Nanotechnology* **2012**, *23*, 075303.
91. Zheng, W. J.; Fei, G. T.; Wang, B.; De Zhang, L., Modulation of transmission spectra of anodized alumina membrane distributed Bragg reflector by controlling anodization temperature. *Nanoscale research letters* **2009**, *4*, 665-667.

92. Rahman, M. M.; Marsal, L. F.; Pallarès, J.; Ferré-Borrull, J., Tuning the photonic stop bands of nanoporous anodic alumina-based distributed Bragg reflectors by pore widening. *ACS applied materials & interfaces* **2013**, *5*, 13375-13381.
93. Ferré-Borrull, J.; Rahman, M. M.; Pallarès, J.; Marsal, L. F., Tuning nanoporous anodic alumina distributed-Bragg reflectors with the number of anodization cycles and the anodization temperature. *Nanoscale research letters* **2014**, *9*, 1-6.
94. Macias, G.; Ferré-Borrull, J.; Pallarès, J.; Marsal, L. F., 1-D nanoporous anodic alumina rugate filters by means of small current variations for real-time sensing applications. *Nanoscale research letters* **2014**, *9*, 1-6.
95. Santos, A.; Yoo, J. H.; Rohatgi, C. V.; Kumeria, T.; Wang, Y.; Losic, D., Realization and advanced engineering of true optical rugate filters based on nanoporous anodic alumina by sinusoidal pulse anodization. *Nanoscale* **2016**. (8), 1360-1373.
96. Santos, A.; Vojkuvka, L.; Alba, M.; Balderrama, V. S.; Ferré-Borrull, J.; Pallares, J.; Marsal, L. F., Understanding and morphology control of pore modulations in nanoporous anodic alumina by discontinuous anodization. *physica status solidi (a)* **2012**, *209*, 2045-2048.
97. Li, J.; Li, C.; Chen, C.; Hao, Q.; Wang, Z.; Zhu, J.; Gao, X., Facile method for modulating the profiles and periods of self-ordered three-dimensional alumina taper-nanopores. *ACS applied materials & interfaces* **2012**, *4*, 5678-5683.
98. Santos, A.; Kumeria, T.; Wang, Y.; Losic, D., In situ monitored engineering of inverted nanoporous anodic alumina funnels: On the precise generation of 3d optical nanostructures. *Nanoscale* **2014**, *6*, 9991-9999.
99. Santos, A.; Ferré-Borrull, J.; Pallarès, J.; Marsal, L. F., Hierarchical nanoporous anodic alumina templates by asymmetric two-step anodization. *Physica Status Solidi* **2011**, *3*, 668-674.
100. Yamamoto, Y.; Baba, N.; Tajima, S., Coloured materials and photoluminescence centres in anodic film on aluminium. *Nature* **1981**, *289*, 572-574.

101. Velleman, L.; Triani, G.; Evans, P. J.; Shapter, J. G.; Losic, D., Structural and chemical modification of porous alumina membranes. *Microporous and Mesoporous Materials* **2009**, *126*, 87-94.
102. Losic, D.; Simovic, S., Self-ordered nanopore and nanotube platforms for drug delivery applications. *Expert Opinion Drug Delivery* **2009**, *6*, 1363-1381.
103. Choy, K. L., Chemical Vapor deposition of coatings. *Progress in Materials Science* **2003**, *48*, 57-170.
104. Park, S.; Kim, Y-S.; Kim, W. B.; Jon, S., Carbon nanosyringe array as a platform for intracellular delivery. *Nano Letters* **2009**, *9*, 1325-1329.
105. Aramesh, M.; Fox, K.; Lau, D. W. M.; Fang, J.; Ostrikov, K.; Prawer, S.; Cervenka, J., Multifunctional three-dimensional nanodiamond-nanoporous alumina nanoarchitectures. *Carbon* **2014**, *75*, 452-464.
106. Tsud, N.; Yoshitake, M., Vacuum vapor deposition of phenylphosphonic acid on amorphous alumina. *Surface Science* **2007**, *601*, 3060-3066.
107. Jani, A. M. M.; Kempson, I. M.; Losic, D.; Voelcker, N. H., Dressing in layers: layering surface functionalities in nanoporous aluminum oxide membranes. *Angewandte Chemie* **2010**, *122*, 8105-8109.
108. Szczepanski, V.; Vlassiuk, I.; Smirnov, S., Stability of silane modifiers on alumina nanoporous membranes. *Journal of membrane science* **2006**, *281*, 587-591.
109. Vissiouk, I.; Krasnoslobodtsev, A.; Smirnov, S.; Germann, M., "Direct" detection and separation of DNA using nanoporous alumina filters. *Langmuir* **2004**, *20*, 9913-9915.
110. Vissiouk, I.; Takmakov, P.; Smirnov, S., Sensing DNA hybridization via ionic conductance through a nanoporous electrode. *Langmuir* **2005**, *21*, 4776-4778.

111. Odom, D. J.; Baker, L. A.; Martin, C. R., Solvent-extraction and langmuir-adsorption-based transport in chemically functionalized nanopore membranes. *The Journal of Physical Chemistry B* **2005**, *109*, 20887-20894.
112. Lee, S. W.; Shang, H.; Haasch, R. T.; Petrova, V.; Lee, G. U., Transport and functional behaviour of poly (ethylene glycol)-modified nanoporous alumina membranes. *Nanotechnology* **2005**, *16*, 1335.
113. Chen, Y.; Santos, A.; Wang, Y.; Kumeria, T.; Wang, Wang, C.; Li, J.; Losic, D., Interferometric nanoporous anodic alumina photonic coatings for optical sensing. *Nanoscale* **2015**, *7*, 7770-7779.
114. La Flamme, K. E.; Popat, K. C.; Leoni, L.; Markiewicz, E.; La Tempa, T. J.; Roman, B. B.; Grimes, C. A.; Desai, T. A., Biocompatibility of nanoporous alumina membranes for immunoisolation. *Biomaterials* **2007**, *28*, 2638-2645.
115. Takmakov, P.; Vlasiouk, I.; Smirnov, S., Application of anodized aluminum in fluorescence detection of biological species. *Analytical and bioanalytical chemistry* **2006**, *385*, 954-958.
116. Vlasiouk, I.; Takmakov, P.; Smirnov, S., Sensing DNA hybridization via ionic conductance through a nanoporous electrode. *Langmuir* **2005**, *21*, 4776-4778.
117. Sehayek, T.; Lahav, M.; Popovitz-Biro, R.; Vaskevich, A.; Rubinstein, I., Template synthesis of nanotubes by room-temperature coalescence of metal nanoparticles. *Chemistry of materials* **2005**, *17*, 3743-3748.
118. Lei, Y.; Cai, W.; Wilde, G., Highly ordered nanostructures with tunable size, shape and properties: A new way to surface nano-patterning using ultra-thin alumina masks. *Progress in Materials Science* **2007**, *52*, 465-539.

119. Qiu, T.; Zhang, W.; Lang, X.; Zhou, Y.; Cui, T.; Chu, PK., Controlled assembly of highly Raman-enhancing silver nanocap arrays templated by porous anodic alumina membranes. *Small* 2009, 5(20), 2333-2337.
120. Zhang, L.; Fang, Y.; Zhang, P., Laser-MBE of nickel nanowires using AAO template: A new active substrate of surface enhanced Raman scattering. *Spectrochimica Acta Part A* **2008**, (69) 91–95.
121. Lupi, C.; Felli, F.; Ippoliti, L.; Caponero, M. A.; Ciotti, M.; Nardelli, V.; Paolozzi, A., Metal coating for enhancing the sensitivity of fiber Bragg grating sensors at cryogenic temperature. *Smart Materials and Structures* **2005**, 14, N71-N76.
122. Dai, J.; Yang, M.; Yu, X.; Lu, H., Optical hydrogen sensor based on etched fiber Bragg sputtered with Pd/Ag composite film. *Optical Fiber Technology* **2013**, 19, 26-30.
123. Ando, M.; Chabicovsky, R.; Haruta, M., Optical hydrogen sensitivity of nobel metal-tungsten oxide composite films prepared by sputtering deposition. *Sensors and Actuators B* **2001**, 76, 13-17.
124. Hernández-Eguía, L. P.; Ferré-Borrull, J.; Macias, G.; Pallarès, J.; Marsal, L. F., Engineering optical properties of gold-coated nanoporous anodic alumina for biosensing. *Nanoscale Research Letters* **2014**, 9, 414.
125. Alvarez, S. D.; Derfus, A. M.; Schwartz, M. P.; Bhatia, S. N.; Sailor, M. J., The compatibility of hepatocytes with chemically modified porous silicon with reference to in vitro biosensors. *Biomaterials* **2009**. (30), 26-34.
126. Kumeria, T.; Santos, A., Sensing and biosensing applications of nanoporous anodic alumina. In *Electrochemically engineered nanoporous materials - Methods, properties and applications*, Losic, D.; Santos, A., Eds. Springer International Publishing AG - Germany: Australia, **2015**; Chapter 3.

127. Santos, A.; Macías, G.; Ferré-Borrull, J.; Pallarès, J.; Marsal, L. F., Photoluminescent enzymatic sensor based on nanoporous anodic alumina. *ACS Applied Materials and Interfaces* **2012**, *4*, 3584-3588.
128. Jia, R. P.; Shen, Y.; Luo, H. Q.; Chen, X. G.; Hu, Z. D.; Xue, D. S., Enhanced photoluminescence properties of morin and trypsin absorbed on porous alumina films with ordered pores array. *Solid State Communications* **2004**, *130*, 367-372.
129. Skosura-Muñiz, A. de la, Mekoçi, Nanoparticle based enhancement of electrochemical DNA hybridization signal using nanoporous electrodes. *The Royal Society of Chemistry* **2010**, *46*, 9007-9009.
130. Hiep, H. M.; Yoshikawa, H.; Tamiya, E., Interference localized surface plasmon resonance nanosensor tailored for the detection of specific biomolecular interactions. *Analytical Chemistry* **2010**, *82*, 1221-1227.
131. Kim, D-K.; Kerman, K.; Saito, M.; Sathuluri, R. R.; Endo, T.; Yamamura, S.; Kwon, Y-S., Tamiya, E., Label-free DNA biosensor based on localized surface plasmon resonance coupled with interferometry. *Analytical Chemistry* **2007**, *79*, 1855-1864.
132. Fan, Y.; Hotta, K.; Yamaguchi, A.; Teramae, N., Enhanced fluorescence in a nanoporous waveguide and its quantitative analysis. *Optics Express* **2012**, *20*, 12850-12859.
133. Dhathathreyan, A., Real-time monitoring of invertase activity immobilized in nanoporous aluminium oxide. *The Journal of Physical Chemistry B* **2011**, *115*, 6678-6682.
134. Nayak, D. R.; Bhat, N.; Umapathy, S., Surface enhanced Raman scattering on anodized alumina templates for bio-sensing applications. *Physics of Semiconductor Devices* **2013**, 577-579.
135. El-Said, W. A.; Kim, T-H.; Kim, H.; Choi, J-W., Analysis of intracellular state based on controlled 3D nanostructures mediated surface enhanced raman scattering. *Plos One* **2011**, *6* (2), e15836.

136. Zhang, C.; Smirnov, A. I.; Bahn, D.; Grebel, H., Surface enhanced raman scattering of biospecies on anodized aluminium oxide films. *Chemical Physics Letters* **2007**, *440*, 239-243.
137. Pan, S.; Rothberg, L. J., Interferometric sensing of biomolecular binding using nanoporous aluminum oxide templates. *Nano letters* **2003**, *3*, 811-814.
138. Alvarez, S. D.; Li, C.-P.; Chiang, C. E.; Schuller, I. K.; Sailor, M. J., A label-free porous alumina interferometric immunosensor. *Acs Nano* **2009**, *3*, 3301-3307.
139. Hotta, K.; Yamaguchi, A.; Teramae, N. Nanoporous waveguide sensor with optimized nanoarchitectures for highly sensitive label-free biosensing. *ACS Nano* **2012**, *6*(2), 1541-1547.
140. Santos, A.; Macías, G.; Ferré-Borrull, J., Pallarès, J.; Marsal L. F., Photoluminescent enzymatic sensor based on nanoporous anodic alumina. *ACS Applied Materials and Interfaces* **2012**, *4*, 3584-3588.
141. Ji, N.; Ruan, W.; Wang, C.; Lu, Z.; Zhao, B., Fabrication of silver decorated anodic aluminum oxide substrate and its optical properties on surface-enhanced Raman scattering and thin film interference. *Langmuir* **2009**, *25*(19), 11869-11873.
142. Kumeria, T.; Santos, A.; Losic, D., Ultrasensitive nanoporous interferometric sensor for label-free detection of Gold (III) ions. *ACS Applied Materials and Interfaces* **2013**, *5*(22), 11783-11790.
143. Schmitt, H.-M.; Brecht, A.; Piehler, J.; Gauglitz, G., An integrated system for optical biomolecular interaction analysis. *Biosensors and Bioelectronics* **1997**, *12*, 809-816.
144. Gauglitz, G.; Brecht, A.; Kraus, G.; Mahm, W., Chemical and biochemical sensors based on interferometry at thin layers. *Sensors and Actuators B: Chemical* **1993**, *11*, 21-27.
145. Snow, M. R.; Pring, A.; Self, P.; Losic, D.; Shapter, J., The origin of the color of pearls in iridescence from nano-composite structures of the nacre. *American Mineralogist* **2004**, *89*, 1353-1358.

146. Vukusic, P.; Sambles, J.; Lawrence, C.; Wootton, R., Quantified interference and diffraction in single Morpho butterfly scales. *Proceedings of the Royal Society of London. Series B: Biological Sciences* **1999**, *266*, 1403-1411.
147. Brecht, A.; Gauglitz, G., Optical probes and transducers. *Biosensors and Bioelectronics* **1995**, *10* (9), 923-936.
148. Gauglitz, G., Direct optical sensors: principles and selected applications. *Analytical and bioanalytical chemistry* **2005**, *381*, 141-155.
149. Gauglitz, G., Direct optical detection in bioanalysis: an update. *Analytical and bioanalytical chemistry* **2010**, *398*, 2363-2372.
150. Kumeria, T.; Parkinson, L.; Losic, D., A nanoporous interferometric micro-sensor for biomedical detection of volatile sulphur compounds. *Nanoscale research letters* **2011**, *6*, 1-7.
151. Pacholski, C.; Sartor, M.; Sailor, M. J.; Cunin, F.; Miskelly, G. M., Biosensing using porous silicon double-layer interferometers: reflective interferometric fourier transform spectroscopy. *Journal of the American Chemical Society* **2005**, *127*, 11636-11645.
152. Brecht, A.; Ingenhoff, J.; Gauglitz, G., Direct monitoring of antigen-antibody interactions by spectral interferometry. *Sensors and Actuators B* **1992**, *6*, 96-100.
153. Brecht, A.; Gauglitz, G., Interferometric immunoassay in a FIA-system: a sensitive and rapid approach in label-free immunosensing. *Biosensors and Bioelectronics* **1993**, *8*, 387-392.
154. Brecht, A.; Lang, G.; Gauglitz, G., Wavelength dependencies in interferometric measurements of thin protein films. *Fresenius' Journal of Analytical Chemistry* **1993**, *346*, 615-617.
155. Dieterle, F.; Belge, G.; Betsch, C.; Gauglitz, G., Quantification of the refrigerants R22 and R134a in mixtures by means of different polymers and reflectometric interference spectroscopy. *Analytical and bioanalytical chemistry* **2002**, *374*, 858-867.



156. Tünnemann, R.; Mehlmann, M.; Süßmuth, R. D.; Bühler, B.; Pelzer, S.; Wohlleben, W.; Fiedler, H.-P.; Wiesmüller, K.-H.; Gauglitz, G.; Jung, G., Optical biosensors. Monitoring studies of glycopeptide antibiotic fermentation using white light interference. *Analytical chemistry* **2001**, *73*, 4313-4318.
157. Yan, H.; Kraus, G.; Gauglitz, G., Detection of mixtures of organic pollutants in water by polymer film receptors in fibre-optical sensors based on reflectometric interference spectrometry. *Analytica chimica acta* **1995**, *312*, 1-8.
158. Sauer, M.; Brecht, A.; Charisse, K.; Maier, M.; Gerster, M.; Stemmler, I.; Gauglitz, G.; Bayer, E., Interaction of chemically modified antisense oligonucleotides with sense DNA: a label-free interaction study with reflectometric interference spectroscopy. *Analytical chemistry* **1999**, *71*, 2850-2857.
159. Kröger, K.; Jung, A.; Reder, S.; Gauglitz, G., Versatile biosensor surface based on peptide nucleic acid with label free and total internal reflection fluorescence detection for quantification of endocrine disruptors. *Analytica Chimica Acta* **2002**, *469*, 37-48.
160. Reichl, D.; Krage, R.; Krumme, C.; Gauglitz, G., Sensing of volatile organic compounds using a simplified reflectometric interference spectroscopy setup. *Applied Spectroscopy* **2000**, *54*, 583-586.
161. Birkert, O.; Tünnemann, R.; Jung, G.; Gauglitz, G., Label-free parallel screening of combinatorial triazine libraries using reflectometric interference spectroscopy. *Analytical chemistry* **2002**, *74*, 834-840.
162. Tschmelak, J.; Kumpf, M.; Käppel, N.; Proll, G.; Gauglitz, G., Total internal reflectance fluorescence (TIRF) biosensor for environmental monitoring of testosterone with commercially available immunochemistry: Antibody characterization, assay development and real sample measurements. *Talanta* **2006**, *69*, 343-350.

163. Pröll, F.; Möhrle, B.; Kumpf, M.; Gauglitz, G., Label-free characterisation of oligonucleotide hybridisation using reflectometric interference spectroscopy. *Analytical and Bioanalytical Chemistry* **2005**, 382, 1889-1894.
164. Yantasee, W.; Lin, Y.; Li, X.; Fryxell, G. E.; Zemanian, T. S.; Viswanathan, V. V., Nanoengineered electrochemical sensor based on mesoporous silica thin-film functionalized with thiol-terminated monolayer. *Analyst* **2003**, 128, 899-904.
165. Saha, S.; Arya, S. K.; Singh, S. P.; Sreenivas, K.; Malhotra, B. D.; Gupta, V., Nanoporous cerium oxide thin film for glucose biosensor. *Biosensors and Bioelectronics* **2008**, 24, 2040-2045.
166. Singh, S. P.; Arya, S. K.; Pandey, P.; Malhotra, B. D., Cholesterol biosensor based on rf sputtered zinc oxide nanoporous thin film. *Applied Physics Letters* **2007**, 91, 063901.
167. Tai, W-P.; Oh, J-H., Fabrication and humidity sensing properties of nanostructured TiO<sub>2</sub>-SnO<sub>2</sub> thin films. *Sensors and Actuators B* **2002**, 85, 154-157.
168. Ghadiri, M. R., Moteshareei, K., Lin, S. Y., Sailor, M. J., Dancil, K. P. S., Porous semiconductor-based optical interferometric sensor. U.S. Patent No. 6,248,539, **2001**.
169. Janshoff, A.; Dancil, K.-P. S.; Steinem, C.; Greiner, D. P.; Lin, V. S.-Y.; Gurtner, C.; Moteshareei, K.; Sailor, M. J.; Ghadiri, M. R., Macroporous p-type silicon Fabry-Perot layers. Fabrication, characterization, and applications in biosensing. *Journal of the American Chemical Society* **1998**, 120, 12108-12116.
170. Bjorklund, R. B.; Zangoie, S.; Arwin, H., Color changes in thin porous silicon films caused by vapor exposure. *Applied physics letters* **1996**, 69, 3001-3003.
171. Ouyang, H.; Christophersen, M.; Viard, R.; Miller, B. L.; Fauchet, P. M., Macroporous silicon macrocavities for macromolecule detection. *Advanced Functional Materials* **2005**, 15, 1851-1859.

172. Lin, V. S.-Y.; Motesharei, K.; Dancil, K.-P. S.; Sailor, M. J.; Ghadiri, M. R., A porous silicon-based optical interferometric biosensor. *Science* **1997**, *278*, 840-843.
173. Cunin, F.; Schmedake, T. A.; Link, J. R.; Li, Y. Y.; Koh, J.; Bhatia, S. N.; Sailor, M. J., Biomolecular screening with encoded porous-silicon photonic crystals. *Nature Materials* **2002**, *1*, 39-41.
174. Chan, S.; Fauchet, P. M.; Li, Y.; Rothberg, L. J.; Miller, B. L., Porous silicon microcavities for biosensing applications. *Physica Status Solidi* **2000**, *182*, 541-546.
175. Ilyas, S.; Böcking, T.; Kilin, K.; Reece, P. J.; Gooding, J.; Guas, K.; Gal, M., Porous silicon based narrow line-width rugate filters. *Optical Materials* **2007**, *29*, 619-622.
176. Pacholski, C.; Yu, C.; Miskelly, G. M.; Godin, D.; Sailor, M. J., Reflective interferometric fourier transform spectroscopy: a self-compensating label-free immunosensor using double-layers of porous SiO<sub>2</sub>. *Journal of the American Chemical Society* **2006**, *128*, 4250-4252.
177. Pacholski, C.; Perelman, L. A.; VanNieuwenhze, M. S.; Sailor, M. J., Small molecule detection by reflective interferometric Fourier transform spectroscopy (RIFTS). *physica status solidi (a)* **2009**, *206*, 1318-1321.
178. Perelman, L. A.; Pacholski, C.; Li, Y. Y.; VanNieuwenhze, M. S.; Sailor, M. J., pH-triggered release of vancomycin from protein-capped porous silicon films. *Nanomedicine* **2008**, *3*, 31-43.
179. Pacholski, C., Photonic crystal sensors based on porous silicon. *Sensors* **2013**, *13*, 4694-4713.
180. Lin, H.; Gao, T.; Fantini, J.; Sailor, M. J., A porous silicon-palladium composite film for optical interferometric sensing of hydrogen. *Langmuir* **2004**, *20*, 5104-5108.
181. Li, J.; Sailor, M. J., Synthesis and characterization of a stable, label-free optical biosensor from TiO<sub>2</sub>-coated porous silicon. *Biosensors and Bioelectronics* **2014**, *55*, 372-378.

182. Anglin, E. J.; Schwartz, M. P.; Ng, V. P.; Perelman, L. A.; Sailor, M. J., Engineering the chemistry and nanostructure of porous silicon Fabry-Pérot films for loading and release of a steroid. *Langmuir* **2004**, *20*, 11264-11269.
183. Anderson, M. A.; Tinsley-Bown A.; Allcock, P.; Perkins, E. A.; Snow, P.; Hollings, M.; Smith, R. G.; Reeves, C.; Squirrell, D. J.; Nicklin, S.; Cox, T. I., Sensitivity of the optical properties of porous silicon layers to the refractive index of liquid in the pores. *Physica Status Solidi* **2003**, *197*, 528-533.
184. Recio-Sánchez, G.; Torres-Costa, V.; Manso, M.; Gallach, D.; López-García, J.; Martín-Palma, R. J., Towards the development of electrical biosensors based on nanostructured porous silicon. *Materials* **2010**, *3*, 755-763.
185. Pacholski, C.; Sartor, M.; Sailor, M. J.; Cunin, F.; Miskelly, G., Biosensing using porous silicon double-layer interferometers reflective interferometric fourier transform spectroscopy. *Journal of the American Chemical Society* **2005**, *127*, 11636-11645.
186. Kilian, K. A.; Böcking, T.; Gaus, K.; Gal, M.; Gooding, J. J., Peptide-modified optical filters for detecting protease activity. *Acs Nano* **2007**, *1*, 355-361.
187. Orosco, M. M.; Pacholski, C.; Miskelly, G. M.; Sailor, M. J., Protein-coated porous-silicon photonic crystals for amplified optical detection of protease activity. *Advanced Materials* **2006**, *18*, 1393-1396.
188. Massad-Ivanir, N.; Shtenberg, G.; Zaidman, T.; Segal, E., Construction and characterisation of porous SiO<sub>2</sub>/hydrogel hybrids as optical biosensors for rapid detection of bacteria. *Advance Functional Materials* **2010**, *20*, 2269-2277.
189. Sailor, M. J., Color me sensitive: amplification and discrimination in photonic silicon nanostructures. *ACS Nano* **2007**, *1*, 248-252.
190. Mun, K.-S.; Alvarez, S. D.; Choi, W.-Y.; Sailor, M. J., A stable, label-free optical interferometric biosensor based on TiO<sub>2</sub> nanotube arrays. *Acs Nano* **2010**, *4*, 2070-2076.

191. Kumeria, T.; Santos, A.; Losic, D., Ultra sensitive nanoporous interferometric sensor for label-free detection of gold(III) ions. *ACS Applied Materials Interfaces* **2013**, *5*, 11783-11790.
192. Kumeria, T.; Rahman, M. M.; Santos, A.; Ferré-Borrull, J.; Marsal, L. F.; Losic, D., Nanoporous anodic alumina rugate filters for sensing of ionic mercury: toward environmental point-of-analysis systems. *ACS Applied Materials Interfaces* **2014**, *6*, 12971-12978.
193. An, H. C.; An, J. Y.; Kim, B.-W., Improvement of sensitivity in an interferometry by controlling pore size on the anodic aluminum oxide chip pore-widening technique. *Korean Journal of Chemical Engineering* **2009**, *26*, 160-164.
194. Macias, G.; Ferré-Borrull, J.; Pallarès, J.; Marsal, L. F., Effect of pore diameter in nanoporous anodic alumina optical biosensors. *Analyst* **2015**, *140*, 4848-4854.
195. Kumeria, T.; Losic, D., Controlling interferometric properties of nanoporous anodic aluminium oxide. *Nanoscale research letters* **2012**, *7*, 1-10.
196. Kumeria, T.; Losic, D., Reflective interferometric gas sensing using nanoporous anodic aluminium oxide (AAO). *physica status solidi (RRL)-Rapid Research Letters* **2011**, *5*, 406-408.
197. Dronov, R.; Jane, A.; Shapter, J. G.; Hodges, A.; Voelcker, N. H., Nanoporous alumina-based interferometric transducers ennobled. *Nanoscale* **2011**, *3*, 3109-3114.
198. Macias, G.; Hernández-Eguía, L. P.; Ferré-Borrull, J.; Pallares, J.; Marsal, L. F., Gold-coated ordered nanoporous anodic alumina bilayers for future label-free interferometric biosensors. *ACS applied materials & interfaces* **2013**, *5*, 8093-8098.
199. Kumeria, T.; Gulati, K.; Santos, A.; Losic, D., Real-time and in situ drug release monitoring from nanoporous implants under dynamic flow conditions by reflectometric interference spectroscopy. *ACS Applied Materials and Interfaces* **2013**, *5*, 5436-5442.

200. Rumeria, T.; Rahman, M. M.; Santos, A.; Ferré-Borrull, J.; Marsal, L. F.; Losic, D., Nanoporous anodic alumina rugate filters for sensing of ionic mercury: toward environmental point-of-analysis systems. *ACS Applied Material Interfaces* **2014**, *6*, 12971-12978.
201. Veliz, I.; Loo, Y.; Castillo, O.; Karachaliou, N.; Nigro, O.; Rosell, R., Advances and challenges in the molecular biology and treatment of glioblastoma-is there any hope for the future? *Annals of Translational Medicine* **2015**, *3(1)*, 7.
202. Akhtar, A.; Fuchs, E.; Mitchison, T.; Shaw, R. J.; Johnston, D. S.; Strasser, A.; Taylor, S.; Walczak, C.; Zerial, M., A decade of molecular cell biology: achievements and challenges. *Nature Reviews Molecular Cell Biology* **2011**, *12*, 669-674.
203. Park, S-M., Toward integrated molecular diagnostic system (iMDx): principles and applications. *IEEE Transactions on Biomedical Engineering* **2014**, *61(5)*, 1506-1521.
204. Lui, C.; Cady, N. C.; Batt, C. A., Nucleic acid-based detection of bacterial pathogens using integrated microfluidic platform systems. *Sensors* **2009**, *9*, 3713-3744.
205. Little, M.C.; Andrews, J.; Moore, R.; Bustos, S.; Jones, L.; Embres, C.; Durmowicz, G.; Harris, J.; Berger, D.; Yanson, K.; et al. Strand displacement amplification and homogeneous real-time detection incorporated in a second-generation DNA probe system, BDProbeTecET. *Clinical Chemistry* **1999**, *45*, 777-784.
206. Mader, A.; Riehle, U.; Brandstetter, T.; Stickeler, E.; Hausen, A. Z.; RÜhe, J., Microarray-based amplification and detection of RNA by nucleic acid sequence based amplification. *Analytical and Bioanalytical Chemistry* **2010**, *379*, 3533-3541.
207. Ge, Y.; Cui, L.; Qi, X.; Shan, J.; Shan, Y.; Qi, Y.; Wu, B.; Wang, H.; Shi, Z., Detection of novel swine origin influenza A virus (H1N1) by real-time nucleic acid-based amplification. *Journal of Virological Methods* **2010**, *163(2)*, 495-497.

208. Mahalanabis, M.; Do, J.; Almuayad, H.; Zhang, J.; Klapperich, C. An integrated disposable device for DNA extraction and helicase dependent amplification. *Biomedical Microdevices* **2010**, *12*, 353–359.
209. Chang, C-C.; Chen, C-C.; Wei, S-C.; Lu, H-H.; Liang, Y-H.; Lin, C-W., Diagnostic devices for isothermal nucleic acid amplification. *Sensors* **2012**, *12*, 8319-8337.
210. Kordas, A.; Papadakis, G.; Milioni, D.; Champ, J., Descroix, S.; Gizeli, E., Rapid *Salmonella* detection using an acoustic wave device combined with the RCA isothermal DNA amplification method. *Sensing and Bio-sensing Research* **2016**, *11*, 121-127.
211. Zhao, W.; Ali, M. M.; Brook, M. A.; Li, Y., Rolling circle amplification: applications in nanotechnology and biodetection with functional nucleic acid. *Angewandte Chemie International Edition* **2008**, *47*, 6330-6337.
212. Ou, L.; Sun, A.; Liu, K., Rolling circle amplification-based biosensors. *Analytical Letters* **2015**, *48*, 1199-1216.
213. Yasui, T.; Ogawa, K.; Kaji, N.; Nilsson, M.; Ajiri, T.; Tokeshi, M.; Horiike, Y.; Baba, Y., Label-free detection of real-time DNA amplification using a nanofluidic diffraction grating. *Scientific Reports* **2016**, *6*, 31642.
214. Liu, X.; Song, M.; Hou, T.; Li, F., Label-free homogenous electroanalytical platform for pesticide detection based on acetylcholinesterase-mediated DNA conformational switch integrated with rolling circle amplification. *ACS Sensors* **2017**, *2*, 562-568.
215. Seidy, P.; Isabel, G., Microarray and nanotechnology applications of functional nanoparticles. *Combinatorial Chemistry & High Throughput Screening* **2006**, *9*, 389-397.

**BLANK PAGE**



## CHAPTER 2.

---

### Method & Materials

**Chapter-2** provides the development of required fabrication process to fabricate variety of NAA platforms, perform their surface modification of NAA structures to specific capture of biomolecule, and use these platforms in RIfS system to evaluate their sensing performance assessment. Lastly, it is described the experiment procedure used to detect specific nucleic acid sequence using solution-based molecular technique that is proposed to be adopted for resistant gene detection using NAA-RIfS detection system.

**BLANK PAGE**

## 2.1. Materials and chemicals

High-purity (99.9997%)  $1.5 \times 1.5 \text{ cm}^2$  square aluminum (Al) substrates 0.32 mm thick were supplied by Goodfellow Cambridge Ltd. (UK). Oxalic acid ( $\text{H}_2\text{C}_2\text{O}_4$ ), Sulfuric acid ( $\text{H}_2\text{SO}_4$ ), phosphoric acid ( $\text{H}_3\text{PO}_4$ ), perchloric acid ( $\text{HClO}_4$ ), chromic acid ( $\text{H}_2\text{CrO}_4$ ), phosphoric acid ( $\text{H}_3\text{PO}_4$ ), hydrochloric acid ( $\text{HCl}$ ), (3-aminopropyl)trimethoxysilane (APTES), hydrogen peroxide ( $\text{H}_2\text{O}_2$ ), glutaraldehyde ( $\text{CH}_2(\text{CH}_2\text{CHO})_2$  – GTA), phosphate buffered saline (PBS), human serum albumin (HSA), chymotrypsin from bovine pancreas, peroxidase from horseradish, human hemoglobin, gelatin from porcine skin, and trypsin from porcine pancreas, indomethacin ( $\text{C}_{19}\text{H}_{16}\text{ClNO}_4$ ), coumarin ( $\text{C}_9\text{H}_6\text{O}_2$ ), sulfadymethoxine ( $\text{C}_{12}\text{H}_{14}\text{N}_4\text{O}_4\text{S}$ ), warfarin ( $\text{C}_{19}\text{H}_{16}\text{O}_4$ ), salicylic acid ( $\text{C}_7\text{H}_6\text{O}_3$ ), ethanol ( $\text{EtOH}$ ,  $\text{C}_2\text{H}_5\text{OH}$ ), sodium hydroxide ( $\text{NaOH}$ ), and quercetin were purchased from SigmaAldrich (Australia) and used as received, without further purification. Ultrapure water Option Q-Purelabs (Australia) was used for preparing the aqueous solutions used in this PhD project. Wizard® Genomic DNA Purification Kit was used from Promega. In the genetic study of this project, we used crop insects including *T. castaneum* QTC4 (phosphine susceptible strain) and *T. castaneum* QTC279 (phosphine resistant strain), which were kindly provided by department of agriculture and fisheries, Queensland.

## 2.2. Electrochemical Anodization for Fabrication of Nanoporous Anodic Alumina

### 2.2.1 The Anodization System

Electrochemical procedure is frequently used for finishing and surface structuring of various metals via controlled anodic dissolution reactions. NAA material used in this project were fabricated using electrochemical anodization<sup>1, 2</sup>. Electrochemical anodization system

consists of anodization unit, a power supply, a digital-to-analogue converter, and computer software (**Figure 2.1**).

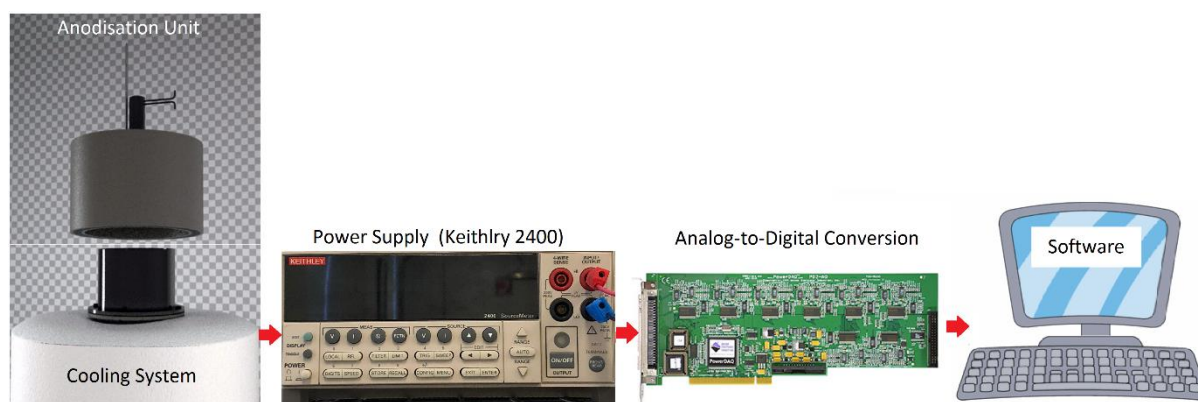


**Figure 2.1.** A schematic diagram of the electrochemical anodization setup including an anodization unit (anodization cell and cooling system), a power supply, an analogue to digital converter card connecting the power supply to a computer.

The electrochemical anodization unit for NAA fabrication consists of an anodization cell combined with cooling system in order to achieve the temperature of interest during anodization. Here, the anodization cell is designed as a custom built container which holds two parts including base and cover (**Figure 2.2**). The base is an open window holder with back copper plate (**Figure 2.2a and 2.2b**). Al chips (15 mm × 15 mm) can be fitted into the holder as the anode electrode. The cover holds platinum wires as the cathode electrodes, there is stirrer to keep consistent temperature of reaction, a thermometer, and electrical connections. The cover is wrapped with an insulation sheet as well (**Figure 2.2c, 2.2d, and 2.2e**). The base of the anodization cell is 6 cm × 4.5 cm I diameter which is enough space for the electrolyte and the electrochemical reaction.

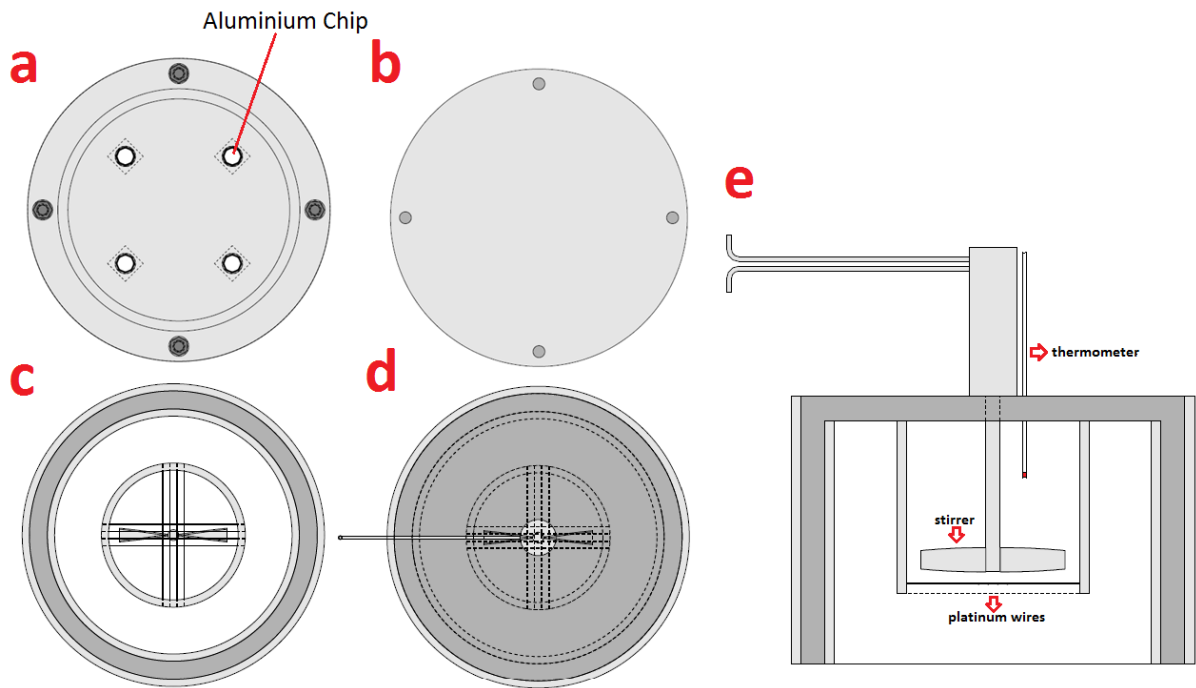


**Figure 2.2.** Anodization cell configuration. a) Top view of anodization cell, and the base is used as an Anode (aluminium act as Anode). b) Back copper plate which is attached to the part of the anodization cell, used for electrical connection. c) Anodization cell, inner part of insulation cover holding platinum wires as cathode and stirrer. d) Top view of insulation cover holding electrical connections and thermometer. The grey color illustrates the insulation sheet. e) Cross-section view of anodization cell' cover.

In the following sections, the detail of the fabrication procedures for three different NAA structures used in this project are described.

### 2.2.2 Fabrication of Nanoporous Anodic Alumina Photonic Film (NAA-PF)

Aluminium (Al) chips were first cleaned in ethanol for 5 min and dried under air stream. Then, they were fitted into the designed anodization cell according **Figure 2.2a**. The electrochemical anodization was performed following a two-step anodization process<sup>3</sup>. According this process, Al chips were polished in a mixture of EtOH: HClO<sub>4</sub> 4:1 (v:v) at 20 V and 5 °C for 3 min in order to achieve smooth mirror surface. The first anodization step was performed in a solution of 0.3 M H<sub>2</sub>C<sub>2</sub>O<sub>4</sub> at 40 V and 6 °C for 20 h (mild anodization). Then, the produced nanoporous layer was etched away in a mixture of 0.2 M H<sub>2</sub>CrO<sub>4</sub> and 0.4 M H<sub>3</sub>PO<sub>4</sub> for 3 h at 70 °C. Subsequently, the second anodization step was carried out under the

similar anodization conditions of first step for duration of 2 h. Pore diameter of resulting NAA-PFs were widened by wet chemical etching in a solution of  $\text{H}_3\text{PO}_4$  5 wt% at 35 °C for 15 min.

### **2.2.3 Fabrication of Nanoporous Anodic Alumina Rugate Filter (NAA-RF)**

Al substrates were cleaned under sonication in ethanol (EtOH) for 15 min and dried under air stream. Then, Al chips were fitted into the designed anodization cell. NAA rugate filters were fabricated using sinusoidal pulse anodization approach and galvanostatic mode in sulfuric acid electrolyte<sup>4</sup>. Subsequently, Al substrates were electro polished using a mixture of  $\text{HClO}_4$  and EtOH 1:4 (v:v) at 20 V and 5 °C for 3 min. After electro polishing, Al substrates were anodised in the above mentioned anodization cell using 1.1 M sulfuric acid as electrolyte. The temperature of anodization was constantly kept at -1 °C using the cooling system. The anodization process started with a first stage at constant current density of 1.12  $\text{mA cm}^{-2}$  for 1 h. After 1 hour, the anodization current density was set to be modified in a sinusoidal fashion between high ( $J_{\text{Max}} = 1.12 \text{ mA cm}^{-2}$ ) and low ( $J_{\text{Min}} = J_{\text{Offset}} = 0.28 \text{ mA cm}^{-2}$ ) values. The sinusoidal modification was repeated for 150 cycles with certain anodization period (i.e., 650, 700, 750 seconds). Finally, NAA rugate filters were pore widened by wet chemical etching in 5 wt %  $\text{H}_3\text{PO}_4$  at 35 °C for 6 min. Furthermore, the underlying aluminium was removed in a saturated solution of  $\text{HCl}/\text{CuCl}_2$ .

### **2.2.4 Fabrication of Bilayered Nanoporous Anodic Alumina (BL-NAA)**

Al chips were anodised following triple step anodization process. As mentioned before, Al chips were sonicated in ethanol to remove organic particles. Then, Al chips were electrochemically polished in a mixture of EtOH:  $\text{HClO}_4$  4:1 (v: v) at 20 V and 5°C for 3 min to get a smooth surface. 0.3M oxalic acid electrolyte, 20 V and 5 °C were defined as anodization conditions for all steps. First step of anodization was carried out during 20 hours. Then, the produced nanoporous layer was etched away in a mixture of 0.2 M  $\text{H}_2\text{CrO}_4$  and 0.4 M  $\text{H}_3\text{PO}_4$

for 3 h at 70 °C. The second and third steps of anodization were performed in a solution of 0.3 M H<sub>2</sub>C<sub>2</sub>O<sub>4</sub> at 40 V and 5 °C according to a particular timing of anodization (i.e., 3, 4.5, 6, and 9 hr). A pore widening step was used to increase diameter of nanopores by a wet chemical etching method in an aqueous solution of H<sub>3</sub>PO<sub>4</sub> 5 wt% at 35 °C for 15 min. Furthermore, the underlying aluminium was removed in a saturated solution of HCl/CuCl<sub>2</sub>.

### 2.3. Surface Chemistry Functionalization Using CVD

Functionalization of NAA surface is significant step in the process of capture detection using a RIfS sensor. Here, prepared NAAs were mainly functionalized with APTES using a chemical vapour deposition (CVD) process.

All types of NAA structures used in this project were chemically functionalised with 3-aminopropyltriethoxysilane (APTES) following a well-established protocol <sup>5, 6</sup>. First, NAA substrates were immersed in 30 wt% H<sub>2</sub>O<sub>2</sub> for 15 min at 90 °C. After that, NAA substrates and a small container filled with 1 mL APTES were placed in a glass desiccator (**Figure 2.3b**). The desiccator was sealed properly and vacuumed using a pump. Then, the desiccator was kept at 110°C for 3 hours. As a result, silane molecules were immobilised onto the inner surface of NAA nanopores.

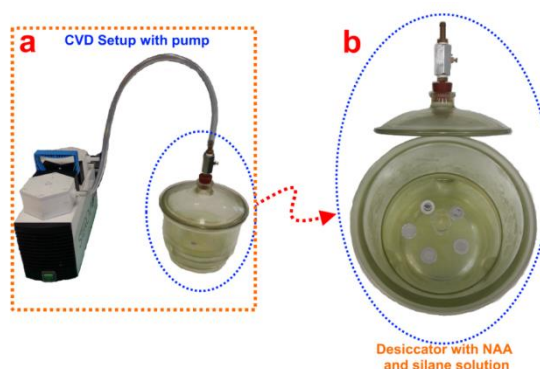


**Figure 2.3.** Digital photographs of (a) CVD procedure used for silanisation of NAA sensing substrates in this study. (b) Open desiccator shows NAA sensing substrates with APTES solution (source [6]).

## 2.4. Real-Time Monitoring of Target Analyte using Reflectometric Interference Spectroscopy (RIfS).

Real-time monitoring presents crucial advantages over batch processing based sensing approach. In real-time monitoring, there is the ability to monitor the analyte-receptor binding as it occurs, whilst in batch processing sensing, signal can only be measured in the beginning and at the end of binding event. Real-time monitoring also present extensive data points which is essential for better understanding of binding kinetics.

In this thesis, a custom built flow cell is used for real-time monitoring. The flow cell is designed to be re-useable for multiple sensing processes. It has a base and top cover which is made of borosilicate glass. The borosilicate glass has 0.5 mm holes for inlet and outlet ports. Prepared NAA can be accommodated into the flow cell. There is a square cavity of  $1.6 \times 1.6$  mm<sup>2</sup> and 100  $\mu$ m deep to deliver the analyte fluid (**Figure 2.4**).

The RIfS optical setup used in this thesis consists of a white light source (HL 1LL, Ocean Optics, USA) connected to one end of an optical probe (R400-7 Vis-NIR, Ocean Optics, USA) that carries the light onto NAA sensing platform. The illumination spot was adjusted to 2 mm in diameter by a lens system (VIS Collimating Lens, 350–2000 nm, Ocean Optics). The reflected light is collected by the collection fibers (the other end of optical probe) and is transferred to a miniature spectrometer (USB4000 VIS-NIR, Ocean Optics, USA). A digital picture of the RIfS setup combined with flow cell, is shown in **Figure 2.4**. Note that, the optical probe held vertically using a micro manipulator device to focus light on NAA sensing platform at a normal angle. Notice that, RIfS optical setup is highly sensitive to external vibrations that causes large noises in the RIfS signal. Therefore, the RIfS sensing setup was fixed on an anti-vibration table to grip all optical assemblies. The reflection spectra of NAA platform were acquired from 400 to 1000 nm and saved at intervals of 30 s, with an integration time of 10 ms



and 10 average measurements. RIFS spectra were processed in Igor Pro library (Wavemetrics) in order to estimate reflection peak position ( $\lambda_{Peak}$ ) and the effective optical thickness ( $OT_{eff}$ ) of NAAs during the entire process of monitoring.

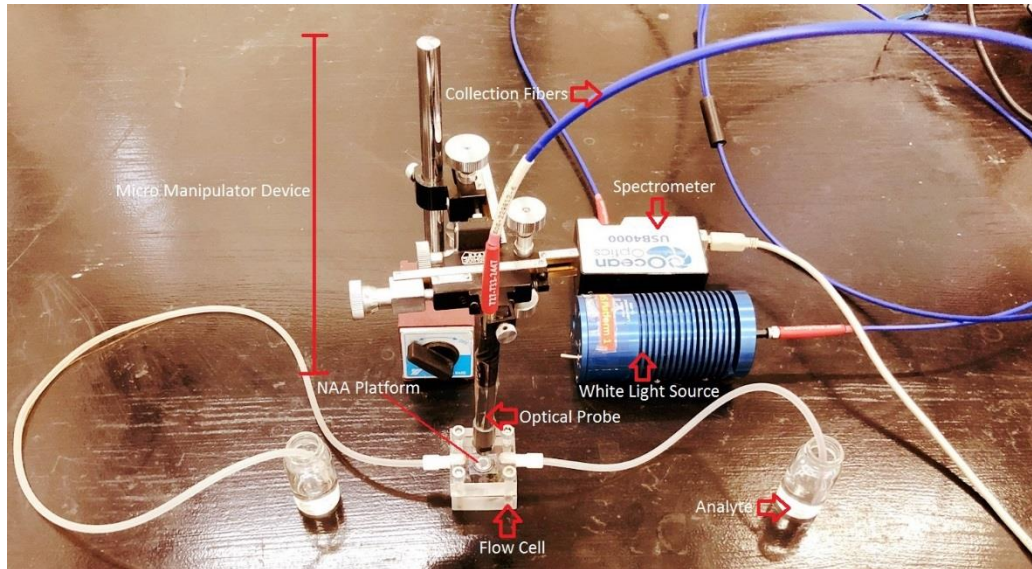


**Figure 2.4.** RIFS set up clamped on to anti-vibration table. The RIFS set up consists of: A flowing cell which accommodates NAA sensing platform, optical probe, light source, spectrometer, optical collection fibres, and micromanipulator device.

## 2.5. Molecular Genetic Analysis.

In this thesis, genomic DNA extraction, polymerase chain amplification (PCR) and rolling circle amplification (RCA) are used to detect a known mutation associated with phosphine resistant *Tribolium castaneum* (*T. castaneum*) in a population.

### 2.5.1 Genomic DNA Preparation

Genomic DNA was extracted from susceptible and resistant populations of *T. castaneum*, using the protocol provided by Wizard® Genomic DNA Purification Kit (Promega). Briefly, an individual beetle was freeze dried with liquid nitrogen and homogenised in nuclei lysis solution in order to break cells and membrane structures. Then the mixture centrifuged for 10

sec at maximum speed. The supernatant of nuclei lysate solution incubated at 37°C for 30 min, after 3 µl of RNase was added to degrade RNA molecules. Samples were centrifuged at 14000 rpm for 4 min at room temperature. The supernatant was then gently mixed with isopropanol and again centrifuged as above. Then, the supernatant was removed and pellet was properly washed with 70% ethanol and then air dried. Finally, 50 µl of DNA rehydration solution was added to each sample tube and were incubated at 4°C for overnight to achieve purified genomic DNA templates. **Figure 2.5** presents the summary of sequential steps during genomic DNA extraction from beetles' tissue.

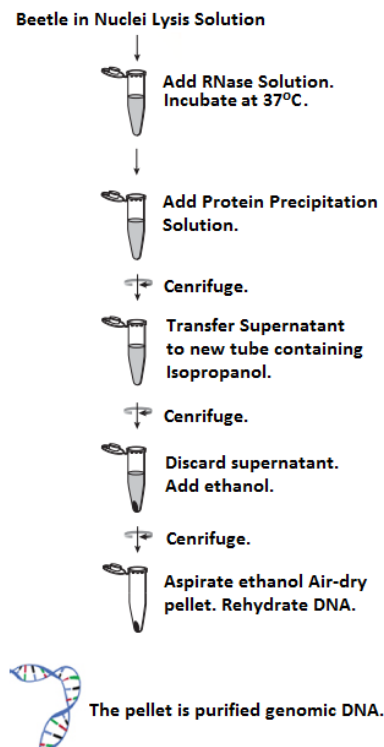



**Figure 2.5.** An illustration of genomic DNA extraction protocol used in this study.


### 2.5.2. Bioinformatics Analysis

Dihydrolipoamide dehydrogenase (DLD) gene nucleotide sequences from *T. castaneum* strain QTC4 Susceptible (KX907540.1) & *T. castaneum* strain QTC931 (KX907541.1) were retrieved from the NCBI database (<https://www.ncbi.nlm.nih.gov>). The DLD primer set (forward and reverse) used for polymerase chain reaction (PCR), padlock probe for RCA


reaction, and DLD allele-specific target and non-target sequences were then designed using the PrimerQuest design tool ([www. idtdna.com/SciTools](http://www.idtdna.com/SciTools)) in order to confirm the presence of the SNP in the *T. castaneum* strains. The sequence were designed as below:

 *Forward primer for PCR amplification:*

(Tcdld F): **5' AAAGGAAAATGCTGTCAAGGC 3'**

 *Reverse primer for PCR amplification:*

(Tcdld R): **5' CTGTAATTTTCCCATGTCCGTTG 3'**


 *Padlock probe for RCA reaction:*

**5' CCAGTTAAAGC**CTTGACAGCATTTTCCTAGAATGAA  
GATAGCGCATC GTAGGACGAAAA**GTTGCGCTATGCTT** **3'**

Note that, the padlock probe was designed so that the 11 bp at the 5' end and the 14 bp at the 3' end are complementary to the target (*T. castaneum* DLD gene region containing SNP). The two terminal **T** nucleotides located at the 3' end of the padlock sequence dictate the specificity of detection towards resistant alleles which contain the AA SNPs at the complementary location.

 *DLD allele-specific target sequence for RCA reaction:*

(T.cas\_Res\_RCA): **5' GCTTTAACTGGAAGCATAGCG 3'**

 *Non-target sequence for RCA reaction:*

(T.cas\_Sus\_RCA): **5'GCTTTAACTGGGGGCATAGCG 3'**

Finally, Biological Sequence Alignment Editor Software (*BioEdit*) was used in order to analyse PCR product sequences <sup>7</sup>.

### **2.5.3. PCR Amplification and Sequencing**

Genomic DNA was amplified by PCR using the selected primers in a 50- $\mu$ l reaction volume containing 5  $\mu$ l of genomic DNA, 1  $\mu$ l of each primer, (forward and reverse). 4  $\mu$ l dNTPs, 0.25  $\mu$ l Takara Taq- polymerase enzyme in 5  $\mu$ l 10x reaction buffer supplied with the enzyme. Amplification was carried out in a gradient thermocycler, manufactured by Kyrattec (SC200), programmed for an initial 2 min and 30 sec, then followed by 30 cycles of 30 sec at 95°C, 30 sec at 56°C, and 30 sec at 72°C, a final step was also performed for 3 min at 72°C.

Amplification products were visualized by gel electrophoresis technique using 0.8% agarose and RedSafe nucleic acid stain (iNtRON). The remaining PCR product was purified using the UltraClean PCR clean-up kit (MO BIO laboratories) and sent for Sanger sequencing at AGRF, Adelaide.

### **2.5.4. Padlock Probe Ligation and Rolling Circle Amplification (RCA)**

A 73-mer oligonucleotide (as mentioned above) with a 5' phosphate modification used as RCA linear template (padlock probe). The ligation and circularization of the padlock probe is dependent on the interaction between these two complementary sequences of padlock probe with Allele-specific resistant target/ non-target susceptible (**Figure 2.6**).



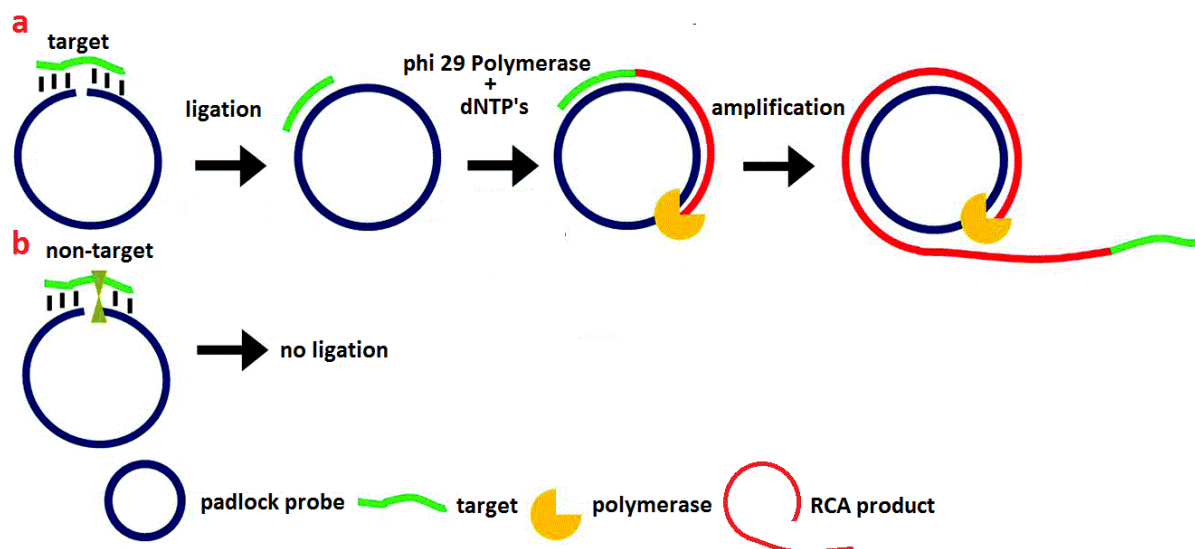


**Figure 2.7.** Ligation-rolling circle amplification for SNP detection.

## 2.6. References

- 1- Datta, M.; Harris, D., Electrochemical micromachining: an environmentally friendly, high speed processing technology. *Electrochimica Acta* **1997**, *42*, 3007-3013.
- 2- Datta, M.; Landolt, D., Fundamental aspects and applications of electrochemical microfabrication. *Electrochimica Acta* **2000**, *45*, 2535-2558.
- 3- Masuda, H.; Yada, K.; Osaka, A., Self-ordering of cell configuration of anodic porous alumina with large-size pores in phosphoric acid solution. *Japanese Journal of Applied Physics* **1998**, *37*, L1340.
- 4- Santos, A.; Yoo, J. H.; Rohatgi, C. V.; Kumeria, T.; Wang, Y.; Losic, D., Realisation and advanced engineering of true optical rugate filters based on nanoporous anodic alumina by sinusoidal pulse anodisation. *Nanoscale* **2016**, *8*, 1360-1373.

- 5- Jani, Md. A. M.; Kempson, I. M.; Losic, D.; Voelcker, N. H., Dressing in layers: layering surface functionalities in nanoporous aluminium oxide membranes. *Angewandte Chemie International Edition* **2010**, (49), 7933-7937.
- 6- Kumeria, T.; **2015**; Development of nanopore based label-free optical sensors; Doctor of philosophy, engineering (nanotechnology); The University of Adelaide, Adelaide.
- 7- Hall, T. A., BioEdit: a user friendly biological sequence alignment editor and analysis program for windows 95/98/NT. *Nucleic Acid Symposium Series* **1999**, (41), 95-98.

**BLANK PAGE**



## CHAPTER 3.

---

### Enzymatic Sensor Combining NAA and RfS

This chapter is based on the following the peer-reviewed article:

**Mahdiah Nemati**, Abel Santos, Tushar Kumeria, Dusan Losic. Label-free real-time quantification of enzyme levels by interferometric spectroscopy combined with gelatin-modified nanoporous anodic alumina photonic films. *Analytical Chemistry* 87 (17) (2015) 9016-9024.

**BLANK PAGE**

## Statement of Authorship

Title of Paper	Lable-Free Real-Time Quantification of Enzyme Levels by Interferometric Spectroscopy Combined with Gelatin-Modified Nanoporous Anodic Alumina Photonic Films
Publication Status	<input checked="" type="checkbox"/> Published <input type="checkbox"/> Accepted for Publication <input type="checkbox"/> Submitted for Publication <input type="checkbox"/> Unpublished and Unsubmitted work written in manuscript style
Publication Details	

### Principal Author

Name of Principal Author (Candidate)	Mahdieh Nemati		
Contribution to the Paper	Prepared the first draft of manuscript, edited, and revised the manuscript.		
Overall percentage (%)	85%		
Certification:	This paper reports on original research I conducted during the period of my Higher Degree by Research candidature and is not subject to any obligations or contractual agreements with a third party that would constrain its inclusion in this thesis. I am the primary author of this paper.		
Signature	<table border="1"> <tr> <td>Date</td> <td>12.12.2017</td> </tr> </table>	Date	12.12.2017
Date	12.12.2017		

### Co-Author Contributions

By signing the Statement of Authorship, each author certifies that:

- i. the candidate's stated contribution to the publication is accurate (as detailed above);
- ii. permission is granted for the candidate to include the publication in the thesis; and
- iii. the sum of all co-author contributions is equal to 100% less the candidate's stated contribution.

Name of Co-Author	Abel Santos		
Contribution to the Paper	Co-supervise, edited, revised the manuscript, and corresponding author.		
Signature	<table border="1"> <tr> <td>Date</td> <td>14/12/17</td> </tr> </table>	Date	14/12/17
Date	14/12/17		

Name of Co-Author	Tushar Kumeria		
Contribution to the Paper	Edited and revised the manuscript.		
Signature	<table border="1"> <tr> <td>Date</td> <td>14/12/17</td> </tr> </table>	Date	14/12/17
Date	14/12/17		

Please cut and paste additional co-author panels here as required.

**CHAPTER 3: M. Nemati**, A. Santos, T. Kumeria, D. Lotic "Label-Free Real-Time Quantification of Enzyme Levels by Interferometric Spectroscopy Combined with Gelatin-Modified Nanoporous Anodic Alumina Photonic Films" *Analytical Chemistry*, 2015, **87**, 9016-9024.

---

Name of Co-Author	Dusan Lotic		
Contribution to the Paper	Supervised the development of the work, edited the manuscript and corresponding author.		
Signature		Date	20/12/2017

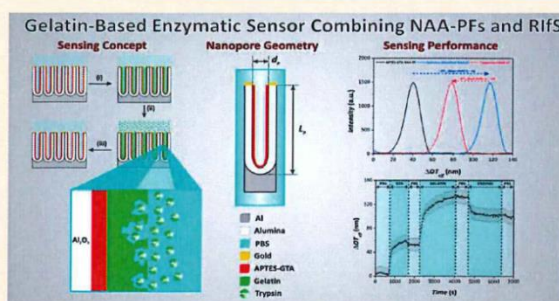
## Label-Free Real-Time Quantification of Enzyme Levels by Interferometric Spectroscopy Combined with Gelatin-Modified Nanoporous Anodic Alumina Photonic Films

Mahdieh Nemati, Abel Santos,\* Tushar Kumeria, and Dusan Losic\*

School of Chemical Engineering, The University of Adelaide, Engineering North Building, 5005 Adelaide, South Australia, Australia

**S** Supporting Information

**ABSTRACT:** Herein, we present an interferometric sensor based on the combination of chemically functionalized nanoporous anodic alumina photonic films (NAA-PFs) and reflectometric interference spectroscopy (RIfS) aimed to detect trace levels of enzymes by selective digestion of gelatin. The fabrication and sensing performance of the proposed sensor were characterized in real-time by estimating the changes in effective optical thickness (i.e., sensing principle) of gelatin-modified NAA-PFs (i.e., sensing element) during enzymatic digestion. The working range ( $WR$ ), sensitivity ( $S$ ), low limit of detection ( $LLoD$ ), and linearity ( $R^2$ ) of this enzymatic sensor were established by a series of experiments with different concentrations of gelatin (i.e., specific chemical sensing element) and trypsin (i.e., analyte), a model protease enzyme with relevant implications as a biomarker in the diagnosis of several diseases. The chemical selectivity of the sensor was demonstrated by comparison of gelatin digestion by other nonspecific enzyme models such as chymotrypsin and horseradish peroxidase. Furthermore, the role of the chemical sensing element (i.e., gelatin) was assessed by using hemoglobin instead of gelatin. Finally, we demonstrated that this sensor can be readily used to establish the kinetic parameters of enzymatic reactions. The obtained results revealed that the presented sensor has a promising potential to be used as a point-of-care system for fast detection of gastrointestinal diseases at early stages.



Enzymes play vital roles in numerous functions of living organisms by catalyzing chemicals and speeding up molecular reactions.<sup>1</sup> For instance, the catalysis of substrates by proteinase enzymes is a significant part of the enzymatic pattern in metabolic and pathophysiological pathways. Proteolytic enzymes, in particular the category of serine proteases, are known as hallmarks of cancer invasion, progression, and metastasis, being related to a broad range of proteolytic activities associated with the growth of malignant cells. Among the different subfamilies of serine proteases, trypsin is of special interest given that this enzyme is involved in different pancreatic functions. Excessive levels of trypsin can lead to a series of events that eventually can produce pancreatic self-digestion and pancreatitis.<sup>2</sup> Trypsin is a digestive enzyme produced by pancreatic acinar cells, the function of which is to cleave peptide bonds on the C-terminal of lysine and arginine amino acid residues.<sup>3</sup> Therefore, the development of advanced sensing systems with cutting edge capabilities aimed to detect trace levels of enzymes is of critical importance to diagnose and identify diseases at an opportune time, when a suitable medical treatment can be implemented. Traditional enzyme assays include electrophoresis, chromatography, radiometric assays by isotope labeling, fluorometric assays, calorimetry, microscale thermophoresis, chemiluminescence, and so on.<sup>4-9</sup> However,

these techniques are time-consuming, require tedious preparation protocols, and must be operated by highly trained personnel. In recent years, an intensive research activity has aimed to develop ultrasensitive, user-friendly, fast, and cost-competitive enzymatic sensors that can overcome the aforementioned limitations of traditional analytical techniques used to establish levels of enzymes. An important part of such research activity has focused on the development of enzymatic sensors based on electrochemical principles.<sup>10-12</sup> Typically, these sensors use enzymes as electrochemical transduction elements aiming to detect other relevant analytes such as lactate, glucose, and urea through enzymatic reactions taking place in the electrode where enzymes are immobilized.<sup>13,14</sup> A remarkable example of that is the glucose sensor based on glucose oxidase, which changed the lives of millions of patients suffering from diabetes. Nevertheless, similar configurations can be also readily used to quantify levels of enzymes as an analyte. For instance, electrodes modified with gelatins have been used to detect enzymes by means of electrochemical signals, which undergo quantitative changes when the gelatin immobilized

Received: June 12, 2015

Accepted: August 10, 2015

Published: August 10, 2015

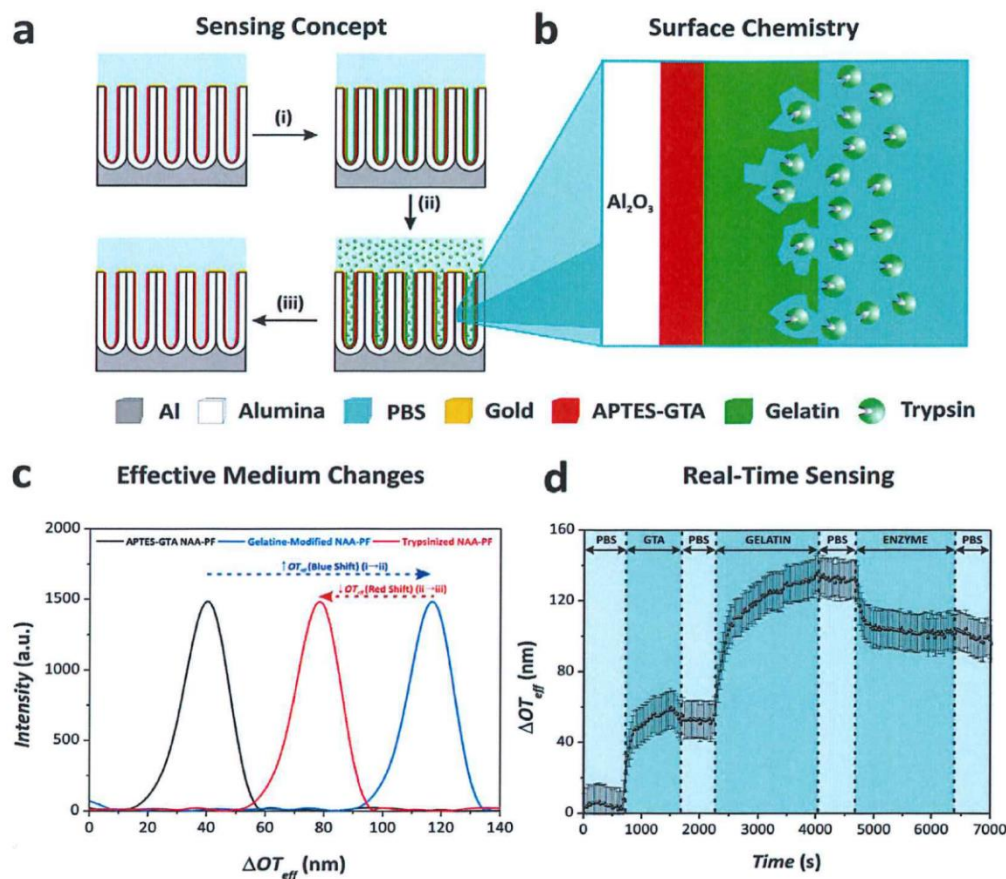


**Figure 1.** Scheme of the sensing concept used in our enzymatic sensors based on the combination of gelatin-modified NAA-PFs and RIFs. a) Sensing process: (i) Amine groups of APTES-modified NAA-PFs are activated by GTA and gelatin molecules immobilized onto the inner surface of NAA-PFs. (ii) Gelatin-modified NAA-PFs are exposed to analyte solutions containing enzymes. (iii) Gelatin is selectively digested by enzymes. b) Details of the surface chemistry used in the proposed enzymatic sensor where gelatin act as the chemical selective element toward enzyme molecules. c) Representative example of effective optical thickness changes in gelatin-modified NAA-PFs measured by RIFs. d) Example illustrating real-time changes in the effective optical thickness of NAA-PFs during the different stages, including GTA activation, gelatin immobilization, and gelatin digestion (NB: Fresh PBS solution was flowed after each stage in order to remove physisorbed molecule).

onto the electrode surface is selectively digested by enzymes present in the analyte sample.<sup>15,16</sup> Alternative optical sensors have also demonstrated a very promising potential to detect trace levels of enzymes by combining different optical techniques and sensing platforms such as nanoparticles and nanoporous materials.<sup>17–20</sup> In particular, the use of nanoporous materials such as porous silicon and nanoporous anodic alumina (NAA) has resulted in several sensing systems featuring unique cutting-edge capabilities for detecting enzymes by means of different strategies.<sup>21–24</sup> Optical sensing platforms based on nanoporous materials can provide multiple advantages such as a large specific surface area to accommodate chemically selective probes and enhance optical signals from analyte molecules, a homogeneous and versatile nanoporous structure that can be engineered to create a broad range of photonic structures with precisely designed optical signals, chemical and physical stability, and so forth.<sup>25,26</sup>

The combination of gelatin-modified photonic structures based on porous silicon and reflectivity spectroscopy was introduced by Killian et al., who made good use of this sensing concept to detect metalloprotease enzyme released from stimulated human macrophage cells.<sup>27</sup> This study demonstrated that this label-free system can achieve an unprecedented low limit of detection (i.e., as low as 1 pg). More recently, Krismastuti et al. used a similar strategy combining nanoporous anodic alumina photonic films (NAA-PFs) chemically modified with polyelectrolytes with reflectometric interference spectroscopy (RIFs) in order to detect proteinase K by enzymatic degradation of the polyelectrolyte layers decorating the inner surface of nanopores in NAA-PFs.<sup>28</sup> Regardless of these advances, more extensive fundamental research must be carried out in order to develop more sophisticated label-free optical systems aimed to monitor levels of enzymes in real-time and to understand the different parameters playing a role in the performance of these sensors. These systems could open new

opportunities toward analytical tools for fundamental studies on cell expression, which is a critical factor to understand a broad range of biological processes such as cell migration, tissue remodeling, and immune responses to diseases.

In this scenario, we present for the first time a combination of gelatin-modified nanoporous anodic alumina photonic films with reflectometric interference spectroscopy aiming to detect trace levels of trypsin enzyme. In this system, gelatin is used as the chemical sensing element, which undergoes selective chemical degradation when trypsin enzyme is present in the analyte sample. Figure 1 illustrates the concept of the proposed sensing system, in which both the fabrication of the sensor and quantification of enzyme levels are monitored in real-time through changes in the effective optical thickness of NAA-PFs established by RIfS. The sensing performance of the proposed sensor is systematically assessed through a series of experiments with different concentrations of enzyme. Furthermore, the chemical selectivity of this sensing system is demonstrated by exposure to other nonselective enzymes. Finally, we determine the role of gelatin as a chemically selective sensing element.

## EXPERIMENTAL SECTION

**Materials.** High purity (99.9997%) circular aluminum (Al) chips 0.32 mm thick and 1.5 cm in diameter were supplied by Goodfellow Cambridge Ltd. (UK). Oxalic acid ( $\text{H}_2\text{C}_2\text{O}_4$ ), perchloric acid ( $\text{HClO}_4$ ), chromic acid ( $\text{H}_2\text{CrO}_4$ ), phosphoric acid ( $\text{H}_3\text{PO}_4$ ), (3-aminopropyl)trimethoxysilane (APTES), hydrogen peroxide ( $\text{H}_2\text{O}_2$ ), glutaraldehyde ( $\text{CH}_2(\text{CH}_2\text{CHO})_2$  - GTA), phosphate buffered saline (PBS), chymotrypsin from bovine pancreas, peroxidase from horseradish, hemoglobin human, gelatin from porcine skin, and trypsin from porcine pancreas (180 TAME units  $\text{mg}^{-1}$ ) were purchased from Sigma-Aldrich (Australia) and used as received, without further purification. Ethanol ( $\text{C}_2\text{H}_5\text{OH}$  - EtOH) was supplied by ChemSupply (Australia). Ultrapure water Option Q-Purelabs (Australia) was used for preparing the aqueous solutions used in this study.

**Fabrication of Nanoporous Anodic Alumina Photonic Crystals.** Al chips were anodized in an electrochemical cell with a circular window of 1 cm in diameter following a two-step anodization process reported elsewhere.<sup>29–32</sup> In this process, Al chips were first sonicated in ethanol and ultrapure water for 15 min each and subsequently dried under air stream. Prior to anodization, Al chips were electrochemically polished in a mixture of EtOH: $\text{HClO}_4$  4:1 (v:v) at 20 V and 5 °C for 3 min in order to achieve a mirrorlike smooth surface. The first anodization step was carried out in an aqueous solution of 0.3 M  $\text{H}_2\text{C}_2\text{O}_4$  at 40 V and 6 °C for 20 h. Then, the resulting NAA layer was chemically etched away in a mixture of 0.2 M  $\text{H}_2\text{CrO}_4$  and 0.4 M  $\text{H}_3\text{PO}_4$  for 3 h at 70 °C. Next, the second anodization step was performed under the same anodization conditions for 2 h. The diameter of nanopores in the resulting photonic films was widened by wet chemical etching in an aqueous solution of  $\text{H}_3\text{PO}_4$  5 wt% at 35 °C for 15 min.

**Surface Chemistry Functionalization.** NAA-PFs were chemically functionalized with 3-aminopropyltriethoxysilane (APTES) following a well-established protocol.<sup>33</sup> In brief, hydroxyl groups were created in the inner surface of NAA-PFs by immersion in 30 wt%  $\text{H}_2\text{O}_2$  at 90 °C during 15 min. After that, silane molecules were immobilized onto the inner surface of NAA nanopores by chemical vapor deposition. This process was carried out in a chemical reactor under vacuum at 135 °C for 3 h. Finally, NAA-PFs were coated with an ultrathin gold

film (i.e., 5 nm) deposited by a sputter coater equipped with film thickness monitor (sputter coater 108auto, Cressington, USA) in order to enhance the interference of light as reported elsewhere.<sup>34,35</sup>

**Sensing Assessment of Gelatin-Modified NAA-PFs.** The sensing performance of gelatin-modified NAA-PFs was assessed by measuring changes in the effective optical thickness of these photonic films with the concentration of trypsin. Reflectometric interference spectroscopy (RIfS) was the technique of choice to establish the working range (WR), sensitivity (S), low limit of detection (LLoD), and linearity ( $R^2$ ) of gelatin-modified NAA-PFs.<sup>36–41</sup> These sensing characteristics were evaluated by measuring the changes in the effective optical thickness of NAA-PFs ( $\Delta OT_{\text{eff}}$ ) estimated by eq 1

$$OT_{\text{eff}} = 2n_{\text{eff}}L_p \cos \theta \quad (1)$$

where  $OT_{\text{eff}}$  is the effective optical thickness of the film,  $n_{\text{eff}}$  is its effective refractive index,  $L_p$  is its physical thickness, and  $\theta$  is the angle of incidence of light (i.e., in the case of RIfS  $\theta = 0^\circ$ ). Note that  $\Delta OT_{\text{eff}}$  associated with the different fabrication and sensing stages was monitored in real-time using a flow cell combined with a RIfS system (see details in the Supporting Information). Briefly, a stable baseline was first obtained by flowing phosphate buffer saline (PBS) solution at room temperature through the flow cell, where APTES-modified NAA-PFs were sandwiched. After stabilization, glutaraldehyde (GTA) solution (2.5 v%) at room temperature was flowed for 15 min in order to activate amine functional groups ( $-\text{NH}_2$ ) of APTES molecules immobilized onto the inner surface of NAA-PFs. Then, fresh PBS solution at room temperature was flowed again for 10 min in order to remove physisorbed GTA molecules. After this, 1 mg  $\text{mL}^{-1}$  gelatin solution at 35 °C was flowed through the system for 30 min in order to functionalize the inner surface of NAA-PFs. Note that the temperature of gelatin was kept constant throughout this process in order to avoid its gelation, which would block the flow of medium through the cell. Next, fresh PBS solutions at 35 °C and room temperature, respectively, were flowed to remove physisorbed gelatin molecules for 5 min each. Then, the analyte solutions containing different concentrations of trypsin (i.e., 0.125, 0.3, 0.5, 0.6, and 1 mg  $\text{mL}^{-1}$ ) at room temperature were flowed through the system until total digestion of gelatin using freshly prepared gelatin-modified NAA-PFs for each concentration of enzyme. Finally, fresh PBS solution at room temperature was flowed for 10 min in order to establish the final  $\Delta OT_{\text{eff}}$  associated with enzymatic digestion of gelatin. Note that all the solutions used in this study (i.e., GTA, gelatin and trypsin) were prepared in fresh PBS at pH 7.5.

**Assessment of Chemical Selectivity.** The effect of the amount of gelatin immobilized onto the inner surface of NAA-PFs on the sensing performance was assessed by measuring the effective optical thickness change associated with different concentrations of gelatin (i.e., 1, 3, 5, and 7 mg  $\text{mL}^{-1}$ ) while keeping constant the concentration of trypsin in the analyte solution (i.e., 1 mg  $\text{mL}^{-1}$ ). Furthermore, the chemical selectivity of the proposed system was evaluated by measuring  $\Delta OT_{\text{eff}}$  after exposure to analyte solutions containing non-specific enzymes such as chymotrypsin and horseradish peroxidase (i.e., 1 mg  $\text{mL}^{-1}$ ). This analysis was further extended by analyzing the effect of the chemical sensing probe. In this experiment, hemoglobin was immobilized onto the inner surface of NAA-PFs instead of gelatin using the above-mentioned protocol. Hemoglobin-modified NAA-PFs

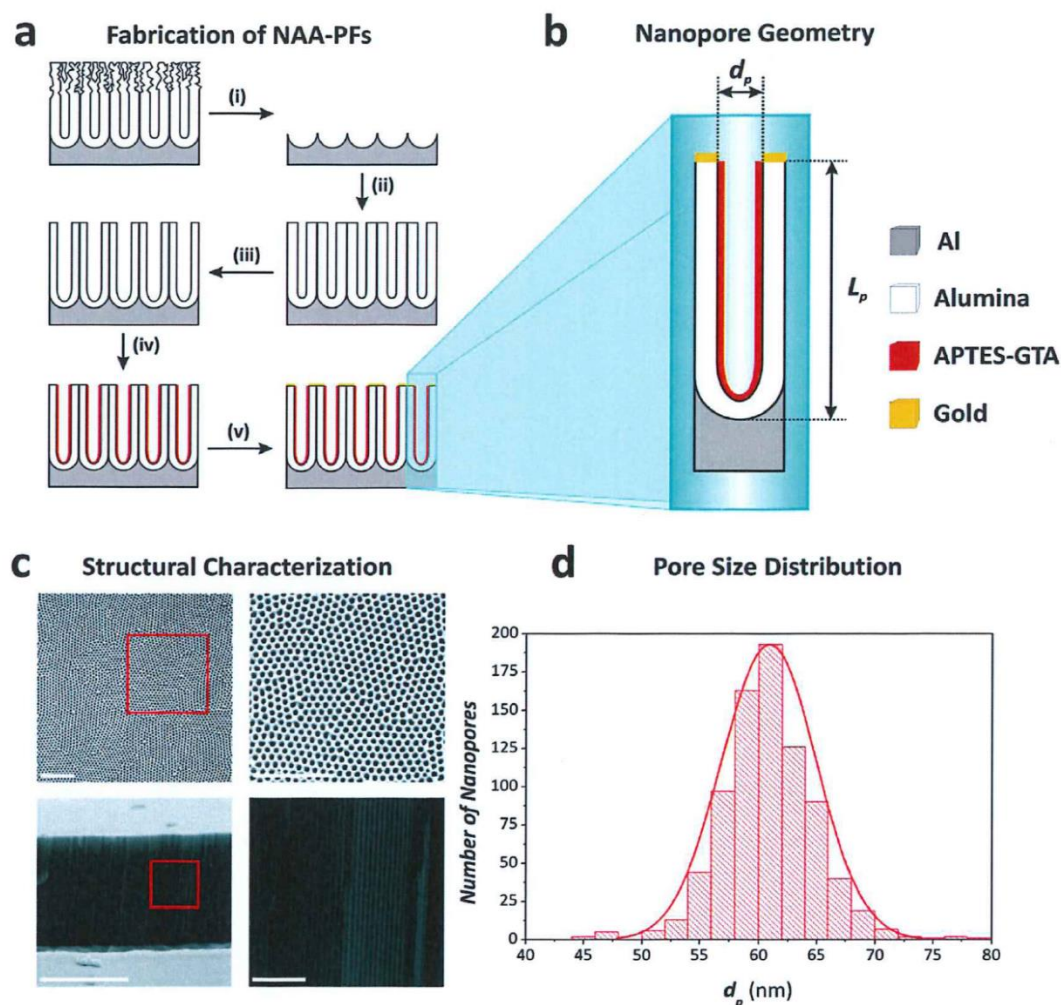


**Figure 2.** Fabrication process and structural characterization of NAA-PFs. a) Fabrication process of NAA-PFs by two-step anodization of aluminum: (i) First step and NAA removal. (ii) Second anodization step. (iii) Pore widening. (iv) APTES functionalization. (v) Gold coating. b) Magnified schematic diagram of nanopores in NAA-PFs showing a description of the main geometric features (i.e.,  $d_p$  and  $L_p$ ). c) SEM structural characterization of NAA-PFs. Top-Left: Top SEM view (scale bar = 1  $\mu\text{m}$ ). Top-Right: Magnified view of red square shown in (Top-Left) (scale bar = 1  $\mu\text{m}$ ). Bottom-Left: Cross-section SEM view (scale bar = 5  $\mu\text{m}$ ). Bottom-Right: Magnified view of red square shown in (Bottom-Left) (scale bar = 1  $\mu\text{m}$ ). d) Pore size distribution in NAA-PFs used in this study ( $60 \pm 5$  nm).

were exposed to a trypsin solution of controlled concentration (i.e., 1 mg mL<sup>-1</sup>), and changes in  $OT_{\text{eff}}$  of the film were measured in real-time by RIFS.

**Enzyme Kinetics Analysis.** The initial reaction velocity ( $V_0$ ) of the digestion of gelatin by trypsin was obtained using a linear fit of  $\Delta OT_{\text{eff}}$  versus time plot. Data acquired between the starting point of the reaction and 3 min after trypsin digestion were used in the fit. The  $V_0$  for each concentration of gelatin (1, 3, 5, and 7 mg mL<sup>-1</sup>) were plotted against the concentration of trypsin. A nonlinear least-squares fit was used to determine the Michealis-Menten parameters by the expression given in eq 2

$$V_0 = V_{\text{max}}[\text{Gelatin}]/(K_m + [\text{Gelatin}]) \quad (2)$$

where  $V_{\text{max}}$  is the maximum velocity,  $K_m$  is the Michaelis constant when the reaction rate is half of  $V_{\text{max}}$  and  $[\text{Gelatin}]$  is the concentration of gelatin.

**Structural Characterization of NAA-PFs.** The structural characteristics of NAA-PFs were established by field emission gun scanning electron microscopy (FEG-SEM FEI Quanta 450). SEM image analysis was performed using the standard image processing package ImageJ (public domain program developed at the RSB of the NIH).<sup>42</sup>

**Fourier Transform Infrared Spectroscopy (FT-IR) Analysis.** Chemically modified NAA-PFs were analyzed by Fourier transform IR (FT-IR) spectroscopy (Figure S2 – Supporting Information). FT-IR spectra were collected in a Nicolet 6700 ThermoFisher spectrometer, and the number of scans was set to 32, with a resolution of 4 cm<sup>-1</sup>. All spectra



were collected in the range 4000–1100  $\text{cm}^{-1}$  in transmission mode.

## RESULTS AND DISCUSSION

### Structural and Chemical Characterization of NAA-PFs.

The optical interference properties and sensing performance of NAA-PFs rely strongly on the structural characteristics of the film, including its pore diameter ( $d_p$ ) and its thickness ( $L_p$ ) (Figures 2a and b).<sup>43–45</sup> SEM image analysis was used to establish the geometric features of NAA-PFs produced in our study. This analysis revealed that NAA-PFs presented average  $d_p$  and  $L_p$  of  $60 \pm 5$  nm and  $4.0 \pm 0.5$   $\mu\text{m}$ , respectively (Figures 2c and d). These photonic films showed optimal photonic properties to be used as platforms for detection of trypsin, featuring well-resolved fringes across their RIFS spectrum. Figure 2c depicts top and cross-section view SEM images of a NAA-PF featuring hexagonally arranged nanopores across the surface with straight cylindrical geometry vertically aligned from top to bottom. As mentioned above, NAA-PFs were chemically modified with APTES in order to endow these photonic films with amine functional groups for covalent immobilization of gelatin molecules. FT-IR spectroscopy data shown in Figure S2 prove the successful silanization of NAA-PFs by the protocol used in our study.

**Detection of Trypsin by Combination of Gelatin-Modified NAA-PFs and RIFS.** NAA-PFs modified with gelatin were used as sensing platforms to detect trypsin molecules in a selective manner. In this process, the effective optical thickness change obtained by applying fast Fourier transform to the RIFS spectrum of NAA-PFs was used as the sensing parameter.<sup>46</sup> Figure 3a shows the sensing approach used in our study with an example of real-time monitoring of the different stages of the process used to detect trypsin molecules. This process is clearly defined by three stages: namely; (i) chemical activation of amine groups by GTA, (ii) chemical functionalization of inner surface of NAA-PFs with gelatin, and (iii) trypsin digestion of gelatin. It is worth mentioning that fresh phosphate buffer saline (PBS) solution was flowed after each of these stages in order to remove physisorbed molecules from the surface of NAA-PFs and to establish the actual  $\Delta OT_{\text{eff}}$  associated with each of these chemical processes. Furthermore, whereas the effective optical thickness of NAA-PFs underwent a red shift (i.e., shift toward longer wavelengths) during GTA activation and gelatin functionalization stages, a blue shift (i.e., shift toward shorter wavelengths) took place during the enzymatic digestion of gelatin immobilized onto the inner surface of NAA-PFs. This is in good agreement with previous studies using similar sensing strategies.<sup>27,28</sup> Note that, as mentioned above, a stable baseline was first obtained by flowing fresh PBS solution for 10 min. This was followed by injection of GTA solution for activation of amine groups of APTES molecules immobilized onto the inner surface of NAA-PFs. A rapid and sharp increase of  $OT_{\text{eff}}$  was observed during this stage. Subsequently, PBS solution was flowed again in order to remove physisorbed GTA molecules. Just after, gelatin solution was flowed through the system, and the  $OT_{\text{eff}}$  of NAA-PFs underwent another sharp increase as a result of the immobilization of gelatin molecules onto GTA-activated amine groups. After flowing fresh PBS solution to remove physisorbed gelatin molecules, the corresponding analyte solution with controlled concentration of trypsin was flowed. In the course of this stage, the  $OT_{\text{eff}}$  of NAA-PFs decreased sharply as a result of the digestion of gelatin by trypsin molecules. Finally, fresh PBS solution was

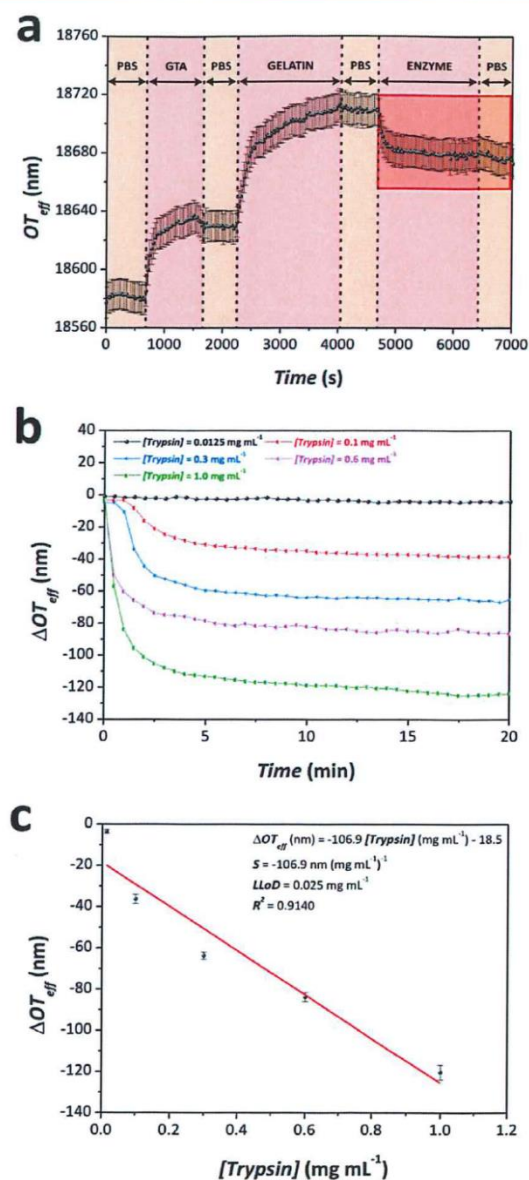


**Figure 3.** Sensing performance of gelatin-modified NAA-PFs for detection of trypsin. a) Real-time changes in the effective optical thickness of NAA-PFs during the different stages, including GTA activation, gelatin immobilization, and gelatin digestion for  $[\text{Trypsin}] = 0.3$   $\text{mg mL}^{-1}$  (NB: Red rectangle indicates the trypsin digestion stage). Real-time monitoring of effective optical thickness change in gelatin-modified NAA-PFs during trypsin digestion for each concentration of trypsin (i.e., 0.0125, 0.1, 0.3, 0.6, and 1.0  $\text{mg mL}^{-1}$ ). b) Calibration curve for trypsin digestion obtained from (b).

flowed again in order to establish the actual  $\Delta OT_{\text{eff}}$  associated with the chemical digestion of gelatin. Five different concentrations of trypsin (i.e., 0.125, 0.3, 0.5, 0.6, and 1  $\text{mg mL}^{-1}$ ) were analyzed to establish the sensing characteristics of this enzymatic sensor in terms of working range, sensitivity, low limit of detection, and linearity (Figure 3b). Figure 3c shows

the calibration curve that correlates the effective optical thickness change with the concentration of trypsin, revealing a linear relationship between  $\Delta OT_{\text{eff}}$  and  $[Trypsin]$  within the concentration range from 0.125 to 1 mg mL<sup>-1</sup>. A linear fitting within the WR established a  $S$  of  $-106.9 \pm 16.2$  nm (mg mL<sup>-1</sup>)<sup>-1</sup>, a  $LLoD$  of  $0.025 \pm 0.005$  mg mL<sup>-1</sup>, and a  $R^2$  of 0.9140. Note that the sensitivity and the low limit of detection of the system were estimated from the slope of the fitting line shown in Figures 3c and 3σ, respectively. As far as the response time is concerned, our results determined that the higher the concentration of trypsin the faster the response of the sensor. This system can provide response times as fast as 4.5 min for a concentration of 1 mg mL<sup>-1</sup> of trypsin (Figure 3b). Therefore, the proposed enzymatic sensor can be used to quantify the concentration of trypsin in analyte samples by changes in the effective optical thickness of gelatin-modified NAA-PFs measured by RIFS.

**Effect of Chemical Sensing Element on Sensing Performance.** As mentioned before, gelatin plays a critical role as the chemical sensing element endowing NAA-PFs with chemical selectivity toward trypsin molecules. In order to explore the effect of gelatin on the sensing performance of this sensor, we functionalized NAA-PFs with different concentrations of gelatin (i.e., 1, 3, 5, and 7 mg mL<sup>-1</sup>). Figures 4a and b show the results, which revealed that the higher the concentration of gelatin the more sensitive the response of the NAA-PFs. Therefore, the sensitivity of the proposed system can be further improved by increasing the concentration of gelatin used to functionalize the inner surface of NAA-PFs. When more concentration of gelatin is used, more sensing molecules are immobilized onto the inner surface of NAA-PFs. These sensing molecules are digested by trypsin when gelatin-modified NAA-PFs are exposed to the analyte solution, producing bigger changes in the effective optical thickness of the film (i.e., sensing parameter). This makes the sensing platform more sensitive toward changes in the effective medium produced by trypsinized gelatin. In addition, this sensing system enables the estimation of the kinetics of gelatin digestion by trypsin (*vide supra*). The initial reaction velocity of gelatin digestion was obtained by a linear fit of the effective optical thickness change and the reaction time (i.e., 3 min) for each concentration of gelatin (1, 3, 5, and 7 mg mL<sup>-1</sup>).  $V_0$  obtained for each concentration of gelatin were plotted against the concentration of trypsin by a nonlinear least-squares fit in order to establish the Michaelis–Menten parameters of this enzymatic reaction, as reported elsewhere (Figure 4c).<sup>47</sup> This analysis revealed that the digestion of gelatin by trypsin under the conditions used in our experiments presented a  $V_{\text{max}}$  of  $10.696 \pm 0.605$  (mg mL<sup>-1</sup>) min<sup>-1</sup> (i.e.,  $1925 \pm 117$  (TAME units mL<sup>-1</sup>) min<sup>-1</sup>) with a Michaelis constant of  $0.460 \pm 0.170$  mg mL<sup>-1</sup> (i.e.,  $42.92$  μM). The Michaelis–Menten parameters for trypsin digestion under the aforementioned conditions were found to be smaller and bigger than those reported for trypsin when the digestion of the substrate is performed in bulk solution (i.e.,  $4450$  (TAME units mL<sup>-1</sup>) min<sup>-1</sup> and  $4.8$  μM), respectively.<sup>48</sup> Nevertheless, it is worth stressing that these differences could be associated with a limitation of the activity of the enzyme molecules when digesting gelatin immobilized inside a nanoporous network.

**Chemical Selectivity of Gelatin-Modified NAA-PFs toward Trypsin.** The chemical selectivity toward analyte molecules is strongly dependent on the chemical affinity between the sensing element (i.e., gelatin) and the analyte

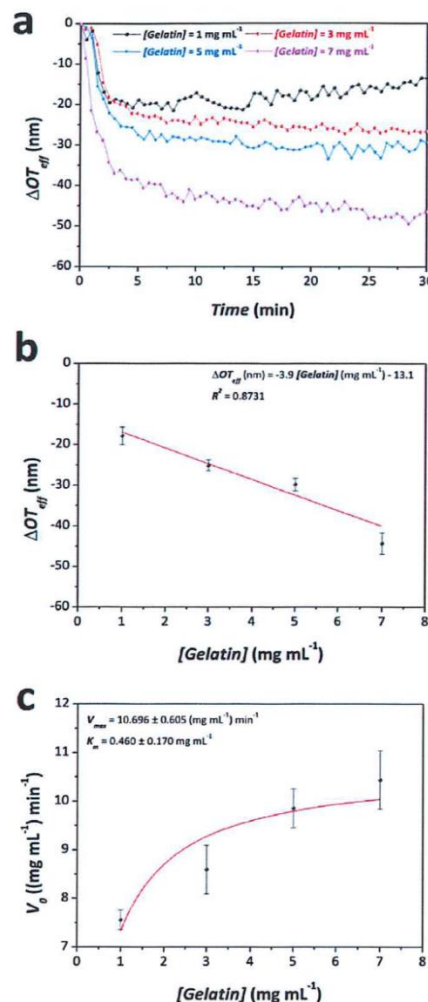
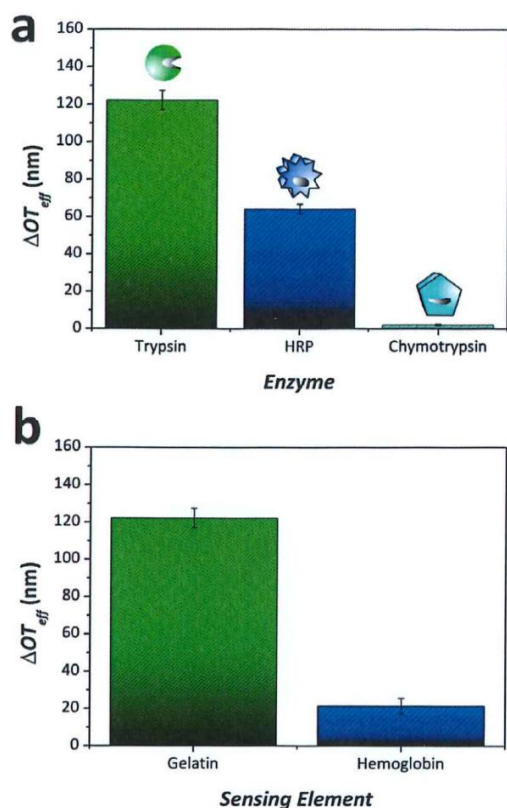


Figure 4. Effect of chemical sensing element (i.e., gelatin) on the performance of gelatin-modified NAA-PFs for detection of trypsin. a) Real-time monitoring of effective optical thickness change in gelatin-modified NAA-PFs during trypsin digestion as a function of the concentration of gelatin. b) Calibration curve for trypsin digestion at different concentrations of gelatin. c) Nonlinear least-squares fit used to establish the Michaelis–Menten parameters.

molecules (i.e., trypsin). In order to demonstrate the chemical selectivity of our sensing platform, we exposed gelatin-modified NAA-PFs to two nonspecific enzyme molecules, chymotrypsin and horseradish peroxidase. Like trypsin, chymotrypsin is a digestive enzyme produced by the pancreas, which plays a critical role in the duodenum where it breaks down proteins and polypeptides. Chymotrypsin is activated by the presence of trypsin, and it cleaves amide bonds in peptides. In contrast, horseradish peroxidase is a heme-containing enzyme, which is typically obtained from the roots of horseradish. Horseradish peroxidase utilizes hydrogen peroxide to oxidize a broad variety of organic and inorganic compounds. The obtained results, which are summarized in Figure 5a, revealed that whereas chymotrypsin molecules produced an almost negligible change



**Figure 5.** Chemical selectivity of gelatin-modified NAA-PFs. a) Effective optical thickness changes associated with trypsin, horseradish peroxidase (HRP), and chymotrypsin for NAA-PFs functionalized with 1 mg mL<sup>-1</sup> gelatin (NB: concentration of enzymes = 1 mg mL<sup>-1</sup>). b) Effective optical thickness changes associated with gelatin and hemoglobin-modified NAA-PFs at a concentration of 1 mg mL<sup>-1</sup> (NB: [*Trypsin*] = 1 mg mL<sup>-1</sup>).

in the effective optical thickness of gelatin-modified NAA-PFs (i.e.,  $2.1 \pm 0.5$  nm), horseradish peroxidase could partially digest gelatin, producing a significant change in the effective optical thickness of the film of  $64.1 \pm 2.5$  nm, which is still 2-fold lower than that produced by trypsin molecules (i.e.,  $122.1 \pm 5.2$  nm). These results can be associated with the affinity of each enzyme molecule toward gelatin, which was found to follow the order trypsin > horseradish peroxidase > chymotrypsin. We further demonstrated the critical role of the chemical sensing element on the performance of the proposed sensor by using hemoglobin instead of gelatin. To this end, a NAA-PF was chemically functionalized with hemoglobin following the above-mentioned protocol. Then, the hemoglobin-modified NAA-PF was exposed to 1 mg mL<sup>-1</sup> of trypsin, and changes in the effective optical thickness of the film were measured in real-time by RIFS. The  $\Delta OT_{eff}$  produced in the hemoglobin-modified film was found to be  $21.5 \pm 4.1$  nm, which is 6-fold lower than that obtained when gelatin was used as the chemical sensing element ( $122.1 \pm 5.2$  nm) (Figure 5b). These results denote that the sensitivity of this system is highly dependent on the affinity between sensing element and analyte molecules.

Finally, Table 1 compiles a comprehensive summary with the most representative state-of-the-art optical-based enzymatic

**Table 1.** Summary of the Most Representative Studies Combining Optical Sensing Techniques and Nanoporous Platforms<sup>a</sup>

technique	target enzyme	platform	LLoD	ref
reflection spectroscopy	metalloprotease	pSi	1–2 pM	27
	glutathione-S-transferase	pSi	50 $\mu\text{g mm}^{-2}$	49
surface plasmon resonance	invertase	NAA	10 nM	50
photoluminescence	morin	NAA	5 $\mu\text{M}$	51
	trypsin	NAA	40 $\mu\text{g mL}^{-1}$	52
reflectometric interference spectroscopy	proteinase K	NAA	0.06 $\text{mg mL}^{-1}$	28
	trypsin	NAA	0.025 $\text{mg mL}^{-1}$	this work

<sup>a</sup>NB: pSi = porous silicon; NAA = nanoporous anodic alumina.

sensors using nanoporous sensing platforms reported in recent years and details of the characteristics and performances of these systems. As these results reveal, our enzymatic sensor features a good sensing performance as compared to similar systems. Nevertheless, it is worth noting that there is still a considerable margin to improve the sensing performance of the proposed sensor by combining this sensing approach with more sensitive photonic structures based on NAA as well as to enhance its chemical selectivity by using different sensing elements.

## CONCLUSIONS

To summarize, this study has reported on the development of an innovative enzymatic sensor based on the combination of gelatin-modified nanoporous anodic alumina photonic films and reflectometric interference spectroscopy. The sensing performance of this sensing system for the detection of trypsin enzyme was systematically assessed through a series of experiments, from which the different sensing characteristics were established. The obtained results revealed that this sensor presents a working range from 0.0125 to 1 mg mL<sup>-1</sup>, a sensitivity of  $-106.9 \pm 16.2$  nm (mg mL<sup>-1</sup>)<sup>-1</sup>, a low limit of detection of  $0.025 \pm 0.005$  mg mL<sup>-1</sup>, and a linearity of 0.9140. Furthermore, we established the role of the chemical sensing element (i.e., gelatin) on the sensing performance of the system. This analysis demonstrated that the higher the concentration of gelatin used to functionalize the surface of NAA-PFs the more sensitive the system. In addition, we estimated the kinetics parameters for the enzymatic reaction between gelatin and trypsin from the above-mentioned results. The chemical selectivity of our enzymatic sensor was evaluated by measuring changes in the effective optical thickness of gelatin-modified NAA-PFs after exposure to two nonselective enzymes such as chymotrypsin and horseradish peroxidase. These results revealed that, whereas the system is highly selective toward the presence of chymotrypsin, horseradish peroxidase can partially degrade gelatin immobilized onto the inner surface of NAA-PFs. We further assessed the chemical selectivity of this system by using hemoglobin as the chemical sensing element instead of gelatin.

The aforementioned set of results verifies that the proposed enzymatic sensing platform has a promising potential to be used as a point-of-care system for quick diagnosis of gastrointestinal diseases such as pancreatitis.

## ■ ASSOCIATED CONTENT

### ■ Supporting Information

The Supporting Information is available free of charge on the ACS Publications website at DOI: [10.1021/acs.analchem.5b02225](https://doi.org/10.1021/acs.analchem.5b02225).

Information about the RfIS system; FT-IR analysis of sensing platforms after each functionalization stage (PDF)

## ■ AUTHOR INFORMATION

### ■ Corresponding Authors

\*Phone: 61 8 8313 1535. Fax: 61 8 8303 4373. E-mail: [abel.santos@adelaide.edu.au](mailto:abel.santos@adelaide.edu.au). Web page: <http://www.adelaide.edu.au/directory/abel.santos> (A.S.).

\*Phone: 61 8 8313 4648. Fax: 61 8 8303 4373. E-mail: [dusan.losic@adelaide.edu.au](mailto:dusan.losic@adelaide.edu.au). Web page: <http://www.adelaide.edu.au/directory/dusan.losic> (D.L.).

### ■ Author Contributions

Dr. Abel Santos designed the experimental part of this work. Ms. Mahdiah Nemati carried out the experiments assisted and supervised by Dr. Abel Santos and Dr. Tushar Kumeria. The obtained results were discussed and analyzed by all the authors. The final version of the manuscript was written through contributions of all the authors. All the authors have given approval to the final version of the manuscript.

### ■ Notes

The authors declare no competing financial interest.

## ■ ACKNOWLEDGMENTS

The authors are thankful for the support provided by the Australian Research Council (ARC) through the grants number DE140100549, DP120101680, and FT110100711 and the School of Chemical Engineering (UoA). The authors thank the Adelaide Microscopy (AM) centre for FEG-SEM characterization.

## ■ ABBREVIATIONS

NAA, nanoporous anodic alumina; NAA-PFs, nanoporous anodic alumina photonic films; RfIS, reflectometric interference spectroscopy

## ■ REFERENCES

- (1) Guisan, J. M. *Immobilization of Enzymes and Cells*; Humana Press: Totowa, NJ, 2006.
- (2) Netzel-arnett, S.; Hooper, J. D.; Szabo, R.; Madison, E. L.; Quigley, J. P.; Bugge, H.; Antalis, T. M. *Cancer Metastasis Rev.* **2003**, *22*, 237–258.
- (3) Soreide, K.; Janssen, E. A.; Körner, H.; Baak, J. P. A. *J. Pathol.* **2006**, *209*, 147–156.
- (4) Shimokawa, K.; Katayama, M.; Matsuda, Y.; Takahashi, H.; Hara, I.; Sato, H.; Kaneko, S. *Mol. Hum. Reprod.* **2002**, *8*, 32–36.
- (5) Everley, P. A.; Gartner, C. A.; Haas, W.; Saghatelian, A.; Elias, J. E.; Cravatt, B. F.; Zetter, B. R.; Gygi, S. P. *Mol. Cell. Proteomics* **2007**, *6*, 1771–1777.
- (6) Huhtala, M. L.; Pesonen, K.; Kalkkinen, N.; Stenman, U. H. *J. Biol. Chem.* **1982**, *257*, 13713–13716.
- (7) Xue, W.; Zhang, G.; Zhang, D. A. *Analyst* **2011**, *136*, 3136–3141.

- (8) Campanella, L.; Bonanni, A.; Favero, G.; Tomassetti, M. *Anal. Bioanal. Chem.* **2003**, *375*, 1011–1016.
- (9) Korpan, Y. I.; Gonchar, M. V.; Sibirny, A. A.; Martelet, C.; El, A. V.; Gibson, T. D.; Soldatkin, A. P. *Biosens. Bioelectron.* **2000**, *15*, 77–83.
- (10) Mross, S.; Pierrat, S.; Zimmerman, T.; Kraft, M. *Biosens. Bioelectron.* **2015**, *70*, 376–391.
- (11) Grieshaber, D.; MacKenzie, R.; Vörös, J.; Reimhult, E. *Sensors* **2008**, *8*, 1400–1458.
- (12) Ronkainen, N. J.; Halsall, H. B.; Heineman, W. R. *Chem. Soc. Rev.* **2010**, *39*, 1747–1763.
- (13) Cass, T.; Ligler, F. S. *Immobilized Biomolecules in Analysis: A Practical Approach*; Oxford University Press: Oxford, 1999.
- (14) Morimoto, K.; Upadhyay, S.; Higashiyama, T.; Ohgami, N.; Kusakabe, H.; Fukuda, J.; Suzuki, H. *Sens. Actuators, B* **2007**, *124*, 477–485.
- (15) Saum, A. G. E.; Cumming, R. H.; Rowell, F. J. *Biosens. Bioelectron.* **2000**, *15*, 305–313.
- (16) Marrakchi, M.; Dzyadevych, S. V.; Biloivan, O. A.; Martelet, C.; Temple, P.; Jaffrezic-Renault, N. *Mater. Sci. Eng., C* **2006**, *26*, 369–373.
- (17) Liu, Y.; Wang, S.; Zhang, C.; Su, X.; Huang, S.; Zhao, M. *Anal. Chem.* **2013**, *85*, 4853–4857.
- (18) Ou, L. J.; Li, X. Y.; Li, L. J.; Liu, H. W.; Sun, A. M.; Liu, K. J. *Analyst* **2015**, *140*, 1871–1875.
- (19) Li, X.; Zhu, S.; Xu, B.; Zhang, J.; Yang, B.; Tian, W. *Nanoscale* **2013**, *5*, 7776–7779.
- (20) Thorek, D. L. J.; Ogirala, A.; Beattie, B. J.; Grimm, J. *Nat. Med.* **2013**, *19*, 1345–1350.
- (21) Santos, A.; Macias, G.; Ferré-Borrull, J.; Pallarès, J.; Marsal, L. F. *ACS Appl. Mater. Interfaces* **2012**, *4*, 3584–3588.
- (22) Dhathathreyan, A. J. *Phys. Chem. B* **2011**, *115*, 6678–6682.
- (23) Jia, R. P.; Shen, Y.; Luo, H. Q.; Chen, X. G.; Hu, Z. D.; Xue, D. S. *Solid State Commun.* **2004**, *130*, 367–372.
- (24) Qiao, H.; Guan, B.; Gooding, J. J.; Reece, P. J. *Opt. Express* **2010**, *18*, 15174–15182.
- (25) Santos, A.; Kumeria, T.; Losic, D. *Materials* **2014**, *7*, 4297–4320.
- (26) Kumeria, T.; Santos, A.; Losic, D. *Sensors* **2014**, *14*, 11878–11918.
- (27) Kilian, K. A.; Lai, L. M. H.; Magenau, A.; Cartland, S.; Böcking, T.; Girolamo, N. D.; Gal, M.; Gaus, K.; Gooding, J. J. *Nano Lett.* **2009**, *9*, 2021–2025.
- (28) Krismastuti, F. S. H.; Bayat, H.; Voelcker, N. H.; Schönherr, H. *Anal. Chem.* **2015**, *87*, 3856–3863.
- (29) Masuda, H.; Fukuda, K. *Science* **1995**, *268*, 1466–1468.
- (30) Masuda, H.; Hasegawa, F. J. *J. Electrochem. Soc.* **1997**, *144*, L127–L130.
- (31) Masuda, H.; Yada, K.; Osaka, A. *Jpn. J. Appl. Phys.* **1998**, *37*, L1340–L1342.
- (32) Nielsch, K.; Choi, J.; Schwirn, K.; Wehspohn, R. B.; Gösele, U. *Nano Lett.* **2002**, *2*, 677–680.
- (33) Md Jani, A. M.; Kempson, I. M.; Losic, D.; Voelcker, N. H. *Angew. Chem., Int. Ed.* **2010**, *49*, 7933–7937.
- (34) Dronov, R.; Jane, A.; Shapter, J. G.; Hodges, A.; Voelcker, N. H. *Nanoscale* **2011**, *3*, 3109–3114.
- (35) Kumeria, T.; Losic, D. *Nanoscale Res. Lett.* **2012**, *7*, 88.
- (36) Santos, A.; Kumeria, T.; Losic, D. *Anal. Chem.* **2013**, *85*, 7904–7911.
- (37) Santos, A.; Balderrama, V. S.; Alba, M.; Formentín, P.; Ferré-Borrull, J.; Pallarès, J.; Marsal, L. F. *Adv. Mater.* **2012**, *24*, 1050–1054.
- (38) Pacholski, C.; Sartor, M.; Sailor, M. J.; Cunin, F.; Miskelly, G. M. *J. Am. Chem. Soc.* **2005**, *127*, 11636–11645.
- (39) Pacholski, C.; Yu, C.; Miskelly, G. M.; Godin, D.; Sailor, M. J. *J. Am. Chem. Soc.* **2006**, *128*, 4250–4252.
- (40) Kumeria, T.; Rahman, M. M.; Santos, A.; Ferré-Borrull, J.; Marsal, L. F.; Losic, D. *Anal. Chem.* **2014**, *86*, 1837–1844.
- (41) Rahman, M. M.; Garcia-Caurel, E.; Santos, A.; Marsal, L. F.; Pallarès, J.; Ferré-Borrull, J. *Nanoscale Res. Lett.* **2012**, *7*, 474.

- (42) Abràmoff, M. D.; Magalhaes, P. J.; Ram, S. J. *Biophotonics Int.* **2004**, *11*, 36–42.
- (43) Kumeria, T.; Santos, A.; Rahman, M. M.; Ferré-Borrull, J.; Marsal, L. F.; Losic, D. *ACS Photonics* **2014**, *1*, 1298–1306.
- (44) Rahman, M. M.; Marsal, L. F.; Pallarès, J.; Ferré-Borrull, J. *ACS Appl. Mater. Interfaces* **2013**, *5*, 13375–13381.
- (45) Santos, A.; Kumeria, T.; Losic, D. *TrAC, Trends Anal. Chem.* **2013**, *44*, 25–38.
- (46) Alvarez, S. D.; Li, C. P.; Chiang, C. E.; Schuller, I. K.; Sailor, M. J. *ACS Nano* **2009**, *3*, 3301–3307.
- (47) Orosco, M. M.; Pacholski, C.; Sailor, M. J. *Nat. Nanotechnol.* **2009**, *4*, 255–258.
- (48) Evin, L. B.; Vásquez, J. R.; Craik, C. S. *Proc. Natl. Acad. Sci. U. S. A.* **1990**, *87*, 6659–6663.
- (49) DeLouise, L. A.; Kou, P. M.; Miller, B. L. *Anal. Chem.* **2005**, *77*, 3222–3230.
- (50) Dhathathreyan, A. *J. Phys. Chem. B* **2011**, *115*, 6678–6682.
- (51) Jia, R. P.; Shen, Y.; Luo, H. Q.; Chen, X. G.; Hu, Z. D.; Xue, D. *S. Solid State Commun.* **2004**, *130*, 367–372.
- (52) Santos, A.; Macias, G.; Ferré-Borrull, J.; Pallarès, J.; Marsal, L. F. *ACS Appl. Mater. Interfaces* **2012**, *4*, 3584–3588.

# Supporting Information

## Label-Free Real-Time Quantification of Enzyme Levels by Interferometric Spectroscopy Combined with Gelatin-Modified Nanoporous Anodic Alumina Photonic Films

Mahdieh Nemati, Abel Santos<sup>\*</sup>, Tushar Kumeria and Dusan Losic<sup>\*</sup>

School of Chemical Engineering, The University of Adelaide, Engineering North Building, 5005 Adelaide, Australia.

\*E-Mail: [abel.santos@adelaide.edu.au](mailto:abel.santos@adelaide.edu.au) ; [dusan.losic@adelaide.edu.au](mailto:dusan.losic@adelaide.edu.au)

## S1. RIFS System and Sensing Principle

In this study, we used the effective optical thickness change as a sensing principle to develop enzymatic sensors based on the selective digestion of gelatin by enzymes. The effective optical thickness changes in NAA-PFs were monitored in real-time using a flow cell combined with a RIFS system. This system is composed of a bifurcated optical probe that focuses white light from a source (LS-1LL, Ocean Optics, USA) on the surface of these photonic coatings with an illumination spot of 2 mm in diameter. Reflected light from this spot is collected by the collection fiber, which is assembled in the same optical probe. Reflected light is then transferred to a miniature spectrometer (USB4000+VIS-NIR-ES, Ocean Optics, USA). UV-visible optical spectra were acquired from 400 to 1000 nm and saved at intervals of 30 s, with an integration time of 10 ms and 10 average measurements. These RIFS spectra were processed in Igor Pro library (Wavemetrics, USA) in order to estimate  $\Delta OT_{eff}$ . The flow rate of the different solutions through the flow cell was maintained constant at  $100 \mu\text{L min}^{-1}$  by a syringe pump (Fusion 200 Touch series, Chemyx Inc., USA). **Figure S1** depicts an example of RIFS spectra of a gelatin-modified NAA-PF as well as the FFT spectra used to estimate  $\Delta OT_{eff}$  in the course of the different stages (i.e. baseline, GTA activation, gelatin functionalization and trypsin digestion).  $\Delta OT_{eff}$  experienced red shifts during GTA activation and gelatin immobilization stages and a blue shift during enzymatic digestion.

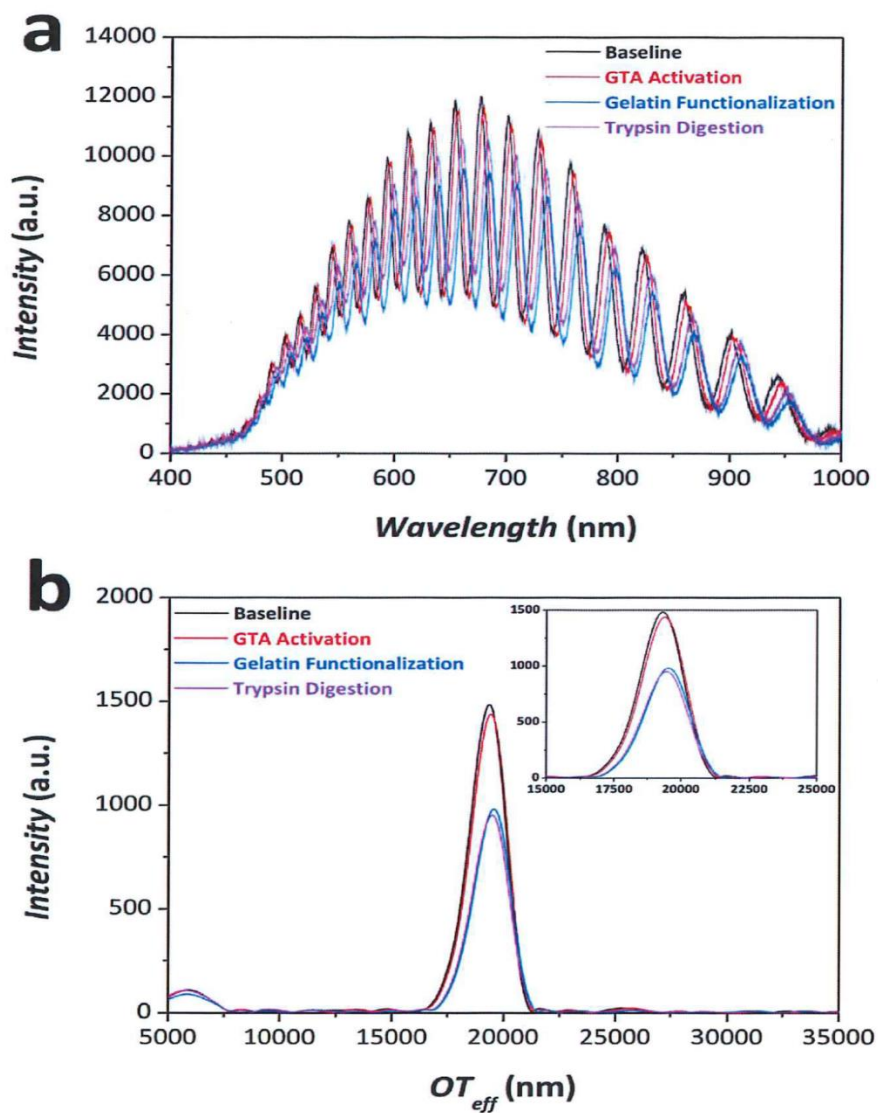


Figure S1. Real-time monitoring of enzymatic reaction by RfS. a) RfS spectra. b) FFT spectra with inset showing details of the FFT peaks after each step of the sensing process.



## S2. FT-IR Characterization of Gelatin-Modified NAA-PFs

FT-IR analysis of NAA-PFs during the different functionalization stages made it possible to verify the successful functionalization process used in our study. **Figure S2** shows a representative FT-IR spectrum of a NAA-PF after each fabrication/functionalization stage. As this graph shows, alumina peaks in as-produced NAA-PF are clearly denoted by two peaks located at  $1472\text{ cm}^{-1}$  and  $1565\text{ cm}^{-1}$ . APTES functionalization is validated by the existence of two vibrational modes located at  $2863\text{ cm}^{-1}$  and  $2930\text{ cm}^{-1}$ , which correspond to propyl groups of APTES molecules immobilized onto the surface of the NAA-PF. Gelatin modification is successfully verified by the appearance of two vibrational modes at  $1260\text{ cm}^{-1}$  and  $1633\text{ cm}^{-1}$  associated with amide III and amide I stretching vibrational modes of gelatin molecules. These peaks vanish from the FT-IR spectrum of the NAA-PF after trypsin digestion of gelatin, denoting the successful digestion reaction.

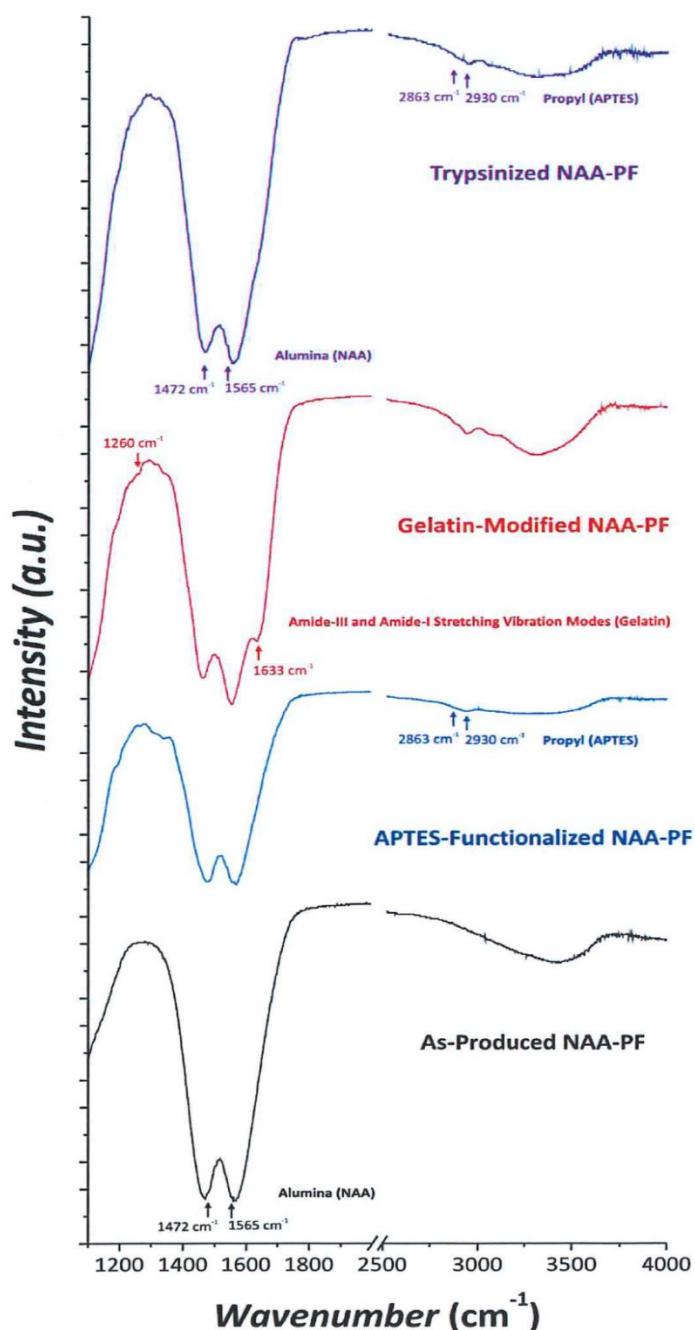


Figure S2. FT-IR spectra of NAA-PFs during the different stages of fabrication and sensing.

**BLANK PAGE**

## CHAPTER 4.

---

### NAA Rugate Filters Combined with RfS for Pharmaceutical Detection

This chapter is based on the following the peer-reviewed article:

**Mahdih Nemati**, Abel Santos, Cheryl Suwen Law, Dusan Losic. Assessment of binding affinity between drugs and human serum albumin photonic crystals. *Analytical Chemistry* 88 (11) (2016) 5971-5980.

**BLANK PAGE**

## Statement of Authorship

Title of Paper	Assessment of Binding Affinity between Drugs and Human Serum Albumin Using Nanoporous Anodic Alumina Photonic Crystals
Publication Status	<input checked="" type="checkbox"/> Published <input type="checkbox"/> Accepted for Publication <input type="checkbox"/> Submitted for Publication <input type="checkbox"/> Unpublished and Unsubmitted work written in manuscript style
Publication Details	

### Principal Author

Name of Principal Author (Candidate)	Mahdieh Nemati
Contribution to the Paper	Prepared the first draft of manuscript, edited, and revised the manuscript.
Overall percentage (%)	85%
Certification:	This paper reports on original research I conducted during the period of my Higher Degree by Research candidature and is not subject to any obligations or contractual agreements with a third party that would constrain its inclusion in this thesis. I am the primary author of this paper.
Signature	Date 12.12.2017

### Co-Author Contributions

By signing the Statement of Authorship, each author certifies that:

- i. the candidate's stated contribution to the publication is accurate (as detailed above);
- ii. permission is granted for the candidate to include the publication in the thesis; and
- iii. the sum of all co-author contributions is equal to 100% less the candidate's stated contribution.

Name of Co-Author	Abel Santos
Contribution to the Paper	Co-supervise, edited, revised the manuscript, and corresponding author.
Signature	Date 14/12/17

Name of Co-Author	Cheryl Suwen Law
Contribution to the Paper	Edited and revised the manuscript.
Signature	Date 14/12/2017

Please cut and paste additional co-author panels here as required.

**CHAPTER 4: M. Nemati, A. Santos, C. S. Law, D. Losic** "Assessment of Binding Affinity between Drugs and Human Serum Albumin Using Nanoporous Anodic Alumina Photonic Crystals " *Analytical Chemistry*, 2016, **88**, 5971-5980.

---

Name of Co-Author	Dusan Losic		
Contribution to the Paper	Supervised the development of the work, edited the manuscript and corresponding author.		
Signature		Date	20/12/2012

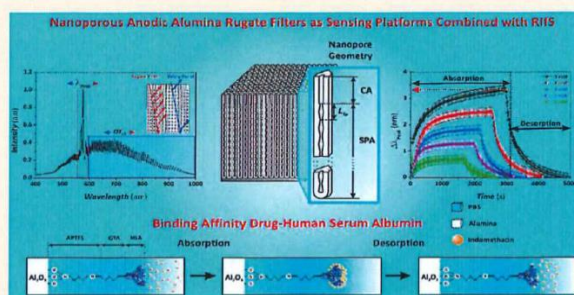
## Assessment of Binding Affinity between Drugs and Human Serum Albumin Using Nanoporous Anodic Alumina Photonic Crystals

Mahdiah Nemati, Abel Santos,\* Cheryl Suwen Law, and Dusan Losic\*

School of Chemical Engineering, The University of Adelaide, Engineering North Building, 5005 Adelaide, Australia

**S** Supporting Information

**ABSTRACT:** In this study, we report an innovative approach aiming to assess the binding affinity between drug molecules and human serum albumin by combining nanoporous anodic alumina rugate filters (NAA-RFs) modified with human serum albumin (HSA) and reflectometric interference spectroscopy (RiFS). NAA-RFs are photonic crystal structures produced by sinusoidal pulse anodization of aluminum that present two characteristic optical parameters, the characteristic reflection peak ( $\lambda_{\text{Peak}}$ ), and the effective optical thickness of the film ( $\text{OT}_{\text{eff}}$ ), which can be readily used as sensing parameters. A design of experiments strategy and an ANOVA analysis are used to establish the effect of the anodization parameters (i.e., anodization period and anodization offset) on the sensitivity of HSA-modified NAA-RFs toward indomethacin, a model drug. To this end, two sensing parameters are used, that is, shifts in the characteristic reflection peak ( $\Delta\lambda_{\text{Peak}}$ ) and changes in the effective optical thickness of the film ( $\Delta\text{OT}_{\text{eff}}$ ). Subsequently, optimized NAA-RFs are used as sensing platforms to determine the binding affinity between a set of drugs (i.e., indomethacin, coumarin, sulfadymethoxine, warfarin, and salicylic acid) and HSA molecules. Our results verify that the combination of HSA-modified NAA-RFs with RiFS can be used as a portable, low-cost, and simple system for establishing the binding affinity between drugs and plasma proteins, which is a critical factor to develop efficient medicines for treating a broad range of diseases and medical conditions.



In the past decade, the discovery of new drugs and therapeutic agents has yielded outstanding improvements in quality of life, health, and life expectancy.<sup>1,2</sup> These significant advancements made by pharmaceutical research and innovation have resulted in drug discoveries that can address or minimize the effects associated with a broad range of diseases and medical conditions, including chronic pain, arthritis, cancer, metabolic and gastrointestinal disorders, infectious and cardiovascular diseases, and mental disorders.<sup>3,4</sup> One key factor playing a critical role in this innovation-driven progress is to understand the underlying mechanisms in drug efficacy and failure. For instance, pharmacokinetics (i.e., the fate of substances administered externally to a living organism) of drugs and medicaments is a critical aspect to take into account in the design of effective therapeutics.<sup>5,6</sup> Most of the drugs bind reversibly to plasma proteins present in the serum and blood such as glycoprotein and human serum albumin (HSA). Therefore, the affinity of medicaments toward these proteins is of critical importance to determine the overall pharmacokinetic profile of any therapeutic substance. Clinical patients present different levels of these proteins, which in turn makes the free concentration of drug patient-dependent. As a result, the therapeutic effect of medicaments with high affinity toward these circulating proteins could have a significant variance as a function of the levels of these biomolecules. This phenomenon can also extend the activity of a given drug for a longer time

period given that the complexes formed between medicaments and proteins can replenish the concentration of free drug as this is removed from the body. Hence, establishment of the affinity between drugs and circulating proteins is a critical factor to consider in the design and assessment of medicines.

Although the drug–protein affinity should be established on a patient-by-patient basis using serum or blood samples, some analytical techniques can provide an accurate estimation of this binding affinity by using simple molecules such as HSA. These simplified analyses can be readily used to design more effective therapeutics in a time-effective and cost-competitive manner, when many compounds must be screened. Some of these analytical methods have been extensively used by pharmaceutical industry, including ultrafiltration, centrifugation, size exclusion and affinity chromatography, dialysis, spectroscopy, electrophoresis, and surface plasmon resonance (SPR).<sup>7–9</sup> Most of these analytical techniques are based on changes in intrinsic parameters of molecules and complexes (e.g., spectroscopic signature, mobility, charge, etc.) or on separation processes. Among the different alternative techniques, reflectometric interference spectroscopy (RiFS) has demonstrated

Received: March 12, 2016

Accepted: April 29, 2016

Published: April 29, 2016



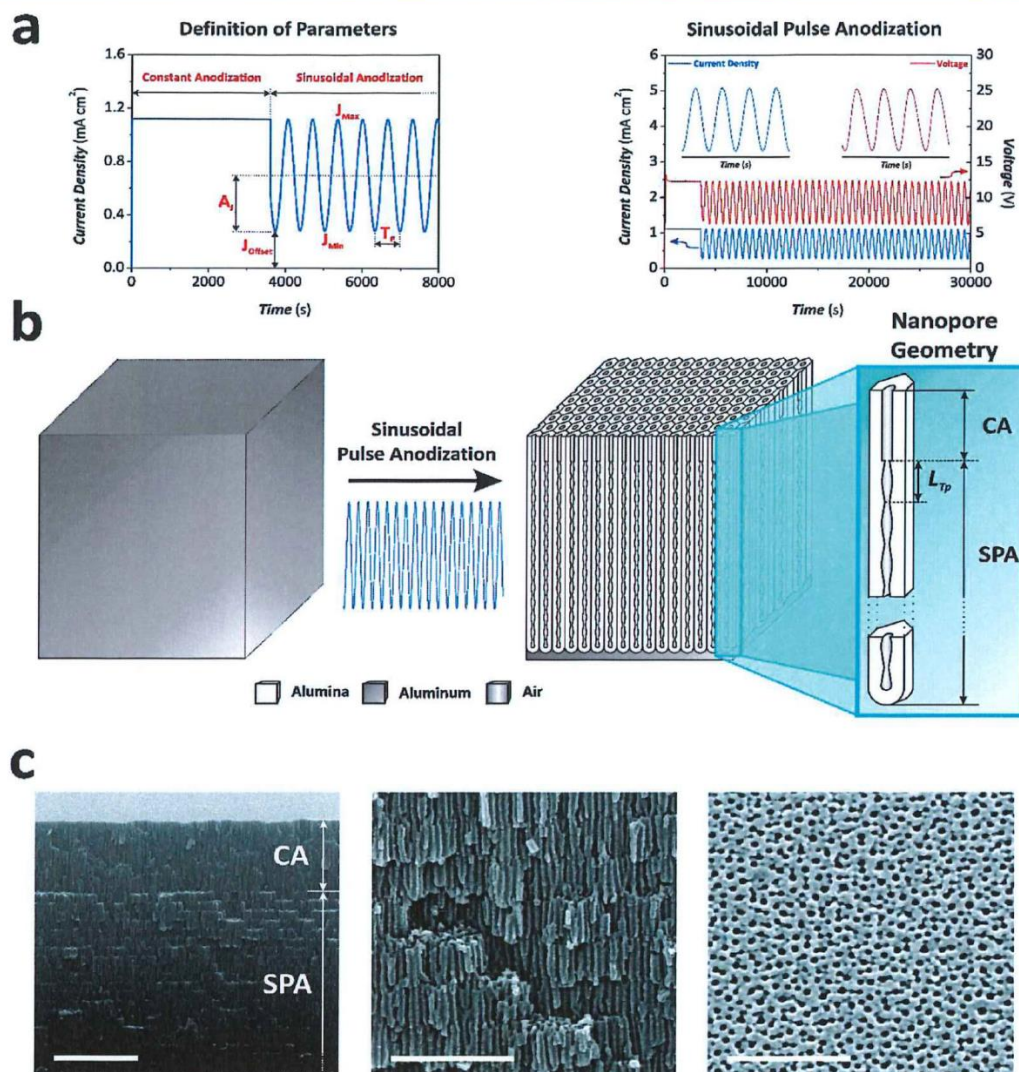


**Figure 1.** Concept of sinusoidal pulse anodization approach used to produce nanoporous anodic alumina rugate filters. (a) Example of sinusoidal anodization wave with  $T_p = 750$  s used to fabricate NAA-RFs (left, definition of anodization parameters:  $T_p$  = anodization period,  $A_J$  = anodization amplitude,  $J_{Offset}$  = anodization offset,  $J_{Max}$  = current density maximum, and  $J_{Min}$  = current density minimum; left, example of anodization profile with insets showing details of the current density and voltage profiles). (b) Schematic illustration of the conversion of aluminum substrates into NAA-RFs by sinusoidal pulse anodization and graphical definition of period length ( $L_{TP}$ ). (c) Representative cross-section and top view SEM images of NAA-RFs produced by sinusoidal pulse anodization approach [left, general cross-section view SEM image of a NAA-RF produced with  $T_p = 750$  s,  $A_J = 0.42$  mA cm<sup>-2</sup>,  $J_{Offset} = 0.28$  mA cm<sup>-2</sup>,  $N_p = 150$  pulses,  $T_{An} = -1$  °C, and  $t_{pw} = 6$  min (scale bar = 2 μm), where CA and SPA denote the layers produced at constant and sinusoidal pulse anodization modes, respectively; center, magnified view of part a (scale bar = 500 nm); right, top view SEM image of a NAA-RF (scale bar = 250 nm)].

outstanding capabilities and versatility for different sensing applications.<sup>10,11</sup> RfS is a label-free optical sensing technique that relies upon the multiple reflection of white light at the interfaces of solid thin films.<sup>12,13</sup> As a result of this light-matter interaction, constructive and destructive interferences of the reflected light form a characteristic interference pattern by the Fabry-Pérot effect.<sup>14,15</sup> These interferences can be used as sensing principle to detect analytes of interest in real-time, with precision. The analytical use of RfS was pioneered by Gauglitz and co-workers, who used solid films based on glass and

biopolymers with a sensitive layer (i.e., layer where the binding events between analyte and capturing molecules occur).<sup>16</sup> Sailor and co-workers exploited the combination of RfS with porous silicon photonic crystals, which are photonic structures that can guide, reflect, confine, and transmit light in a selective manner by engineering their nanoporous structure.<sup>17,18</sup> Recently, we have also demonstrated and exploited the combination of RfS with nanoporous anodic alumina (NAA) photonic crystals, which are produced by electrochemical oxidation (i.e., anodization) of aluminum substrates.<sup>19-24</sup>

Nanoporous photonic crystals present a set of advantages over their solid counterparts: namely, (i) nanopores that can accommodate capturing molecules, increasing the specific surface area for sensing, (ii) nanopores that can act as physical filters to separate analytes, and (iii) ability to engineer the interaction light matter to enhance the sensing performance.<sup>25,26</sup> The pore geometry of NAA can be precisely engineered by different electrochemical approaches. Therefore, the effective medium of this nanoporous material can be rationally engineered in order to create a set of photonic crystal structures such as distributed Bragg reflectors, optical microcavities, waveguides, Fabry–Pérot interferometers, and rugate filters, which are the base of a broad range of optical sensing systems.<sup>27–39</sup> Among these photonic crystal structures, rugate filters (RFs) are of special interest given that their optical spectrum features a well-resolved intense characteristic reflection peak. When the effective medium of a NAA-RF is modified, its characteristic reflection peak undergoes shifts that can be used as sensing principle to detect analytes of interest or establish kinetic parameters associated with biological binding events. Recently, we reported on an innovative anodization approach, so-called sinusoidal pulse anodization, aimed at producing NAA-RFs with finely tuned photonic properties.<sup>40</sup>

Herein, we assess and establish the binding affinity between a set of drugs and HSA by combining HSA-modified NAA-RFs with RIFs. First, the nanoporous structure of NAA-RFs is systematically optimized by evaluating the binding affinity between HSA-modified NAA-RFs and indomethacin, a model drug. NAA-RFs are optimized following a design of experiments (DoE) approach as a function of two fabrication parameters (i.e., anodization period and anodization offset) focusing on maximizing the sensitivity on the sensor performance. Finally, the most sensitive HSA-modified NAA-RF structures are used as optical platforms combined with RIFs to establish the binding affinity between HSA as proof of the versatility of this system to be used as a generic device for establishing protein binding affinity.

## ■ EXPERIMENTAL SECTION

**Materials.** High-purity (99.9997%)  $1.5 \times 1.5 \text{ cm}^2$  square aluminum (Al) substrates 0.32 mm thick were supplied by Goodfellow Cambridge Ltd. (UK). Sulfuric acid ( $\text{H}_2\text{SO}_4$ ), phosphoric acid ( $\text{H}_3\text{PO}_4$ ), perchloric acid ( $\text{HClO}_4$ ), hydrochloric acid (HCl), copper(II) chloride ( $\text{CuCl}_2$ ), (3-aminopropyl)triethoxysilane (APTES), hydrogen peroxide ( $\text{H}_2\text{O}_2$ ), glutaraldehyde (GTA,  $\text{C}_5\text{H}_8\text{O}_2$ ), human serum albumin (HSA), phosphate buffered saline (PBS), indomethacin ( $\text{C}_{19}\text{H}_{16}\text{ClNO}_4$ ), coumarin ( $\text{C}_9\text{H}_6\text{O}_2$ ), sulfadymethoxine ( $\text{C}_{12}\text{H}_{14}\text{N}_4\text{O}_4\text{S}$ ), warfarin ( $\text{C}_{15}\text{H}_{16}\text{O}_4$ ), salicylic acid ( $\text{C}_7\text{H}_6\text{O}_3$ ), and ethanol (EtOH,  $\text{C}_2\text{H}_5\text{OH}$ ) were purchased from Sigma-Aldrich (Australia) and used as received, without further purification. All the aqueous solutions used in this study were prepared using ultrapure water Option Q-Purelabs (Australia).

**Fabrication of Nanoporous Anodic Alumina Rugate Filters.** NAA-RFs were fabricated following a sinusoidal pulse anodization approach under mild conditions and galvanostatic mode (i.e., current density control) in sulfuric acid electrolyte.<sup>40</sup> A definition of the different parameters of the sinusoidal anodization waves used in our study and a representative anodization profile used to produce NAA-RFs photonic crystal structure are shown in Figure 1a. Prior to anodization, Al substrates were cleaned under sonication in ethanol (EtOH) and distilled water for 15 min each and finally dried under air

stream. Subsequently, Al substrates were electropolished using a mixture of  $\text{HClO}_4$  and EtOH 1:4 (v:v) at 20 V and  $5 \text{ }^\circ\text{C}$  for 3 min. After electropolishing, Al substrates were anodized in a thermally isolated custom-built anodization reactor using an aqueous solution 1.1 M sulfuric acid, the temperature of which was kept at  $-1 \text{ }^\circ\text{C}$  throughout the whole process. The anodization process started with a first stage at constant current density of  $1.12 \text{ mA cm}^{-2}$  for 1 h. Then, the sinusoidal pulse mode was set in order to engineer the effective medium of NAA in depth (Figure 1b). During this process, the anodization current density was modified in a sinusoidal fashion between high ( $J_{\text{Max}} = 1.12 \text{ mA cm}^{-2}$ ) and low ( $J_{\text{Min}} = J_{\text{Offset}} = 0.28 \text{ mA cm}^{-2}$ ) values according to eq 1:

$$J(t) = A_j \cdot \left[ \sin\left(\frac{2\pi}{T_p} \cdot t\right) + 1 \right] + J_{\text{Offset}} \quad (1)$$

Here  $J(t)$  is the current density at a given time  $t$ ,  $A_j$  is the current density amplitude,  $T_p$  is the anodization period, and  $J_{\text{Offset}}$  is the current density offset (see Figure 1a).

It is worth noting that the nanoporous layer created during the first stage of this process was used as a shuttle to achieve a homogeneous pore growth before setting anodization to sinusoidal mode. Furthermore, the electrolyte solution was modified with 25 v% of EtOH in order to prevent it from freezing at temperatures below  $0 \text{ }^\circ\text{C}$ .<sup>41,42</sup> Finally, the pore size of NAA-RFs was widened by wet chemical etching in an aqueous solution 5 wt %  $\text{H}_3\text{PO}_4$  at  $35 \text{ }^\circ\text{C}$  for 6 min. This enlargement of the pore size made possible the flow of HSA molecules inside the nanopores of NAA-RFs in order to create the desired surface chemistry for drug binding affinity assessment. Note that these photonic crystals were coated with a thin film of gold of 5 nm using a sputter coater equipped with film thickness monitor (sputter coater 108auto, Cressington) in order to enhance the interference effect and enhance the RIFs signal for sensing experiments.<sup>43,44</sup> Furthermore, the underlying aluminum substrate was chemically removed in a saturated solution of HCl/ $\text{CuCl}_2$  using an etching cell with a window of 8 mm in diameter.

**Optical Characterization.** Shifts in the characteristic reflection peak position ( $\Delta\lambda_{\text{peak}}$ ) and changes in the effective optical thickness ( $\Delta\text{OT}_{\text{eff}}$ ) of HSA-modified NAA-RFs produced as a result of the binding with drug molecules were monitored by a RIFs system composed of a bifurcated optical probe that focuses white light from a light source (LS-1LL, Ocean Optics) on the surface of NAA-RFs. The illumination spot was adjusted to 2 mm in diameter by a lens system (VIS Collimating Lens, 350–2000 nm, Ocean Optics). The reflected light was collected by the collection fiber, which is assembled around the same optical probe, and directly transferred to a miniature spectrometer (USB4000+VIS-NIR-ES, Ocean Optics). The reflection spectra of NAA-RFs were acquired from 400 to 1000 nm and saved at intervals of 30 s, with an integration time of 10 ms and 10 average measurements. RIFs spectra were processed in Igor Pro library (Wavemetrics) in order to estimate  $\Delta\lambda_{\text{peak}}$  and  $\Delta\text{OT}_{\text{eff}}$ .

**Optimization of HSA-Modified NAA-RFs.** Two anodization parameters (i.e., anodization period  $T_p$  and anodization offset  $J_{\text{Offset}} - k = 2$ ) were systematically modified in order to establish the optimization path between the fabrication parameters and the sensitivity of the NAA-RFs-RIFs system.  $T_p$  and  $J_{\text{Offset}}$  were modified from 650 to 750 s ( $\Delta T_p = 50 \text{ s}$ ) and from 0.140 to  $0.420 \text{ mA cm}^{-2}$  with  $\Delta J_{\text{Offset}} = 0.105 \text{ mA}$

$\text{cm}^{-2}$ , respectively. The rest of the anodization parameters were kept constant in all these samples [i.e.,  $A_j = 0.42 \text{ mA cm}^{-2}$  and number of sinusoidal pulses ( $N_p$ ) = 150 pulses]. Therefore, a set of nine NAA-RFs ( $3^2 = 9$ ) were fabricated following the aforementioned approach (Table 1). These NAA-RFs were

**Table 1. Summary of the Fabrication Conditions Used To Produce the Nanoporous Anodic Alumina Rugate Filters Utilized in This Study To Establish the Binding Affinity between Drugs and Human Serum Albumin Molecules**

$T_p$ (s)	$J_{\text{Offset}}$ ( $\text{mA cm}^{-2}$ )		
	0.14	0.28	0.42
650	NAA-RF <sub>650-0.14</sub>	NAA-RF <sub>650-0.28</sub>	NAA-RF <sub>650-0.42</sub>
700	NAA-RF <sub>700-0.14</sub>	NAA-RF <sub>700-0.28</sub>	NAA-RF <sub>700-0.42</sub>
750	NAA-RF <sub>750-0.14</sub>	NAA-RF <sub>750-0.28</sub>	NAA-RF <sub>750-0.42</sub>

chemically functionalized in order to determine the most sensitive HSA-modified NAA-RF structure toward indomethacin molecules as a function of  $T_p$  and  $J_{\text{Offset}}$ . In this process, NAA-RFs were first silanized with APTES following a well-

established functionalization process.<sup>45,46</sup> Briefly, NAA-RFs were hydroxylated in  $\text{H}_2\text{O}_2$  30 wt % for 10 min at  $90^\circ\text{C}$  in order to increase the number of hydroxyl groups on the surface of alumina. Subsequently, hydroxylated NAA-RFs were modified with APTES by chemical vapor deposition process under vacuum at  $110^\circ\text{C}$  for 3 h. After APTES modification, NAA-RFs were washed with ethanol and water, dried under an air stream, and stored under dry conditions until further use. Both the immobilization of HSA and the detection of indomethacin molecules were performed in real-time by RfS using an acrylic-based flow cell. Shifts in the characteristic reflection peak position of each NAA-RF ( $\lambda_{\text{Peak}}$ ) and changes in the effective optical thickness of the whole film ( $\text{OT}_{\text{eff}}$ ) were monitored in real-time by RfS. Five analytical solutions of indomethacin (1, 2, 3, 4, and 5 mM) were prepared in PBS modified with 5 v% EtOH in order to increase the solubility of this hydrophobic drug. Note that the different solutions were flowed through the flow cell at a constant rate of  $100 \mu\text{L min}^{-1}$  by a syringe pump (Fusion 200 Touch series, Chemyx Inc.). Table 1 provides a comprehensive summary of these NAA-RFs (experimental matrix), the objective of which was to evaluate

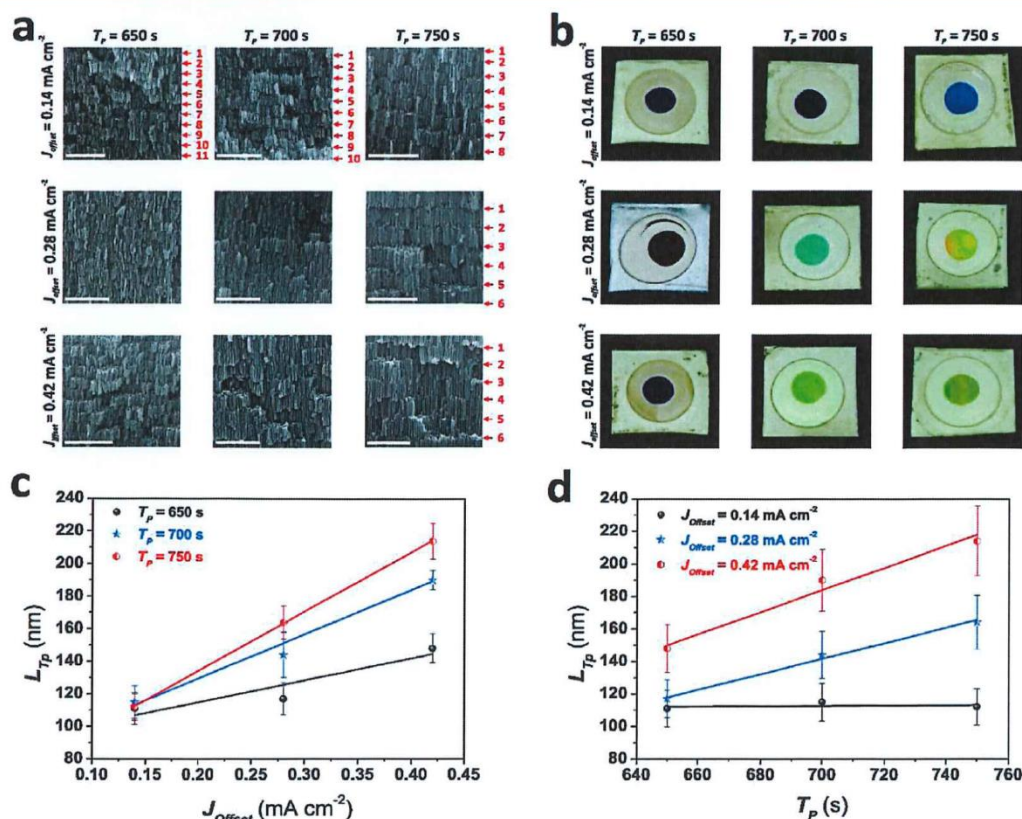


**Figure 2.** Tunability of the characteristic period length ( $L_{T_p}$ ) in NAA-RFs by the anodization period ( $T_p$ ) and the anodization offset ( $J_{\text{Offset}}$ ). (a) Magnified cross-section view SEM images of NAA-RFs produced with  $T_p = 650, 700,$  and  $750 \text{ s}$  and  $J_{\text{Offset}} = 0.14, 0.28,$  and  $0.42 \text{ mA cm}^{-2}$  (fixed parameters:  $A_j = 0.42 \text{ mA cm}^{-2}$ ,  $N_p = 150$  pulses,  $T_{\text{An}} = -1^\circ\text{C}$ , and  $t_{\text{pw}} = 6 \text{ min}$ ) (scale bars = 500 nm) (note that red arrows in these images denote the interfaces between consecutive anodization periods,  $L_{T_p}$ ). (b) Digital pictures of these NAA-RFs displaying different interferometric colors as a function of  $T_p$  and  $J_{\text{Offset}}$  (note that the underlying aluminum substrate was chemically etched away in a saturated solution of  $\text{HCl}/\text{CuCl}_2$  using an etching cell with a window of 8 mm in diameter). (c) Linear dependence of  $L_{T_p}$  on  $J_{\text{Offset}}$  for  $T_p = 650, 700,$  and  $750 \text{ s}$ . (d) Linear dependence of  $L_{T_p}$  on  $T_p$  for  $J_{\text{Offset}} = 0.14, 0.28,$  and  $0.42 \text{ mA cm}^{-2}$ .

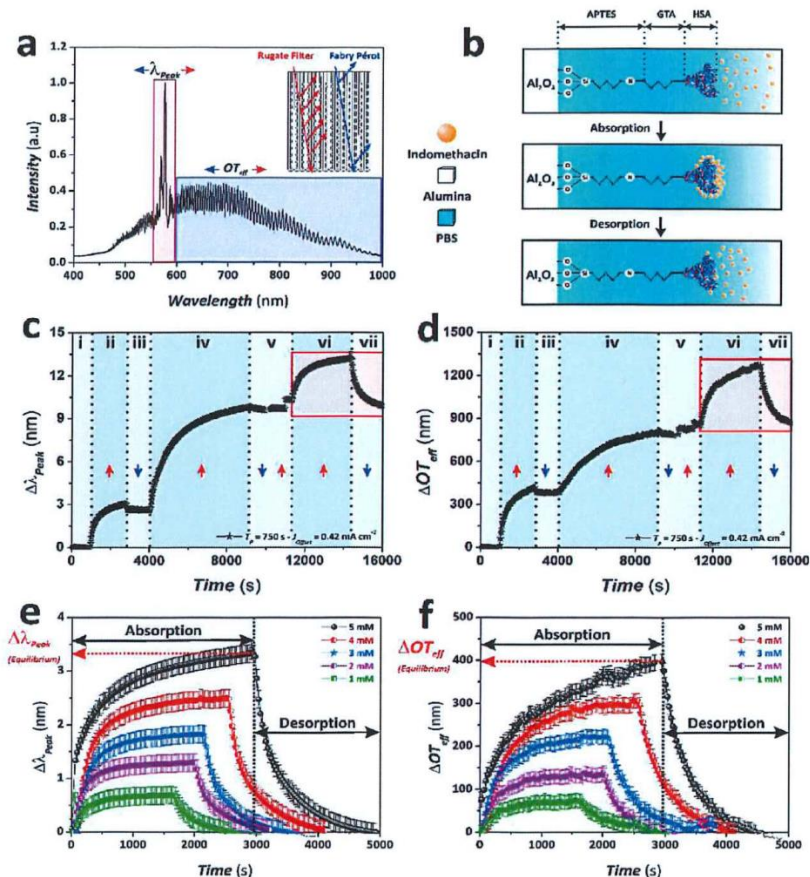


**Figure 3.** Sensing concept used to establish the binding affinity between HSA and indomethacin molecules by combining HSA-functionalized NAA-RFs and RIFS. (a) Representative RIFS spectrum of a NAA-RF ( $T_p = 650$  s,  $J_{\text{offset}} = 0.42$  mA cm $^{-2}$ , and  $t_{\text{pw}} = 0$  min) showing the areas in the spectrum used to establish changes in  $\lambda_{\text{peak}}$  and  $OT_{\text{eff}}$  associated with binding between HSA and indomethacin molecules. (b) Schematic illustration describing the reversible binding event between HSA and indomethacin molecules with adsorption and desorption stages after injection of indomethacin analytical solutions and fresh PBS, respectively. (c, d) Representative real-time measurements for  $\Delta\lambda_{\text{peak}}$  and  $\Delta OT_{\text{eff}}$  showing the shifts in the position of the characteristic peak position and changes in the effective optical thickness of NAA-RFs during the different stages (blue and red arrows indicate areas where  $\Delta\lambda_{\text{peak}}$  and  $\Delta OT_{\text{eff}}$  undergo blue and red shifts, respectively): (i) PBS baseline, (ii) GTA activation, (iii) PBS washing, (iv) HSA immobilization, (v) PBS washing and PBS–EtOH baseline, (vi) indomethacin detection in PBS–EtOH, and (vii) PBS–EtOH washing (note the example corresponding to a NAA-RF produced with  $T_p = 750$  s and  $J_{\text{offset}} = 0.42$  mA cm $^{-2}$ ). (d) Detail of the absorption and desorption stages (red square in parts c and d) for  $\Delta\lambda_{\text{peak}}$  and  $\Delta OT_{\text{eff}}$  vs time as a function of the concentration of indomethacin (1, 2, 3, 4, and 5 mM).

the effect of each of these parameters on the photonic properties and sensitivity ( $S$ ) of NAA-RFs measured by two parameters: namely, (i) changes in the position of the characteristic reflection peak ( $\Delta\lambda_{\text{peak}}$ ) and (ii) changes in the effective optical thickness of the whole NAA-RF ( $\Delta OT_{\text{eff}}$ ). We applied an analysis of variance (ANOVA) for a  $3^k$ -factorial design of experiments (DoE) in order to discern objectively the effect of  $T_p$  and  $J_{\text{offset}}$  on the studied variable (i.e.,  $S$ , sensitivity of HSA-modified NAA-RFs toward indomethacin molecules).<sup>47,48</sup> A DoE strategy makes it possible to optimize the number of experiments while establishing possible quadratic effects in the relationship between the anodization parameters and the sensitivity of the NAA-RFs-RIFS system.

In this study, three null hypotheses were tested by means of the aforementioned ANOVA test, namely, the following, if  $\alpha_i$  and  $\beta_j$  quantify the effects of  $T_p$  and  $J_{\text{offset}}$ , respectively:

(i)  $H_0$ ,  $\alpha_i = 0$  (there is no significant effect of  $T_p$  on  $S$ );

(ii)  $H_1$ ,  $\beta_j = 0$  (there is no significant effect of  $J_{\text{offset}}$  on  $S$ );  
 (iii)  $H_2$ ,  $(\alpha\beta)_{ij} = 0$  (there is no significant effect of the anodization parameters interaction (i.e.,  $T_p \cdot J_{\text{offset}}$ ) on  $S$ ).

If these hypotheses were rejected, the alternative hypotheses would be accepted. These alternative hypotheses are the following:

(i\*)  $H_0^*$ ,  $\alpha_i \neq 0$  (there is a significant effect of  $T_p$  on  $S$ );  
 (ii\*)  $H_1^*$ ,  $\beta_j \neq 0$  (there is a significant effect of  $J_{\text{offset}}$  on  $S$ );  
 (iii\*)  $H_2^*$ ,  $(\alpha\beta)_{ij} \neq 0$  (there is a significant effect of the anodization parameters interaction (i.e.,  $T_p \cdot J_{\text{offset}}$ ) on  $S$ ).

**Establishment of Binding Affinity between Drugs and HSA-Modified NAA-RFs by RIFS.** A set of the most sensitive NAA-RF structures for each of the aforementioned sensing parameters (i.e.,  $\Delta\lambda_{\text{peak}}$  and  $\Delta OT_{\text{eff}}$ ) toward indomethacin molecules were fabricated and functionalized following the above-mentioned anodization and silanization protocols. These

samples were used to assess the binding affinity between HSA molecules immobilized onto NAA-RFs and a set of drug model molecules, including indomethacin, coumarin, sulfadymethoxine, warfarin, and salicylic acid. These sensing experiments were performed according to the process shown in the **Optical Characterization** section using  $\Delta\lambda_{\text{peak}}$  and  $\Delta\text{OT}_{\text{eff}}$  as sensing parameters (*vide supra*).

**Structural Characterization.** The structural characteristics of NAA-RFs were established by a field emission gun scanning electron microscope (FEG-SEM FEI Quanta 450). These images were subsequently analyzed by ImageJ (public domain program developed at the RSB of the NIH) in order to measure the period length in the different NAA-RF structures.<sup>49</sup>

All the aforementioned experiments were repeated three times with freshly modified NAA-RFs and analytical solutions, and the characteristic parameters were calculated as averages and standard deviations.

## RESULTS AND DISCUSSION

### Structural Characterization and Optical Optimization of NAA-RFs.

The optical properties and sensing performance of NAA-RFs are strongly dependent on the period thickness ( $L_{\text{Tp}}$ ) (Figure 1b). Figure 1c shows representative cross-section and top view images of NAA-RFs. These photonic structures are composed of stacked layers of nanopores with sinusoidally modified porosity in depth, which are generated by the sinusoidal fabrication process described above. Figure 2a shows cross-section SEM images with magnified views of the NAA-RFs used in this study, which were produced using nine different combinations of  $T_{\text{p}}$  and  $J_{\text{Offset}}$  (see Table 1). Digital images of these photonic films reveal that the interferometric color, an optical property established by the position of the characteristic reflection peak ( $\lambda_{\text{peak}}$ ), undergoes a red shift toward longer wavelengths when  $T_{\text{p}}$  and  $J_{\text{Offset}}$  increase (Figure 2b).<sup>40</sup> SEM image analysis reveals that  $L_{\text{Tp}}$  increases linearly with the anodization period and the anodization offset (Figure 2c,d). Nevertheless, we found slight differences in the dependence of  $L_{\text{Tp}}$  with  $T_{\text{p}}$  and  $J_{\text{Offset}}$ . As Figure 2c shows, the longer the anodization period is, the stronger the dependence is for  $L_{\text{Tp}}$  on  $J_{\text{Offset}}$ . The slope of the fitting line for the dependence of  $L_{\text{Tp}}$  on  $J_{\text{Offset}}$  for  $T_{\text{p}} = 650, 700,$  and  $750$  s was found to be  $135 \pm 50, 272 \pm 23,$  and  $365 \pm 4$  nm  $(\text{mA cm}^{-2})^{-1}$ , respectively. Figure 2d shows the linear fittings describing how  $L_{\text{Tp}}$  varies with  $T_{\text{p}}$  for the different values of  $J_{\text{Offset}}$ . This graph reveals that the dependence of  $L_{\text{Tp}}$  on  $T_{\text{p}}$  for  $J_{\text{Offset}} = 0.14, 0.28,$  and  $0.42$  mA  $\text{cm}^{-2}$  was  $0.0162 \pm 0.04, 0.477 \pm 0.04,$  and  $0.680 \pm 0.10$  nm  $\text{s}^{-1}$ , respectively.

### Optimization of Sensing Performance of HSA-Modified NAA-RFs Combined with RIFs.

The above-mentioned NAA-RFs (Table 1) were modified with human serum albumin and used as sensing platforms to establish the binding affinity between immobilized HSA and indomethacin molecules as a function of the fabrication parameters (i.e.,  $T_{\text{p}}$  and  $J_{\text{Offset}}$ ). Indomethacin is commonly used as a prescription drug to reduce stiffness, fever, pain, and swelling. This drug was used as a model drug molecule due to its well-known affinity toward HSA and other serum proteins. In this study, two sensing parameters were used in order to establish the most sensitive NAA-RF structures toward indomethacin molecules: namely, (i) shifts in the characteristic reflection peak ( $\Delta\lambda_{\text{peak}}$ ) and (ii) changes in the effective optical thickness of the film ( $\Delta\text{OT}_{\text{eff}}$ ). Whereas the former parameter was established by following the position of  $\lambda_{\text{peak}}$  in the RIFs spectrum of NAA-

RFs, the latter was obtained by applying fast Fourier transform to the RIFs spectrum of NAA-RFs.<sup>50</sup> Figure 3a (inset) shows a schematic illustration of a NAA rugate filter and the interfering light beams at the different interfaces forming these photonic crystal structures. The reflectivity spectrum of NAA-RFs is derived from two sources: namely, (i) the interference of light from all layers of the multilayered NAA-RF structure and (ii) the Fabry–Pérot interference spectrum produced by the reflections of light at the interfaces bordering the NAA-RF film.<sup>50</sup> As a result, the RIFs spectrum of NAA-RFs displays a narrow and well-defined characteristic reflection peak, which corresponds to the photonic stop band of the photonic crystals, and small sideband fringes produced by the Fabry–Pérot interference in the photonic film (Figure 3a). In our experiments, the characteristic reflection peak ( $\lambda_{\text{peak}}$ ) was separated from the Fabry–Pérot fringes region in order to apply an FFT to the selected region and estimate the effective optical thickness ( $\text{OT}_{\text{eff}}$ ) of the film.<sup>50</sup> Both optical parameters were used as sensing references to establish the most sensitive NAA-RFs structures toward indomethacin molecules. Figure 3b shows a schematic illustration of the sensing approach used in our study to establish the binding affinity between drug molecules and HSA-modified NAA-RFs. Figure 3c,d displays examples of this process using HSA-modified NAA-RFs and RIFs with  $\Delta\lambda_{\text{peak}}$  and  $\Delta\text{OT}_{\text{eff}}$  as the sensing reference parameters, respectively. This process is divided into three stages: (i) chemical activation of amine ( $-\text{NH}_2$ ) groups present on the surface of NAA by GTA, (ii) immobilization of HSA molecules on the surface of activated NAA-RFs, and (iii) adsorption–desorption of drug molecules from HSA-modified NAA-RFs. First, fresh PBS (pH 7.4) solution was flowed at a rate of  $100 \mu\text{L min}^{-1}$  through the flow cell, where APTES-functionalized NAA rugate filters were placed. A stable baseline for  $\Delta\lambda_{\text{peak}}$  and  $\Delta\text{OT}_{\text{eff}}$  was achieved after 15 min (i, Figure 3c,d). After this, a 2.5 v% GTA solution in PBS was flowed through the system for 30 min in order to activate the amine groups present on the inner surface of NAA-RFs (ii, Figure 3c,d). In this stage,  $\Delta\lambda_{\text{peak}}$  and  $\Delta\text{OT}_{\text{eff}}$  underwent a red shift due to the interaction between activated amine groups present on the inner surface of NAA-RFs and GTA molecules. Fresh PBS solution was flowed again after GTA activation for 15 min in order to remove physisorbed GTA molecules from the surface of NAA-RFs. As a result,  $\Delta\lambda_{\text{peak}}$  and  $\Delta\text{OT}_{\text{eff}}$  decreased slightly during this process (iii, Figure 3c,d). Next, a 1 mg  $\text{mL}^{-1}$  solution of HSA in PBS was injected into the system and flowed at  $100 \text{ mL min}^{-1}$  for 1 h (iv, Figure 3c,d). A marked red shift was observed both in sensing parameters as a result of the binding event between GTA-activated APTES-modified NAA-RFs and HSA molecules.

Then, fresh PBS solution was flowed through the flow cell in order to wash away physisorbed HSA molecules (v, Figure 3c,d). Prior to injection of indomethacin analytical solutions, a baseline in a modified PBS solution containing EtOH 5 v% was obtained for 15 min in order to compensate the addition of ethanol to improve the solubility of indomethacin, which is a highly hydrophobic therapeutic. The binding interaction between HSA and indomethacin molecules present in the PBS solution resulted in a sharp red shift both in  $\Delta\lambda_{\text{peak}}$  and  $\Delta\text{OT}_{\text{eff}}$  (vi, Figure 3c,d), which continued until the HSA molecules present in the inner surface of NAA-RFs were saturated by indomethacin molecules (i.e., equilibrium stage = end of vi, Figure 3c,d). After this, fresh PBS solution containing 5 v% EtOH was flowed through the system in order to desorb

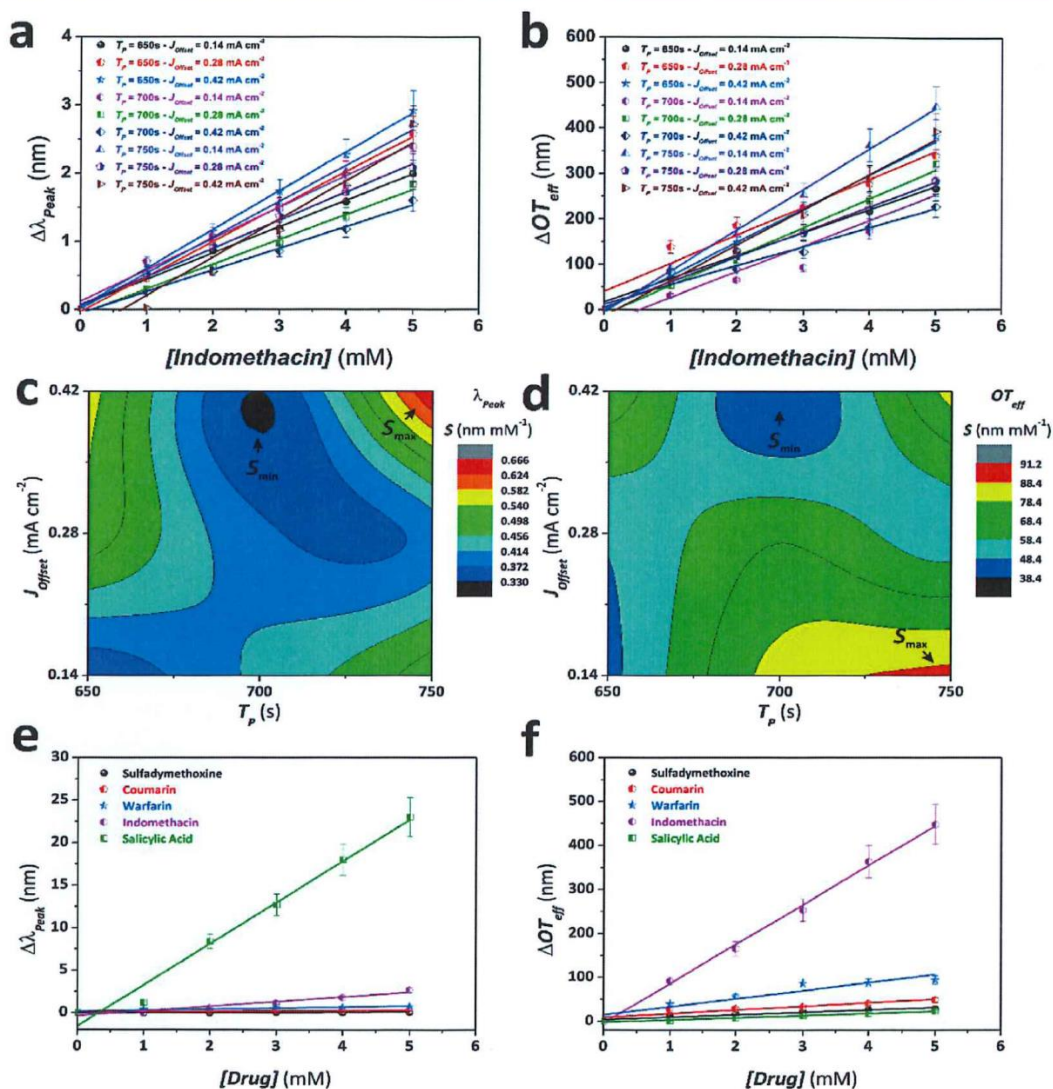


**Figure 4.** Optical optimization and establishment of binding affinity between drug molecules and HSA-modified NAA-RFs by RIFs. (a) Linear fitting lines showing the linear dependence between  $\Delta\lambda_{\text{Peak}}$  and the different concentrations of indomethacin (1, 2, 3, 4, and 5 mM) for each type of NAA-RF. (b) Linear fitting lines showing the linear dependence between  $\Delta OT_{\text{eff}}$  and the different concentrations of indomethacin (1, 2, 3, 4, and 5 mM) for each type of NAA-RF. (c) Contour map showing the distribution of sensitivity ( $S$ ) as a function of the fabrication parameters (i.e.,  $T_p$  and  $J_{\text{Offset}}$ ) for  $\Delta\lambda_{\text{Peak}}$  calculated from part a. (d) Contour map showing the distribution of sensitivity ( $S$ ) as a function of the fabrication parameters (i.e.,  $T_p$  and  $J_{\text{Offset}}$ ) for  $\Delta OT_{\text{eff}}$  calculated from part b. (e) Linear fitting lines showing the dependence between  $\Delta\lambda_{\text{Peak}}$  and the different concentrations of the drugs assessed in this study for NAA-RF<sub>750-0.42</sub>. (f) Linear fitting lines showing the dependence between  $\Delta OT_{\text{eff}}$  and the different concentrations of the drugs assessed in this study for NAA-RF<sub>750-0.14</sub>.

indomethacin from HSA molecules (vii, Figure 3c,d). Note that the binding event between indomethacin molecules and HSA molecules is a reversible reaction. Therefore, both  $\Delta\lambda_{\text{Peak}}$  and  $\Delta OT_{\text{eff}}$  underwent a blue shift until the original baseline (i.e., vi, Figure 3c,d) was reached. A summary of the obtained results for  $\Delta\lambda_{\text{Peak}}$  and  $\Delta OT_{\text{eff}}$  for each analytical solution of indomethacin (1, 2, 3, 4, and 5 mM) are displayed in Figure 3e,f. This process is characterized by two stages: (i) adsorption stage, when the analytical solution of drug is injected into the flow cell, and (ii) desorption stage, when fresh PBS solution is

flowed through the flow cell and drug molecules are released from HSA. The total changes in  $\Delta\lambda_{\text{Peak}}$  and  $\Delta OT_{\text{eff}}$  can be calculated as indicated in Figure 3e,f.

Figure 4a,b shows the linear fittings for  $\Delta\lambda_{\text{Peak}}$  and  $\Delta OT_{\text{eff}}$  as a function of the concentration of indomethacin for the different NAA-RFs structures used in this study (Table 1). These graphs show that  $\Delta\lambda_{\text{Peak}}$  and  $\Delta OT_{\text{eff}}$  have a linear dependence with the concentration of indomethacin. A linear fitting between  $\Delta\lambda_{\text{Peak}}$  and  $\Delta OT_{\text{eff}}$  and the concentration of indomethacin makes it possible to estimate the sensitivity,  $S$

(i.e., slope of the fitting line), the low limit of detection, LLoD (i.e., calculated as  $3\sigma$ ), and the linearity,  $R^2$  (i.e., correlation coefficient of the fitting line), for each NAA-RF. The obtained results, summarized in Table S1 (Supporting Information), reveal that the NAA-RF structures with the highest sensitivity for  $\Delta\lambda_{\text{Peak}}$  and  $\Delta\text{OT}_{\text{eff}}$  were NAA-RF<sub>750-0.42</sub> ( $S = 0.66 \pm 0.03 \text{ nm mM}^{-1}$ , LLoD =  $0.65 \pm 0.02 \text{ mM}$ , and  $R^2 = 0.985$ ) and NAA-RF<sub>750-0.14</sub> ( $S = 91.1 \pm 3.4 \text{ nm mM}^{-1}$ , LLoD =  $0.41 \pm 0.03 \text{ mM}$ , and  $R^2 = 0.994$ ), respectively. Figure 4c,d shows contour maps displaying the dependence of  $S$  on the fabrication parameters ( $T_{\text{p}}$  and  $J_{\text{Offset}}$ ) for  $\Delta\lambda_{\text{Peak}}$  and  $\Delta\text{OT}_{\text{eff}}$ . These graphs denote that the distribution of  $S$  with  $T_{\text{p}}$  and  $J_{\text{Offset}}$  is fairly homogeneous for both the cases (i.e.,  $\Delta\lambda_{\text{Peak}}$  and  $\Delta\text{OT}_{\text{eff}}$ ) since the distribution of color fields (i.e., increment in  $S$ ) is concentrically homogeneous around the minimum values, which are located at  $T_{\text{p}} = 700 \text{ s}$  and  $J_{\text{Offset}} = 0.14 \text{ mA cm}^{-2}$  for  $\Delta\lambda_{\text{Peak}}$  and  $\Delta\text{OT}_{\text{eff}}$ . However, although the lines between color fields are closer to each other in a similar manner, it is worth noting that contour lines in  $\Delta\lambda_{\text{Peak}}$  are much closer around the proximity of the maximum value ( $T_{\text{p}} = 750 \text{ s}$  and  $J_{\text{Offset}} = 0.42 \text{ mA cm}^{-2}$ ) than those of  $\Delta\text{OT}_{\text{eff}}$  indicating a much stronger dependence of  $S$  on  $T_{\text{p}}$  and  $J_{\text{Offset}}$ . In order to gain a more objective insight into the dependence of  $S$  on  $T_{\text{p}}$  and  $J_{\text{Offset}}$  we performed an ANOVA analysis for the sensitivity obtained by measuring both sensing parameters ( $\Delta\lambda_{\text{Peak}}$  and  $\Delta\text{OT}_{\text{eff}}$ ).

The ANOVA analysis (Table 2) was performed using the values of  $S$  measured from  $\Delta\lambda_{\text{Peak}}$  and  $\Delta\text{OT}_{\text{eff}}$  and the values of

Table 2. Summary of the ANOVA Analysis Performed in Our Study To Establish the Most Optimal NAA-RF Structures As a Function of the Fabrication Parameters ( $T_{\text{p}}$  and  $J_{\text{Offset}}$ )

source of variance	SS	DF	MS	$F_0$
Sensing Parameter $\Delta\lambda_{\text{Peak}}$				
$T_{\text{p}}$ (s)	0.1032	2	0.0516	166.9
$J_{\text{Offset}}$ (mA cm <sup>-2</sup> )	0.0414	2	0.0207	66.9
$T_{\text{p}}J_{\text{Offset}}$ (s mA cm <sup>-2</sup> )	0.1472	4	0.0368	119.0
model	0.2917	8	0.0365	117.9
error	0.0056	18	3.0922	
total	0.2973	26		
Sensing Parameter $\Delta\text{OT}_{\text{eff}}$				
$T_{\text{p}}$ (s)	1688.9	2	844.4	51.7
$J_{\text{Offset}}$ (mA cm <sup>-2</sup> )	1195.1	2	597.6	36.6
$T_{\text{p}}J_{\text{Offset}}$ (s mA cm <sup>-2</sup> )	5545.6	4	1386.4	84.8
model	8429.6	8	1053.7	64.5
error	294.2	18	16.3	
total	8723.9	26		

Table 3. Summary of Binding Affinity between Drug Molecules and HSA-Functionalized NAA-RFs Obtained from  $\Delta\lambda_{\text{Peak}}$  (NAA-RF<sub>750-0.42</sub>) and  $\Delta\text{OT}_{\text{eff}}$  (NAA-RF<sub>750-0.14</sub>) and Comparison with the Binding Affinity Reported in the Literature

drug	sensing parameter				literature <sup>a</sup> level
	$\Delta\lambda_{\text{Peak}}$		$\Delta\text{OT}_{\text{eff}}$		
	$S$ (nm mM <sup>-1</sup> )	level	$S$ (nm mM <sup>-1</sup> )	level	
indomethacin	$0.560 \pm 0.067$	M	$89.8 \pm 2.3$	H	H
sulfadymethoxine	$0.027 \pm 0.005$	L	$5.5 \pm 0.7$	M	H
warfarin	$0.138 \pm 0.024$	M	$18.4 \pm 3.2$	H	H
coumarin	$0.045 \pm 0.012$	L	$8.3 \pm 1.7$	M	M
salicylic acid	$4.850 \pm 0.317$	H	$4.9 \pm 0.3$	M	M

<sup>a</sup>Values obtained from ref 9.

each parameter were estimated using the equations shown in Table S2 (Supporting Information). In this analysis, the hypotheses  $H_0$ ,  $H_1$ , and  $H_2$  are assessed by comparing the value of  $F_0$  (i.e., test statistic calculated from the ANOVA table) and the corresponding value of the  $F$ -distribution for a significance level of 95%. Our analysis for  $S$  obtained from  $\Delta\lambda_{\text{Peak}}$  denotes that the hypotheses  $H_0$  and  $H_1$  are both rejected since the individual effects of these anodization parameters are significant (i.e.,  $166.9$  and  $66.9 > F_{(0.05;2;27)} = 3.4$ , respectively). Therefore, the alternative hypotheses  $H_0^*$  and  $H_1^*$  are accepted. This analysis also reveals that the interaction between  $T_{\text{p}}$  and  $J_{\text{Offset}}$  ( $T_{\text{p}}J_{\text{Offset}}$ ) is significant as well because  $119.0 > F_{(0.05;4;27)} = 2.7$ . Thus, the hypothesis  $H_2$  is also rejected and the alternative hypothesis  $H_2^*$  accepted. As a result, it is concluded that all the fabrication parameters (i.e.,  $T_{\text{p}}$ ,  $J_{\text{Offset}}$  and their interaction  $T_{\text{p}}J_{\text{Offset}}$ ) have a significant effect over  $S$ . Nevertheless, the magnitudes of  $H_0^*$ ,  $H_1^*$ , and  $H_2^*$  have different weight over the studied variable  $S$ , being 47.3%, 19.0%, and 33.7% for  $T_{\text{p}}$ ,  $J_{\text{Offset}}$  and their interaction  $T_{\text{p}}J_{\text{Offset}}$  respectively. Hence,  $S$  is found to have a stronger dependence on  $T_{\text{p}}$  when  $\Delta\lambda_{\text{Peak}}$  is used as the sensing parameter.

As far as the ANOVA analysis on  $S$  obtained from  $\Delta\text{OT}_{\text{eff}}$  is concerned, it shows that the hypotheses  $H_0$  and  $H_1$  are both rejected as the individual effects of  $T_{\text{p}}$  and  $J_{\text{Offset}}$  are both significant (i.e.,  $51.7$  and  $36.6 > F_{(0.05;2;27)} = 3.4$ , respectively). As a result, the alternative hypotheses  $H_0^*$  and  $H_1^*$  are accepted. Furthermore, it is found that the interaction between  $T_{\text{p}}$  and  $J_{\text{Offset}}$  ( $T_{\text{p}}J_{\text{Offset}}$ ) is also significant since  $84.8 > F_{(0.05;4;27)} = 2.7$ . Therefore, the hypothesis  $H_2$  is rejected and the alternative hypothesis  $H_2^*$  accepted. In this case, it is established that  $T_{\text{p}}$ ,  $J_{\text{Offset}}$  and their interaction  $T_{\text{p}}J_{\text{Offset}}$  all have a significant effect over  $S$ . However, the magnitudes of  $H_0^*$ ,  $H_1^*$ , and  $H_2^*$  have weights of 29.9%, 21.1%, and 49.0%. Therefore,  $S$  has a more marked dependence on the interaction  $T_{\text{p}}J_{\text{Offset}}$  when  $\Delta\text{OT}_{\text{eff}}$  is used as the sensing parameter.

**Assessment of Binding Affinity between Drugs and HSA-Modified NAA-RFs by RfS.** A set of the most sensitive NAA-RFs structures toward indomethacin molecules (NAA-RF<sub>750-0.42</sub> and NAA-RF<sub>750-0.14</sub> for  $\Delta\lambda_{\text{Peak}}$  and  $\Delta\text{OT}_{\text{eff}}$  respectively) were used in order to establish the binding affinity between a set of drugs (i.e., indomethacin, coumarin, sulfadymethoxine, warfarin, and salicylic acid) and HSA molecules by RfS using  $\Delta\lambda_{\text{Peak}}$  and  $\Delta\text{OT}_{\text{eff}}$  as sensing parameters. This set of experiments was carried out following the above-mentioned protocol (*vide supra*) in a flow cell where five analytical solutions of each drug (1, 2, 3, 4, and 5 mM) were flowed at a constant rate ( $100 \mu\text{L min}^{-1}$ ). The obtained results for  $\Delta\lambda_{\text{Peak}}$  and  $\Delta\text{OT}_{\text{eff}}$  are summarized in Table 3 and Figure 4e,f, respectively.  $\Delta\lambda_{\text{Peak}}$  establishes that the binding

affinity between HSA and the aforementioned set of drugs follows the order salicylic acid ( $S = 4.850 \pm 0.317 \text{ nm mM}^{-1}$ ) > indomethacin ( $S = 0.560 \pm 0.067 \text{ nm mM}^{-1}$ ) > warfarin ( $S = 0.138 \pm 0.024 \text{ nm mM}^{-1}$ ) > coumarin ( $S = 0.045 \pm 0.012 \text{ nm mM}^{-1}$ ) > sulfadymethoxine ( $S = 0.027 \pm 0.005 \text{ nm mM}^{-1}$ ). In contrast,  $\Delta OT_{\text{eff}}$  establishes that the binding affinity between these drugs and HSA molecules follows the order indomethacin ( $S = 89.8 \pm 2.3 \text{ nm mM}^{-1}$ ) > warfarin ( $S = 18.4 \pm 3.2 \text{ nm mM}^{-1}$ ) > coumarin ( $S = 8.3 \pm 1.7 \text{ nm mM}^{-1}$ ) > sulfadymethoxine ( $S = 5.5 \pm 0.7 \text{ nm mM}^{-1}$ ) > salicylic acid ( $S = 4.9 \pm 0.3 \text{ nm mM}^{-1}$ ).

Previous studies have reported that, whereas the binding affinity between indomethacin, sulfadymethoxine, warfarin, and HSA molecules is high, coumarin and salicylic acid present an interaction with medium strength toward this plasma protein.<sup>9</sup> Our results using  $\Delta\lambda_{\text{peak}}$  as the sensing parameter establish salicylic acid as a drug molecule with high affinity toward HSA molecules, whereas indomethacin and warfarin have medium affinity, and coumarin and sulfadymethoxine present a low affinity toward HSA. However, indomethacin and warfarin have high affinity toward HSA molecules, and coumarin, sulfadymethoxine, and salicylic acid are found to be drug molecules with medium affinity when  $\Delta OT_{\text{eff}}$  is used as the sensing parameter. These results reveal a higher degree of agreement between the results obtained by benchmark techniques<sup>9</sup> and those obtained in this study by  $\Delta OT_{\text{eff}}$ . Therefore, it can be concluded that  $\Delta OT_{\text{eff}}$  is a more reliable sensing parameter than  $\Delta\lambda_{\text{peak}}$  to be used in the proposed sensing system combining NAA-RFs and RIFS.

## CONCLUSIONS

This study has reported on an approach that aims to assess the binding affinity between drug molecules and human serum albumin by combining HSA-modified NAA-RFs with RIFS. First, we carried out a systematic analysis of the structural features and optical properties of NAA-RFs produced by sinusoidal pulse anodization. These photonic crystal structures present two characteristic optical parameters, the characteristic reflection peak ( $\lambda_{\text{peak}}$ ), and the effective optical thickness of the film ( $OT_{\text{eff}}$ ), which can be readily used as sensing parameters. A set of nine NAA-RFs were used to establish the most sensitive structures toward indomethacin molecules, a model drug, as a function of two fabrication parameters (i.e.,  $T_p$ , anodization period, and  $J_{\text{offset}}$ , anodization offset). A design of experiment strategy made it possible to establish the effect of these anodization parameters on the sensitivity of HSA-modified NAA-RFs using two sensing parameters, that is, shifts in the characteristic reflection peak ( $\Delta\lambda_{\text{peak}}$ ) and changes in the effective optical thickness of the film ( $\Delta OT_{\text{eff}}$ ). An ANOVA analysis established that the anodization period, the anodization offset, and their interaction have all significant effects on the sensing performance of NAA-RFs for both sensing parameters (i.e.,  $\Delta\lambda_{\text{peak}}$  and  $\Delta OT_{\text{eff}}$ ). Nevertheless, whereas  $T_p$  was found to be the parameter with the most significant influence over  $S$  in the case of  $\Delta\lambda_{\text{peak}}$ , the interaction  $T_p \cdot J_{\text{offset}}$  was the parameter with the strongest influence over the sensitivity of NAA-RFs for  $\Delta OT_{\text{eff}}$ . Our analysis also revealed that the most sensitive structures toward indomethacin molecules were NAA-RF<sub>750-0.42</sub> and NAA-RF<sub>750-0.14</sub> for  $\Delta\lambda_{\text{peak}}$  and  $\Delta OT_{\text{eff}}$  respectively. Subsequently, we used these NAA-RF structures in order to establish the binding affinity between a set of drugs (i.e., indomethacin, coumarin, sulfadymethoxine, warfarin, salicylic acid) and HSA molecules. We found that, in the case

of NAA-RFs, the binding affinity between drug molecules and HSA is dependent on the sensing parameter used. Whereas  $\Delta\lambda_{\text{peak}}$  established salicylic acid as the drug molecule with the highest affinity toward HSA molecules, indomethacin was found to be the drug with the strongest affinity when  $\Delta OT_{\text{eff}}$  was used as the sensing parameter. Although the low limit of detection achieved by our system is slightly higher than that of benchmark techniques such as SPR, the obtained results are certainly promising, and there is still margin for improvement by further optimization strategies. The proposed sensing system combining HSA-modified NAA-RFs and RIFS provides a reliable means of assessing the binding affinity of drugs with a set of features such as portability, low cost, and easy operation that makes it a promising alternative to benchmark techniques such as SPR.

## ASSOCIATED CONTENT

### Supporting Information

The Supporting Information is available free of charge on the ACS Publications website at DOI: 10.1021/acs.analchem.6b00993.

Further information about the fitting lines and sensing parameters used to establish the most sensitive NAA-RF structures and equations of ANOVA (PDF)

## AUTHOR INFORMATION

### Corresponding Authors

\*Phone: +61 8 8313 1535. Fax: +61 8 8303 4373. E-mail: [abel.santos@adelaide.edu.au](mailto:abel.santos@adelaide.edu.au). Web page: <http://www.adelaide.edu.au/directory/abel.santos>.

\*Phone: + 61 8 8313 4648. Fax: +61 8 8303 4373. E-mail: [dusan.losic@adelaide.edu.au](mailto:dusan.losic@adelaide.edu.au). Web page: <http://www.adelaide.edu.au/directory/dusan.losic>.

### Author Contributions

A.S. conceived the idea and designed the experimental part of this work. N.M. carried out the experiments assisted by C.S.L. and A.S. The obtained results were discussed and analyzed by all the authors. The final version of the manuscript was written through contributions of all the authors. All the authors have given approval to the final version of the manuscript.

### Notes

The authors declare no competing financial interest.

## ACKNOWLEDGMENTS

Authors acknowledge the support provided by the Australian Research Council (ARC) through Grants DE140100549, DP120101680, and FT110100711 and the School of Chemical Engineering (UoA). Authors thank the Adelaide Microscopy (AM) centre for FEG-SEM characterization.

## ABBREVIATIONS

NAA-RF nanoporous anodic alumina rugate filters  
HSA human serum albumin  
RIFS reflectometric interference spectroscopy

## REFERENCES

- (1) Munos, B. *Nat. Rev. Drug Discovery* **2009**, *8*, 959–968.
- (2) Mullard, A. *Nat. Rev. Drug Discovery* **2011**, *10*, 82–85.
- (3) Knutsen, L. J. S. *Drug Discovery Today* **2011**, *16*, 476–484.
- (4) Khanna, I. *Drug Discovery Today* **2012**, *17*, 1088–1102.
- (5) Kola, L.; Landis, J. *Nat. Rev. Drug Discovery* **2004**, *3*, 711–715.



- (6) Andersson, S.; Armstrong, A.; Björe, A.; Bowker, S.; Chapman, S.; Davies, R.; Donald, C.; Egner, B.; Elebring, T.; Holmqvist, S.; Inghardt, T.; Johannesson, P.; Johansson, M.; Johnstone, C.; Kemmitt, P.; Kihlberg, J.; Korsgren, P.; Lemurell, M.; Moore, J.; Pettersson, J. A.; Pointon, H.; Pontén, F.; Schofield, P.; Selmi, N.; Whittamore, P. *Drug Discovery Today* **2009**, *14*, 598–604.
- (7) Oravcová, J.; Böhs, B.; Lindner, W. J. *Chromatogr., Biomed. Appl.* **1996**, *677*, 1–28.
- (8) Hage, D.; Tweed, S. J. *Chromatogr., Biomed. Appl.* **1997**, *699*, 499–525.
- (9) Frostell-Karlsson, A.; Remaeus, A.; Roos, H.; Andersson, K.; Borg, P.; Hämäläinen, M.; Karlsson, R. J. *Med. Chem.* **2000**, *43*, 1986–1992.
- (10) Kraus, G.; Brecht, A.; Vasic, V.; Gauglitz, G. *Fresenius' J. Anal. Chem.* **1994**, *348*, 598–602.
- (11) Yan, H. M.; Kraus, G.; Gauglitz, G. *Anal. Chim. Acta* **1995**, *312*, 1–8.
- (12) Kraus, G.; Gauglitz, G. *Chemom. Intell. Lab. Syst.* **1995**, *30*, 211–221.
- (13) Haake, H. M.; Schütz, A.; Gauglitz, G. *Fresenius' J. Anal. Chem.* **2000**, *366*, 576–585.
- (14) Birkert, O.; Tünnemann, R.; Jung, G.; Gauglitz, G. *Anal. Chem.* **2002**, *74*, 834–840.
- (15) Belge, G.; Beyerlein, D.; Betsch, C.; Eichhorn, K. J.; Gauglitz, G.; Grundke, K.; Voit, B. *Anal. Bioanal. Chem.* **2002**, *374*, 403–411.
- (16) Gauglitz, G.; Brecht, A.; Kraus, G.; Mahm, W. *Sens. Actuators, B* **1993**, *11*, 21–27.
- (17) Curtis, C. L.; Doan, V. V.; Credo, G. M.; Sailor, M. J. *J. Electrochem. Soc.* **1993**, *140*, 3492–3494.
- (18) Lin, V. S. Y.; Motesharei, K.; Dancil, K. S.; Sailor, M. J.; Ghadiri, M. R. *Science* **1997**, *278*, 840–843.
- (19) Masuda, H.; Fukuda, K. *Science* **1995**, *268*, 1466–1468.
- (20) Masuda, H.; Hasegawa, F. J. *J. Electrochem. Soc.* **1997**, *144*, L127–L130.
- (21) Masuda, H.; Yada, K.; Osaka, A. *Jpn. J. Appl. Phys.* **1998**, *37*, L1340–L1342.
- (22) Nielsch, K.; Choi, J.; Schwirn, K.; Wehrspohn, R. B.; Gösele, U. *Nano Lett.* **2002**, *2*, 677–680.
- (23) Lee, W.; Park, J. S. *Chem. Rev.* **2014**, *114*, 7487–7556.
- (24) Santos, A.; Kumeria, T.; Losic, D. *TrAC, Trends Anal. Chem.* **2013**, *44*, 25–38.
- (25) Santos, A.; Kumeria, T.; Losic, D. *Materials* **2014**, *7*, 4297–4320.
- (26) Kumeria, T.; Santos, A.; Losic, D. *Sensors* **2014**, *14*, 11878–11918.
- (27) Santos, A.; Balderrama, V. S.; Alba, M.; Formentín, P.; Ferré-Borrull, J.; Pallarès, J.; Marsal, L. F. *Adv. Mater.* **2012**, *24*, 1050–1054.
- (28) Santos, A.; Kumeria, T.; Wang, Y.; Losic, D. *Nanoscale* **2014**, *6*, 9991–9999.
- (29) Santos, A.; Kumeria, T.; Losic, D. *Anal. Chem.* **2013**, *85*, 7904–7911.
- (30) Chen, Y.; Santos, A.; Wang, Y.; Kumeria, T.; Wang, C.; Li, J.; Losic, D. *Nanoscale* **2015**, *7*, 7770–7779.
- (31) Kumeria, T.; Rahman, M. M.; Santos, A.; Ferré-Borrull, J.; Marsal, L. F.; Losic, D. *Anal. Chem.* **2014**, *86*, 1837–1844.
- (32) Chen, Y.; Santos, A.; Wang, Y.; Kumeria, T.; Ho, D.; Li, J.; Wang, C.; Losic, D. *Sci. Rep.* **2015**, *5*, 12893.
- (33) Nemati, M.; Santos, A.; Kumeria, T.; Losic, D. *Anal. Chem.* **2015**, *87*, 9016–9024.
- (34) Kumeria, T.; Rahman, M. M.; Santos, A.; Ferré-Borrull, J.; Marsal, L. F.; Losic, D. *ACS Appl. Mater. Interfaces* **2014**, *6*, 12971–12978.
- (35) Kumeria, T.; Santos, A.; Rahman, M. M.; Ferré-Borrull, J.; Marsal, L. F.; Losic, D. *ACS Photonics* **2014**, *1*, 1298–1306.
- (36) Rahman, M. M.; Marsal, L. F.; Pallarès, J.; Ferré-Borrull, J. *ACS Appl. Mater. Interfaces* **2013**, *5*, 13375–13381.
- (37) Chen, Y.; Santos, A.; Wang, Y.; Kumeria, T.; Li, J.; Wang, C.; Losic, D. *ACS Appl. Mater. Interfaces* **2015**, *7*, 19816–19824.
- (38) Wang, Y.; Chen, Y.; Kumeria, T.; Ding, F.; Evdokiou, A.; Losic, D.; Santos, A. *ACS Appl. Mater. Interfaces* **2015**, *7*, 9879–9888.
- (39) Chen, Y.; Santos, A.; Ho, D.; Wang, Y.; Kumeria, T.; Li, J.; Wang, C.; Losic, D. *Electrochim. Acta* **2015**, *174*, 672–681.
- (40) Santos, A.; Yoo, J.; Rohatgi, C.; Kumeria, T.; Wang, Y.; Losic, D. *Nanoscale* **2016**, *8*, 1360–1373.
- (41) Santos, A.; Formentín, P.; Ferré-Borrull, J.; Pallarès, J.; Marsal, L. F. *Mater. Lett.* **2012**, *67*, 296–299.
- (42) Wang, Y.; Santos, A.; Evdokiou, A.; Losic, D. *Electrochim. Acta* **2015**, *154*, 379–386.
- (43) Dronov, R.; Jane, A.; Shapter, J. G.; Hodges, A.; Voelcker, N. H. *Nanoscale* **2011**, *3*, 3109–3114.
- (44) Kumeria, T.; Losic, D. *Nanoscale Res. Lett.* **2012**, *7*, 88.
- (45) Jani, A. M. Md.; Kempson, I. M.; Losic, D.; Voelcker, N. H. *Angew. Chem., Int. Ed.* **2010**, *49*, 7933–7937.
- (46) Kumeria, T.; Santos, A.; Losic, D. *ACS Appl. Mater. Interfaces* **2013**, *5*, 11783–11790.
- (47) Santos, A.; Montero-Moreno, J. M.; Bachmann, J.; Nielsch, K.; Formentín, P.; Ferré-Borrull, J.; Pallarès, J.; Marsal, L. F. *ACS Appl. Mater. Interfaces* **2011**, *3*, 1925–1932.
- (48) Montgomery, D. C. *Design and Analysis of Experiments*, 5th ed.; John Wiley & Sons Inc.: New York, 2001.
- (49) Abramoff, M. D.; Magalhaes, P. J.; Ram, S. J. *Biophotonics Int.* **2004**, *11*, 36–42.
- (50) Pacholski, C.; Sailor, M. J. *Phys. Status Solidi C* **2007**, *4*, 2088–2092.

# Supporting Information

## Assessment of Binding Affinity between Drugs and Human Serum Albumin using Nanoporous Anodic Alumina Photonic Crystals

Mahdieh Nemati<sup>1</sup>, Abel Santos<sup>1\*</sup>, Cheryl Suwen Law<sup>1</sup> and Dusan Losic<sup>1\*</sup>

<sup>1</sup>School of Chemical Engineering, The University of Adelaide, Engineering North Building, 5005 Adelaide, Australia

\*E-Mail: [abel.santos@adelaide.edu.au](mailto:abel.santos@adelaide.edu.au) ; [dusan.losic@adelaide.edu.au](mailto:dusan.losic@adelaide.edu.au)

## S.1 Summary of Sensing Parameters for NAA-RFs

Table S1 summarizes the different sensing parameters (i.e. sensitivity –  $S$ , low limit of detection –  $LLoD$  and linearity –  $R^2$ ) obtained for the different NAA-RF structures used in our study (Table 1) for each of the sensing parameters (i.e.  $\Delta\lambda_{Peak}$  and  $\Delta OT_{eff}$ ).

Table S1. Summary of the sensing parameters obtained for the different NAA-RFs by measuring  $\Delta\lambda_{Peak}$  and  $\Delta OT_{eff}$  by RIFS.

NAA-RF Structure	Sensing Parameter $\Delta\lambda_{Peak}$		
	$S$ (nm mM <sup>-1</sup> )	$LLoD$ (mM)	$R^2$
NAA-RF <sub>650-0.14</sub>	0.37 ± 0.03	0.28 ± 0.01	0.997
NAA-RF <sub>650-0.28</sub>	0.52 ± 0.01	0.23 ± 0.02	0.998
NAA-RF <sub>650-0.42</sub>	0.56 ± 0.01	0.39 ± 0.02	0.994
NAA-RF <sub>700-0.14</sub>	0.42 ± 0.01	0.33 ± 0.03	0.996
NAA-RF <sub>700-0.28</sub>	0.38 ± 0.01	0.51 ± 0.01	0.991
NAA-RF <sub>700-0.42</sub>	0.33 ± 0.01	0.44 ± 0.02	0.993
NAA-RF <sub>750-0.14</sub>	0.52 ± 0.02	0.52 ± 0.03	0.990
NAA-RF <sub>750-0.28</sub>	0.39 ± 0.01	0.29 ± 0.01	0.997
NAA-RF <sub>750-0.42</sub>	0.66 ± 0.03	0.65 ± 0.02	0.985

NAA-RF Structure	Sensing Parameter $\Delta OT_{eff}$		
	$S$ (nm mM <sup>-1</sup> )	$LLoD$ (mM)	$R^2$
NAA-RF <sub>650-0.14</sub>	45.7 ± 0.8	0.20 ± 0.01	0.998
NAA-RF <sub>650-0.28</sub>	49.9 ± 2.2	0.48 ± 0.02	0.992
NAA-RF <sub>650-0.42</sub>	74.3 ± 3.3	0.48 ± 0.01	0.992
NAA-RF <sub>700-0.14</sub>	82.6 ± 8.3	1.10 ± 0.03	0.960
NAA-RF <sub>700-0.28</sub>	67.0 ± 2.8	0.45 ± 0.01	0.993
NAA-RF <sub>700-0.42</sub>	38.5 ± 5.2	1.47 ± 0.02	0.931
NAA-RF <sub>750-0.14</sub>	91.1 ± 3.4	0.41 ± 0.03	0.994
NAA-RF <sub>750-0.28</sub>	53.6 ± 1.4	0.29 ± 0.02	0.997
NAA-RF <sub>750-0.42</sub>	82.2 ± 3.8	0.51 ± 0.01	0.991

## S.2 ANOVA Calculations

The ANOVA table shown in the manuscript (**Table 2**) was calculated from the equations shown in **Table S2**, where SS is the sum of squares of the corresponding source, DF denotes the degree of freedom of such source, MS corresponds to the mean square of the corresponding source,  $F_0$  is the test statistic of that source, a and b denote the total number of levels corresponding to  $T_P$  and  $J_{Offset}$ , respectively, and n is the total number of replications. The strategy for testing the hypotheses  $H_0$ ,  $H_1$  and  $H_2$  was to compare the value of  $F_0$  calculated from the ANOVA table to the value of the F-distribution for a significance level of 95% (i.e. 0.05) with the corresponding value of DF(Source) and DF(Error) (i.e.  $F_{(0.05; DF(Source); DF(Error))}$ ). In this way, the tested null hypotheses (i.e.  $H_0$ ,  $H_1$  and  $H_2$ ) associated with each case enumerated in section 2.3 (i.e. cases i, ii and iii) were rejected when:

- i)  $H_0: F_{0-T_P} \geq F_{(0.05; DF(T_P); DF(Error))}$
- ii)  $H_1: F_{0-J_{Offset}} \geq F_{(0.05; DF(J_{Offset}); DF(Error))}$
- iii)  $H_2: F_{0-T_P \cdot J_{Offset}} \geq F_{(0.05; DF(T_P \cdot J_{Offset}); DF(Error))}$

**Table S2.** Summary of the equations used to calculate the different ANOVA parameters.

Source	SS	DF	MS	$F_0$
$T_P$	$SS_{R_v} = \frac{1}{bn} \sum_{i=1}^a y_{i..}^2 - \frac{y_{...}^2}{abn}$	$a-1$	$MS_{R_v} = \frac{SS_{R_v}}{a-1}$	$F_{0-R_v} = \frac{MS_{R_v}}{MS_E}$
$J_{Offset}$	$SS_{V_{HA}} = \frac{1}{an} \sum_{j=1}^b y_{.j.}^2 - \frac{y_{...}^2}{abn}$	$b-1$	$MS_{V_{HA}} = \frac{SS_{V_{HA}}}{b-1}$	$F_{0-V_{HA}} = \frac{MS_{V_{HA}}}{MS_E}$
$T_P \cdot J_{Offset}$	$SS_{R_v \cdot V_{HA}} = \left( \frac{1}{n} \sum_{i=1}^a \sum_{j=1}^b y_{ij.}^2 - \frac{y_{...}^2}{abn} \right) - SS_{R_v} - SS_{V_{HA}}$	$(a-1)(b-1)$	$MS_{R_v \cdot V_{HA}} = \frac{SS_{R_v \cdot V_{HA}}}{(a-1)(b-1)}$	$F_{0-R_v \cdot V_{HA}} = \frac{MS_{R_v \cdot V_{HA}}}{MS_E}$
Error	$SS_E = SS_T - \left( \frac{1}{n} \sum_{i=1}^a \sum_{j=1}^b y_{ij.}^2 - \frac{y_{...}^2}{abn} \right)$	$ab(n-1)$	$MS_E = \frac{SS_E}{ab(n-1)}$	
Total	$SS_T = \sum_{i=1}^a \sum_{j=1}^b \sum_{k=1}^n y_{ijk}^2 - \frac{y_{...}^2}{abn}$	$abn-1$		

**BLANK PAGE**

## CHAPTER 5.

---

### **Bilayered NAA Combined with RfS for Multi-Point Sensing Purposes**

This chapter is based on the following the peer-reviewed article:

**Mahdieh Nemati**, Abel Santos, Dusan Losic. Fabrication and Optimization of Bilayered Nanoporous Anodic Alumina Structures as Multi-Point Sensing Platform, *Sensors*, 18(2) (2018), 470.

**BLANK PAGE**

## Statement of Authorship

Title of Paper	Structural Engineering and Optimization of Bilayered Nanoporous Anodic Alumina Structures as Multi-Point Sensing Platform		
Publication Status	<input checked="" type="checkbox"/> Published	<input type="checkbox"/> Accepted for Publication	<input type="checkbox"/> Unpublished and Unsubmitted work written in manuscript style
	<input type="checkbox"/> Submitted for Publication		
Publication Details			

### Principal Author

Name of Principal Author (Candidate)	Mahdieh Nemati		
Contribution to the Paper	Prepared the first draft of manuscript, edited, and revised the manuscript.		
Overall percentage (%)	85%		
Certification:	This paper reports on original research I conducted during the period of my Higher Degree by Research candidature and is not subject to any obligations or contractual agreements with a third party that would constrain its inclusion in this thesis. I am the primary author of this paper.		
Signature		Date	12.12.2017

### Co-Author Contributions

By signing the Statement of Authorship, each author certifies that:

- i. the candidate's stated contribution to the publication is accurate (as detailed above);
- ii. permission is granted for the candidate to include the publication in the thesis; and
- iii. the sum of all co-author contributions is equal to 100% less the candidate's stated contribution.

Name of Co-Author	Abel Santos		
Contribution to the Paper	Co-supervise, edited, and revised the manuscript.		
Signature		Date	19/12/17

Name of Co-Author	Dusan Losic		
Contribution to the Paper	Supervised the development of the work, edited the manuscript and corresponding author.		
Signature		Date	20/12/2017

Please cut and paste additional co-author panels here as required.





Article

# Fabrication and Optimization of Bilayered Nanoporous Anodic Alumina Structures as Multi-Point Interferometric Sensing Platform

Mahdieh Nemati <sup>1</sup>, Abel Santos <sup>1,2,3</sup> and Dusan Losic <sup>1,\*</sup> 

<sup>1</sup> School of Chemical Engineering, The University of Adelaide, Engineering North Building, Adelaide 5005, Australia; mahdieh.nemati@adelaide.edu.au (M.N.); abel.santos@adelaide.edu.au (A.S.)

<sup>2</sup> Institute for Photonics and Advanced Sensing (IPAS), The University of Adelaide, Adelaide 5005, Australia

<sup>3</sup> ARC Centre of Excellence for Nanoscale BioPhotonics (CNBP), The University of Adelaide, Adelaide 5005, Australia

\* Correspondence: dusan.losic@adelaide.edu.au; Tel.: +61-8-8313-4648

Received: 19 December 2017; Accepted: 31 January 2018; Published: 6 February 2018

**Abstract:** Herein, we present an innovative strategy for optimizing hierarchical structures of nanoporous anodic alumina (NAA) to advance their optical sensing performance toward multi-analyte biosensing. This approach is based on the fabrication of multilayered NAA and the formation of differential effective medium of their structure by controlling three fabrication parameters (i.e., anodization steps, anodization time, and pore widening time). The rationale of the proposed concept is that interferometric bilayered NAA (BL-NAA), which features two layers of different pore diameters, can provide distinct reflectometric interference spectroscopy (RiFS) signatures for each layer within the NAA structure and can therefore potentially be used for multi-point biosensing. This paper presents the structural fabrication of layered NAA structures, and the optimization and evaluation of their RiFS optical sensing performance through changes in the effective optical thickness (EOT) using quercetin as a model molecule. The bilayered or funnel-like NAA structures were designed with the aim of characterizing the sensitivity of both layers of quercetin molecules using RiFS and exploring the potential of these photonic structures, featuring different pore diameters, for simultaneous size-exclusion and multi-analyte optical biosensing. The sensing performance of the prepared NAA platforms was examined by real-time screening of binding reactions between human serum albumin (HSA)-modified NAA (i.e., sensing element) and quercetin (i.e., analyte). BL-NAAs display a complex optical interference spectrum, which can be resolved by fast Fourier transform (FFT) to monitor the EOT changes, where three distinctive peaks were revealed corresponding to the top, bottom, and total layer within the BL-NAA structures. The spectral shifts of these three characteristic peaks were used as sensing signals to monitor the binding events in each NAA pore in real-time upon exposure to different concentrations of quercetin. The multi-point sensing performance of BL-NAAs was determined for each pore layer, with an average sensitivity and low limit of detection of 600 nm (mg mL<sup>-1</sup>)<sup>-1</sup> and 0.14 mg mL<sup>-1</sup>, respectively. BL-NAAs photonic structures have the capability to be used as platforms for multi-point RiFS sensing of biomolecules that can be further extended for simultaneous size-exclusion separation and multi-analyte sensing using these bilayered nanostructures.

**Keywords:** nanoporous anodic alumina; structural fabrication; reflectometric interference spectroscopy; optical sensors; biomolecule detection

## 1. Introduction

There are an increasing number of research studies focused on exploring new nanoporous materials and their applications in highly sensitive chemical and biosensing devices which are cost-effective and more sensitive due to their specific surface areas and the unique properties of their pore structures. Among them, nanoporous anodic alumina (NAA) fabricated by electrochemical anodization has been extensively explored for optical transduction systems in a broad range of sensing applications including biomedical, pharmaceutical, industrial, and environmental [1]. The versatile nanoporous structure of NAA makes it an excellent optical platform to develop sensing devices based on broad ranges of detection principles including UV-Vis, surface plasmon resonance, reflective interference, optical waveguiding, Raman spectroscopy and others [2–4]. NAA pore structures are highly sensitive to any alteration of the effective medium including the binding of molecules, which can be subsequently translated into readable optical signals [5–8]. Reflectometric interference spectroscopy (RiFS) is one of most attractive optical sensing techniques used for development of low cost and simple sensing devices [9–12]. The method is based on interaction of optical platforms and light reflection where reflected light is amplified at specific wavelengths with enhanced reflections, creating characteristic interferometric spectra due to the Fabry-Pérot effect. In NAAs, the Fabry-Pérot effect can be described by Equation (1),

$$EOT = 2n_{\text{eff}} L \cos \theta = m\lambda, \quad (1)$$

where EOT is the effective optical thickness of the NAA film,  $n_{\text{eff}}$  is its effective refractive index,  $L$  is its physical thickness,  $m$  is the order of wavelength oscillation in the spectrum of RiFS,  $\lambda$  is maximum wavelength, and  $\theta$  is the incidence angle of light. This expression can be used to quantify changes in the effective medium of the NAA platform, using effective optical thickness changes ( $\Delta EOT$ ) as the sensing parameter [13]. RiFS using optical platforms were extensively explored by the Gauglitz group and others to detect a broad range of analytes including organic molecules, gases, DNA, pesticides, etc. [14–17].

In contrast to RiFS, systems based on solid optical platforms, the combination of RiFS with nanoporous platforms such as NAA has a set of attractive properties such as a high effective surface area which increases the number of binding centres and effective medium that can be fabricated with precision to create NAA structures with highly sensitive sensing platforms [1,18]. Our previous studies demonstrated that the NAA can be successfully used for the development of highly sensitive RiFS devices for a broad range of applications including organic molecules, enzymes, drugs, cancer cells, etc. [13,19–22]. To advance sensing and optical (RiFS) performance of these NAA platforms many strategies have been employed using structural fabrication methods to optimise pore structures, introduce appropriate surface modifications and design of RiFS sensing devices combining with microfluidics [23,24]. Several studies have demonstrated that the nanoporous structure of NAA can be precisely fabricated by different anodization approaches to generate multi-dimensional photonic crystal structures such as distributed Bragg reflectors and funnel-like photonic films that can significantly improve their sensing performance [25,26]. Marshal's group and others recently demonstrated that funnel-like NAA structures (multi-layered NAA films featuring a decreasing pore diameter from top to bottom) can provide characteristic RiFS properties that could offer new sensing applications [27–30]. It is indicated that bilayered NAA (BL-NAA) nanostructures feature a complex RiFS spectrum, which can be resolved by Fourier transform (FFT) to discern characteristic peaks associated with each layer and be independently utilized to monitor and quantify molecular binding events occurring in each layer within the BL-NAA structure [31–33]. However, more fundamental and applied studies are needed in order to fully understand RiFS characteristics of bi-layered and multi-layered NAA structures and exploit their potential for multi-point and multi sensing applications.

In this study, we fabricated bi-layered NAA films (BL-NAA) with hierarchical funnel-like structures in order to explore their RiFS performances and potential to be used for advance biosensing, including multi-analyte detection. Our fabrication approach consisted of several sequential

anodization and chemical etching steps, which enable the design of bi-layered optical structures with a specific pore diameter and length in depth. It is proposed that fabricated BL-NAA structures will feature three distinct and well-resolved peaks in their FFT spectrum that correspond to each physical layer (top layer I, bottom layer II, and total layer III). These characteristic peaks are proposed for independent molecular sensing inside pores in order to explore their simultaneous size-exclusion and multi analytes detection. Quercetin is a plant flavonoid present in various fruits, vegetables and medicinal herbs [34] that has as antioxidant [35,36] properties with the potential for therapeutic applications such as neuroprotective effect, cardiovascular protection, anti-cancer, and anti-inflammatory properties [37–39]. To achieve selectivity, the surface chemistry was functionalized with human serum albumin (HSA) attached on 3-aminopropyl) trimethoxysilane (APTES) in order to endow these with chemical selectivity towards polyphenol quercetin. Binding events between quercetin and HSA molecules are measured in real-time measurements through changes of effective optical thickness (EOT) of each layer in the FFT spectrum of BL-NAA by reflective interferometric spectroscopy (RIFS), enabling the assessment of the optical sensing performance of BL-NAAs platform. A systematic study analysing the effect of the geometric features of BL-NAA on the sensitivity and low limit of detection was performed in order to determine the limitations and potential of this system for multi-analyte and size-exclusion biosensing.

## 2. Materials and Methods

### 2.1. Materials

High purity (99.9997%) aluminum foils (Al) 0.32 mm thick were supplied by Goodfellow Cambridge Ltd. (Huntingdon, UK). Oxalic acid ( $C_2H_2O_4$ ), perchloric acid ( $HClO_4$ ), phosphoric acid ( $H_3PO_4$ ), chromic acid ( $H_2CrO_4$ ), (3-aminopropyl)trimethoxysilane (APTES), hydrogen peroxide ( $H_2O_2$ ), glutaraldehyde ( $CH_2(CH_2CHO)_2$ —GTA), sodium hydroxide (NaOH), human serum albumin (HSA), quercetin ( $C_{15}H_{10}O_7$ ), and phosphate buffer saline (PBS) were purchased from Sigma-Aldrich (Australia). Ultrapure water from Option Q—Purelabs (Australia) was used for preparing the aqueous solutions used in this study.

### 2.2. Fabrication of Bilayered NAA Films (BL-NAAs) and NAAs

Al samples were anodized in an electrochemical cell by a multiple step anodization process. Al samples were first sonicated in ethanol to remove organic residue and electrochemically polished in a mixture of EtOH:  $HClO_4$  4:1 (v:v) at 20 V and 5 °C for 3 min to achieve a smooth surface. The first anodization step was performed in a solution of 0.3 M  $H_2C_2O_4$  at 40 V and 5 °C for 20 h. After that, the NAA structure was etched in an aqueous solution of 0.2 M  $H_2CrO_4$  and 0.4 M  $H_3PO_4$  at 70 °C for 3 h. Two anodization steps were carried out using 0.3 M  $H_2C_2O_4$  at 40 V and 5 °C for different duration. The fabrication protocol for each BL-NAA platform is detailed in Table 1. A pore widening treatment between anodization steps was used to increase the diameter of the nanopores. This process was carried out by wet chemical etching in an aqueous solution of  $H_3PO_4$  5 wt. % at 35 °C for 15 min (Table 1). Figure 1 shows a generic illustration of the fabrication process used to produce BL-NAA. We fabricated two control NAAs wer under the same anodization conditions featuring straight nanopores from top to bottom at 0 and 15 in of pore widening treatment (Table 1).

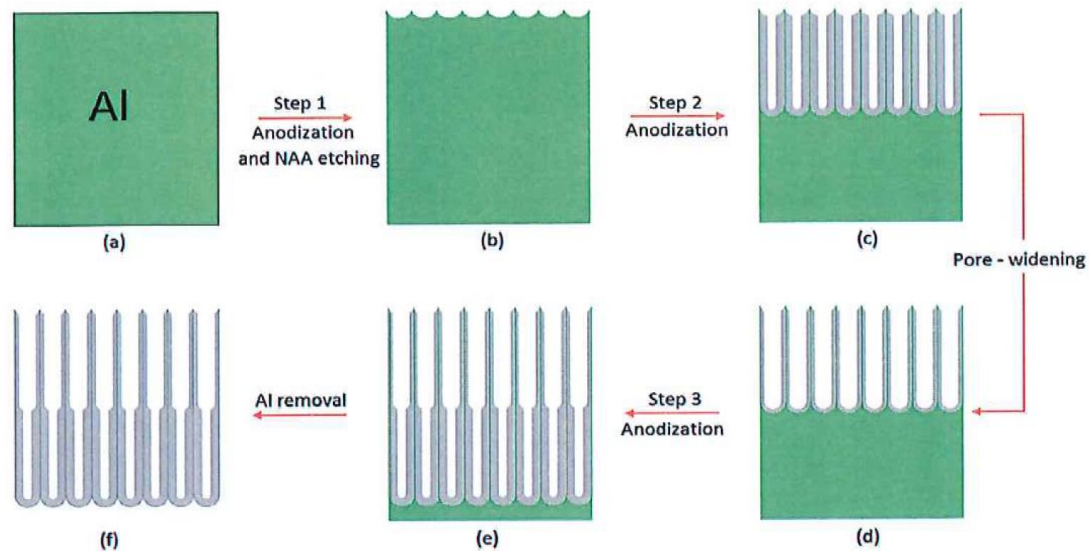


**Figure 1.** Fabrication process of interferometric bilayered nanoporous anodic alumina (BL-NAA) structures. (a) Electro polished high purity aluminum; (b) First step of anodization and resulting chemically etched nanostructure; (c) Second step of anodization results top layer of BL-NAAs; (d) Pore-widening leads to nanopores with a larger pore diameter; (e) Third step of anodization results in the bottom layer of the nanopore structure which has a smaller pore diameter compared to top layer; (f) Supporting aluminum was removed from the backside of platform. \* Note that, stage (e) was not included for nanoporous anodic alumina (NAAs) fabrication.

**Table 1.** Fabrication protocol of BL-NAAs and NAAs that combines anodization and pore widening steps (BL-NAA<sub>(25/75)</sub> represent ratio in lengths of pore layers with 25% top layer with larger pore diameters and 75% of layer with layer with smaller pore diameters, BL-NAA<sub>(50/50)</sub> with equal length of both layers and the BL-NAA<sub>(75/25)</sub> structure with 75% top layer with larger pore diameters and 25% of layer with layer with smaller pore diameters, and NAA<sub>(1)</sub> with uniform structures with large pore diameters and NAA<sub>(2)</sub> with smaller pore diameters.)

Anodized Anodic Aluminum Platforms		Step (1) Anodization (h)	Step (2) Anodization (h)	Pore Widening (min)	Step (3) Anodization (h)
NAAF	BL-NAA <sub>(25/75)</sub>	20	3	15	6
	BL-NAA <sub>(50/50)</sub>	20	4.5	15	4.5
	BL-NAA <sub>(75/25)</sub>	20	6	15	3
NAA	NAA <sub>(1)</sub>	20	9	15	N/A <sup>1</sup>
	NAA <sub>(2)</sub>	20	9	N/A <sup>1</sup>	N/A <sup>1</sup>

<sup>1</sup> N/A: Not applied.

### 2.3. Surface Chemistry Functionalization of BL-NAAs and NAAs

The fabricated BL-NAAs and NAAs were chemically functionalized with APTES following a well-established protocol [1,40]. In brief, hydroxyl groups were created on the inner surface of BL-NAAs and NAAs by immersion in 30 wt. % H<sub>2</sub>O<sub>2</sub> at 90 °C over 15 min. After that, silane molecules were immobilized onto the inner surface of BL-NAA nanopores by chemical vapor deposition method. This process was carried out under vacuum condition at 135 °C for 3 h. Finally, BL-NAAs and NAAs were coated with an ultrathin gold film (i.e., 5 nm) deposited by a sputter coater (sputter coater 108auto, Cressington, Redding, CA, USA) in order to enhance the light interference as reported elsewhere [41].

#### 2.4. Optical Sensitivity Assessment of BL-NAAs and NAAs by RIFS

The sensing performance of BL-NAAs and NAAs was assessed by measuring changes of the EOT in each optical layer using quercetin as a sensing agent model to establish the sensing parameters including sensitivity ( $S$ ), linearity ( $R^2$ ), and low limit of detection ( $LOD$ ). These sensing parameters were estimated by measuring shifts in the EOT of each layer according to Equation (1).

Real-time screening of EOT shifts was performed using a RIFS system combined with a cell flow system. The APTES functionalized BL-NAAs and NAAs were placed into the flow cell, where phosphate buffer saline (PBS) was allowed to flow until a stable baseline was achieved. In order to immobilize HSA onto the surface, 2.5% glutaraldehyde was used as a cross-linker and flowed through the system for 30 min over BL-NAAs and NAAs. GTA molecules activate the amine functional group ( $-NH_2$ ) of APTES molecules inside nanopores of BL-NAAs and NAAs.

PBS was flowed again for 15 min to wash non-covalent bound of GTA molecules. After this,  $1 \text{ mg mL}^{-1}$  human serum albumin (HSA) solution was allowed to flow through the system for 1.5 h in order to immobilize HSA onto the inner surface of BL-NAA and NAAs. Next, PBS solution was allowed to flow for 15 min to remove physisorbed HSA molecules. After that, analytical solutions of the analyte agent, quercetin, with different concentrations (i.e., 0.05, 0.125, 0.25, 0.375, 0.5, 1 mM) were allowed to flow through the system until a stable line was achieved confirming that all HSA molecules were saturated with quercetin. Finally, PBS solution was let flow to establish the total EOT changes associated to HSA-Quercetin binding. Note that, this process was carried out at pH 7.5 and room temperature.

#### 2.5. Structural Characterization of BL-NAAF and NAAs

The structural characteristics of the prepared BL-NAAs and NAAs (top and fractured structures) were established by field emission scanning electron microscopy (FEG-SEM FEI Quanta 450, ThermoFisher Scientific, OR, USA). Imaging was performed at least on four different spots for each sample in order to probe the reproducibility of process and uniformity of the fabricated structures.

### 3. Results and Discussion

#### 3.1. Structural Characterisation of Prepared BL-NAAs and NAAs

The morphology of BL-NAAs prepared using different anodization conditions to make materials with different thicknesses and pore diameters of each layer and control NAAs structures (with single pore layer) characterized by SEM are presented in Figure 2 for BL-NAAs and in the supplementary information for the control NAAs structures. A representative top view SEM image of BL-NAAs confirmed the same pore shape and uniform pore size on the surface for BL-NAA<sub>(25/75)</sub>, BL-NAA<sub>(50/50)</sub>, BL-NAA<sub>(75/25)</sub>, NAA<sub>(1)</sub>, and NAA<sub>(2)</sub> (supplementary information). Table 2 shows the overall pore dimensions of BL-NAAs and NAAs structures. The pore diameters of the top layer for BL-NAA<sub>(25/75)</sub>, BL-NAA<sub>(50/50)</sub>, BL-NAA<sub>(75/25)</sub>, NAA<sub>(1)</sub> generated by anodization and pore widening process was confirmed to be about 55 nm and similar for all samples. The pore diameters of NAA<sub>(2)</sub> prepared only by the anodization process are 45 nm in size and the bottom layer pore sizes were confirmed by cross-sectional imaging. Cross-sectional images of BL-NAA revealed two stack layers of cylindrical and vertical ordered nanostructures, the top layer with larger and the bottom layer with smaller pore diameters was confirmed by a series of SEM images (Figure 2f). The series of cross section images with different magnifications showed three different types of bi-layered structures with thicknesses of  $30 \pm 1.5$  to  $32 \pm 1.6 \mu\text{m}$  and different length of top and bottom layers. The length of the top nanoporous layer was  $9 \pm 0.45 \mu\text{m}$  for BL-NAA<sub>(25/75)</sub>,  $15 \pm 0.75 \mu\text{m}$  for BL-NAA<sub>(50/50)</sub> and  $22 \pm 1.1 \mu\text{m}$  for BL-NAA<sub>(75/25)</sub>. Consequently, the length of the bottom layer was determined as  $22 \pm 1.1 \mu\text{m}$  for BL-NAA<sub>(25/75)</sub>,  $15 \pm 0.75 \mu\text{m}$  for BL-NAA<sub>(50/50)</sub>, and BL-NAA<sub>(75/25)</sub>,  $10 \pm 0.5 \mu\text{m}$ . Table 2 summarized the nanopore dimensions for BL-NAAs. It is observed that the bottom layers have smaller pore diameters which caused funnel like bi-layered structures. The bottom layers of nanostructures,

BL-NAA<sub>(25/75)</sub>, BL-NAA<sub>(50/50)</sub>, BL-NAA<sub>(75/25)</sub> all showed a 45 nm pore diameter. The results of the SEM characterization can be explained due to the fact that the top layer formation of the bilayered structures occurred during the second step of anodization and the second step of anodization is responsible for bottom layer fabrication. It is also understood that the pore-widening process is the main reason that differences arise in pore diameters between the top layer and bottom layer which forms a funnel like structure. This was clearly proved where the control NAA<sub>(1)</sub> and control NAA<sub>(2)</sub> platforms revealed a single layer of nanostructure when one step of anodization and pore-widening process was eliminated.

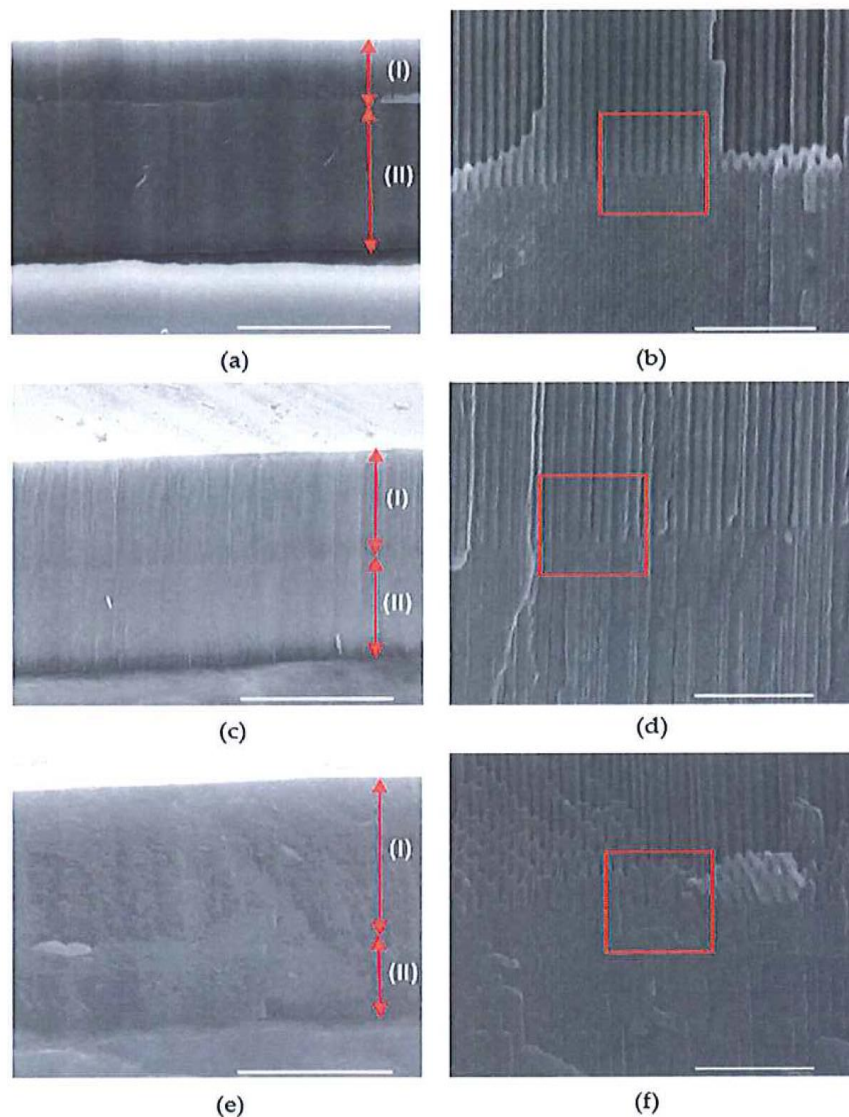


**Figure 2.** Scanning electron microscopy (SEM) structural characterization of fabricated BL-NAAs showing the length of pore layers and pore diameters. (a) Cross-section view of BL-NAA<sub>(25/75)</sub>, scale bar is 20  $\mu\text{m}$ . (b) Cross-section view of BL-NAA<sub>(25/75)</sub>, scale bar is 1  $\mu\text{m}$ . (c) Cross-section view of BL-NAA<sub>(50/50)</sub>, scale bar is 20  $\mu\text{m}$ . (d) Cross-section view of BL-NAA<sub>(50/50)</sub>, scale bar is 1  $\mu\text{m}$ . (e) Cross-section view of BL-NAA<sub>(75/25)</sub>, scale bar is 20  $\mu\text{m}$ . (f) Cross-section view of BL-NAA<sub>(75/25)</sub>, scale bar is 1  $\mu\text{m}$ .

**Table 2.** Pore dimensions of BL-NAAs and NAAs structures.

Anodized Anodic Aluminum Platforms		Top Layer Thickness ( $\mu\text{m}$ )	Bottom Layer Thickness ( $\mu\text{m}$ )	Nanopore thickness ( $\mu\text{m}$ )	Pore Diameter (Top/Bottom Layer) (nm)
NAAF	BL-NAA <sub>(25/75)</sub>	9 $\pm$ 0.45	22 $\pm$ 1.1	30 $\pm$ 1.5	55 $\pm$ 2.75/45 $\pm$ 2.25
	BL-NAA <sub>(50/50)</sub>	15 $\pm$ 0.75	15 $\pm$ 0.75	30 $\pm$ 1.5	55 $\pm$ 2.75/45 $\pm$ 2.25
	BL-NAA <sub>(75/25)</sub>	22 $\pm$ 1.1	10 $\pm$ 0.5	32 $\pm$ 1.6	55 $\pm$ 2.75/45 $\pm$ 2.25
NAA	NAA <sub>(1)</sub>	N/A <sup>1</sup>	N/A <sup>1</sup>	22 $\pm$ 1.1	55 $\pm$ 2.75
	NAA <sub>(2)</sub>	N/A <sup>1</sup>	N/A <sup>1</sup>	23.5 $\pm$ 1.17	45 $\pm$ 2.25

<sup>1</sup> N/A: Not applicable.

### 3.2. Characterization and Optimization of RIfS Signals from BL-NAAs and NAAs Platforms

As confirmed by SEM images, BL-NAA platforms feature a bilayered structure with larger pore diameters from the top, 55 nm, to smaller pore diameter at the bottom, 45 nm, with three different thicknesses of top and bottom layers. The fast Fourier transform (FFT) spectra of BL-NAAs, generated from optical interference pattern (see details of optical interference pattern in Supplementary Information), demonstrated more complex patterns than NAAs with a single layer structure. Figure 3 summarizes the FFT spectra of five different NAA structures analyzed in this study, including BL-NAA<sub>(25/75)</sub>, BL-NAA<sub>(50/50)</sub>, BL-NAA<sub>(75/25)</sub>, NAA<sub>(1)</sub>, and NAA<sub>(2)</sub>. FFT spectra from BL-NAA<sub>(25/75)</sub>, BL-NAA<sub>(50/50)</sub>, BL-NAA<sub>(75/25)</sub> (Figure 3a–c) feature three characteristic peaks with specific EOT with diverse FFT intensities that are used for sensing in this work. As can be seen, three peaks for BL-NAA<sub>(25/75)</sub> are observed at EOT<sub>(I)</sub> = 38,000  $\pm$  1900 nm, EOT<sub>(II)</sub> = 59,000  $\pm$  2950 nm, and EOT<sub>(III)</sub> = 95,000  $\pm$  4750 nm, BL-NAA<sub>(50/50)</sub> showed EOT<sub>(I)</sub> = 59,000  $\pm$  2950 nm, EOT<sub>(II)</sub> = 61,000  $\pm$  3050 nm, and EOT<sub>(III)</sub> = 120,000  $\pm$  6000 nm, BL-NAA<sub>(75/25)</sub> also showed EOT<sub>(I)</sub> = 38,000  $\pm$  1900 nm, EOT<sub>(II)</sub> = 71,000  $\pm$  3550 nm, and EOT<sub>(III)</sub> = 107,000  $\pm$  5350 nm. FFT peaks for EOT<sub>(I)</sub>, EOT<sub>(II)</sub>, and EOT<sub>(III)</sub> correspond to the top, bottom, and total layers within the structure of BL-NAA platforms with three levels of light reflection. This result is in agreement with previous studies showing similar optical responses [32]. This phenomenon can be readily used to achieve unique sensing capabilities associated with EOT changes of each of these three peaks. In contrast to BL-NAAs, NAA<sub>(1)</sub> and NAA<sub>(2)</sub> showed a single peak in their FFT spectra, which is associated with the EOT of the nanoporous film (Figure 3d,e). Detection of quercetin using HSA-modified BL-NAAs and NAAs through RIfS was used to demonstrate the sensitivity of these optical platforms across all three optical layers. In this process, the EOT change obtained by applying FFT was used as sensing parameter to monitor in real-time the binding events occurring in each of the sensing layers.

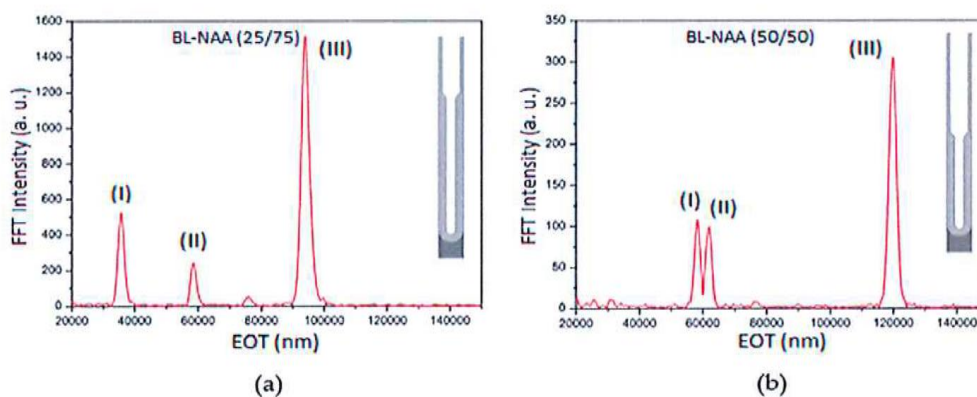


**Figure 3.** Cont.

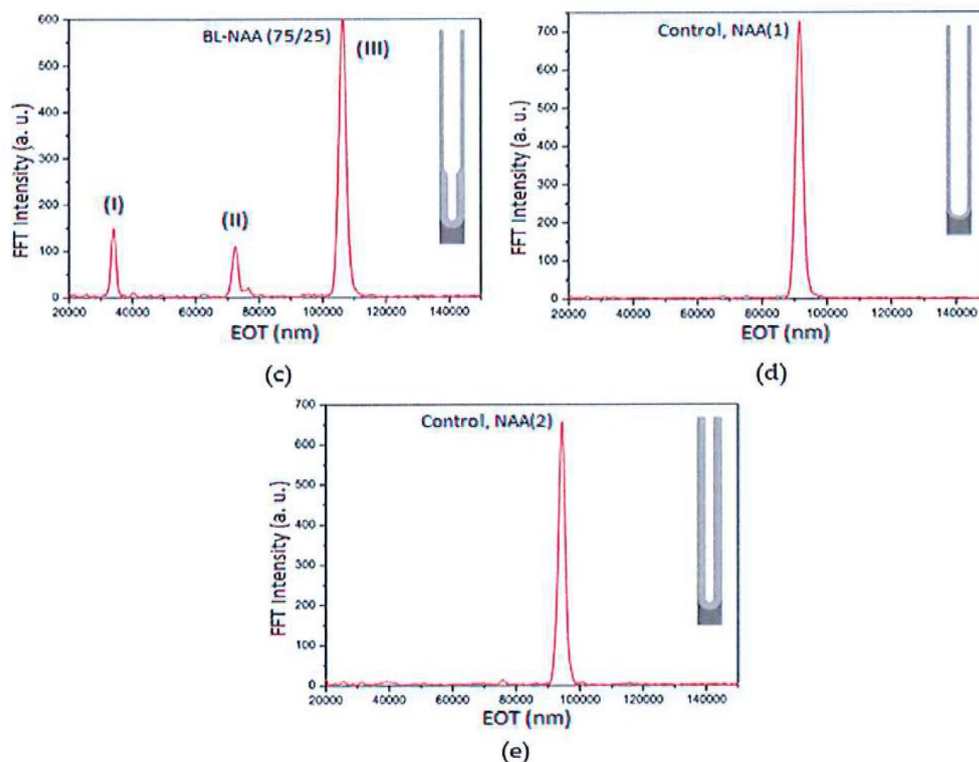


**Figure 3.** Comparison of FFT spectra of BL-NAAFs and NAAs with single layer and bilayer of nanoporous alumina structure. (a) Bi-layer structured of BL-NAA<sub>(25/75)</sub> produced during (Step1 = 20 h, step 2 = 3 h, 15 min pore widening, and step 3 = 6 h with no further pore widening), resulted in three optical peaks including (I), (II), and (II) various light reflection properties (e.g., FFT intensity and effective optical thickness); (b) Bi-layer structured of BL-NAA<sub>(50/50)</sub> produced during (Step 1 = 20 h, step 2 = 4.5 h, 15 min pore widening, and step 3 = 4.5 h with no further pore widening), resulted in three optical peaks including (I), (II), and (II) various light reflection properties (e.g., FFT intensity and effective optical thickness); (c) Bi-layer structured of BL-NAA<sub>(75/25)</sub> produced during (Step 1 = 20 h, step 2 = 6 h, 15 min pore widening, and step 3 = 3 h with no further pore widening), resulted in three optical peaks including (I), (II), and (II) various light reflection properties (e.g., FFT intensity and effective optical thickness). (d,e) Single-layer of control NAA<sub>(1)</sub>, and control NAA<sub>(2)</sub> with a unique FFT.

### 3.3. The Evaluation of BL-NAA and NAA Sensing Platforms for Biomolecules Sensing

Figure 4 illustrates the proposed molecular distribution and binding reaction of sensing molecules inside larger and smaller pores of BL-NAA and continuous RfS signals ( $\Delta$ EOT as the sensing parameter) obtained during different stages of our study to assess the sensing performance of BL-NAA platforms. This sensing process is based on real-time monitoring of EOT of each corresponding nanoporous layers that were monitored through all steps from the fabrication of sensing surface to final sensing of analyte molecules (Figure 4b). The following steps are observed in the figure including (i) amine ( $-NH_2$ ) group activation by GTA; (ii) HSA functionalization of inner surface of BL-NAAs and NAAs; and (iii) quercetin binding reaction to HSA. Changes of EOT were observed during GTA, HSA and quercetin flow into the system which means the binding reaction between the molecules and the inner surface of BL-NAAs. Finally, sensing of quercetin molecules revealed stable and higher EOT where all HSA molecules are saturated and no further binding reaction occurred showing the sensing capabilities of this system.



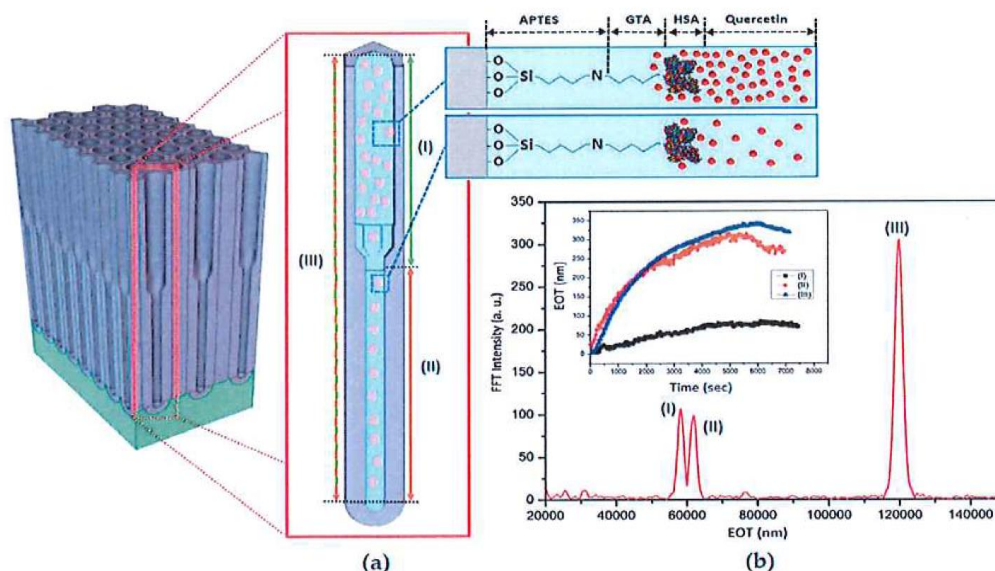


**Figure 4.** The proposed RIfS sensing concept using BL-NAAs platforms showing changes of EOT signals during surface modification and the preparation of sensing layer (HSA) and sensing analyte molecules (quercetin) showing the binding activity between HSA-modified pore surface and quercetin. (a) Schematic illustration of binding event between HSA and quercetin in the environment of fresh PBS (pH = 7.5) in the top and bottom pore layer. BL-NAAs and NAAs were modified with silane molecules before subjecting them to real-time monitoring process; (b) typical FFT spectra of BL-NAA<sub>(50/50)</sub> showing 3 distinguished peaks that are related to two pore layers and used for sensing showing time response RIfS signal that present EOT measurement quercetin (0.375 mM) binding activity in all 3 optical layers simultaneously.

The obtained results for  $\Delta EOT$  for each analytical solution of quercetin (0.05, 0.125, 0.25, 0.375, 0.5, and 1 mM) using BL-NAAs with different layer thicknesses and control NAAs are displayed and summarized in Figures 5–8 and Table 3. The calculation of linear fitting lines between  $\Delta EOT$  and the concentration of quercetin was used to estimate the sensitivity,  $S$  which is the slope of the fitting lines, the low limit of detection, LLOD which is calculated as  $3\sigma$  according the Equation (2), and the linearity,  $R^2$  which is the correlation coefficient of the fitting line, for each BL-NAA and NAA (Table 3).

$$LLOD = 3\sigma = 3.3 \text{ standard error} \div \text{slope} \quad (2)$$

Figure 5 presents the  $\Delta EOTs$  of BL-NAA<sub>(25/75)</sub> platform with a funnel-like structure consisting of a shorter top layer of large pore diameter (Figure 5a) and a longer bottom layer featuring a smaller pore diameter obtained from the top layer I and combined top and bottom layer (Figure 5d). Generally, the  $\Delta EOT_{(III)}$  signal from combined top and bottom layer (optical layer 3) showed higher values compared to  $\Delta EOT_{(I)}$  taken from the first layers. The  $\Delta EOT_{(I)}$  and  $\Delta EOT_{(III)}$  were calculated with maximum changes of 300 nm and 450 nm, respectively and were obtained for the highest concentration of quercetin 1 mM (Figure 5a,d). Notice that the  $\Delta EOT_{(II)}$  measurement from the bottom layer is not included during investigation of this type of BL-NAA platform due to the lack of sufficient optical efficiency of the bottom layer of the BL-NAA<sub>(25/75)</sub> platform which caused failure in the EOT screening. Calibration graphs also showed that the  $\Delta EOT$  has a linear dependence with quercetin concentrations (Figure 5b,e). Comparative calibration graphs (Figure 5b vs. 5e) also showed a higher precision of measurement taken from optical layer III evidenced by the correlation factors  $R^2$  BL-NAA<sub>(25/75)</sub> (I) = 0.922 and BL-NAA<sub>(25/75)</sub> (III) = 0.948 (Table 3). It is seen that layer (III), has a

smaller dispersion around the fitting line compared to layer (I), indicating a stronger linear relationship of layer (III) than layer (I) (Figure 5b,e). The sensing performance evaluation of BL-NAA<sub>(25/75)</sub> resulted in values of  $S_{(I)} = 378 \pm 48 \text{ (nm mM}^{-1}\text{)}$  and  $S_{(III)} = 418 \pm 43 \text{ (nm mM}^{-1}\text{)}$  for BL-NAA<sub>(25/75)</sub> (I) and BL-NAA<sub>(25/75)</sub> (III), respectively. These results showed both optical layer (I) and optical layer (III) acted as highly sensitive sensing areas with the ability of  $LLOD_{(I)} = 0.034 \text{ mM}$  and  $LLOD_{(III)} = 0.074 \text{ mM}$  quercetin detection.

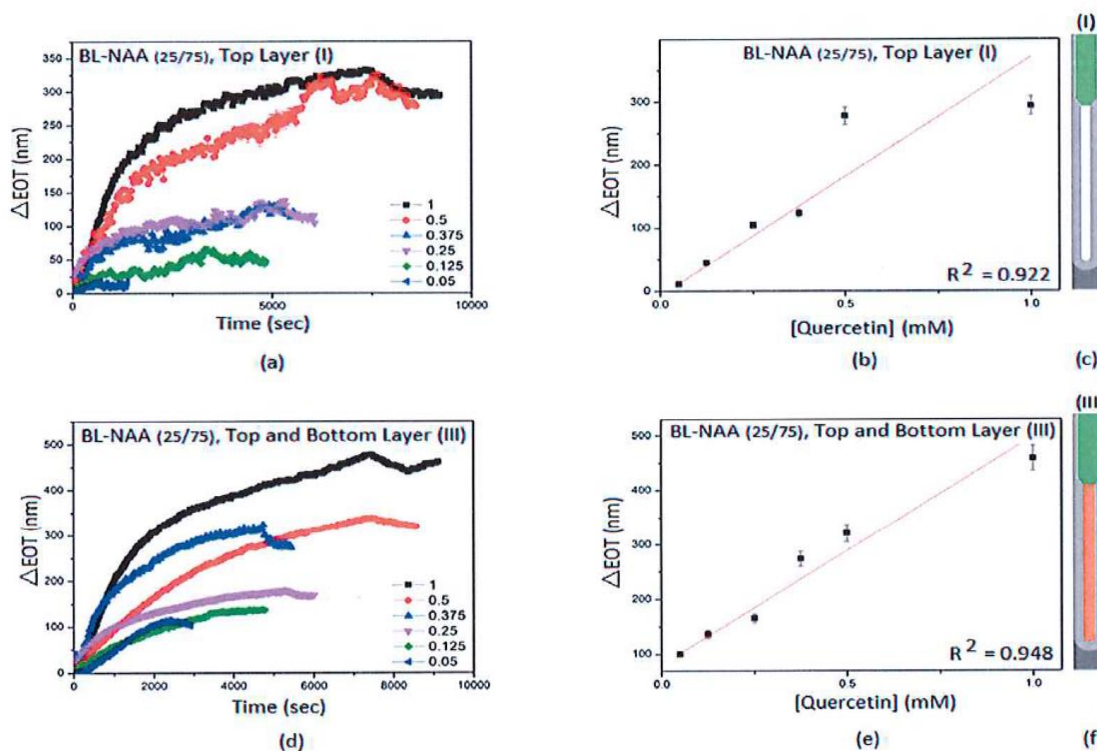


**Figure 5.** Time response curves showing effective optical thickness (EOT) changes and Linear fitting line for BL-NAA<sub>(25/75)</sub> (funnel structure with shorter top layer with large pore diameters and longer bottom layer with smaller pore diameters) sensing platforms measured by RIFS as a function of the quercetin concentration (0.05, 0.125, 0.25, 0.375, 0.5, and 1 mM). (a)  $\Delta EOT_{(I)}$  generated from the top structural layer of the BL-NAA<sub>(25/75)</sub> platform; (b) Linear fitting line for BL-NAA<sub>(25/75)</sub> between  $\Delta EOT_{(I)}$  and the different concentrations of quercetin (0.05, 0.125, 0.25, 0.375, 0.5, and 1 mM); (c) Scheme of the representative optical layer as a function of  $\Delta EOT_{(I)}$  assessment; (d)  $\Delta EOT_{(III)}$  generated from the top and bottom nanoporous structure of the BL-NAA<sub>(25/75)</sub> platform; (e) Linear fitting line for BL-NAA<sub>(25/75)</sub> between  $\Delta EOT_{(III)}$  and the different concentration of quercetin (0.05, 0.125, 0.25, 0.375, 0.5, and 1 mM). (f) Scheme of representative optical layer as a function of  $\Delta EOT_{(III)}$  assessment.

Figure 6 summarizes the response time graphs of  $\Delta EOTs$  of BL-NAA<sub>(50/50)</sub> platform (funnel structure equal length of top layer of large diameters and longer layer with smaller pore diameters) obtained from layer (I), layer (II), and layer (III) using a series of standard quercetin concentrations. These results were used to make corresponding calibration curves with schematic illustrations of a singular nanopore structure highlighting layer (I) in green color, layer (II) in orange color and layer (III) in green/orange color used for sensing in each graph. The time response graphs, for each optical layer (The  $\Delta EOT_{(I)}$ ,  $\Delta EOT_{(II)}$  and  $\Delta EOT_{(III)}$ ) showed different values for the maximum concentration of quercetin (1 mM) starting from 120 nm, 270 nm, and 420 nm, respectively, (Figure 6a,d,g) indicating

a different sensitivity for each layer. The sigmoidal curve fitting shows that the  $\Delta EOT$  has a sigmoidal dependence with the concentration of quercetin (Figure 6b,e,h). However, there are linear correlations amongst quercetin concentrations (i.e., 0.25, 0.375, and 0.5 mM). The dispersion of those data points represents similar  $R^2$  values of the top layer (I), bottom layer (II) and top and bottom layer (III) which are BL-NAA<sub>(50/50)</sub> (I) = 0.943, BL-NAA<sub>(50/50)</sub> (II) = 0.912, and BL-NAA<sub>(50/50)</sub> (III) = 0.942 (Table 3). The sensing performance of BL-NAA<sub>(50/50)</sub>, evaluated by sensitivity graphs, showed values of  $S_{(I)} = 389 \pm 66$  (nm mM<sup>-1</sup>),  $S_{(II)} = 462 \pm 70$  (nm mM<sup>-1</sup>), and  $S_{(III)} = 1207 \pm 208$  S (nm mM<sup>-1</sup>) for BL-NAA<sub>(50/50)</sub> (I), BL-NAA<sub>(50/50)</sub> (II) and BL-NAA<sub>(50/50)</sub> (III), respectively which suggest optical layer (III) acted as a highly sensitive sensing area, and optical layer (I) and (II) did not act as high sensitive sensing areas. Optical layer (I) was the least sensitive when compared to two other optical layers.  $LLOD_{(I)} = 0.148$  mM,  $LLOD_{(II)} = 0.1$  mM, and  $LLOD_{(III)} = 0.168$  mM were evaluated for the limit of quercetin detection. The sensitivity of optical layer III compared with results of the funnel with a shorter top layer significantly decreased from  $S_{(III)} = 1207 \pm 208$  to  $S_{(III)} = 418 \pm 43$  S (nm mM<sup>-1</sup>).

Figure 7 summarizes response time graphs of  $\Delta EOT$ s based on BL-NAA (75/25), platform (funnel structure with longer thickness of top layer of large diameters and shorter layer with smaller pore diameters) obtained from layer (I), layer (II), and layer (III) using BL-NAA (50/50), and a series of standard quercetin concentrations. The pertinent calibration curves are shown of  $\Delta EOT$  and quercetin concentrations, with schematic illustrations of the singular nanopore structure highlighting layer (I) in green color, layer (II) in orange color and layer (III) in green/orange color. According to the results, the  $\Delta EOT_{(I)}$ ,  $\Delta EOT_{(II)}$ , and  $\Delta EOT_{(III)}$  obtained from the highest quercetin concentrations showed maximum changes of 100 nm, 370 nm, and 460 nm, respectively (Figure 7a,d,g) which suggests the highest sensitivity for optical layer III. The calibration graph shows that  $\Delta EOT$  has linear dependence with the all concentration of quercetin of layer (I) (Figure 7b). However, there is a sigmoid correlation with the concentrations of the quercetin of layer (II) and layer (III) (Figure 7e,h). The dispersion of data points around the fitting curves for  $\Delta EOT_{(I)}$   $\Delta EOT_{(II)}$  represents a strong correlation between the top layer (I) and bottom layer (II). Evidenced by the calculated  $R^2$  are BL-NAA<sub>(75/25)</sub> (I) = 0.841, BL-NAA<sub>(75/25)</sub> (II) = 0.857, and BL-NAA<sub>(75/25)</sub> (III) = 0.793, presented in Table 3.

The evaluated sensing performance of BL-NAA<sub>(75/25)</sub> gave values  $S_{(I)} = 107 \pm 26$  (nm mM<sup>-1</sup>),  $S_{(II)} = 884 \pm 245$  (nm mM<sup>-1</sup>) and  $S_{(III)} = 670 \pm 227$  S (nm mM<sup>-1</sup>) for BL-NAA<sub>(75/25)</sub> (I), BL-NAA<sub>(75/25)</sub> (II) and BL-NAA<sub>(75/25)</sub> (III), respectively. These results showed that optical layers (III) and (II) acted as highly sensitive sensing areas, and that optical layer (I) did not act as a high sensitive sensing area.  $LLOD_{(I)} = 0.179$  mM,  $LLOD_{(II)} = 0.160$  mM and  $LLOD_{(III)} = 0.256$  mM are evaluated for the limit of quercetin detection.

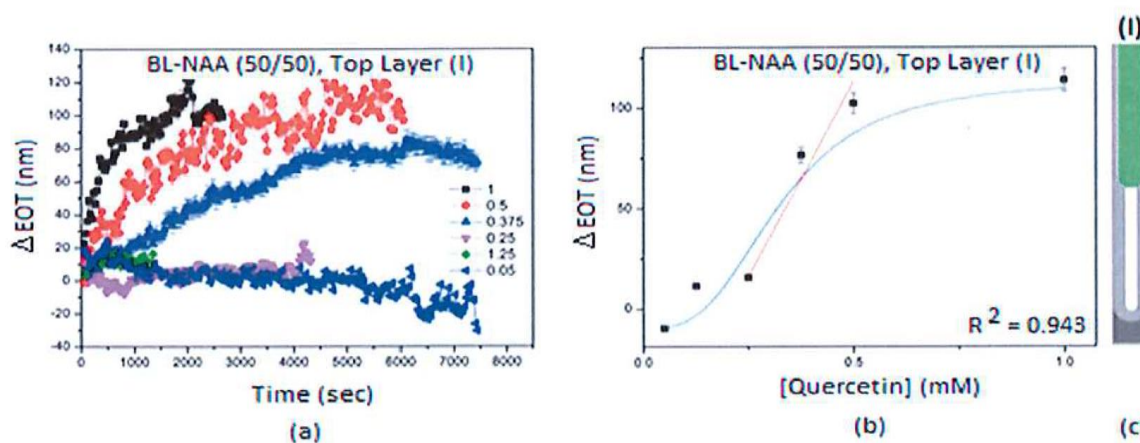
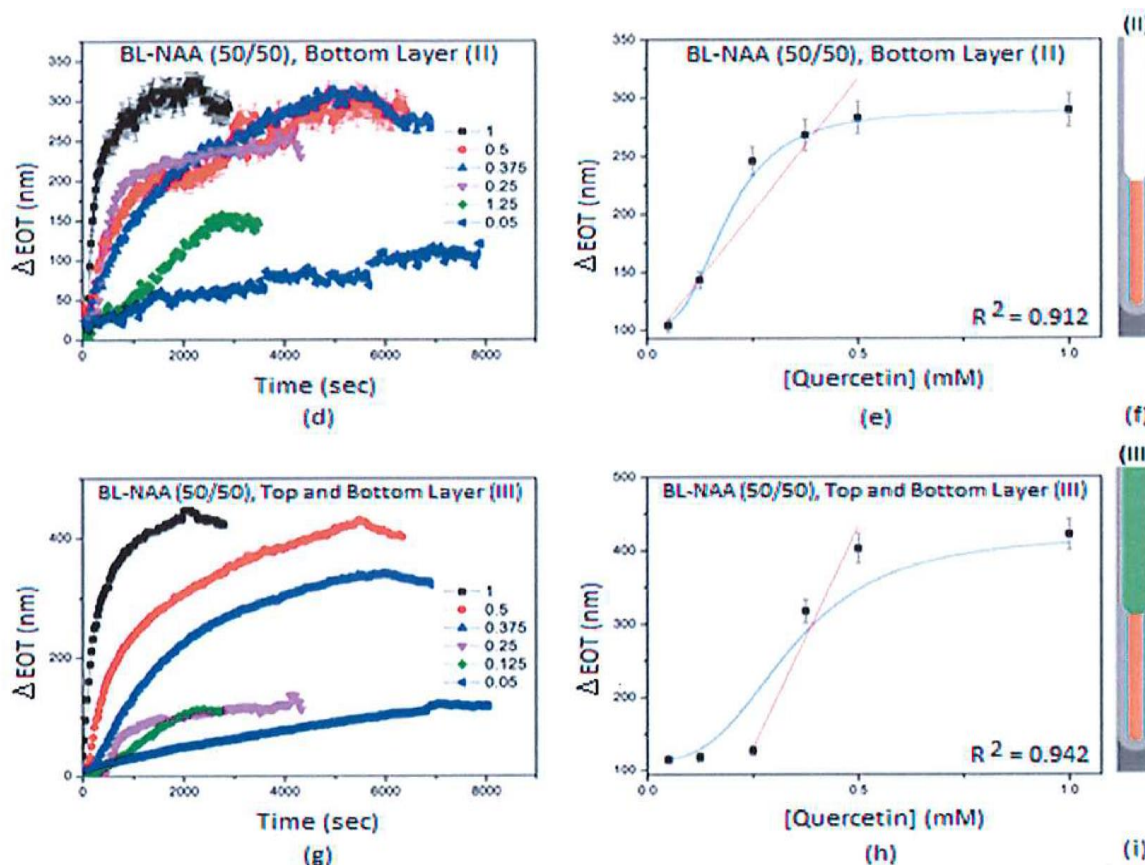


Figure 6. Cont.



**Figure 6.** Time response curve showing effective optical thickness changes and sigmoidal curve fitting for BL-NAA<sub>(50/50)</sub> (funnel structure with equal top layer with large diameters and bottom layer with smaller pore diameters) sensing platforms measured by RIfS as a function of quercetin concentration (0.05, 0.125, 0.25, 0.375, 0.5, and 1 mM). (a)  $\Delta EOT_{(I)}$  generated from the top structural layer of the BL-NAA<sub>(50/50)</sub> platform; (b) Sigmoid fit (blue) and the linear fit (red) for BL-NAA<sub>(50/50)</sub> between  $\Delta EOT_{(I)}$  and the different concentration of quercetin (0.05, 0.125, 0.25, 0.375, 0.5, and 1 mM) are presented; (c) Scheme of representative optical layer as a function of  $\Delta EOT_{(I)}$  assessment; (d)  $\Delta EOT_{(II)}$  generated from the bottom structural layer of the BL-NAA<sub>(50/50)</sub> platform; (e) Sigmoid fit (blue) and the linear fit (red) for BL-NAA<sub>(50/50)</sub> between  $\Delta EOT_{(II)}$  and the different concentration of quercetin (0.05, 0.125, 0.25, 0.375, 0.5, and 1 mM) are presented; (f) Scheme of representative optical layer as a function of  $\Delta EOT_{(II)}$  assessment; (g)  $\Delta EOT_{(III)}$  generated from the top and bottom nanoporous structure of BL-NAA<sub>(50/50)</sub> platform; (h) Sigmoid fit (blue) and the linear section (red) for BL-NAA<sub>(50/50)</sub> between  $\Delta EOT_{(III)}$  and the different concentration of quercetin (0.05, 0.125, 0.25, 0.375, 0.5, and 1 mM) are presented; (i) Scheme of representative optical layer as a function of  $\Delta EOT_{(III)}$  assessment.

Figure 8 summarizes response time  $\Delta EOT$ s graphs based on the single layer of NAA<sub>(1)</sub> and NAA<sub>(2)</sub>, used as control corresponding to calibration graphs and schematic illustrations of the singular nanopore structure highlighted in brown color. According to the results,  $\Delta EOT$  of NAA<sub>(1)</sub> shows higher values compared to  $\Delta EOT$  of NAA<sub>(2)</sub> (Figure 8a,d). These graphs also show that  $\Delta EOT$ s have a sigmoid dependence with the concentration of quercetin (Figure 8b,e). The dispersion of data points around the curve for the  $\Delta EOT$  of NAA<sub>(1)</sub> represents a stronger correlation compared with the  $\Delta EOT$  for NAA<sub>(2)</sub>, evidenced by  $R^2$  0.946 for NAA<sub>(1)</sub> and 0.799 for NAA<sub>(2)</sub> (Table 3). The sensing performance evaluation of NAA<sub>(1)</sub> resulted in a value of  $S = 842 \pm 139$  (nm mM<sup>-1</sup>). These results showed that

the single optical layer of  $NAA_{(1)}$  acted as a highly sensitive sensing platform.  $LLOD = 0.188$  mM of  $NAA_{(1)}$  is evaluated for the limit of quercetin detection. The sensing performance evaluation of  $NAA_{(2)}$  resulted in a value of  $S = 521 \pm 174$  (nm  $mM^{-1}$ ). These results showed the single optical layer of  $NAA_{(2)}$  did not act as a highly sensitive sensing platform. The  $LLOD = 0.449$  mM of  $NAA_{(2)}$  was evaluated for the limit of quercetin detection. Control  $NAA_{(1)}$  showed a higher level of sensitivity which means a larger pore diameter can affect the sensing performance.

The obtained sensitivity results of the overall optical sensing performance for BL-NAAs and NAAs in this study are summarized in Figure 9 and Table 3. According to the data, optical layer (I) of BL- $NAA_{(25/75)}$  showed almost similar  $S$  with the optical layer (I) of BL- $NAA_{(50/50)}$  whilst optical layer (I) of BL- $NAA_{(75/25)}$  showed a lower  $S$  than optical layer (I) of BL- $NAA_{(50/50)}$  and BL- $NAA_{(25/75)}$ . These results confirmed that the shorter top layer of the bilayered structure has the better sensitivity and stronger optical capability. The optical layer (II) of BL- $NAA_{(75/25)}$  revealed the highest sensitivity compared to optical layers (II) of BL- $NAA_{(25/75)}$  and BL- $NAA_{(50/50)}$  which further leads us to the conclusion that the shorter structural layer in a bilayered structure caused higher sensitivity. This is an important conclusion that should be considered when designing optimal sensing of multilayered NAA structures. Therefore, thick and in-depth fabrication of bilayered nanostructures reduced the optical characteristics of nanostructures, as seen by failed optical screening for optical layer (II) of BL- $NAA_{(25/75)}$ . Interestingly, optical layer (III) of BL- $NAA_{(50/50)}$  showed highest sensitivity compared to optical layers (III) of BL- $NAA_{(25/75)}$ , BL- $NAA_{(75/25)}$ . The value of sensitivities for optical layer (III) of BL- $NAA_{(50/50)}$  was higher compared to the single layer structures used in this study ( $NAA_{(1)}$  and  $NAA_{(2)}$ ). Therefore, BL- $NAA_{(50/50)}$  can be the proper choice of optimized bilayered structures due to its capability in multi-point sensing with high sensitivity at each layer. Additionally, control  $NAA_{(1)}$  depicted a single path of  $\Delta EOT$  screening. Control NAAs demonstrated the significant role of pore widening in sensing performance, where a lack of pore widening process diminishes  $S$ , significantly. Considerably, BL-NAAs could establish the multiple sensing pathways of a diverse range of sensing features. The sensitivities of these five nanoporous anodic alumina platforms are summarized in Figure 9.

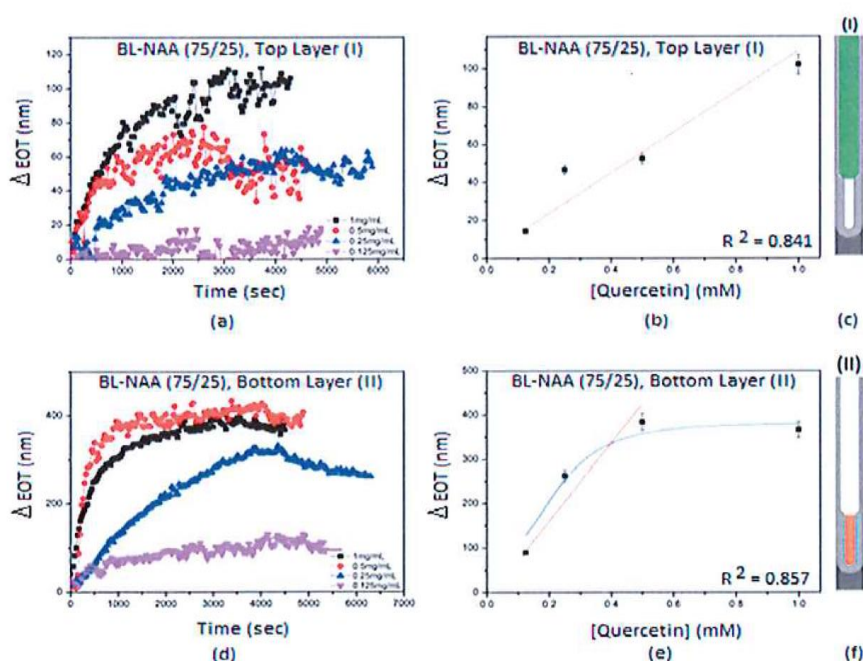
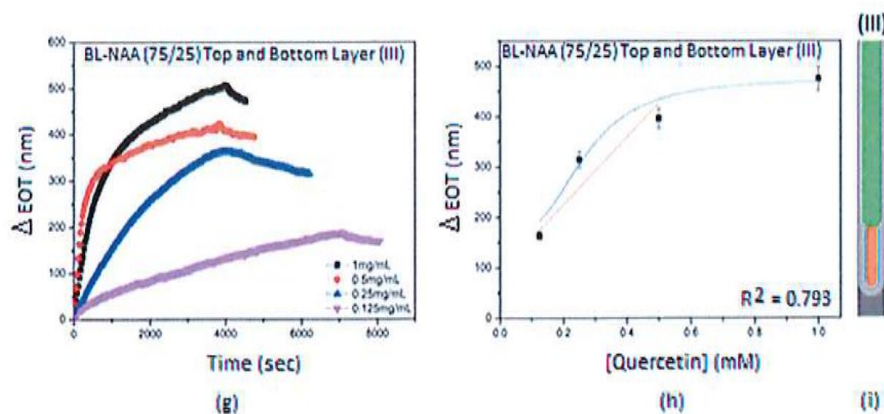


Figure 7. Cont.



**Figure 7.** Time response curve showing effective optical thickness changes and fitting curves for BL-NAA<sub>(75/25)</sub> (funnel structure with longer top layer with large diameters and shorter bottom layer with smaller pore diameters) sensing platforms measured by RIFS as a function of quercetin concentration (0.125, 0.25, 0.5, and 1 mM). (a)  $\Delta EOT_{(I)}$  generated from top structural layer of BL-NAA<sub>(75/25)</sub> platform; (b) Linear fitting line for BL-NAA<sub>(75/25)</sub> between  $\Delta EOT_{(I)}$  and the different concentration of quercetin (0.125, 0.25, 0.5, and 1 mM); (c) Scheme of representative optical layer as a function of  $\Delta EOT_{(I)}$  assessment; (d)  $\Delta EOT_{(II)}$  generated from bottom structural layer of BL-NAA<sub>(75/25)</sub> platform; (e) Sigmoid fit (blue) and the linear fit (red) for BL-NAA<sub>(75/25)</sub> between  $\Delta EOT_{(II)}$  and the different concentration of quercetin (0.125, 0.25, 0.5, and 1 mM) are presented; (f) Scheme of representative optical layer as a function of  $\Delta EOT_{(II)}$  assessment; (g)  $\Delta EOT_{(III)}$  generated from the top and bottom nanoporous structure of the BL-NAA<sub>(75/25)</sub> platform; (h) Sigmoid fit (blue) and the linear fit (red) for BL-NAA<sub>(75/25)</sub> between  $\Delta EOT_{(III)}$  and the different concentration of quercetin (0.05, 0.125, 0.25, 0.375, 0.5, and 1 mM) are presented; (i) Scheme of representative optical layer as a function of  $\Delta EOT_{(III)}$  assessment.

**Table 3.** Result of sensing performance of BL-NAAs and NAAs by  $\Delta EOT$  measurement.

Sample	Optical Layer	S (nm mM <sup>-1</sup> )	LLOD (mM)	R <sup>2</sup>
BL-NAA <sub>(25/75)</sub>	(I)	378 ± 48	0.034	0.922
	(II)	ND <sup>1</sup>	ND <sup>1</sup>	ND <sup>1</sup>
	(III)	418 ± 43	0.074	0.948
BL-NAA <sub>(50/50)</sub>	(I)	389 ± 66	0.148	0.943
	(II)	462 ± 70	0.1	0.912
	(III)	1207 ± 208	0.168	0.942
BL-NAA <sub>(75/25)</sub>	(I)	107 ± 26	0.179	0.841
	(II)	884 ± 245	0.160	0.857
	(III)	670 ± 227	0.256	0.793
NAA <sub>(1)</sub>	Single layer	842 ± 139	0.188	0.946
NAA <sub>(2)</sub>	Single layer	521 ± 174	0.449	0.799

<sup>1</sup> ND means Not Detectable.

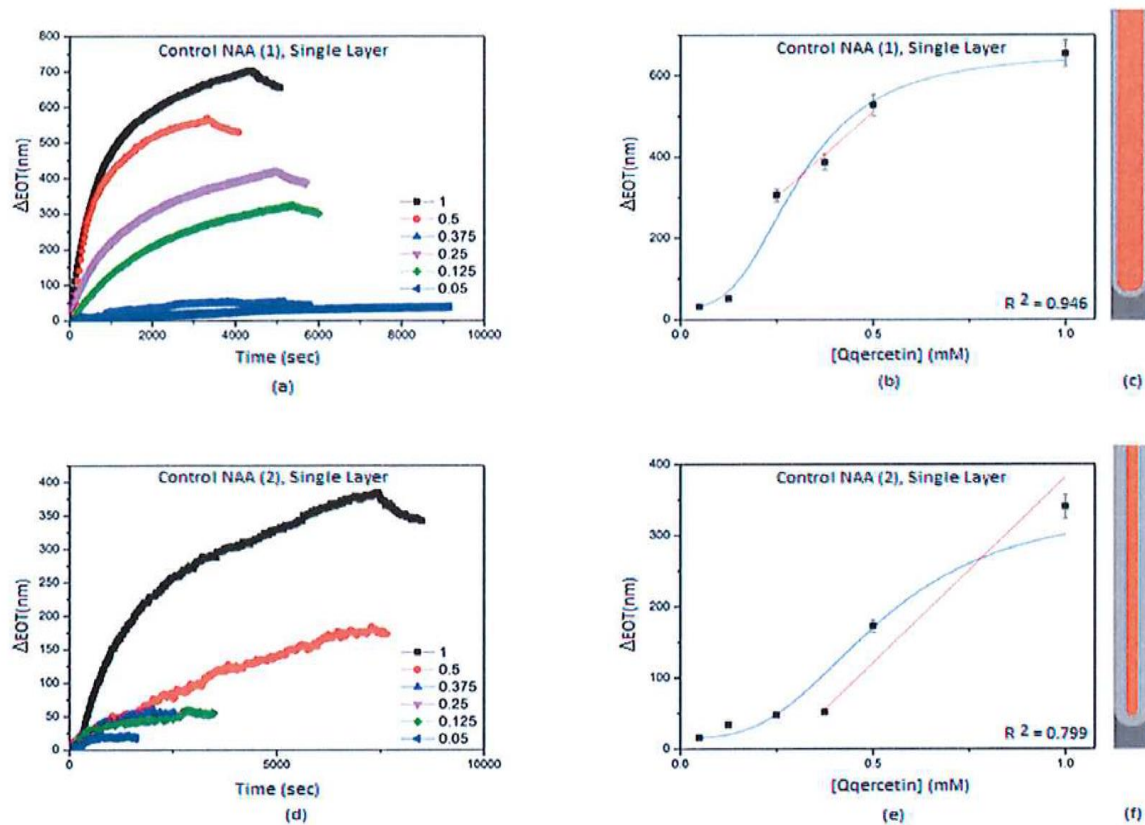


**Figure 8.** Time response curves showing effective optical thickness changes and fitting curves for control  $NAA_{(1)}$  and  $NAA_{(2)}$  sensing platforms measured by RIFs as a function of quercetin concentration (0.05, 0.125, 0.25, 0.375, 0.5, and 1 mM). (a)  $\Delta EOT$  generated from single layer nanoporous structure of  $NAA_{(1)}$  platform; (b) Sigmoid fit (blue) and the linear fit (red) for  $NAA_{(1)}$  between  $\Delta EOT$  and the different concentration of quercetin (0.05, 0.125, 0.25, 0.375, 0.5, and 1 mM) are presented; (c) Scheme of representative optical layer as a function of  $\Delta EOT$  assessment; (d)  $\Delta EOT$  generated from single layer nanoporous structure of  $NAA_{(2)}$  platform; (e) Sigmoid fit (blue) and the linear fit (red) for  $NAA_{(2)}$  between  $\Delta EOT$  and the different concentration of quercetin (0.05, 0.125, 0.25, 0.375, 0.5, and 1 mM) are presented; (f) Scheme of representative optical layer as a function of  $\Delta EOT$  assessment.

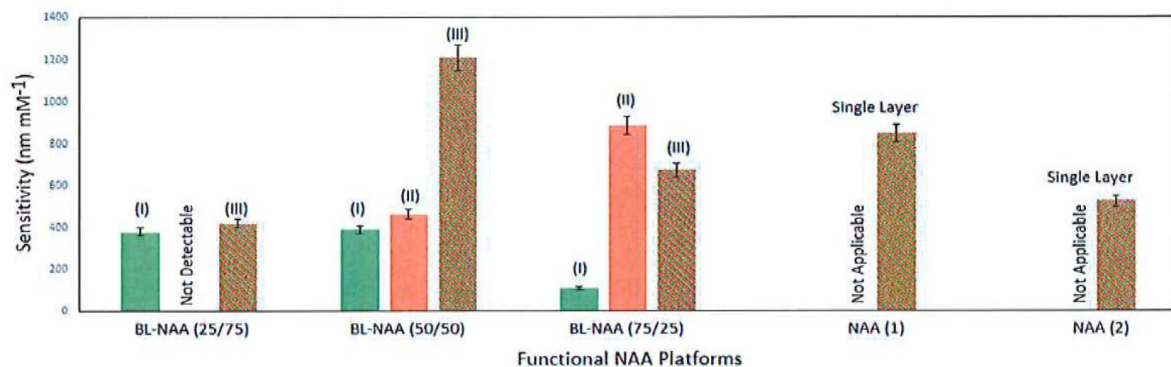


**Figure 9.** Bar chart summarizing the sensitivities (i.e., the slope of linear fittings shown in Figures 5–8) for BL-NAAs and NAAs sensing platforms modified with HSA-quercetin.

#### 4. Conclusions

In this work fabrication of bilayered NAA with a funnel-like nanopore structure (larger pore diameter on top and smaller pore diameter on the bottom) was successfully demonstrated using a combination of sequential anodization steps and pore widening process and was confirmed by systematic structural SEM characterizations. The bilayered nanostructures present complex RfS and FFT spectra, which can be readily and independently used as a sensing pattern. A set of three BL-NAAs platforms with different lengths of porous layers were evaluated to establish the most sensitive pore structures for a quercetin molecule, a model plant flavonol, and detection as a function of three optical layers (i.e., optical layer I, optical layer II, optical layer III). The design of sensing strategy made it possible to establish the effect of each optical layer on the sensitivity of the BL-NAAs using a sensing parameter, that is, changes in the effective optical thickness of the film ( $\Delta EOT$ ). Our analysis revealed that BL-NAA<sub>(50/50)</sub> has the most sensitive sensing pattern amongst BL-NAAs platforms. However, in comparison between a top and bottom structure, the bottom layer with less thickness features higher sensitivity. These results indicate that all these three layers can be used independently for sensing which means that with different surface chemistries this platform can be used for multi analyte biosensing. We believe these types of bilayered NAA structures, with further development of selective chemistry inside the pores, are a promising platform for the footprint development of multi-point sensing RfS devices for analysis of complex analyte systems including biological and environmental samples.

**Supplementary Materials:** The following are available online at [www.mdpi.com/1424-8220/18/2/470/s1](http://www.mdpi.com/1424-8220/18/2/470/s1), Fabrication and optimization of nanoporous anodic alumina structures as multi-point interferometric sensing platform.

**Acknowledgments:** Authors thank the support provided by the Australian Research Council (ARC) Grants FT110100711, DE140100549, the University of Adelaide and the School of Chemical Engineering (UoA).

**Author Contributions:** The work presented in this paper was a collaboration of all authors. M.N. fabricated all materials, the device, performed all characterizations, data processing. A.S. conceived and designed the experiments; the results were interpreted and the paper was written by M.N. and D.L. Final manuscript was written by M.N. and discussed and approved with all authors.

**Conflicts of Interest:** The authors declare no conflict of interest.

#### References

1. Md Jani, A.M.; Losic, D.; Voelcker, N.H. Nanoporous anodic aluminium oxide: Advances in surface engineering and emerging applications. *Prog. Mater. Sci.* **2013**, *58*, 636–704. [[CrossRef](#)]
2. Santos, A.; Kumeria, T.; Losic, D. Nanoporous anodic alumina: A versatile platform for optical biosensors. *Materials* **2014**, *7*, 4297–4320. [[CrossRef](#)] [[PubMed](#)]
3. Sheng, X.; Liu, J.; Coronel, N.; Agarwal, A.M.; Michel, J.; Kimerling, L.C. Integration of self-assembled porous alumina and distributed bragg reflector for light trapping in Si photovoltaic devices. *IEEE Photon. Technol. Lett.* **2010**, *22*, 1394–1396. [[CrossRef](#)]
4. Toccafondi, C.; Thorat, S.; Rocca, R.L.; Scarpellini, A.; Salerno, M.; Dante, S.; Das, G. Multifunctional substrates of thin porous alumina for cell biosensors. *J. Mater. Sci. Mater. Med.* **2014**, *25*, 2411–2420. [[CrossRef](#)] [[PubMed](#)]
5. Yamaguchi, A.; Hotta, K.; Teramae, N. Optical waveguide sensor based on a porous anodic alumina/aluminum multilayer film. *Anal. Chem.* **2009**, *81*, 105–111. [[CrossRef](#)] [[PubMed](#)]
6. Sulka, G.D.; Hnida, K. Distributed bragg reflector based on porous anodic alumina fabricated by pulse anodization. *Nanotechnol* **2012**, *23*, 075303. [[CrossRef](#)] [[PubMed](#)]
7. Rahman, M.M.; Marsal, L.F.; Pallarès, J.; Ferré-Borrull, J. Tuning the photonic stop bands of nanoporous anodic alumina-based distributed bragg reflectors by pore widening. *ACS Appl. Mater. Interfaces* **2013**, *5*, 13375–13381. [[CrossRef](#)] [[PubMed](#)]
8. Dronov, R.; Jane, A.; Shapter, J.G.; Hodges, A.; Voelcker, N.H. Nanoporous alumina-based interferometric transducers ennobled. *Nanoscale* **2011**, *3*, 3109–3114. [[CrossRef](#)] [[PubMed](#)]



9. Brecht, A.; Gauglitz, G. Recent developments in optical transducers for chemical or biomedical applications. *Sens. Actuators B* **1997**, *38*, 1–7. [[CrossRef](#)]
10. Reichl, D.; Krage, R.; Krumme, C.; Gauglitz, G. Sensing of volatile organic compounds using a simplified reflectometric interference spectroscopy set up. *Appl. Spectrosc.* **2000**, *54*, 583–586. [[CrossRef](#)]
11. Belmont, A.-S.; Jaeger, S.; Knopp, D.; Niessner, R.; Gauglitz, G.; Haupt, K. Molecularly imprinted polymer films for reflectometric interference spectroscopic sensors. *Biosens. Bioelectron.* **2007**, *22*, 3267–3272. [[CrossRef](#)] [[PubMed](#)]
12. Leopold, N.; Busche, S.; Gauglitz, G.; Lendl, B. IR absorption and reflectometric interference spectroscopy (RIFS) combined to a new sensing approach for gas analytes absorbed into thin polymer films. *Spectrochim. Acta A Mol. Biomol. Spectrosc.* **2009**, *72*, 994–999. [[CrossRef](#)] [[PubMed](#)]
13. Nemati, M.; Santos, A.; Kumeria, T.; Losic, D. Label-free real-time quantification of enzyme levels by interferometric spectroscopy combined with gelatin-modified nanoporous anodic alumina photonic films. *Anal. Chem.* **2015**, *87*, 9016–9024. [[CrossRef](#)] [[PubMed](#)]
14. Brecht, A.; Gauglitz, G. Optical probes and transducers. *Biosens. Bioelectron.* **1995**, *10*, 923–936. [[CrossRef](#)] [[PubMed](#)]
15. Gauglitz, G. Direct optical sensors: Principles and selected applications. *Anal. Bioanal. Chem.* **2005**, *381*, 141–155. [[CrossRef](#)] [[PubMed](#)]
16. Gauglitz, G. Direct optical detection in bioanalysis: An update. *Anal. Bioanal. Chem.* **2010**, *398*, 2363–2372. [[CrossRef](#)] [[PubMed](#)]
17. Dancil, K.-P.S.; Greiner, D.P.; Sailor, M.J. A porous silicon optical biosensor: Detection of reversible binding of IgG to a protein A-modified surface. *J. Am. Chem. Soc.* **1999**, *121*, 7925–7930. [[CrossRef](#)]
18. Kumeria, T.; Santos, A.; Losic, D. Nanoporous Anodic Alumina Platforms: Engineered Surface Chemistry and Structure for Optical Sensing Applications. *Sensors* **2014**, *14*, 11878–11918. [[CrossRef](#)] [[PubMed](#)]
19. Nemati, M.; Santos, A.; Law, C.S.; Losic, D. Assessment of binding affinity between drugs and human serum albumin using nanoporous anodic alumina photonic crystals. *Anal. Chem.* **2016**, *88*, 5971–5980. [[CrossRef](#)] [[PubMed](#)]
20. Santos, A.; Balderrama, V.; Alba, M.; Formentín, P.; Ferré-Borrull, J.; Pallarès, J.; Marsal, L.F. Nanoporous anodic alumina barcodes: Toward smart optical biosensors. *Adv. Mater.* **2012**, *24*, 1050–1054. [[CrossRef](#)] [[PubMed](#)]
21. Kumeria, T.; Kurkuri, M.D.; Diener, K.R.; Parkinson, L.; Losic, D. Label-free reflectometric interference microchip biosensor based on nanoporous alumina for detection of circulating tumor cells. *Biosens. Bioelectron.* **2012**, *35*, 167–173. [[CrossRef](#)] [[PubMed](#)]
22. Kumeria, T.; Parkinson, L.; Losic, D. A nanoporous interferometric micro-sensor for biomedical detection of volatile Sulphur compounds. *Nanoscale Res. Lett.* **2011**, *6*, 634. [[CrossRef](#)] [[PubMed](#)]
23. Law, C.S.; Santos, A.; Nemati, M.; Losic, D. Structural engineering of nanoporous anodic alumina photonic crystals by sawtooth-like pulse anodization. *ACS Appl. Mater. Interfaces* **2016**, *8*, 13542–13554. [[CrossRef](#)] [[PubMed](#)]
24. Law, C.S.; Sylvia, G.M.; Nemati, M.; Yu, J.; Losic, D.; Abell, A.D.; Santos, A. Engineering of surface chemistry for enhanced sensitivity in nanoporous interferometric sensing platforms. *ACS Appl. Mater. Interfaces* **2017**, *9*, 8929–8940. [[CrossRef](#)] [[PubMed](#)]
25. Losic, D.; Lillo, M.; Losci, D., Jr. Porous alumina with shaped pore geometries and complex pore architectures fabricated by cyclic anodization. *Small* **2009**, *5*, 1392–1397. [[CrossRef](#)] [[PubMed](#)]
26. Losic, D.; Losci, D., Jr. preparation of porous anodic alumina with periodically perforated pores. *Langmuir* **2009**, *25*, 5426–5431. [[CrossRef](#)] [[PubMed](#)]
27. Kumeria, T.; Rahman, M.M.; Santos, A.; Ferré-Borrull, J.; Marsal, F.L.; Losic, D. Structural and optical nanoengineering of nanoporous anodic alumina rugate filters for real-time and label-free biosensing applications. *Anal. Chem.* **2014**, *86*, 1837–1844. [[CrossRef](#)] [[PubMed](#)]
28. Macias, G.; Ferré-Borrull, J.; Pallares, J.; Marsal, L.F. 1-D nanoporous anodic alumina rugate filters by means of small current variations for real-time sensing applications. *Nanoscale Res. Lett.* **2014**, *9*, 315. [[CrossRef](#)] [[PubMed](#)]
29. Zheng, W.J.; Fei, G.T.; Wang, B. Modulation of transmission spectra of anodized alumina membrane distributed Bragg reflector by controlling anodization temperature. *Nanoscale Res. Lett.* **2009**, *4*, 665–667. [[CrossRef](#)] [[PubMed](#)]

30. Santos, A.; Formentín, P.; Pallarès, J.; Ferré-Borrull, J.; Marsal, L.F. Structural engineering of nanoporous anodic alumina funnels with high aspect ratio. *J. Electroanal. Chem.* **2011**, *655*, 73–78. [[CrossRef](#)]
31. Macias, G.; Hernández-Eguía, L.P.; Ferré-Borrull, J.; Pallares, J.; Marsal, L.F. Gold-coated ordered nanoporous anodic alumina bilayers for future label-free interferometric biosensors. *ACS Appl. Mater. Interfaces* **2013**, *5*, 8093–8098. [[CrossRef](#)] [[PubMed](#)]
32. Santos, A.; Kumeria, T.; Wang, Y.; Losic, D. In situ monitoring engineering of inverted nanoporous anodic alumina funnels: On the precise generation of 3D optical nanostructures. *Nanoscale* **2014**, *6*, 9991–9999. [[CrossRef](#)] [[PubMed](#)]
33. Wang, H.; Wang, G. Enhanced the optical transmission efficiency by funnel-shaped nanopore. In Proceedings of the International Conference on Manipulation, Manufacturing and Measurement on the Nanoscale (3M-NANO), Chongqing, China, 18–22 July 2016; pp. 55–58. [[CrossRef](#)]
34. Manach, C.; Scalbert, A.; Morand, C.; Rémécy, C.; Jiménez, L. Polyphenols: Food sources and bioavailability. *Am. J. Clin. Nutr.* **2004**, *79*, 727–747. [[CrossRef](#)] [[PubMed](#)]
35. Burda, S.; Oleszek, W. Antioxidant and antiradical activities of flavonoids. *J. Agric. Food Chem.* **2001**, *49*, 2774–2779. [[CrossRef](#)] [[PubMed](#)]
36. Wang, J.; Zhou, N.; Zhu, Z.; Huang, J.; Li, G. Detection of flavonoids and assay for their antioxidant activity based on enlargement of gold nanoparticles. *Anal. Bioanal. Chem.* **2007**, *388*, 1199–1205. [[CrossRef](#)] [[PubMed](#)]
37. Lamson, D.W.; Brignall, M.S. Antioxidants and cancer III: Quercetin. *Altern Med. Rev.* **2000**, *5*, 196–208. [[PubMed](#)]
38. Jenkins, D.J.A.; Kendall, C.W.; Ransom, T.P.P. Dietary fiber, the evolution of the human diet and coronary heart disease. *Nutr. Res.* **1998**, *18*, 633–652. [[CrossRef](#)]
39. Mukhopadhyay, M.; Singh, A.; Sachchidanand, S.; Berta, A.K. Quercetin inhibits acid-sensing ion channels through a putative binding site in the central vestibular region. *Neuroscience* **2017**, *348*, 264–272. [[CrossRef](#)] [[PubMed](#)]
40. Velleman, L.; Triani, G.; Evans, P.J.; Shapter, J.G.; Losic, D. Structural and chemical modification of porous alumina membranes. *Micropor. Mesopor. Mater.* **2009**, *126*, 87–94. [[CrossRef](#)]
41. Kumeria, T.; Losic, D. Controlling interferometric properties of nanoporous anodic aluminium oxide. *Nanoscale Res. Lett.* **2012**, *7*, 88. [[CrossRef](#)] [[PubMed](#)]



© 2018 by the authors. Licensee MDPI, Basel, Switzerland. This article is an open access article distributed under the terms and conditions of the Creative Commons Attribution (CC BY) license (<http://creativecommons.org/licenses/by/4.0/>).

# Supplementary Materials

## **Fabrication and Optimization of Bilayered Nanoporous Anodic Alumina Structures as Multi-Point Interferometric Sensing Platform**

**Mahdieh Nemati<sup>1</sup>, Abel Santos<sup>1,2,3</sup> and Dusan Losic<sup>1,\*</sup>**

<sup>1</sup> School of Chemical Engineering, The University of Adelaide, Engineering North Building, 5005 Adelaide, Australia ;

<sup>2</sup> Institute for Photonics and Advanced Sensing (IPAS), The University of Adelaide, 5005 Adelaide, Australia;

<sup>3</sup> ARC Centre of Excellence for Nanoscale BioPhotonics (CNBP), The University of Adelaide, 5005 Adelaide, Australia;

\*Correspondence: [dusan.losic@adelaide.edu.au](mailto:dusan.losic@adelaide.edu.au)

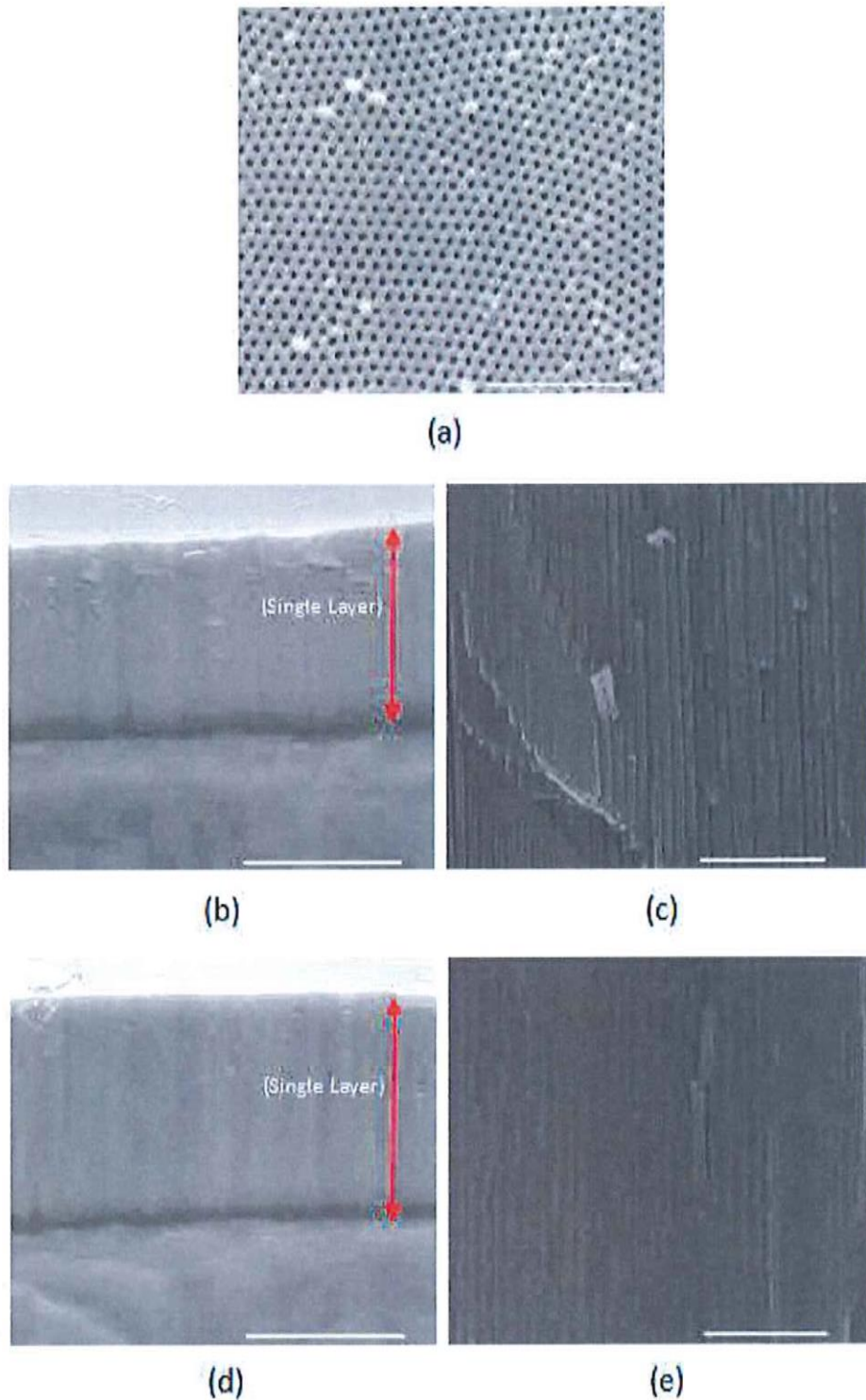
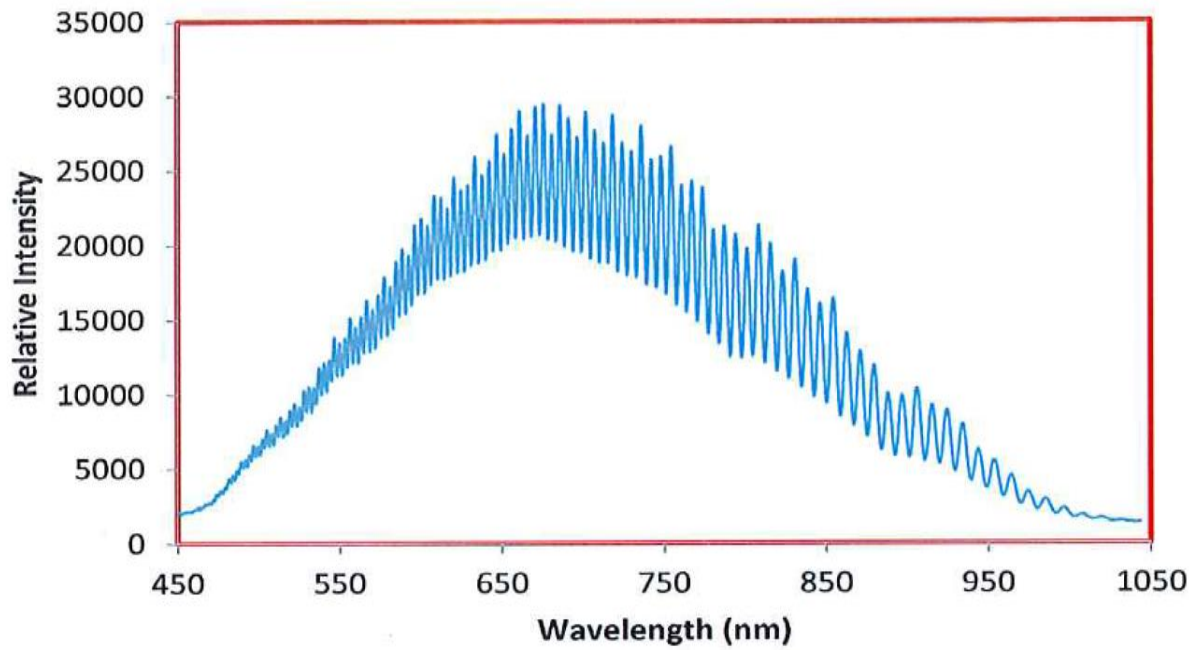
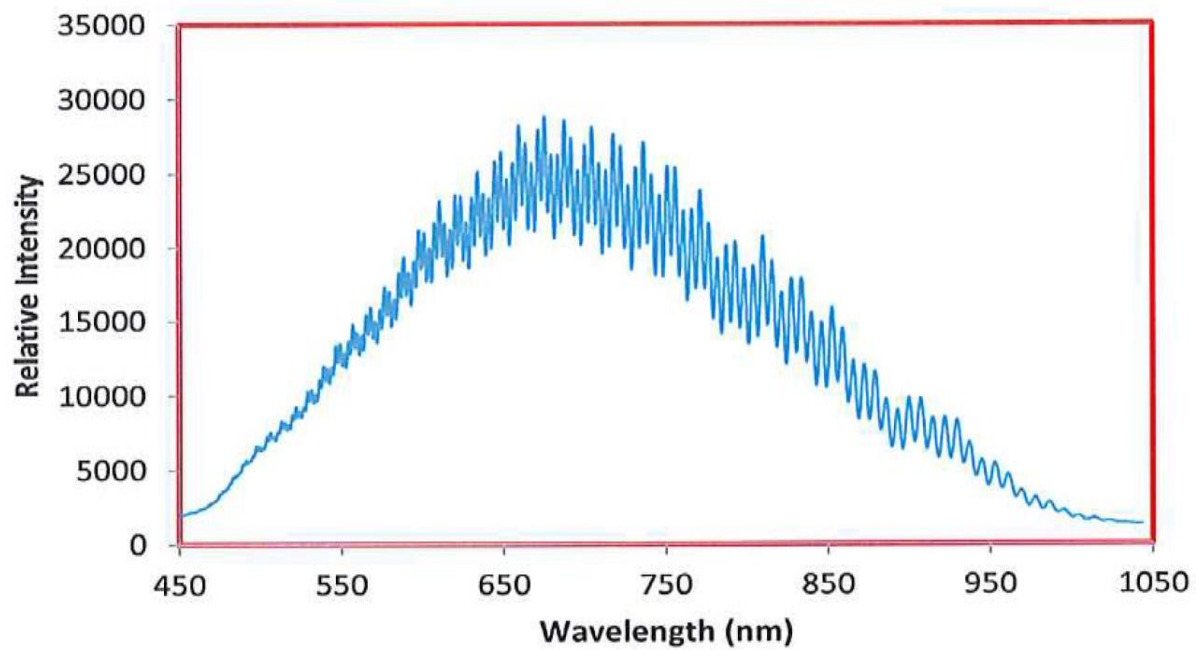


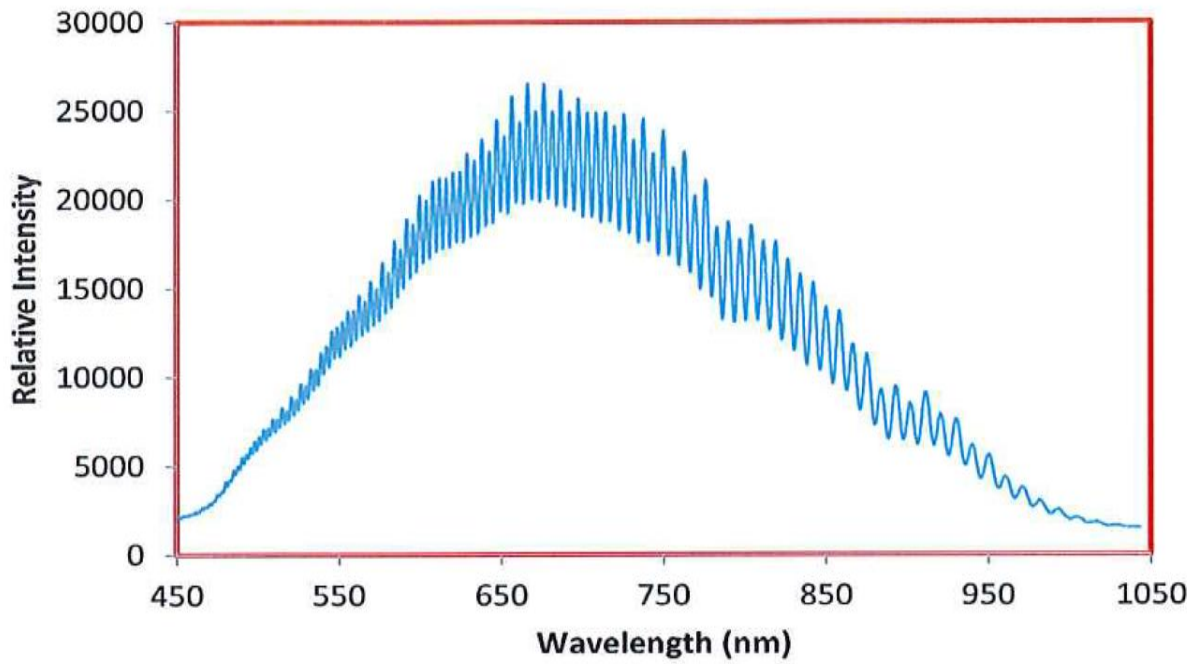
**Figure S1.** (a) Top view SEM image of a BL-NAA/NAA (scale bar= 1 $\mu$ m) showing typical highly ordered NAA pore structures. (h) Cross-section view of NAA<sub>(1)</sub>, scale bar is 20  $\mu$ m. (i) Cross-section view of NAA<sub>(1)</sub>, scale bar is 1  $\mu$ m. (j) Cross-section view of NAA<sub>(2)</sub>, scale bar is 20  $\mu$ m. (k) Cross-section view of NAA<sub>(2)</sub>, scale bar is 1  $\mu$ m. Magnified view of red squares in (c), (e), and (g) show the connection of structural layers where pore diameter of each layer is different. Top layer (I), bottom layer (II) and single layers are marked on images.



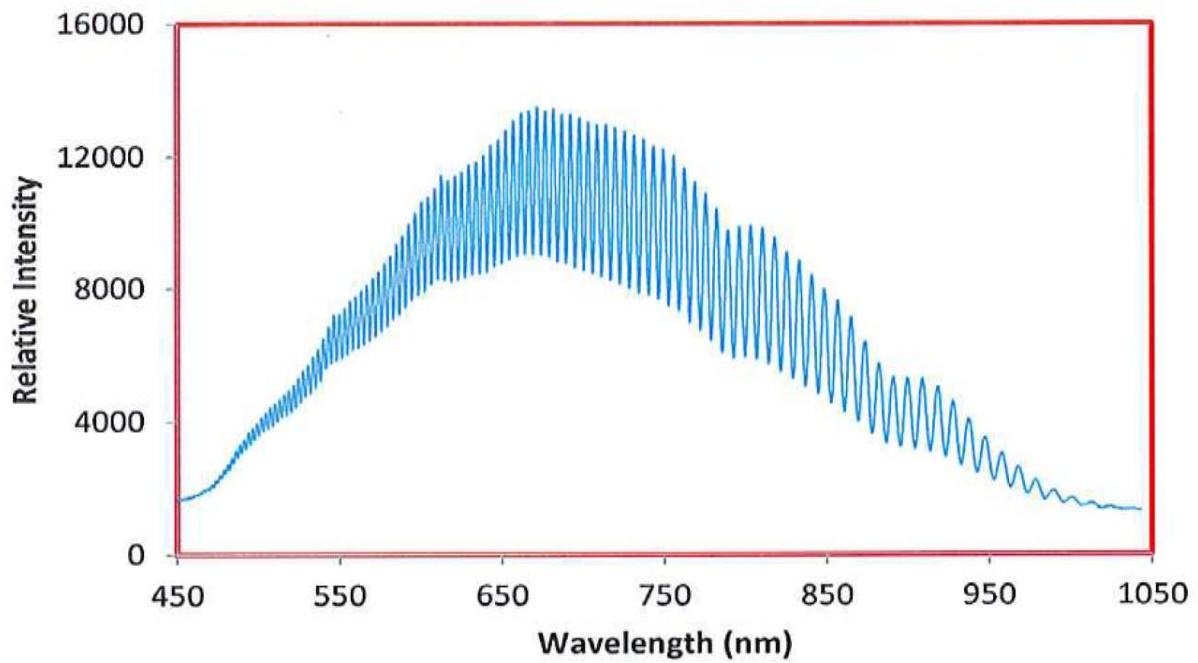
(a)



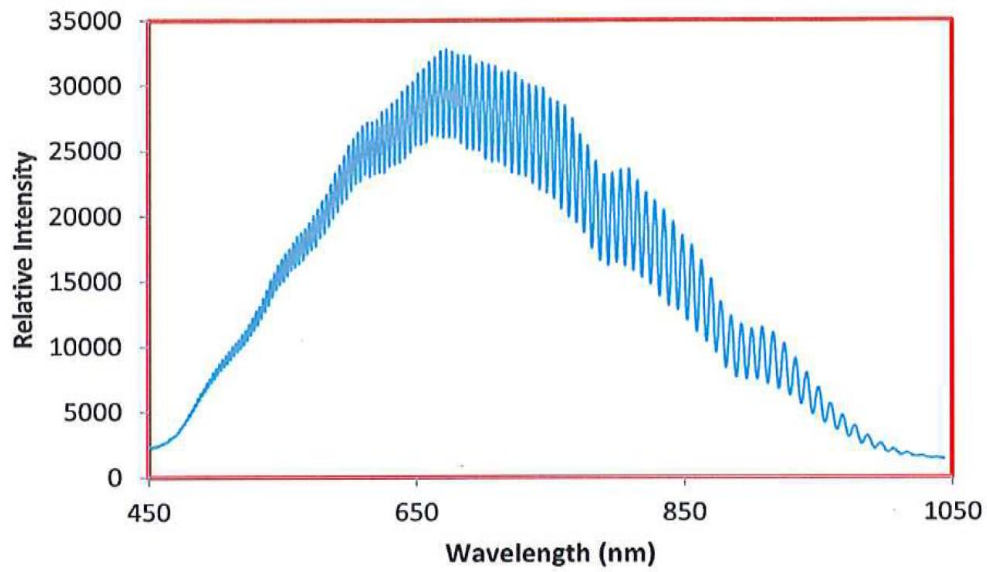
(b)



(c)



(d)



(e)

**Figure S2.** Optical interference pattern generated from Fabry-Pérot effect for all types of BL-NAAs and NAAs in this study. (a) BL-NAA<sub>(25/75)</sub>, (b) BL-NAA<sub>(75/25)</sub>, (c) BL-NAA<sub>(50/50)</sub>, (d) NAA<sub>(1)</sub>, (e) NAA<sub>(2)</sub>. All optical films presented uniform oscillation series in their RfS spectrum.

**BLANK PAGE**



## CHAPTER 6.

---

### **Integration of Molecular Biology with Biosensor Devices**

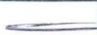
**Chapter-6** discusses the significant role of biotechnology techniques in the enhancement of biosensor devices followed by a preliminary results towards the integration of these techniques with NAA-RIfS. This chapter is written as paper but without of biosensing part which is not completed.

**BLANK PAGE**

## Statement of Authorship

Title of Paper	Detection of Single Nucleotide Polymorphism Associated with Phosphine Resistance in <i>Tribolium Castaneum</i> Using Ligation-Rolling Circle Amplification		
Publication Status	<input type="checkbox"/> Published	<input type="checkbox"/> Accepted for Publication	
	<input type="checkbox"/> Submitted for Publication	<input checked="" type="checkbox"/> Unpublished and Unsubmitted work written in manuscript style	
Publication Details			


### Principal Author


Name of Principal Author (Candidate)	Mahdieh Nemati		
Contribution to the Paper	Prepared the first draft of manuscript, edited, and revised the manuscript.		
Overall percentage (%)	85%		
Certification:	This paper reports on original research I conducted during the period of my Higher Degree by Research candidature and is not subject to any obligations or contractual agreements with a third party that would constrain its inclusion in this thesis. I am the primary author of this paper.		
Signature		Date	12.12.2017

### Co-Author Contributions

By signing the Statement of Authorship, each author certifies that:

- i. the candidate's stated contribution to the publication is accurate (as detailed above);
- ii. permission is granted for the candidate to include the publication in the thesis; and
- iii. the sum of all co-author contributions is equal to 100% less the candidate's stated contribution.

Name of Co-Author	Kelly Hill		
Contribution to the Paper	Supervised the development of the work, edited, revised the manuscript, and corresponding author.		
Signature		Date	14.12.2017

Name of Co-Author	Dusan Losic		
Contribution to the Paper	Supervised the development of the work, edited the manuscript and corresponding author.		
Signature		Date	20/12/2017

Please cut and paste additional co-author panels here as required.

## Abstract

Food safety is of crucial concern when pesticide resistance develops within crop and stored product pests. This can lead to increased pesticide applications resulting from persistent pest presence. To manage this matter, monitoring the emergence and development of pesticide resistance of grain insects is necessary. Molecular detection of resistant population of insects are known as reliable and effective techniques to distinguish between resistant and susceptible individuals but the process can be long and requires specialised equipment and know-how. Not all mechanism of resistance in insects can be detected by a single mutation event. This type of test is restricted to known resistant mechanisms that result from a genetic mutation. In this study, we propose new approach based on the ligation-rolling circle amplification (L-RCA) assay for its application in detecting the resistant-allele of the dihydrolypoamide dehydrogenase gene (DLD) in *T. castaneum* beetles. *T. castaneum* beetles are known as one of the most important stored grain pests and populations have been known to readily develop resistance to fumigants such as phosphine across many areas in Australia. Here, we present L-RCA reaction, demonstrating simple and rapid method to monitor the resistant target allele. The successful application of L-RCA to monitor known insecticide resistant SNPs opens the opportunity to transfer the assay to a biosensor platform for point-of-need detection based on RIFS spectroscopy

## 1. Introduction

Major issues associated with the current stored grain pest management world-wide is the development of pesticide resistance by major grain insects to currently used grain protectants

(insecticides such as phosphine) and a strong market demand of pesticide-free grain products. In Australia, the national grains industry, specifically grain export worth about \$7 billion each year, is under threat and requires an urgent alternative to currently used fumigants to protect stored grain against resistant insects.

To protect stored grain against insect infestations in silos, warehouses, jute bags, bunkers and ships during transportation, fumigation is an effective and readily applied method<sup>1</sup>. An ideal fumigant like phosphine (PH<sub>3</sub>) provides a cost-effective method, capable of penetration into grain bulk quickly, and is easily eliminated from grain by aeration<sup>2</sup>. On the other hand, other alternative fumigants, methyl bromide due to the Montreal Protocol has been phased out since 2005 due its contribution to ozone depletion<sup>3</sup>. This reliance of phosphine fumigation, and the combination of long-term use and sub-optimal fumigation conditions, has led to the selection of resistant insects that is rapidly developed in Australia in last 10 years<sup>4, 5-7</sup>. Susceptible adult insects are killed quickly, usually within a day, but immature eggs and pupal stages are tolerant of phosphine and can survive short exposures to phosphine, even in high concentrations. To kill all stages of the insects' life cycles, the phosphine gas must be present in high enough concentrations for approximately 7 days. Reports indicate that the emergence of resistant populations of *Tribolium castaneum* (*Rust red flour beetle*) poses a major threat to stored agricultural products, specifically in Australia<sup>8</sup>. A detailed genetic analysis at the molecular level by Schlipalius et al. (2002) confirms that there are two positions, or loci, on different chromosomes, of the resistant strain that carry resistance alleles which are labelled as primary resistive gene rph1 and secondary resistance gene, labelled rph2. To aid the implementation of effective management strategies for phosphine resistant *T. castaneum* populations, it would be desirable to be able to quickly and easily monitor the presence of these

genes in trapped insects on the farms. While these two loci have been reported to contain Single Nucleotide Polymorphisms (SNPs) associated with phosphine resistance in *T. castaneum*<sup>9</sup>, the genetic marker that was linked to strong resistance in the beetle, was within the gene encoding the metabolic enzyme dihydrolypoamide dehydrogenase (DLD)<sup>10</sup>. The SNPs within the DLD gene have recently been used as a diagnostic marker for resistant *T. castaneum* population monitoring using the cleaved amplified polymorphic sequence method (CAPS)<sup>11</sup>. While this technique is a well-established and reliable method for SNP monitoring, it still relies on multiple steps including: amplification, digestion and gel electrophoresis. SNPs within the genome account for approximately 90% of sequence variations<sup>12</sup>, and along with their association with specific phenotypes such as resistance<sup>13</sup>, they are commonly used as genetic markers for gene mapping, genetic disorders and identifying genetic structure in populations<sup>14</sup>. This has led to an increasing demand for SNP genotyping detection techniques that are cost-effective, quick, and simple. So far, a variety of techniques have been reported in literature for SNP detection including oligonucleotide ligation, primer extension, endonuclease digestion, and gene amplification<sup>15-21</sup>. SNP detection based on isothermal amplification such as Ligation-Rolling Circle Amplification (L-RCA) offer simplified requirements, in regards to procedure, speed and analysis<sup>22</sup>. The L-RCA reaction consists of a padlock probe designed to match the target DNA sequence at the 3' and 5' ends. In the presence of the target DNA and DNA ligase, the padlock probe becomes the circular template for the RCA reaction. The ligation of the padlock probe is highly dependent on the target sequence and can distinguish a single mismatch at the 3' end (SNP) making circularization fail, which results in a failed RCA reaction.

The RCA amplification technique is capable of rapidly synthesizing a long single-stranded DNA (more than 1000 bases) by a short circular template (less than 100 bases)<sup>23</sup>. The high

speed, robustness, and sensitivity of RCA have attracted researchers in the area of biomolecule detections. Following this, RCA has been used as a signal-amplification tool on microarray-based devices for the proteomics and clinical applications<sup>24-28</sup>. These microarrays were developed with the conjugation of an RCA primer to the detection antibody which, upon coupling of the antigen-antibody, is subsequently immobilised onto the microarray surface. The primer is used for initiation of an RCA reaction, which can be visualised by the subsequent hybridisation of DNA probes in the presence of fluorescent labels. Although microarrays are beneficial as sensitive, specific and miniaturised devices, but their application is expensive due to requirement of sophisticated equipment, and requirement of fluorescent labelling<sup>29</sup>. In order to tackle this disadvantage, the exciting developments in the use of RCA have appeared in the areas of nanotechnology and optical sensors with the functional nucleic acids<sup>30, 31</sup>. For example, a label-free detection of DNA amplification using a nano-fluidic diffraction grating was carried out in real-time and detected DNA molecules ranging from 1fM to 1pM<sup>32</sup>. According to this study, the sensing process occurred in light intensity changes which was attributed to the change of refractive index.

Following this previous work we have developed a method to detect a resistant-allele of the DLD gene which could be adapted to our well-established RIFS optical biosensor device using NAA platform which combines L-RCA reaction and RIfS detection. The detection of phosphine resistant genes from resistant individuals of *T. castaneum*, which can be used as a model insect considering the importance of monitoring populations of these resistant insects in grain storage facilities across Australia. Currently this analysis can be done only in two special

labs that takes 1-2 days and having portable analytical instruments that can provide fast detection is desirable in order to implement appropriate management in a timely fashion. The first step toward the development of this type of biosensors for resistant genes detection is to establish the solution-based L-RCA as assay for identification of the DLD gene mutation in *T. castaneum* that is schematically presented in **Figure 1a**.

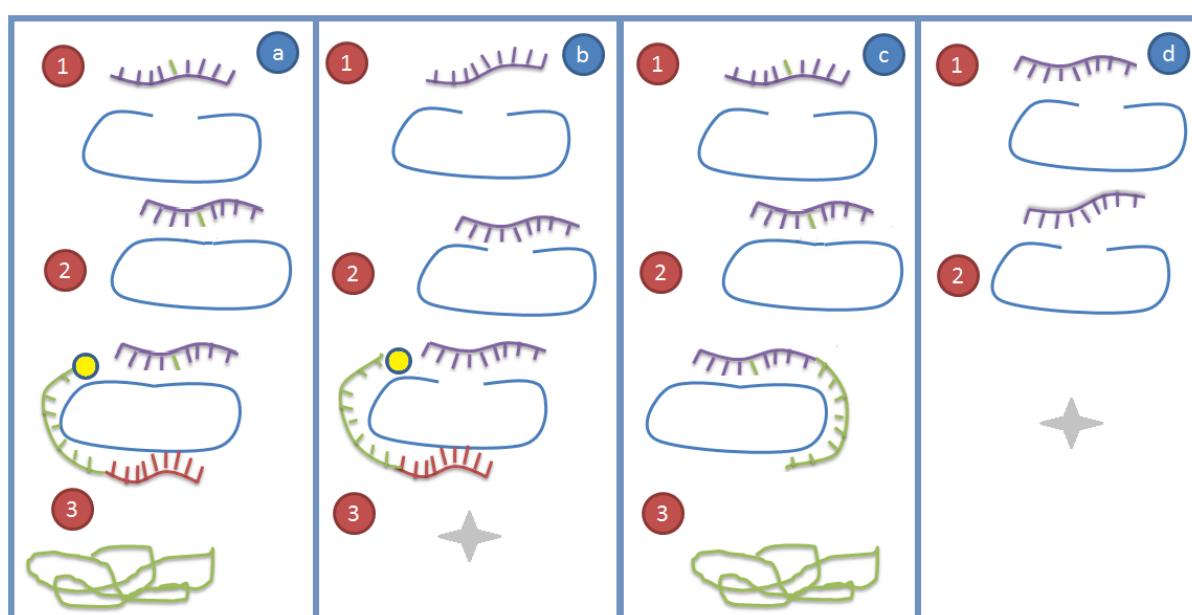


**Figure 1.** Schematic illustration of our strategy for resistant allele detection of DLD gene from *T. castaneum*. This represents the procedure for L-RCA amplification using external padlock primer (a and b) or self-primed L-RCA amplification (c and d). The coloured configurations are as following: purple (susceptible probe non- target), purple with the green dash representing the SNP site (resistant probe target), blue (padlock probe), yellow (DNA polymerase), red (padlock primer), green (amplification product), and the grey star is the sign of no reaction occurring. The reactions start from stage 1 and terminate in stage 3. Stage 1 is the ligation process which are successful in 2a and 2c due to the presence of the target allele. Successful ligation results in amplification products from the RCA reaction as shown in 3a and 3c. However, amplification product was not generated in the lack of circular probe (b and d).

To achieve that, we develop a SNP-based detection strategy using ligation- rolling circle amplification (L- RCA) for the purpose of resistant-allele identification of DLD gene from



*T. castaneum* that could be implemented into NAA-RIfS system schematically presented in **Figure 2**. The sensing concept is based on label-free and real-time monitoring of binding events and producing RCA products by estimating the changes in effective optical thickness (i.e., sensing principle) measured by RIfS. The sensing elements inside NAA nanopores is composed of several components including specific surface chemistry for selective capturing of target probe (i.e., SNP region) required for subsequent RCA reaction.

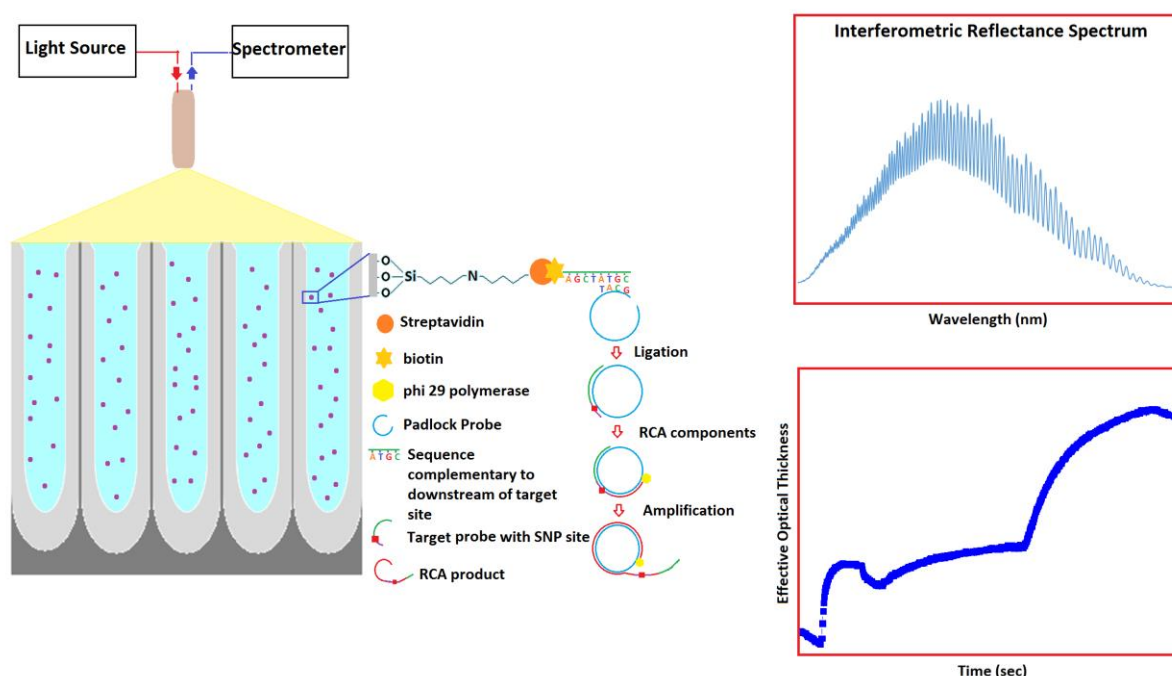


**Figure 2.** A schematic illustration of proposed design for resistant-allele detection of DLD gene from *T. castaneum* using NAA-RIfS biosensor. The sensing elements inside NAA pores is composed of several components including silane terminated amines (APTES) used for immobilization of streptavidin that is used to capture the biotinylated sequence which is complementary to downstream of target site. Target probe (with SNP site) required for initiation of ligation and subsequent RCA reaction for detection of resistant-allele of DLD gene from *T. castaneum*. The effective optical thickness changes in NAA pores is measured by RIfS in real-time.

Herein, we present a SNP-based detection strategy that is performed using solution-based ligation-rolling circle amplification (L-RCA) for the purpose of resistant-allele identification of DLD gene from *T. castaneum*.

## **2. Experimental Section**

**2.1. Insect Strains.** The *T. castaneum* strains used in this study are the QTC4 (phosphine susceptible) and QTC279 (phosphine resistant) strains which were kindly provided by department of agriculture and fisheries, the state of Queensland.

**2.2. Preparation of Genomic DNA.** Genomic DNA was extracted from 4 adult individuals, susceptible and resistant populations of *T. castaneum*, using the protocol described by Wizard® Genomic DNA Purification Kit (Promega). Briefly, an individual beetle was homogenised in nuclei lysis solution, then centrifuged for 10 sec at maximum speed. The supernatant of nuclei lysate solution incubated at 37°C for 30 min, after 3 µl of RNase was added. Samples were centrifuged at 14000 rpm at room temperature for 4 min. The supernatant was then gently mixed with isopropanol and again centrifuged as above. Here, the supernatant was removed and pellet was washed with 70% ethanol and then air dried. Finally, 50 µl of DNA rehydration solution was added to each sample tube and were incubated at 4°C for overnight. The purified genomic DNA templates were subsequently used for PCR amplification.

**2.3. PCR Amplification and Sequencing.** In order to confirm the presence of the SNP in the *T. castaneum* strains used here, the appropriate gene region was amplified using a DLD primer set designed using the PrimerQuest design tool ([www. idtdna.com/SciTools](http://www.idtdna.com/SciTools)), against the dihydrolipoamide dehydrogenase (DLD) gene nucleotide sequences from *T. castaneum* strain

QTC4 Susceptible (KX907540.1) & *T. castaneum* strain QTC931 (KX907541.1) retrieved from the NCBI database (<https://www.ncbi.nlm.nih.gov>). Genomic DNA was amplified by PCR using the selected primers in a 50- $\mu$ l reaction volume containing 5  $\mu$ l of genomic DNA, 1  $\mu$ l of each primer, (Tcdld F: 5' AAAGGAAAATGCTGTCAAGGC 3') and reverse (Tcdld R: 5' CTGTAATTTTCCCATGTCCGTTG 3'). 4  $\mu$ l dNTPs, 0.25  $\mu$ l Takara Taq- polymerase enzyme in 5  $\mu$ l 10x reaction buffer supplied with the enzyme. Then, amplification was carried out in a supercycler gradient cycler, manufactured by Kyratec (SC200), programmed for an initial 2 min and 30 sec, then followed by 30 cycles of 30 sec at 95°C, 30 sec at 56°C, and 30 sec at 72°C, a final step was also performed for 3 min at 72°C. Then, Amplification products were visualized by gel electrophoresis technique using 0.8% agarose and RedSafe nucleic acid stain (iNtRON). The remaining PCR product was purified using the UltraClean PCR clean-up kit (MO BIO laboratories) and sent for Sanger sequencing at AGRF, Adelaide. The sequences were analysed using Biological Sequence Alignment Editor Software (*BioEdit*)<sup>33</sup>.

**2.4. Ligation-Rolling Circle Amplification: Resistant SNP Detection Assay.** A 73-mer oligonucleotide with a 5' phosphate modification (5' CCAGTTAAAGCCTTGACAGCATTTTCCTAGAATGAAGATAGCGCATCGTAGGAC GAAAAGTTGCGCTATGCTT 3') was designed and synthesized to be used as RCA linear template (padlock probe). The padlock probe was designed so that the 11 bp at the 5' end and the 14 bp at the 3' end are complementary to the target (*T. castaneum* DLD gene region containing SNP). The two terminal T nucleotides located at the 3' end of the padlock sequence dictate the specificity of the assay to detect only the resistant alleles which contain the AA SNPs at the complementary location. The ligation and circularization of the padlock probe is dependent on the interaction between these two complementary sequences (see **Figure 3**).

Allele-specific target (T.cas\_Res\_RCA - 5' GCTTTAACTGGAAGCATAGCG 3') and non-target (T.cas\_Sus\_RCA - 5'GCTTTAACTGGGGGCATAGCG 3') sequences were synthesized to represent the SNP-containing region of the *T. castaneum* DLD gene.

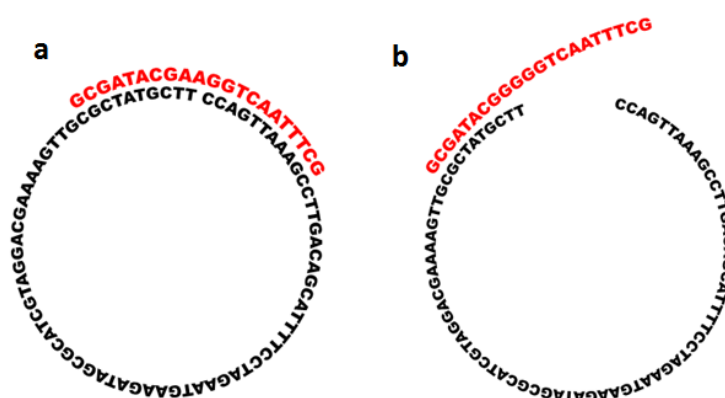


**Figure 3.** Target-dependant circularization of padlock probe. (a) Allele-specific resistant target, (b) non-target susceptible.

**2.5. Padlock Probe Ligation and Rolling Circle Amplification (RCA).** The L-RCA assays begin with the target-dependent ligation of the padlock probe. For detail of reaction compositions see Table 1 in Supplementary Information. Specifically, 50 ng of padlock probe was used in the ligation assay along with 5  $\mu$ l of 10x T<sub>4</sub> DNA ligase buffer (Thermo Fisher Scientific); 5 U T<sub>4</sub> DNA ligase (Thermo Fisher Scientific); 1  $\mu$ l of target or non-target probe and 5% w/v Polyethylene glycol (PEG4000) mixed thoroughly with nuclease-free water to the final volume of 50  $\mu$ l. Ligation reactions were incubated for 1 hour at 22°C. Following this, 4  $\mu$ l of ligation mixture was used directly for the RCA reaction. Other components of RCA reaction were 2.5  $\mu$ l 10x phi29 DNA polymerase reaction buffer (Thermo Fisher Scientific), 200  $\mu$ M dNTPs also added to the reaction tube, and +/- 0.6  $\mu$ M circular padlock probe for some reactions (Supplementary information). Total volume of each reaction was 25  $\mu$ l by adding

sterilized water. Reactions were incubated at 30°C for 2 hours. Amplification products were visualized by gel electrophoresis using 0.8% agarose and RedSafe nucleic acid stain (iNtRON).

### 3. Result and Discussion

**3.1. DLD Amplification and Sequencing.** In order to confirm the presence of the resistant allele in the *T. castaneum* specimens we were provided, the relevant region of the DLD gene<sup>34</sup> was amplified from the genomic DNA template extracted from four adult *T. castaneum* individuals (**Figure 4**).

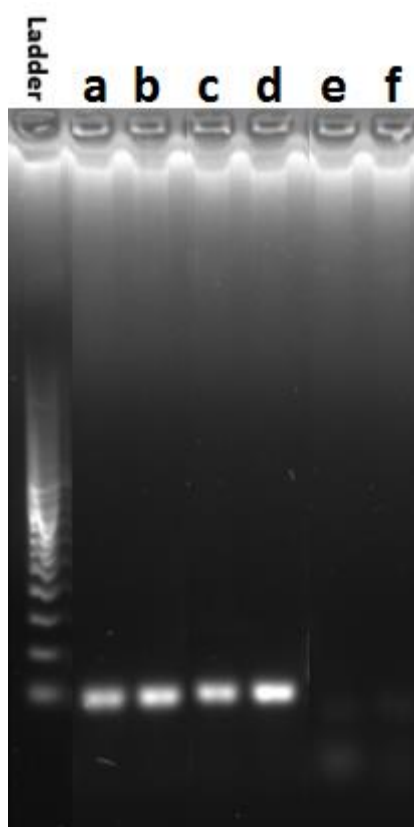


**Figure 4.** Visualization of resistant-susceptible amplified DLD gene products (100 bp) from gDNA of QTC279 and QTC4 *T. castaneum* strains by agarose gel electrophoresis of PCR product with negative control tests. The first lane contains the molecular weight ladder (50-2000 bp). The other lanes are labelled representing various PCR reactions in this study, (a) *T.*

*castaneum* QTC279 DLD-rxn 1, (b) *T. castaneum* QTC4 DLD-rxn 3, (c) *T. castaneum* QTC279 DLD-rxn 2, (d) *T. castaneum* QTC4 DLD-rxn 4, (e) and (f) H<sub>2</sub>O negative controls. PCR products of lanes a, b, c and d represent the DLD gene amplified from *T. castaneum* genomic DNA.

The average length of quality bases obtained from Sanger sequencing the purified PCR products was 37 bp and this provided clear sequence over the SNP-containing region of the DLD gene.

**3.2. Sequence Analysis.** Reverse sequences for the TcDLD primers were aligned using BioEdit software<sup>33</sup>, against known susceptible (QTC4- accession KX907540.1) and resistant (931-KX907541.1) stains from NCBI and two SNPs (A-G) identified (**Figure 5**).

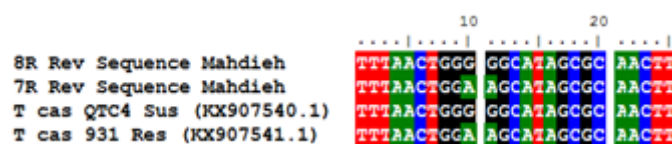


**Figure 5.** Sequence alignment of PCR product in this study with GenBank sequences. “8R Rev Sequence Mahdieh” represented the susceptible *T. castaneum* population, showing GG at position 10 and 11. The “7R Rev Sequence Mahdieh” confirmed the resistant SNP site showing AA positions 10 and 11 in the resistant population.

**3.3. L-RCA Assay.** The L-RCA protocol was able to distinguish between the synthetic resistant probe as target (**Figure 6A and 6C**) and the susceptible probe as non-target (**Figure 6E and 6F**). This indicates that the assay could distinguish between phosphine resistant and phosphine susceptible alleles of the DLD gene in *T. castaneum* based on the SNP site. We have used single stranded oligonucleotides as our targets here which are also capable of acting as the primer of the RCA reaction. However, if we were to move on to a genomic DNA target, we would need to include a padlock primer in order to initiate the L- RCA reaction after the ligation. Here, we have also shown that the L- RCA reaction takes place in the presence of this

padlock primer (**Figure 6C**). L- RCA enabled the continuous replication of the ligated circular single-stranded target DNA molecule. This resulted in a large amplification product which can be seen as greater than 1000 bp compared to corresponding ladder lane. Ligase negative reactions including 5B, 5D and resistant/susceptible target-free reactions including 5G and 5H did not show any amplification. This confirms that L-RCA reaction is dependent on the presence of resistant sequence.



**Figure 6.** L-RCA visualization. Lanes are labelled representing L-RCA tests in this study, (A) resistant target-self primed, (B) Ligase free reaction-resistant target-self primed, (C) resistant target- primed, (D) Ligase free reaction-resistant target-primed, (E) susceptible non target-self primed, (F) susceptible non target- primed, (G) Negative control-self primed, (H) Negative control-primed. Ladder lane 100-1000 bp is highlighted as standard valuation. L-RCA products of lanes A, C are visible.

## 4. Conclusion

Here we have demonstrated the feasibility of using the L-RCA reaction to monitor for resistant alleles in *T. castaneum*. While only demonstrated using synthetic single-stranded oligonucleotides as a model system for the *T. castaneum* DLD gene, we are confident with further work, this would translate to detection of the resistance-related SNP using the PCR product, or more ideally, genomic DNA as the template in the reaction. In the future, we hope to transfer this solution-based genotyping assay to a biosensor platform capable of monitoring biological events by detecting molecular changes at a solution/surface interface. Detection platforms using DNA on solid supports, such as microarrays, allow for the confinement of reactions based on location on the support and lead to the ability to multiplex with other gene targets. Multiplexing would be beneficial in monitoring for resistance mechanisms based on more than one biochemical pathway and involving SNPs on more than one gene target. Microarrays, however, still require fluorescent labelling and the corresponding fluorometry-based readers, and can sometimes suffer with specificity and sensitivity issues<sup>35</sup>. An L-RCA reaction hybridized onto a surface could not only be a sensitive SNP detection method<sup>36,37</sup> but additionally, by coupling the reaction to a transduction mechanism sensitive to small changes<sup>38, 39</sup>, the amplification event could potentially be monitored in real-time without the need of fluorescent labels and readers.

Insect resistance to insecticides is an ever evolving problem and technology towards potentially enabling quick and easy surveillance of known resistant targets in the field would be a helpful tool for pest management. While we focus on genotyping applications in agricult-



ure, L-RCA has also gained considerable attention in advanced bio-recognition studies for protein detection. For instance, highly sensitive protein aptamer detections were developed based on L-RCA<sup>26,28</sup>. This increases the potential applications for an L-RCA based biosensor platform for detection of both protein and nucleic acid targets. While there are many other applications in agriculture such as identification of pathogens and disease, this type of sensor could be of use in other fields such as health and medicine and environmental monitoring.

**NOTE:** This proof-of-concept SNP detection assay is not completed during this PhD thesis to prove proposed.

## References

- 1- Bell, C. H., Fumigation in the 21<sup>st</sup> century. *Crop Production* **2000**, (19), 563-569.
- 2- Chaudhry, M. Q., Phosphine resistance. *Pesticide Outlook* **2000**, (11), 88-91.
- 3- Scheffrahn, RH.; Hsu, RC.; Osbrink, WL.; Su NY., Fluoride and sulphate residues in foods fumigated with sulphuryl fluoride. *Journal of Agricultural and Food Chemistry* **1989**; (37),203–206.
- 4- Mills, K.A., Phosphine resistance: where to now. In: Donahaye, EJ, Navarro, S and Leesch JG, editors. *Proceeding Internatinal Conference on Controlled Atmosphere and Fumigation in Stored Products*, **2000**, 583–591.
- 5- Winks, R.G., Resistance to the fumigant phosphine in a strain of *Tribolium castaneum* (Herbst). **1969**, M.Sc. thesis, University of Queensland, 145p.

- 6- Monro, H.A.U.; Upitis, E.; Bond, E.J., Resistance of a laboratory strain of *S. granarius* (L.) (Coleoptera: Curculionidae) to phosphine. *Journal of Stored Products Research* **1972**, (8), 199-207.
- 7- Attia, El., Insecticide resistance in pyralid moths of grain and stored products. *General and Applied Entomology* **1981**, (13), 3-8.
- 8- Nayak, M.; Emery, R.; Holloway, J.; Phillips, T., Strength and spatio-temporal dynamics of resistance to phosphine and contact insecticides in key stored grain pests. *Plant Biosecurity Cooperative Research Centre* **2016**. Final report
- 9- Jagadeesan, R.; Fotheringham, A.; Ebert, PR.; Schlipalius, DI., Rapid genome wide mapping of phosphine resistance loci by a simple regional averaging analysis in the red flour beetle, *Tribolium castaneum*. *BMC Genomics* **2013**. (14), 650.
- 10- Schlipalius, DI.; Valmas, N.; Tuck, AG.; Jagadeesan, R.; Ma, L.; Kaur, R.; et al. A core metabolic enzyme mediates resistance to phosphine gas. *Science* **2012**. (338), 807-810.
- 11- Chen, Z.; Schlipalius, D.; Opit, G.; Subramanyam, B.; Phillips, T. W., Diagnostic molecular markers for phosphine resistance in U.S. populations of *Tribolium castaneum* and *Rhyzopertha dominica*. *PLoS ONE* **2015**. 10(3), e0121343.
- 12- Li, N.; Mei, L.; Xiang, Y.; Tong, A.; Nishizawa, S.; Teramae, N., Fluorescence detection of single-nucleotide polymorphisms with two simple and low cost methods: a double-DNA-probe method and bulge form method. *Analytica Chimica Acta* **2007**. (597), 97-102.
- 13- McCarthy, J. J.; Hilfiker, R., The use of single-nucleotide polymorphism maps in pharmacogenomics. *Nature Biotechnology* **2000**. (18), 505-508.

- 14- Kuhner, M. K.; Beerli, P.; Yamato, J.; Felsenstein, J., Usefulness of single nucleotide polymorphism data for estimating population parameters. *Genetic* **2000**. (156), 439-447.
- 15- Landegren, U.; Kaiser, R.; Sanders, J.; Hood, L., A ligase-mediated gene detection technique. *Science* **1988**. (241), 1077-1080.
- 16- Wu, DY.; Wallace, RB., The ligation amplification reaction (LAR)—amplification of specific DNA sequences using sequential rounds of template-dependant ligation. *Genomics* **1989**. (4), 560-569.
- 17- Tobe, V. O.; Taylor, S. L.; Nickerson, D. A., Single-well genotyping of diallelic sequence variations by a two-color ELISA-based oligonucleotide ligation assay. *Nucleic Acids Research* **1996**. (24), 3728-3732.
- 18- Alderborn, A.; Kristofferson, A.; Hammerling, U., Determination of single-nucleotide polymorphisms by real-time pyrophosphate DNA sequencing. *Genome Research* **2000**. (10), 1249-1258.
- 19- Beaudet, L.; Bédard, J.; Breton, B.; Mercuri, R.J.; Budarf, M.L., Homogenous assays for single-nucleotide polymorphism typing using AlphaScreen. *Genome Research* **2001**. (11), 600-608.
- 20- Fujii, K.; Matsubara, Y.; Akanuma, J.; Takahashi, K.; Kure, S.; Suzuki, Y.; Imaizumi, M.; Iinuma, K.; Sakatsume, O.; Rinaldo, P.; Narisawa, K., Mutation detection by TaqMan-allele specific amplification: application to molecular diagnosis of glycogen storage disease type Ia and medium-chain acyl-CoA dehydrogenase deficiency. *Human Mutation* **2000**. (15), 189-196.

- 21- Hall, J. G.; Eis, P. S.; Law, S. M.; Reynaldo, L. P., Prudent, J. R.; Marshall, D. J.; Allawi, H. T.; Mast, A. L.; Dahlberg, J. E.; Kwiatkowski, R. W.; Arruda, M. D.; Neri, B. P., Sensitive detection of DNA polymorphisms by the serial invasive signal amplification reaction. *Proceedings of the National Academy of Sciences of the United States of America* **2000**. (97), 8272-8277.
- 22- Qi, X.; Bakht, S.; Devos, K. M.; Gale, M. D.; Osbourn, A., L-RCA (ligation-rolling circle amplification): a general method for genotyping of single nucleotide polymorphisms (SNPs). *Nucleic Acids Research* **2001**. (29), e116.
- 23- Ou, L.; Sun, A.; Liu, K., Rolling circle amplification-based biosensors. *Analytical Letters* **2015**. 48, 1199-1216.
- 24- Schweitzer, B.; Roberts, S.; Grimwade, B.; Shao, W.; Wang, M.; Fu, Q.; Shu, Q.; Laroche, I.; Zhou, Z.; Tchernev, V. T.; Christiansen, J.; Velleca, M.; Kingsmore, S. F., Multiplexed protein profiling on microarrays by rolling-circle amplification. *Nature Biotechnology* **2002**. 20, 359-365.
- 25- Shao, W.; Zhou, Z.; Laroche, I.; Lu, H.; Zong, Q.; Patel, D. D.; Kingsmore, S.; Piccoli, S. P., Optimization of rolling-circle amplified protein microarrays for multiplexed protein profiling. *Journal of Biomedicine and Biotechnology* **2003**. 5, 299-307.
- 26- Zhou, H.; Bouwman, K.; Schotanus, M.; Verweij, C.; Marrero, J. A.; Dillon, D.; Costa, J.; Lizardi, P.; Haab, B. B., Two-color, rolling-circle amplification on antibody microarrays for sensitive, multiplexed serum-protein measurements. *Genome Biology* **2004**. 5 (4), R28.

- 27- Schweitzer, B.; Kingsmore, S. F., Measuring proteins on microarrays. *Current Opinion in Biotechnology* **2002**. 13, 14-19.
- 28- Gao, W-M.; Kuick, R.; Orcekowski, R. P.; Misek, D. E.; Qiu, J.; Greenberg, A. K.; Rom, W. N.; Brenner, D. E.; Omenn, G. S.; Haab, B. B.; Hanash, S. M., Distinctive serum protein profiles involving abundant proteins in lung cancer patients based upon antibody microarray analysis. *BMC Cancer* **2005**. 5, 110.
- 29- Seidy, P.; Isabel, G., Microarray and nanotechnology applications of functional nanoparticles. *Combinatorial Chemistry & High Throughput Screening* **2006**. 9, 389-397.
- 30- Hsu, H-Y.; Huang, Y-Y., RCA combined nanoparticle-based optical detection technique for protein microarray: a novel approach. *Biosensors and Bioelectronics* **2004**. 20, 123-126.
- 31- Huang, Y-Y.; Hsu, H-Y.; Huang, C-J. C., A protein detection technique by using surface plasmon resonance (SPR) with rolling circle amplification (RCA) and nanogold-modified tags. *Biosensors and Bioelectronics* **2007**. 22, 980-985.
- 32- Yasui, T.; Ogawa, K.; Kaji, N.; Nilsson, M.; Ajiri, T.; Tokeshi, M.; Horiike, Y.; Baba, Y., Label-free detection of real-time DNA amplification using a nanofluidic diffraction grating. *Scientific Reports* **2016**. 6, 31642.
- 33- Hall, T. A., BioEdit: a user friendly biological sequence alignment editor and analysis program for windows 95/98/NT. *Nucleic Acid Symposium Series* **1999**. (41), 95-98.
- 34- Oppert, B.; Guedes, R. N. C.; Aikins, M. J.; Perkin, L.; Chen, Z.; Phillips, T. W.; Zhu, K. Y.; Opit, G. P.; Hoon, K.; Sun, Y.; Meredith, G.; Bramlett K.; Hernandez, N. S.;

- Sanderson, B.; Taylor, M. W.; Dhingra, D.; Blakey, B.; Lorenzen, M.; Adedipe, F.; Arthur, F., Genes related to mitochondrial functions are differentially expressed in phosphine-resistant and –susceptible *Tribolium castaneum*. *BMC Genomics* **2015**. (16), 968.
- 35- Draghici, S.; Khatri, P.; Eklund, A. C.; Szallasi, Z., Reliability and reproducibility issues in DNA microarray measurements. *Trends in Genetics* **2006**. 22(2), 101-109.
- 36- Wu, Z-S.; Zhang, S.; Zhou, H.; Shen, G-L.; Yu, R., Universal aptameric system for highly sensitive detection of protein based on structure- switching- triggered rolling circle amplification. *Analytical Chemistry* **2010**. (82), 2221-2227.
- 37- Nallur, G.; Luo, C.; Fang, L.; Cooley, S.; Dave, V.; Lambert, J.; Kukanskis, Kari; Kingsmore, S.; Lasken, R.; Schweitzer, B., Signal amplification by rolling circle amplification on DNA microarrays. *Nucleic Acids Research* **2001**. 29 (23), e118.
- 38- Yang, L.; Fung, C. W.; Cho, E. J.; Ellington, A. D., Real-time rolling circle amplification for protein detection. *Analytical Chemistry* **2007**. (79), 3320-3329.
- 39- Goda, T.; Tabata, M.; Miyahara, Y., Electrical and electrochemical monitoring of nucleic acid amplification. *Frontiers in Bioengineering and Biotechnology* **2015**. (3), 29.

## Supplementary Information

**Table 1.** L-RCA reaction tests

Reaction	Figure 5	Padlock probe	Resistant target	Susceptible non-target	Padlock primer	T <sub>4</sub> DNA ligase	ligase buffer	Phi29 polymerase	dNTPs
Resistant target-self primed	5A	+	+	-	-	+	+	+	+
Ligase free-resistant target-self primed	5B	+	+	-	-	-	-	+	+
Resistant target-primed	5C	+	+	-	+	+	+	+	+
Ligase free-resistant target-primed	5D	+	+	-	+	-	-	+	+
Susceptible non target-self primed	5E	+	-	+	-	+	+	+	+
Susceptible non target-primed	5F	+	-	+	+	+	+	+	+
Negative control-self primed	5G	+	-	-	-	+	+	+	+
Negative control-primed	5H	+	-	-	+	+	+	+	+

**BLANK PAGE**



## CHAPTER 7.

---

### **Conclusions and Recommendations for Future Works**

**Chapter- 7** summarized the research that have been carried and reported in this thesis. This chapter also highlights some perspectives for future work towards smart biosensing technology based on NAA and RfS.

**BLANK PAGE**

## **7.1. Conclusions**

### **7.1.1. Summary**

The research presented in this thesis aims to advance the knowledge about the electrochemical structural engineering and optical characteristics of NAA porous platforms, their surface chemistry modification, and application for development of a label-free, ultrasensitive, portable, and low-cost sensing of biomolecules using reflectometric interference spectroscopy (RIFS). The starting point and major contribution of this thesis is understanding and designing of NAA sensing platform using electrochemical anodization process to improve their optical and photonic properties used for RIFS sensing. For that purpose several electrochemical anodization procedures were developed to make different NAA structures with straight, multilayered layered pore structures and rugate photonic crystal structures to optimise their sensing performances for different applications. Understanding and optimising of NAA structural pore geometry, in particular the ability to generate complex photonic structure was used to develop a NAA rugate filters and NAA bilayered structures. The second major contribution of this thesis is the establishment of surface functionalisation of prepared NAA sensing platforms in order to modify their surface chemistry to provide selective surface functional groups for biosensing purposes. This concept was used to develop a label-free, ultrasensitive, portable, and low-cost detection device for determining bio-analytes in pharmaceutical and medical scenarios. These complex NAA photonic structures were selectively functionalised with silane in order to prove their sensing performances using selected model molecules including proteins, enzymes, organic molecules and DNA. The sensing performance of various NAA structures was optimised using RIFS monitoring and then proved that structural engineering of NAA photonic structure plays crucial roles in determining the sensing performance of the system. The final element of this thesis investigates is the use

of a molecular assay, a Ligation-Rolling Circle Amplification (L-RCA) assay that could potentially be incorporated into our biosensing platform for a portable real-time genotyping system to use in agricultural applications. Specifically, an assay was designed to detect the presence of Single Nucleotide Polymorphisms associated with phosphine resistance in insect pests. This high yield amplification technique makes it possible to potentially adapt this assay into flow conditions used for biosensing with our NAA and RIfS in future. The following sections outline the specific conclusions drawn from all the studies included in this thesis.

### **7.1.2. Label-Free Real-Time Quantification of Enzyme Levels by Interferometric Spectroscopy Combined with Gelatin-Modified Nanoporous Anodic Alumina Photonic Films (Chapter 3)**

A selective and highly sensitive, label-free, and portable biosensor for detection of trypsin using NAA as the sensing substrate and RIfS as the sensing technique was developed. The following conclusions were drawn from this study.

- 1- Series of NAA sensing platforms were successfully fabricated with hexagonally packed cylindrical pores with controllable pore diameters and length that controlled by carefully controlled anodization parameters.
- 2- It was demonstrated that the NAA pore surface could be easily modified with amino functional groups using silane chemistry (APTES) via a simple process of chemical vapour deposition (CVD). The CVD method provided active terminal group for further selective binding of biomolecules to act as sensing probe for broad range of analyte molecules. In this chapter, the surface of NAA was specifically modified with silane having amino-terminus to provide the sensing platform with selectivity towards trypsin molecules.

- 3- The developed trypsin biosensor shows a broad analysis range from 0.0125 to 1.0 mg mL<sup>-1</sup> trypsin molecules with a linear detection range of 0.9140. The lower limit of detection was 0.025 ± 0.005 mg mL<sup>-1</sup> trypsin solution.

The sensor was selective and sensitive for detection of trypsin molecules, not only towards analyte molecules but also towards sensing element. This was confirmed by monitoring the RIfS response on exposure to aqueous solutions of haemoglobin instead of gelatin (i.e. sensing element) at the concentration of 1 mg mL<sup>-1</sup>.

- 4- Finally, the binding kinetics of trypsin with gelatin on NAA surface were obtained by fitting the RIfS data to Michaelis–Menten model. The obtained fitting curve suggests that the enzymatic reaction follow the reaction velocity as the data fits well to Michaelis–Menten non-linear curve. These results showed capability of NAA platform not only to be used for sensing but also for other type of applications such as study binding kinetics and enzymatic reactions.

### **7.1.3. Assessment of Binding Affinity between Drugs and Human Serum Albumin Using Nanoporous Anodic Alumina Photonic Crystals (Chapter4)**

An innovative fabrication and optimisation of NAA produced novel porous crystals as rugate filters and the performance of the prepared rugate filters was established and its application for specific absorption/desorption human serum albumin with different concentrations of indomethacin was demonstrated. The following conclusions were drawn from this study.

- 1- A sinusoidal pulse anodization approach was developed to prepare NAA-RFs with periodically ordered pore structures and specific optical and photonic properties. Nine different types of NAA-RFs were fabricated by modifying the anodization parameters (i.e., anodization period [ $T_P$ ], and anodization offset [ $J_{Offset}$ ]), which enabled the

rational engineering of effective medium of NAA in depth. These NAA-RFs display complex optical reflection spectrum with non-uniform stopband.

- 2- The optical characteristics of these nine NAA-RFs were assessed by measuring two characteristic optical sensing parameters (i.e. reflection peak of stopband and effective optical thickness of the film), by absorption/desorption with indomethacin molecules. The aforementioned sensing parameters showed effective optical thickness is stronger and more sensitive sensing parameter than reflection peak changes.
- 3- The obtained optical response data from these structures revealed that the most sensitive structures toward indomethacin molecules were NAA-RF<sub>( $T_P = 750$ ,  $J_{Offset} = 0.42$ )</sub> and NAA-RF<sub>( $T_P = 750$ ,  $J_{Offset} = 0.14$ )</sub> for reflection peak changes and effective optical thickness changes, respectively.
- 4- The results showed that the fabricated NAA-RFs were highly selective towards detection of indomethacin by assessment of binding affinity between human serum albumin and a set of drug. Lastly, the data was fitted to contour map to verify and validated the dependence of sensitivity on the fabrication parameters ( $T_P$  and  $J_{Offset}$ ) for reflection peak and effective optical thickness changes.
- 5- The proposed sensing system combining HSA-modified NAA-RFs and RIfS provided a reliable binding affinity assessment between human serum albumin and drugs with a set of features such as portability, low cost, and easy operation that makes it a promising alternative to benchmark techniques such as SPR.

Therefore, this chapter contributes to the development of optical biosensor based on the optimisation and structural engineering of the NAA sensing platform with enhanced RIfS signals.

#### **7.1.4. Structural Engineering and Optimization of Bilayered Nanoporous Anodic Alumina Structures as Multi-Point Sensing Platform (Chapter 5)**

An innovative strategy to achieve the optimal design of hierarchical structures on NAA sensing platforms with multiple optical layers (i.e. top layer of hierarchical structure, bottom layer of hierarchical structure, and combination of top and bottom layer) was established to advance optical sensing performance. The sensing performance of the bilayered NAA structures specifically modified with human serum albumin was assessed for sensing of model molecule quercetin in order to evaluate ability of this platform for multi sensing applications. The following conclusions were drawn from this study.

- 1- Three types of bilayered NAA photonic structures featuring different pore geometries (i.e. pore diameters and pore lengths) are fabricated by tailoring the anodization time and number of anodization steps combined with chemical pore widening steps
- 2- The structural characterization of bilayered NAA demonstrated hierarchical nanopore shape with larger pore diameter on top and smaller pore diameter on the bottom.
- 3- The optical characteristics of the triple of NAA photonic structures were evaluated by fast Fourier transform analysis and RIfS spectra showing three distinctive peaks which are capable to support monitoring scheme, independently.
- 4- The RIfS data concludes that bilayered NAAs are multi-functional sensing platforms which enables monitoring sensing parameter (i.e. effective optical thickness changes) at different levels of sensitivity. The sensing performance under specific binding reaction (i.e. human serum albumin and quercetin) certifies the optimal bilayered NAA structure. The bottom layer with less thickness features higher sensitivity than top layer with larger thickness showing capability of this platform to selectively detect molecules using pore structure with different diameters.

- 5- Finally, it was concluded that all these 3 layers can be used independently for sensing which means with different surface chemistries this bilayered NAA can be used for multi analyte biosensing.

### **7.1.5. Towards Detection of Single Nucleotide Polymorphism Associated with Phosphine Resistance in *Tribolium Castaneum* Using Ligation-Rolling Circle Amplification (Chapter 6)**

The long term aim of this work is to design for resistant-allele detection of DLD gene from *T. castaneum* using NAA-RIFS. Although the proof-of-concept is not completed yet, a preliminary result is based on a Ligation-Rolling Circle Amplification (L-RCA) technique for detection of single nucleotide polymorphisms within a gene, known to be associated with insecticide resistance was developed. The following conclusions were drawn from this study.

- 1- The DLD gene from *Tribolium castaneum* specimens was successfully amplified using polymerase chain reaction. The SNP-containing region was confirmed in the resistant population by sequence analysis.
- 2- Using a synthetic, model system to test the assay design, the amplification-RCA, product (>1000 bp). A product was only produced in the assay when tested against an oligonucleotide (oligo) representing the resistant allele sequence was present, and not when the oligo encoding the susceptible allele sequence, demonstrating the specificity of the test.

## **7.2. Recommendations for future works**

This thesis advances the knowledge about the structural engineering and optical features of NAA as a powerful RIFS sensing platform for broad biosensing applications. The results



presented in this thesis are very encouraging showing great potential of NAA platform that needs further improvement and advancement for their translation in real sensing devices. The following points outline future directions in the field of NAA optical platform towards development of portable and low-cost RIFS biomedical devices.

A number of future research activates and new ideas generated from this thesis that requires more studies are outlined below:

- 1- **Engineering of advanced NAA structures:** Although a variety of NAA photonic structures have been produced in this thesis and by other groups s more work is required to develop more versatile photonic structures in NAA such as multi-layered pore structures, multiple branched pore structure, complex pore architectures, to advance their sensing performances. NAA photonic crystals fabricated by electrochemical anodization using variable anodization profile (current or voltages) and different anodization parameters need further optimisation to make structures with precise defined pore diameters, periodicity and length of theses structure with better understanding their impact on RIFS signal required for biosensing. These new NAA photonic structures could provide higher sensitivity detection of a large variety of biomolecules that could also provide versatility of molecules detection, improve sensitivity, selectivity and sensing device design.
- 2- **Surface modifications and functionalization:** The other important part on development of NAA optical sensing is surface modification of internal pore structures with specific functional groups able to provide selective binding of targeting molecules with high sensitivity. This part is not deeply explored in this thesis and considering that number of techniques are available to modify the surface chemistry of NAA and further improve performances of these platforms and extend the application for broad number of molecules in biomedical, pharmaceutical and environmental fields.

Specifically developed of layered surface chemistry inside pores (bilayered or multiple layered) has potential to develop highly advanced platform for multi analyte detection to provide analysis of molecules from complex matrix. Furthermore, more research is recommended to develop surface modification strategies to prepare these “dressed chemistries” inside pores for specific and selective binding of several biomolecules.

- 3- **DNA and Gene Biosensing:** Thirdly, further investigation is needed into the feasibility and applicability of a sensitive and selective genotyping biosensor based on NAA and RIFs. We have focussed on an agriculture application as fast detection and in-field diagnostic capabilities are of great interest in order to make timely control decisions in terms of pest management, yet little is published in this area. We have designed and begun to investigate the feasibility of detecting SNPs with a solution-based L-RCA assay. However, time limitations meant we have not yet determined if this assay can effectively be coupled to the NAA sensor surface. Although, previously the NAA surface has shown to be functional when be modified with DNA probes, therefore, NAA based RIFs has the potential to be used for this L-RCA allele detection technique. This type of biosensor would provide the opportunity to monitor insect pest populations on a label-free platform and in real-time.
- 4- **Sensor and device design improvement:** In this work to evaluate sensing performance of fabricated NAA platform (10 mm in diameter) we used special flow cell combined with RIFs and notebook PC that are not optimised for potential real application. Therefore new design with miniaturised NAA platform combined with new microfluidic system is desirable that will require minor amount of sample and also improve sensitivity.

5- **Applications:** In this thesis the focus of sensing by NAA platform was on biomolecules for biomedical applications. However, this platform is versatile and can be used for broad applications so more studies are recommended to develop devices for industrial, environmental, and agricultural purposes.